Synthesis and Characterisation of Ferrocenyl Monolayers on Silicon surfaces

Mufida Abdualla

A Thesis Submitted in Partial Fulfilment of Requirements for the Degree of Doctor of Philosophy

School of Chemistry

Newcastle University

July 2013

Acknowledgements

First and foremost, I thank God (ALLAH) for giving me the courage to complete this project. My deepest gratitude and appreciation to my supervisors; Dr. Andrew Pike for his support and guidance during the project, and Dr. Michael Hall for his guidance during the synthesis, without them none of the work presented here would have been possible.

Gratitude is also owed to collaboration group, Dr. Shaun Cook and Dr. Benjamin Horrocks for study electron transfer of the ferrocenyl silicon surface by photoelectrochemical transients. I would like also to thank Professor Thomas Wandlowski and his group (Department of Chemistry and Biochemistry, University of Bern) for electrochemical scanning tunnelling spectroscopy study of a ferrocene-modified silicon surfaces**.**

Special thanks must go to Dr Majid Al Nakeeb and Dr. Scott Watson for their comments on some parts of this thesis, and also for their discussions and support during the project.

My deep gratitude to all staff and students in the Chemical Nanoscience Laboratory (School of Chemistry at Newcastle University) for all their discussions and support.

Appreciation is also due to Prof Peter Cumpson and Dr. Anders Barlow for their help in the XPS experiments.

Thanks must go to Azzaytuna University and the Ministry of Higher Education in Libya for the financial support without that this work would never have completed.

My final thanks and deep appreciation must go to my husband, Abduladim, and the reasons for that are numerous and countless. Furthermore, I cannot forget to give a big thank for my son, Abdalmohaimen, who always make me smile and happy after a long and hard working day. I am also extremely grateful to my family (my parents, my sisters, and my brothers) and my family in-law in Libya for their love, support, encouragement and prayers. Finally, I also thank all of my friends for their love and support.

Dedication

This thesis is dedicated to my mother and my father.

Mufida Abdualla

Abstract

A series of ferrocenyl monolayers on hydrogen-terminated Si(111) single crystal and porous silicon have been prepared and characterised by atomic force microscopy (AFM), X-ray photoelectron spectroscopy (XPS), and cyclic voltammetry (CV).

Hydrosilylation modification of hydrogen-terminated Si(111) single crystal and porous silicon with vinylferrocene and ethynylferrocene was shown to produce three different silicon–carbon tethered ferrocenyl surfaces, Si-CH_2-CH_2-Fc, Si-CH=CH-Fc, and Si-C≡C-Fc. Three different grafting procedures were used, a thermally activated method at 110 °C in toluene using vinylferrocene produced the Si-CH_2-CH_2-Fc monolayer, **EFc**. Hydrosilylation at room temperature using ethynylferrocene in the minimum amount of dichloromethane produced the Si-CH=CH-Fc surface, **VFc**. Finally, the reaction of *n*-butyllithium with ethynylferrocene via a nucleophilic substitution reaction (acetylide anion) at the silicon hydride electrode produced the Si-C≡C-Fc surface, **EnFc**. Transmission FTIR analysis confirmed that three different linkages were formed on porous silicon. Data recorded using cyclic voltammetry showed that ferrocenyl silicon monolayers were more stable in acetonitrile than aqueous electrolyte. The maximum surface coverage measured in acetonitrile was 1.3×10^{-10} mol cm^{-2} for the **EFc** surface, 2.7×10^{-11} mol cm^{-2} for the **VFc** surface**,** and 5.4×10^{-11} mol cm^{-2} for the **EnFc** surface.

However, reproducibility of the **EFc**, **VFc** and **EnFc** surfaces was not easy to control. In order to find a way to improve reproducibility, a series of 50:50 mixtures of vinylferrocene and simple alkenes were investigated. The alkenes used for this purpose were hexene (**EFc/C_6**), octene (**EFc/C_8**), decene (**EFc/C_{10}**), and undecene (**EFc/C_{11}**). AFM, XPS and CV were used to analyse these surfaces. Different surface coverages for 50:50 mol:mol in bulk solution of **EFc/C_6**, **EFc/C_8**, **EFc/C_{10}**, and **EFc/C_{11}** were obtained from CV in aqueous and acetonitrile electrolytes. Higher coverage was observed in acetonitrile than water for all 50:50 mixed monolayers, and the **EFc/C_8** surface was the more reproducible surface with a surface coverage of 4.0×10^{-11}mol cm^{-2}. Therefore, a range of more dilute **EFc/C_8** surfaces, 20:80, 10:90 and 1:99 were prepared via reaction with a vinylferrocene/octene mixture and characterised using AFM, XPS and CV. The cyclic voltammograms of dilute mixed monolayers **EFc/C_8** gave different surface coverages in acetonitrile electrolyte. The average observed were 3.03×10^{-11} mol cm^{-2}, 1.84×10^{-12} mol cm^{-2} and 7.95×10^{-13} mol cm^{-2} for 20:80, 10:90 and 1:99 **EFc/C_8** surfaces

respectively. The coverage of mixed **EFc/C$_8$** monolayers determined via CV was found to depend on the mole fraction of vinylferrocene in the initial alkylation solution, and it is possible to control the separation of ferrocene units on the silicon surface by controlling the mole fraction.

In addition, longer alkyl chain linkages between the ferrocene and silicon surface were investigated by two different approaches. In the first approach a ferrocenyl group with an extended tether was first synthesised, 1-(but-1-en-3-yne)ferrocene, and was then attached as a complete unit to the silicon surface using a one-step reaction to give the **BuFc** surface. In the second approach, the ferrocene monolayer was built up from the silicon surface in a two-step reaction procedure. In the first step, the silicon hydride surface was modified with 5-iodo-3-ethyl-2-ethynylthiophene to give the **Tp** surface. In the second step, the **Tp** surface was coupled to ethynylferrocene via the Sonogashira reaction to give the **TpFc** surface. In XPS a new Fe 2p peak and the concurrent disappearance of the I 3d peak was observed for the **TpFc** surface, which confirmed the replacement of the iodine by ethynylferrocene. The surface coverage obtained from CV for **BuFc**, (6.25×10^{-11} mol cm^{-2}), was higher than for **TpFc** surfaces, (7.2×10^{-12} mol cm^{-2}). This is could be due to a lower overall reaction yield being associated with each reaction in the two-step process.

In order to investigate the utility of ferrocene modified silicon surfaces in applications such as charge storage and memory devices, the **EFc** surface was studied using electrochemical scanning tunnelling spectroscopy which showed enhanced tunnelling current response that is directly related to the presence of the redox active ferrocene unit. The rate of electron transfer from ferrocenyl-monolayers to n-Si(111) was measured for both pure and mixed monolayers using light step photoelectrochemical chronoamperometry (PC). The rate constant associated with ferrocene oxidation is weakly dependent on applied potential, and is independent of the type of linkage, and the length of the n-alkyl chains in the mixed monolayers. The photoelectrochemical experiment provides a simple means to detect the extent to which the monolayer discharges in the dark and therefore can be used to assess the feasibility of charge storage in these monolayers.

Abbreviations

SAM	Self-assembled monolayers
LB	Langmuir-Blodgett
PS	Porous silicon
Si-H	Silicon hydride
EFc	Ethylferrocene monolayer on silicon
VFc	Vinylferrocene monolayer on silicon
EnFc	Ethynylferrocene monolayer on silicon
UND	Undecyl monolayer on silicon
OCT	Octyl monolayer on silicon
EFc/C_6	Ethylferrocenyl/hexenyl monolayer on silicon
EFc/C_8	Ethylferrocenyl/octenyl monolayer on silicon
EFc/C_{10}	Ethylferrocenyl/decenyl monolayer on silicon
EFc/C_{11}	Ethylferrocenyl/undecenyl monolayer on silicon
BuFc	1-(But-1,3-dien)ferrocenyl monolayer on silicon
Tp	Thiophene monolayer on silicon
TpFc	Thiophene-ferrocene monolayer on silicon
XPS	X-ray photoelectron spectroscopy
AFM	Atomic Force Microscopy
rms	Root-mean –square
CV	Cyclic voltammetry
FWHM	Full widths at half maximum

Contents

Chapter 1 - Introduction

Self assembled monolayers have been reported for a range of materials on a variety of substrates.[1] The interest in the development of molecular assemblies on surfaces is due to many applications such as sensors and biochips,[2] photovoltaics,[3] fuel cells,[4] biomaterials,[5] and molecular electronics.[3] This thesis is concerned with the fabrication of ferrocene self-assembled monolayers (SAM) on silicon surfaces. In this introductory chapter the preparation of monolayers through different types of chemistry is discussed. In particular, the attraction of utilizing silicon as a substrate for SAM formation is reviewed and ferrocenyl monolayers highlighted. Finally, in light of the following discussion, the contents of the proceeding chapters are outlined.

1.1 Monolayers

1.1.1 General concept of monolayer

Monolayers are formed from closely packed atoms or molecules on a surface as shown in Scheme 1.1.[6,7] Organic materials have been intensely studied in monolayer formation for many years.[6,7] Organic monolayers can allow for the physical and chemical properties of surfaces to be tailored with a high level of control, using molecules which will present specific functionality at the monolayer surface.[6] The selectively of the monolayer can be controlled by changing the end group of the monolayer. For example, by changing the methyl-terminus of a monolayer (hydrophobic surface) to a hydroxyl group (hydrophilic surface).[7] A large amount of literature has been published on ultrathin organic monolayers which can be achieved via a range of interactions between absorbate molecules and the surface substrate. These studies are based on monolayers prepared by physisorption, e.g. Langmuir-Blodgett technique (LB), or chemisorption, e.g. self-assembled monolayers (SAM).[1,6-16]

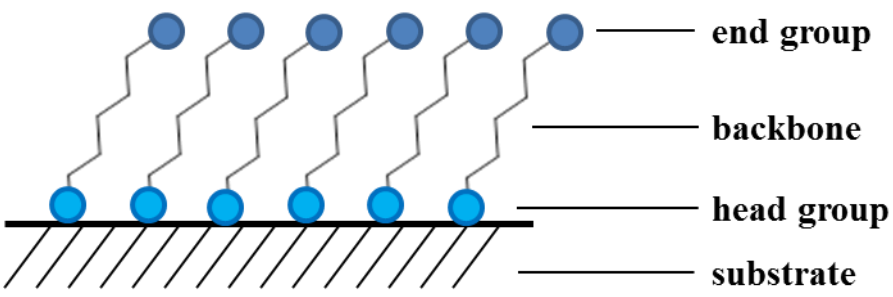

Scheme 1.1. Schematic of a SAM showing a variety of chemical functionalities; dark blue circle indicates chemisorbing head group and light blue circle the functional end group.

1.1.2 Preparation of ultrathin organic monolayers

Two of the most commonly reported methods used to make ultrathin organic monolayers are the Langmuir-Blodgett technique (LB), and self-assembly of monolayers (SAM). This section will describe the general points of both of these methods.

1.1.2.1 Langmuir–Blodgett

Langmuir–Blodgett assembly was the first technique used with organic material to produce one or more monolayers by transfer from a liquid-air interface to a solid support.[6,7] The preparation of LB films requires specialized equipment e.g. LB trough and bar. A trough is usually a water bath used to hold a subphase. In addition, a bar is used to compress the amphiphilic molecules on the surface of the subphase during the preparation of a molecular film, as shown in Scheme 1.2.[6-8] There are many solid substrates which have been used to prepare LB films, but most of these substrates are hydrophilic such as quartz, glass, aluminum, gold and silicon.[6] The polar head-group of the amphiphilic molecules is immersed in the water and the long hydrocarbon chain is pointing towards the air. The amphiphilic molecules are forced to order on the liquid subphase by slowly increasing the surface pressure and then are transferred to a solid substrate whilst maintaining a constant surface pressure as shown in Scheme 1.2.[17] The preparation of LB films is procedurally more complex than SAM formation, due to the LB technique requiring specialized equipment.[7,8] LB films have weak stability due to the non-covalent interaction between absorbate molecules and surface substrate. The LB technique has many advantages such as ability to produce smooth films with consistent thickness. In addition, the LB technique can also assemble molecules into a well-defined and stable structure without damage to the surface. Despite the advantages of the LB technique, there are also disadvantages, the LB films are not stable to high temperatures. Moreover, not all materials are suitable to use as a substrate, as the substrate has to be smooth and hydrophilic.

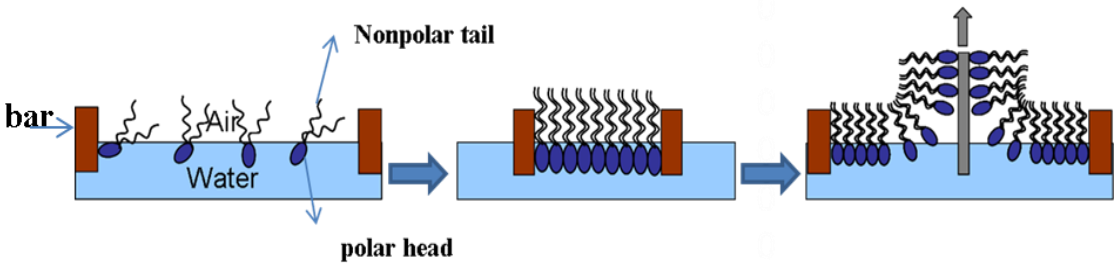

Scheme 1.2. Langmuir–Blodgett film prepared by dipping the solid substrate in a liquid phase containing amphiphilic compounds.

1.1.2.2 Self-assembled monolayers (SAM)

Self-assembled monolayers are organic molecular assemblies formed on a surface spontaneously by adsorption of the molecules. SAMs can be formed from solution or from the gas-phase.[7] There are two types of chemisorption, covalent or metal-ligand interactions. SAMs are generated by the chemisorption of molecules having a head group, backbone, and an end group.

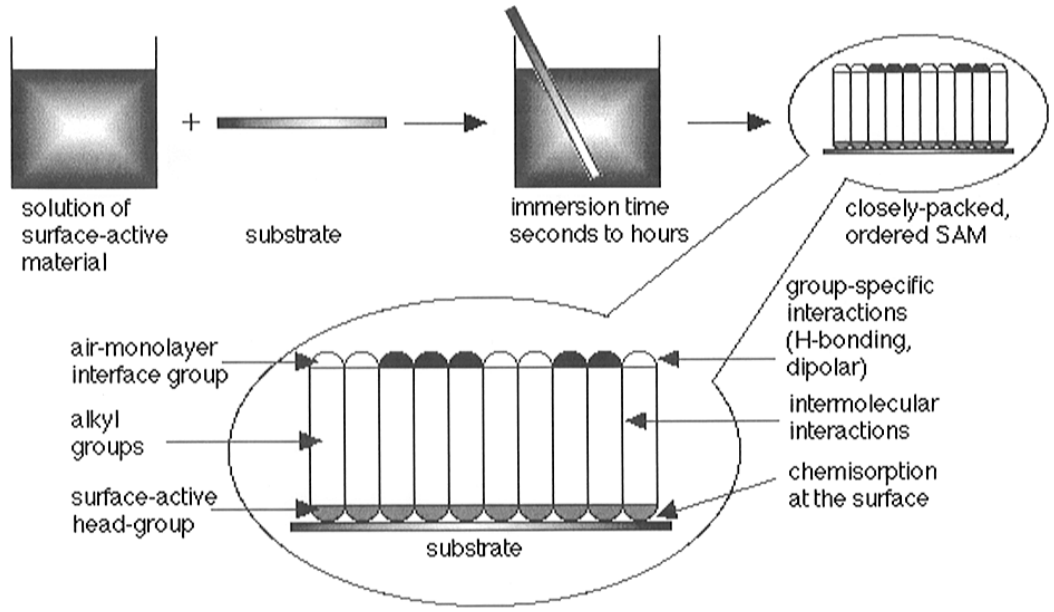

Scheme 1.3. Self-assembled monolayers are formed by simply immersing a substrate into a solution of the surface-active material. The driving force for the spontaneous formation of the 2D assembly includes chemical bond formation of molecules with the surface and intermolecular interactions.[15]

The head group of the molecule has a high affinity for the substrate. The backbone can play a role in the packing of the monolayer according to the kind of backbone, such as an alkyl chain, or aromatic ring, which can give different monolayer packing due to steric effects. The terminal end group, “tail”, can bear a functional group, so it can be

used to introduce other compounds at a later stage. The easy way to prepare a SAM is by immersing the substrate in a solution containing the molecules which will form the self-assembled monolayer, as shown in Scheme 1.3.[7,12,15]

SAMs such as thiol on gold or silanes on silicon are an attractive approach for many reasons such as the stability of these monolayers due to the strong chemisorption of the "head groups"[1,7,12] Moreover, the preparation of these SAMs are relatively easy compared with the Langmuir-Blodgett (LB) technique.[7] Furthermore, SAM formation is an attractive approach for building device monolayers by producing SAMs which bear multifunctional molecules.[7,12]

To summarise, a simple comparison of ultrathin organic monolayers prepared using the Langmuir–Blodgett technique and the self-assembled monolayers technique are shown in Table 1.1, an adaption from Patole's thesis.[17]

Features	LB-technique	SAM-technique
Driving force Between an adsorbate and a substrate	Physisorption, such as hydrogen bonding or Van-der Waals	Strong chemisorption
Types of ordering	The liquid/gas interface is controlled by the ordering of molecules before transfer to substrate	The solid/liquid interface is controlled bythe ordering of molecules.
Stability	Less thermal stability, structural changes during the transfer process	Better thermal and physical stability
Selection and type of molecules	Only long chain amphiphilic compounds	Different organic species can be combined, but specific functional group used depend on the surface
Substrate	Any substrate can be used	Selected surfaces can be used
Film formation control	The transfer film process is important	Kinetics of monolayer formation is important
Solubility restriction	Molecules should be surface active	Restriction by solubility of the molecules

Table 1.1. Comparison of ultrathin organic monolayers formed by Langmuir–Blodgett technique and self-assembled monolayers technique.[17]

In conclusion, the SAM technique can produce highly stable monolayers via an easy preparation compared with LB methods. Therefore, the next section will describe the different types of SAMs that can be produced.

1.2 Types of chemistry for SAM formation

Different types of chemistry can produce SAMs, such as thiols on gold, organosilane based layers on silicon dioxide, aryl diazonium salt derived layers and hydrosilylation

of alkenes on silicon hydride. This section will discuss these different types of SAM and their advantages and disadvantages.[1,7,9,12,15,18]

1.2.1 Organosulfur self-assembled monolayer

Assemblies of organosulfur compounds are one of the most widely used groups to fabricate SAMs and have been extensively studied since the 1980s.[1] There are three types of organosulfur compounds that have been typically used: dialkyl sulfides ($X(CH_2)_mS(CH_2)_nX$), dialkyl disulfides ($X(CH_2)_mS\text{-}S(CH_2)_nX$), and alkanethiols ($HS(CH_2)_nX$) (where n, and m are the number of methylene units, where X is the end group of the alkyl chain such as $-CH_3$, -OH, or –COOH).[1] However, alkanethiols are the organosulfur compounds that have been studied the most, due to the ease of forming a well-defined monolayer.[1,12]

Organosulfur compounds can be adsorbed onto the substrate spontaneously. Although, there are many different metal surfaces that have been used such as, silver, platinum, copper and gold, gold is the most widely used with alkanethiols and has been extensively studied, see Scheme 1.4.[1,12]

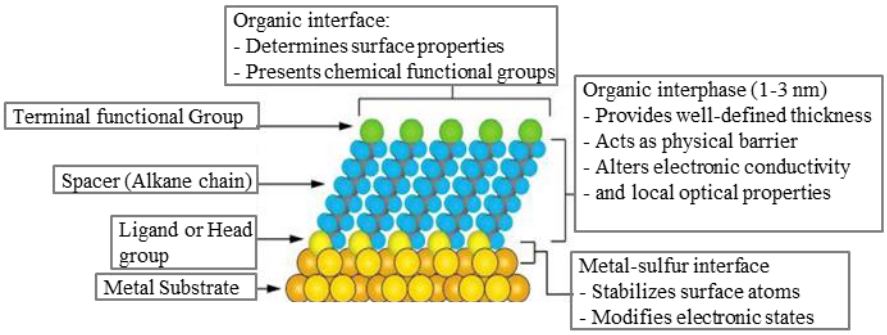

Scheme 1.4. Schematic diagram of an ideal, single-crystalline SAM of alkanethiolates supported on a gold surface. The anatomy and characteristics of the SAM are highlighted.[1]

There are many reasons for choosing gold and alkanethiols for these studies.[1,12,15,19-23] The preparation of gold is not difficult, as gold is relatively inert, and is not readily oxidized. Therefore, gold can be handled easily under ambient conditions. In addition, a flat and large area also can be produced on a gold template, by stripping or as a single crystal.[20] The formation of well-defined alkanethiol monolayers on gold is also feasible.[1] In addition, alkanethiols on gold are good for forming molecular assemblies on electrodes, metallic nanoparticles and surface plasmon resonance based optical devices.[12] The energy of the gold–thiolate bond is only 170 kJ mol^{-1} and due to the polar

nature of the bond, it is regarded as a pseudo-covalent bond. Van der Waals forces between neighbouring molecules stabilize the structure.[12,23] However, they are not stable in ambient conditions (air) for a long time. The gold-thiolate bond is unstable thermally especially in heated solvents.[9,12,22] The reason for instability is the gold–thiolate bond can be oxidised to sulfinates ($–SO_2$) or sulfonates ($–SO_3$).[12,19,21] However, disulphide or thiol /gold bonds have been used in biosensing studies.[9]

1.2.2 Organosilane based layers

Organosilane based monolayers can be produced on different hydroxyl terminated surfaces such as poly(vinylalcohol), glass, oxidised polyethylene, aluminium, iron oxide, zinc oxide, indium tin oxide or silicon/silcon oxide.[12,15] Hydroxylated substrates are important in the fabrication of SAMs of alkylchlorosilanes, alkylaminosilanes, and alkylalkoxysilanes.[12,15] Tian *et al*. reported that the reaction of derivatives of triethoxysilyl with hydroxyl-terminated silicon surfaces affords a covalent molecular layer as shown in Scheme 1.5.[24]

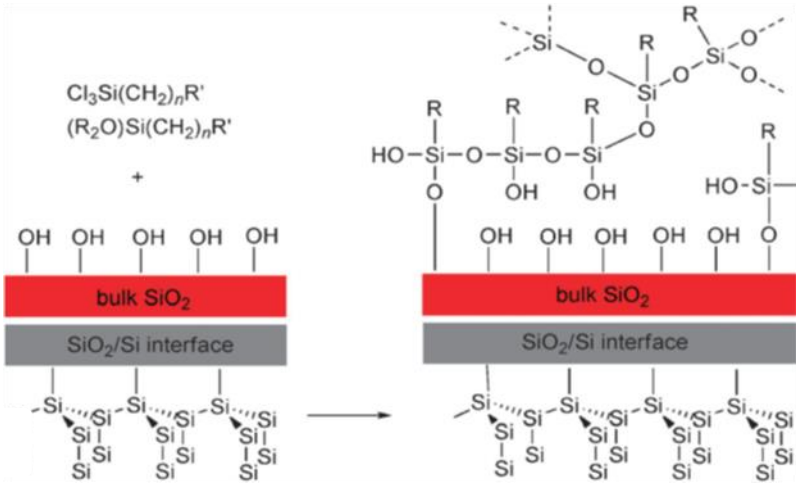

Scheme 1.5. Interactions between hydrocarbon chains and Si–O linkages between adjacent silanols are the driving force in the self-assembly of organosilane systems.[24]

Although there is the advantage of the ease of formation of the SAMs on SiO_2, there are also disadvantages such as lack of control and the weak stability of these monolayers in basic media. Another problem with this approach is that the preparation is very sensitive to reaction conditions, e.g. silane concentration, deposition time, temperature and water content.[12] Silanes are prone to hydrolysis and can undergo hydrolytic polymerization which can cause issues when trying to form well-order monolayers; multilayer

formation and the adventitious formation of polycondensed silane can result, as shown in Scheme 1.5.[12]

1.2.3 Aryl diazonium salt derived layers

In recent years, there has been an increasing interest in aryl diazonium salt derived layers. The reduction of aryl diazonium salts gains much attention because the same system can be used to modify carbon-based substrates such as glassy carbon, graphite, and diamond. In addition, the same system can be used with metals, silicon and indium tin oxide (Scheme 1.6).[2,12]

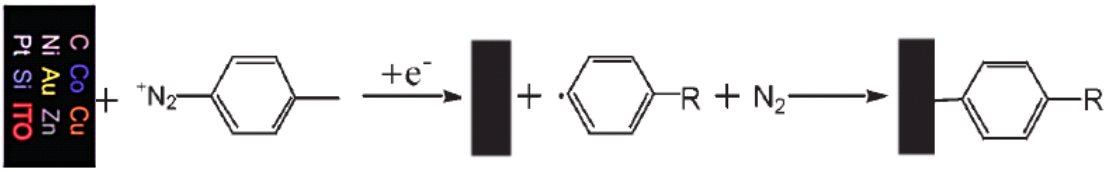

Scheme 1.6. Functionalization of carbon, metals, metal oxides and semiconductor surfaces by grafting, or electrografting, of aryl diazonium salts.

The reduction of aryl diazonium can be achieved in different media, organic or aqueous solvent, with or without applying a potential. Moreover, this system produces high stability layers at high temperature. The disadvantage of this system is that the control of formation of this layer on an electrode surface is not easy.[2,12]

1.2.4 Hydrosilylation reactions at silicon surfaces

Hydrosilylation is a popular strategy to form SAMs on hydride-terminated silicon surfaces, using unsaturated organic compounds, e.g 1-alkenes and 1-alkynes, to produce alkyl and vinyl silanes monolayers as shown in Scheme 1.7.[12] Linford and Chidsey successfully fabricated alkyl monolayers covalent bound to Si(100) and Si(111) in the early 1990s.[25,26]

The key advantage of this strategy is the high stability of the monolayers, due to the nonpolar covalent Si–C bond strength (≈370 kJ). SAMs on silicon surfaces are a possible choice for applications such as integrated circuits (ICs).[18] Both Si(111) and Si(100) can produce SAMs with micro and nanoscale roughness, but smooth monolayers can be prepared only on Si(111). Electrochemical etching can produce porous silicon (PS) with different arrangements of silicon layers depending on the kind of silicon face used.[12]

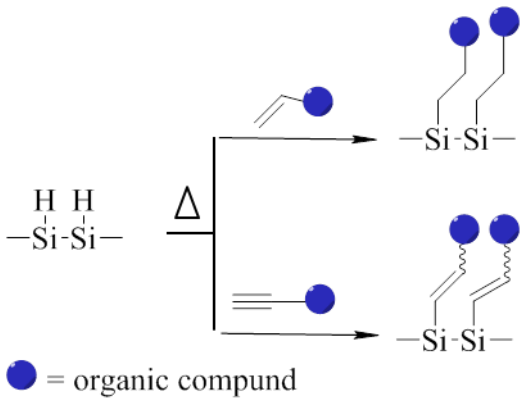

Scheme 1.7. Schematic of hydrosilylation chemistry which involves the insertion of an unsaturated bond, an alkene or an alkyne with Si-H bond, resulting in Si-C bond formation alkyl or alkenyl groups respectively.

Although there are many advantages of using silicon as a surface to fabricate SAMs, it is difficult to achieve a good quality monolayer without the formation of silicon oxide,[9,27] as this oxide provides good electrical insulation of molecular devices on the silicon monolayer.[12,28] There are difficulties associated with preparing densely packed silicon monolayers using ω-functionalized compounds (including -OH,[29,30] -SH,[31] and -NH_2[32]). Since these groups can also react with the Si-H surface. Therefore, a protection step is required for these groups which then must be followed by a deprotection step to allow for further modification of these groups.[13,27,29-32]

There has been a recent return in interest in the surface chemistry of silicon.[18] The modified silicon surface can be used in applications such as integrated circuits (ICs) and computing,[18] because of the high stability of the silicon monolayer under harsh conditions. Therefore, this project will focus on the modified silicon surface. The properties and modification of silicon surfaces will be discussed in the following sections.

1.3 Silicon surface

1.3.1 Silicon bulk

Single crystal silicon is commercially available with high purity and is relatively inexpensive. The most commonly used silicon surface orientations in microelectronic applications are Si(100) and Si(111). There are many publications based on these silicon surfaces.[10,14,18,33] Si(100) has been used widely in the microelectronics industry because of a fortunate matching of the interatomic spacing of silicon atoms with the lattice

constant of silicon dioxide. Whereas, Si(111) is largely used in the laboratory because atomically flat hydrogen passivated Si(111) surfaces can be easily generated by simple etching using HF or NH_4F.[9,10,14,18]

1.3.2 Intrinsic and Doped Silicon

Silicon is a semiconductor with a band gap of 1.12 eV and conductivity of $4.3\times10^{-6}\,\Omega^{-1}\,cm^{-1}$. The conductivity of silicon can be increased using group IIIA elements (B, Al, Ga) or group VA elements (P, As, Sb) as dopants.[10]

The additions of group VA dopants can add extra electrons to the conduction band of silicon and produces n-type silicon. Whereas the addition of group IIIA to silicon creates a lack of valence electrons, or holes, which produces p-type silicon. Scheme 1.8 shows the energy diagrams of intrinsic silicon, n-type and p-type doping. The difference between the energy level of the conduction and valence band is the band gap (E_g), which amounts to 1.12 eV (~1107 nm) for silicon at 300 K.[10]

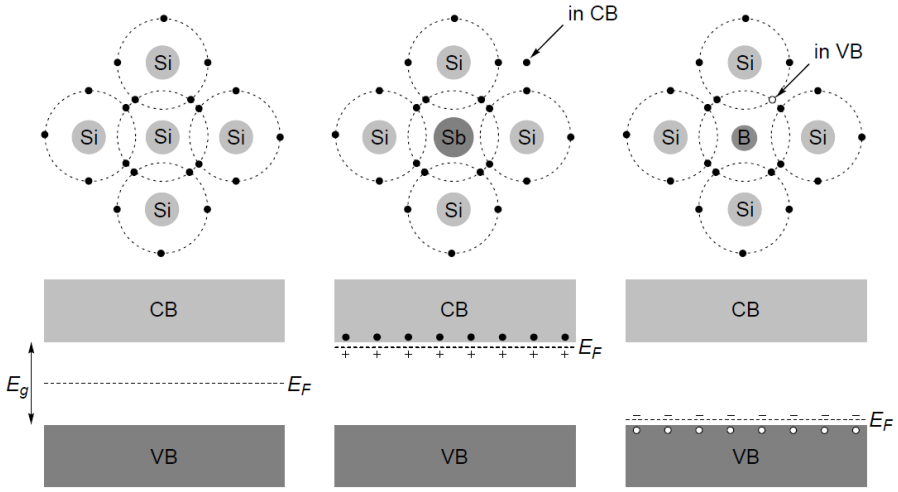

Scheme 1.8. Schematic 2-dimensional representations of crystal lattices (top) and energy diagrams (bottom) of intrinsic silicon, n-type silicon and p-type silicon. The dots and open circles represent electrons and holes, respectively.

The difference in energy gaps between differently doped silicon can be explained by the Fermi level (E_F). Where E_F is an energy level between the valence energy levels and conduction band energy. The Fermi level in intrinsic silicon is located exactly halfway between the valence and conduction bands, whereas in n-type silicon there are additional electron energy levels near to conduction band. The extra electrons can easily

be thermally excited into the conduction band, leaving fixed donor cations near the top of the band gap and producing mobile electrons in the conduction band. Consequently, there are more electrons in the conduction band of silicon than holes in the valence band and the Fermi level energy increases with respect to intrinsic silicon. In the case of p-type silicon, electrons from the valence band can easily be thermally excited into the holes of the doping level, located near the bottom of the band gap. This results in the formation of fixed donor anions and the presence of mobile holes in the valence band (majority charge carriers). Consequently, the number of holes in the valence band is higher than the number of electrons in the conduction band. The Fermi level energy of p-type silicon is therefore decreased with respect to the Fermi level of intrinsic silicon.[10]

1.3.3 Surface preparation

Single-crystal silicon, Si(100) and Si(111), can readily oxidise, when exposed to air (forming a thin surface oxide layer). This native oxide layer can be removed thermally under UHV conditions or chemically by etching the silicon surface with HF or NH_4F as shown in Scheme 1.10.[9,14]

In general, the surface is cleaned thoroughly through a series of washes using solvents such as trichloroethylene, acetone, 2-propanol, and water. Then, a hot piranha solution (mixture of H_2SO_4/H_2O_2), is used to form a uniform oxide layer on the surface. The silicon oxide layer is then stored in nanopure water, until required.[30,34]

A Si(111) wafer bearing Si–H groups after etching with 40% aqueous NH_4F can provide an atomically flat (111) monohydride, SiH, terminated surface,[8,20,35] with terraces on the scale of ~10^2 by ~10^4 nm^2. In the case of Si(100), two hydrogen atoms (SiH_2) after etching with (1–2%) aqueous HF can provide an atomically flat surface, see Scheme 1.9.[36-40]

Apart from flat single-crystalline silicon, porous silicon (PS) can also be produced by etching with HF, where the surface exposes different hydrogen-terminated groups (-SiH_3, -SiH_2, -SiH) see Scheme 1.9.[14]

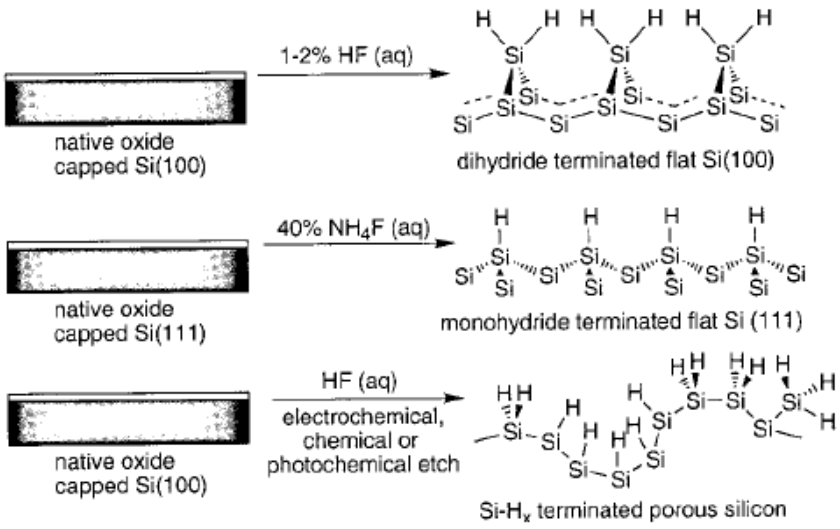

Scheme 1.9. Fluoride-based etching conditions, leading to hydride-terminated flat and porous silicon surfaces.[14]

One advantage of etching silicon is that after etching, a freshly prepared sample can possess > 99% silicon hydride group on the surface ready to be alkylated. These hydride terminated surfaces are important, due to the Si–H and Si–Si bonds being able to serve as chemical handles through which functionalization can be mediated.[1,18] In addition, the ease of preparation of hydrogenated silicon surfaces, and their stability in air,[9,40-42] and also the ability of Si-H to be modified in most solvents (e.g acetonitrile,[43] diethyl ether,[44] mesitylene,[45] hexane,[46] toluene[45]) make Si-H attractive for modification.

1.3.4 Deposition wet chemical approach to Si-C bond formation

There has been considerable attention for organic monolayers based on oxide-free silicon hydride surfaces over the past two decades.[2,12,14,18] The interesting feature of this method is the possibility to generate more complex compounds using bi-functional groups as a linker between the silicon surface and the complex attachment, see Scheme 1.10

In a general approach, a silicon hydride surface is produced after etching a silicon surface with HF, or NH_4F, then an organic compound can be introduced as shown in Scheme 1.10. The organic compound can be divided into three parts: a head group, backbone, and an end group. Every part can play a role in the fabrication of a SAM. The head group is the group which reacts with the silicon hydride such as –OH, C≡C, C=C, CHO, etc. The backbone can play a role in the packing of the monolayer; it could be a simple alkyl chain or an aromatic group. The end group can be, for example, –SH, -OH,

or –I, which can introduce other compounds to generate more complex monolayers, as shown in Scheme 1.10.

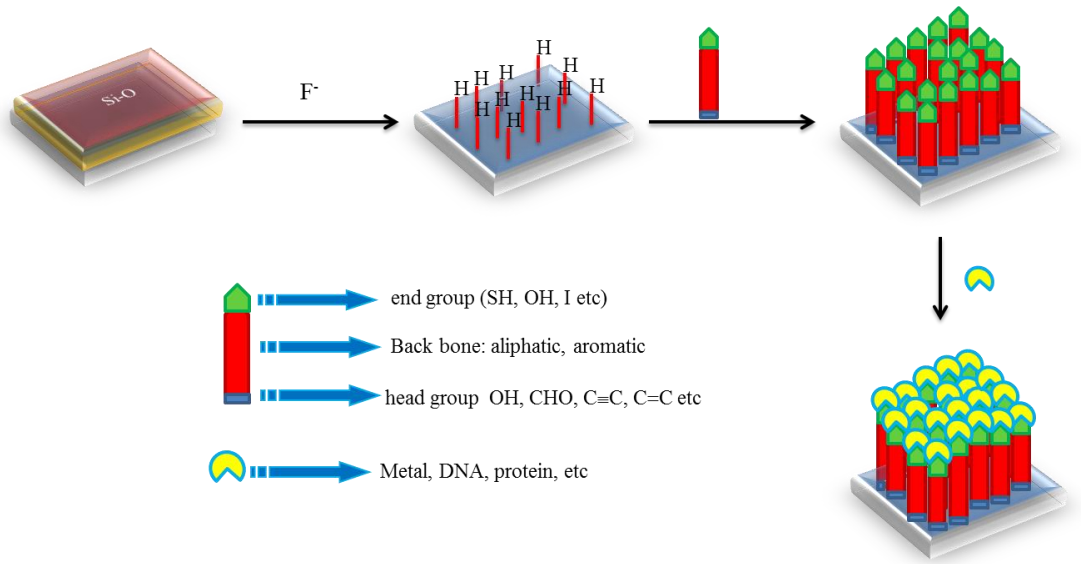

Scheme 1.10. Schematic representation of modification of silicon surface with organic compounds, have one or two functional group. The second functional group can be used for further reaction to introduce more complex compounds such as DNA, and protein.

After SAM modification of a hydrogen-terminated silicon surface with selected bi-functional compounds, a more complex surface can be generated by attaching other compounds such as DNA,[29,30,32,34,47,48] proteins,[49,50] antibodies,[51] carbohydrates,[52] Au nanoparticles,[53] ferrocene groups,[54] or oligothiophenes,[55] as shown in Scheme 1.11. In this approach the biomolecules can be linked to the inorganic chemistry and physical properties of silicon. This is interesting due to possible applications in biosensors.

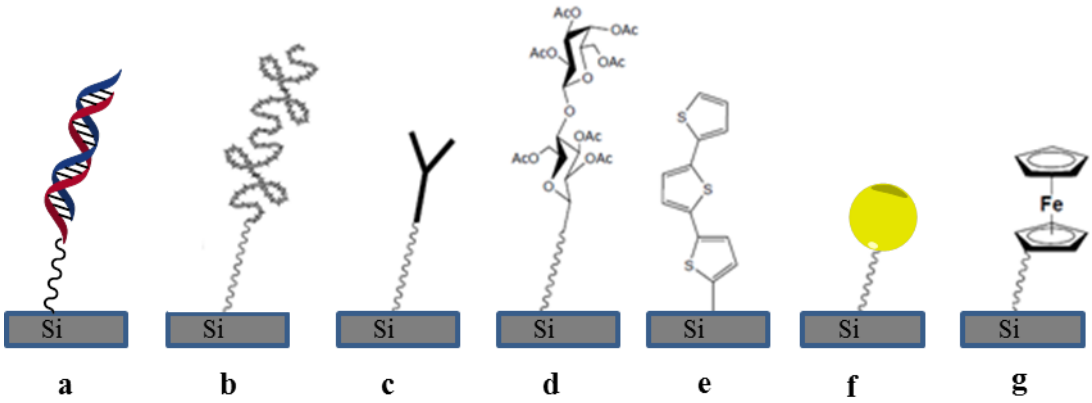

Scheme 1.11. SAMs on silicon surface that been reported a) DNA, b) proteins, c) antibodies, d) carbohydrates, e) oligothiophenes, f) Au nanoparticles, g) ferrocene groups**.**

1.3.5 Compounds have been used to fabricate Si-O, Si-C, and Si-N

There are many organic compounds that can react with a silicon hydride surface to produce different linkages such as Si-C, Si-O, and Si-N.[9,10,12,14,56] Examples of these compounds include alcohols, and aldehydes to produce a Si-O linkage (Scheme 1.12), whereas alkenes alkynes and diazonium salts can produce a Si-C linkage (Scheme 1.12). In addition, Si-N can be produced using amino derivatives with silicon hydride as shown in Scheme 1.12. However, there are more publications on Si-C monolayers than the other types.[54,9,10,12,14,56]

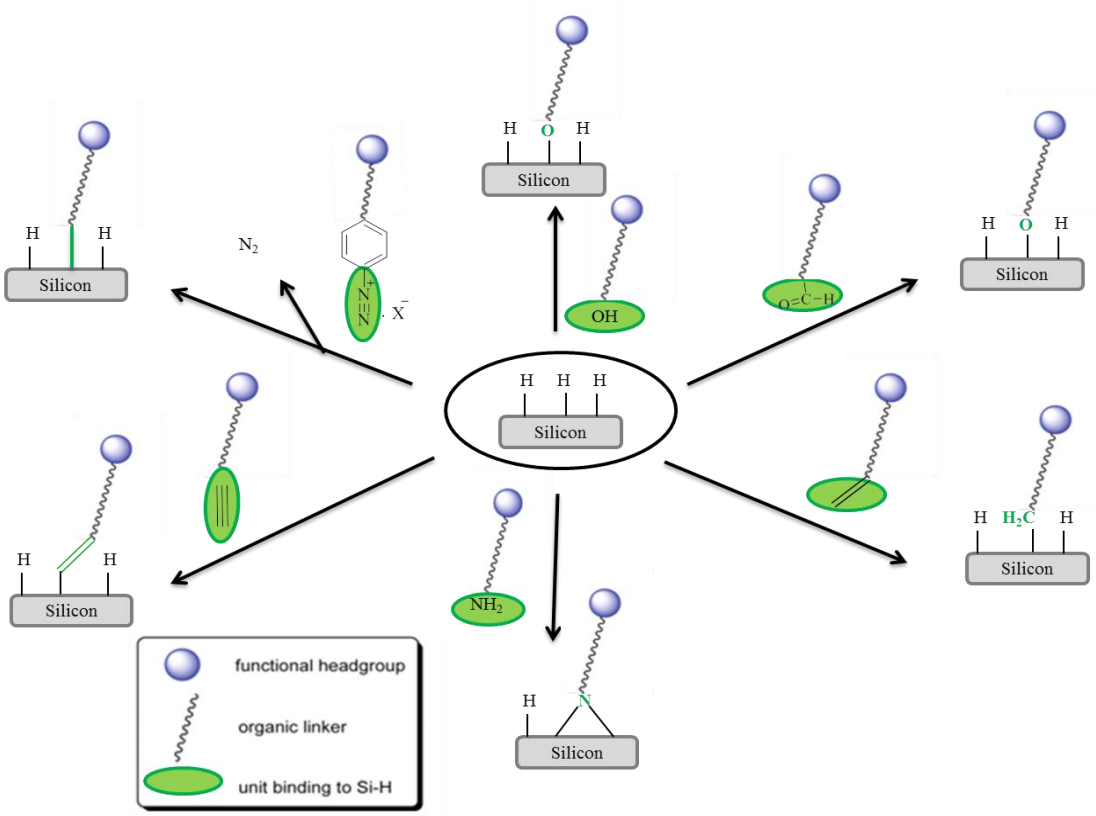

Scheme 1.12. Direct covalent attachment of α,ω-disubstituted bi-functional molecules to Si-H.

1.3.6 Which is the better linkage, Si-O, or Si-C?

Although a variety of different linkages can be utilized, the majority of reports have focused on Si-C and Si-O bound monolayers. The Si-C bond is more stable than the Si-O bond due to the high strength (Si–C, ≈370 kJ mol^{-1}) of the bond over the Si–O bond (Si-O, ≈368 kJ mol^{-1}). The Si-O and Si-C bonds are much stronger and more stable than the Au-S bonds in a gold-thiol based SAM.[57] However, when comparing the Si-C and Si-O bonds, the Si-C bond has a higher electron transfer rate due to the less polar nature of the bond.[10,58]

This project will focus on monolayers containing Si-C linkage between the silicon surface and organic compounds. Several activation methods have been used to fabricate these monolayers, such as hydrosilylation (radical initiator,[25] thermal,[26] UV light, white light), Lewis acid catalysts,[36,37] electrochemistry,[59-61] and halide terminated (Grignard and lithium reagents),[9,46,62,63] see Scheme 1.13.

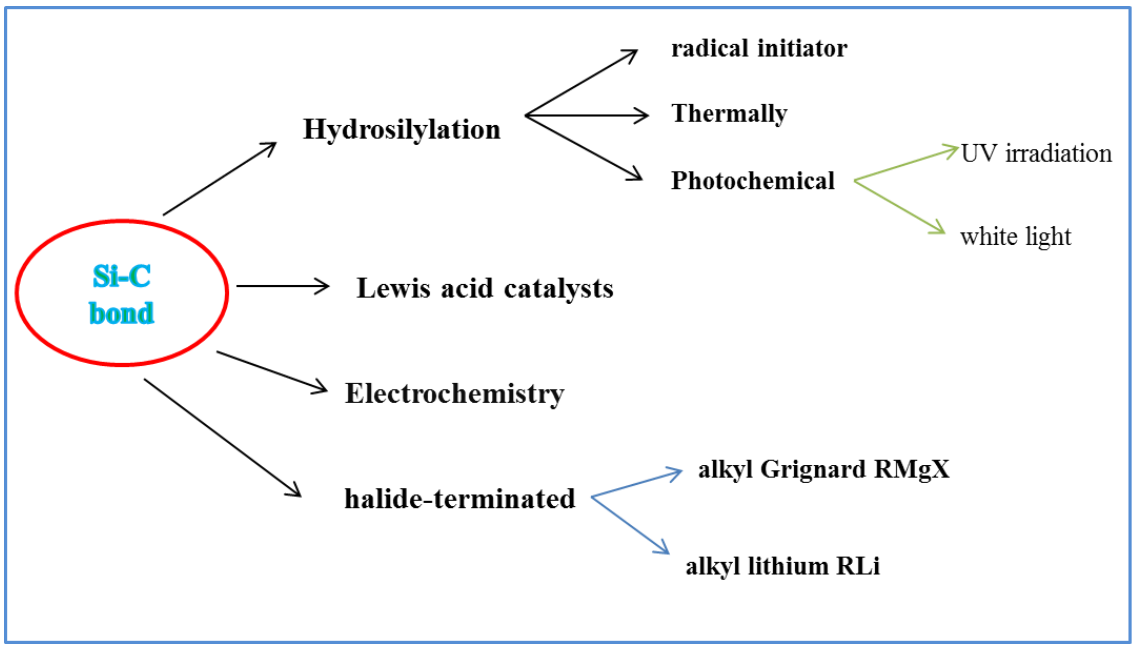

Scheme 1.13. Possible wet chemical approaches to Si-C bond formation.

1.3.7 Wet chemical approaches to Si-C bond formation

1.3.7.1 Hydrosilylation involving a radical initiator

The hydrosilylation reaction can be used to modify a silicon surface with unsaturated molecules. Linford and Chidsey reported the first example of alkyl monolayers covalently bound to Si(111) and Si(100) surfaces.[25] The monolayer was prepared using the pyrolysis of diacyl peroxides ($[CH_3(CH_2)_nC(O)O]_2$, n=16, or 10) for 1 hour at 100 °C. This alkyl monolayer has good stability in boiling solvents such as chloroform, water, acid (2.5 M H_2SO_4), base (1 M NH_4OH), and is also stable when immersed in 48% aqueous HF. However, a little oxidation of the silicon surface is observed when the modified silicon surface is left under ambient conditions in air, which hinders the potential use of this approach for technological applications.[25] This report was followed by other reports from Chidsey and co-workers, in which they described the hydrosilylation reaction of 1-alkenes and 1-alkynes on silicon hydride surfaces in the presence of different concentrations of a diacyl peroxide initiator.[26] The majority of

these studies were with different ratios of a mixture of octadecene/diacyl peroxide. The results showed that an octadecyl monolayer was successfully fabricated in the presence of diacyl peroxide.[26]

1.3.7.2 Thermally include hydrosilylation

Chidsey and co-workers reported that the alkene can be attached to a silicon hydride surface in absence of diacylperoxide initiator at higher temperatures (≥150 °C).[26] Thermal activation clearly demonstrated that alkyl monolayers on silicon are robust enough to tolerate further chemical reactions, and can be built upon directly to produce more sophisticated surfaces. Sung and co-worker have examined the thermal activation route of alkyl monolayers on Si(111) and Si(100), and reported these monolayers are stable in a vacuum up to 615 K which indicates that organic monolayers on silicon can be thermally resistant.[64]

A range of different monolayers have been fabricated via the thermal hydrosilylation of alkynes and alkenes to Si–H terminated porous silicon surfaces over 18-20 h at 110-180 °C, see Scheme 1.14. However, FTIR studies of the of alkyne (sp) group indicates that hydrosilylation does not lead to a surface bound vinyl group (sp^2), but the authors suggested that the alkyl group undergoes two hydrosilylation from sp to sp^2, then sp^2 to sp^3.[65] Simple alkynes and alkenes can be fabricated on silicon hydride surfaces easily with thermal hydrosilylation, but alcohol-terminated alkenes/alkynes could not be employed directly through this method due to the hydroxyl group being able to react with the surface, yielding ill-defined monolayers. Therefore protection of the alcohol is required before fabricating alcohol-terminated monolayers on a silicon hydride surface.[18]

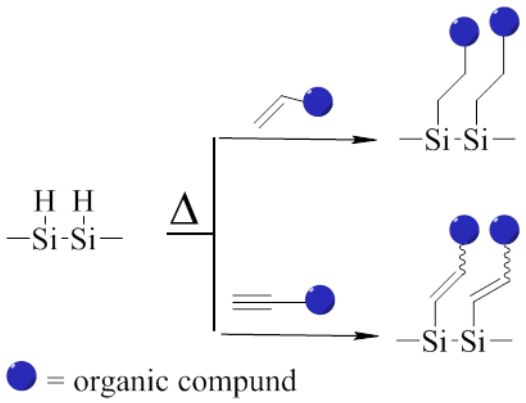

Scheme 1.14. Schematic representation of the thermal hydrosilylation reaction on silicon surface with alkene and alkyne bound through Si-C bonds.

It should be noted that, reaction solvents can affect the ordering monolayers produced by thermal methods.[45] Sievel *et al*. reported such, using 1-hexadecene on hydrogen-terminated silicon with a variety of solvents.[45] Anisole, n-decane, and n-butylbenzene are not good solvents for monolayer preparation at a range of concentrations of 1-hexadecene. However, well-ordered monolayers were formed with solvents such as xylene, cumene, toluene, tert-butylbenzene, and mesitylene at high concentrations of 1-hexadecene (25% and 10% (v/v)). The interesting point they report, is that mesitylene produces high quality monolayers even at significantly lower alkene concentrations (down to 2.5%). The well-ordered monolayers depend on the boiling point of the solvent, volume of the solvent and the concentration of the alkene.[45]

1.3.7.3 Photochemical hydrosilylation

Photochemical hydrosilylation via UV irradiation or white light are possible approaches to modify a silicon surface with unsaturated (alkene/alkyne) compounds (Scheme 1.15). Photochemical hydrosilylation has been used with flat silicon surfaces, whereas photochemical hydrosilylation via white light has been used to modify porous silicon. The advantage of the photochemical approach is that the reaction can be conducted at room temperature.[14,18]

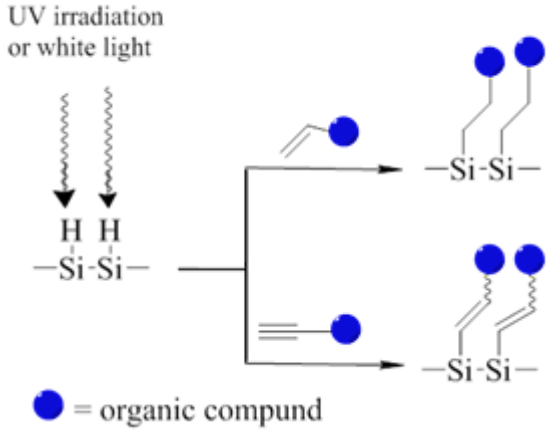

Scheme 1.15. Schematic representation of the UV/ or white-light promoted hydrosilylation reaction on silicon surface with various chemical groups, bound through Si-C bonds.

1.3.7.4 Hydrosilylation and Related Reactions Mediated by Metal Complexes

Lewis acids (e.g. $AlCl_3$, $AlEtCl_2$) have been used as mediators to functionalise porous silicon with alkene and alkyne organic compounds in mild conditions (room temperature) with reaction times of just 1 hour for alkynes and 12 hours for alkenes.[66,67]

However, this method has not been widely used to modify single crystal Si(111)-H (maybe due to low surface coverage), and requires longer reaction times (18 hours) and a higher temperature of 100 °C.[9,46]

1.3.7.5 Electrochemical grafting

Electrochemistry has also been used to produce covalent Si-C monolayers with different chemical derivatives of diazonium salts,[59] halo-alkynes,[60] and terminal alkynes.[61] Allongue *et al.* have reported close-packed phenyl monolayers on hydride-terminated flat n-type Si(111) surfaces using the reduction of 4-nitro- and 4-bromo-benzenediazonium salts in aqueous HF.[59] Electrochemical studies of these monolayers show high stability. Another important advantage of this approach is that the process is cathodic, thus making the surface electron rich during the reaction, which renders it less susceptible to nucleophilic attack by water, suppressing oxidation.[59]
On the other hand, alkyl iodides or bromides and alkynes have been attached successfully to silicon hydride terminated porous silicon.[60] Sailor and co-workers have successfully immobilised alkyl bromides or iodides electrochemically on hydride-terminated porous silicon by passing a 10 mA cm^{-2} cathodic current for a short time (>2 min) at room temperature. The advantages of this method include the short reaction time, commercial availability of alkyl halides, and the high coverage that can be achieved.[60]

Moreover, terminal alkynes also can be grafted electrochemically on silicon hydride terminated PS using electrografting with two different current densities, -9 mA cm^{-2} (cathodic electrografting, CEG) or +9 mA cm^{-2} (anodic electrografting, AEG). Two different linkages have been produced depending on the current bias that has been applied, for example in the case of an anodic potential (AEG) the result shows the complete reduction of all unsaturated bonds (triple bond react with two silicon atom), but in the case of a cathodic potential (CEG) the product is a (Si-C≡C) linkage.[61]

1.3.7.6 Alkylation of halide-terminated

The other approach to create Si-C bonds is alkylation of silicon hydride surface with halide terminated organic compounds such as alkyl Grignard RMgX or alkyl lithium RLi.[9,46,62,63 68]

Bansal *et al.* have reported the alkylation of silicon hydride with ($-C_{10}H_{21}$) alkyl Grignard or lithium reagents in a two-step reaction (Scheme 1.16). Firstly chlorination of silicon hydride with PCl_5 followed by alkylation with $C_{10}H_{21}Li$ or $C_{10}H_{21}MgX$.[62]

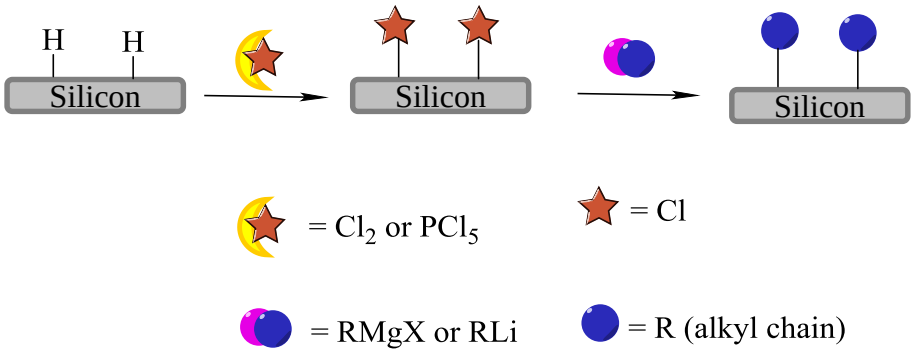

Scheme 1.16. Representative modification of silicon hydride surface with halide-terminated surfaces by two steps, chlorination of silicon hydride surface followed by further reaction (alkylation) of a range of organic molecules such as RMgX or RLi.

It has been reported that the chlorination of the silicon hydride surface followed by alkylation with a Grignard reagent can fully passivate (small alkyl halide ($-CH_3$)), or incompletely (longer alkyl chain) the silicon surface. Large alkyl chains have a radius between 4.5-5.0 Å whereas the distance between Si surface sites on the Si(111) surfaces is 3.8 Å, so packing is incomplete due to van der Waals interactions between methylene units of adjacent alkyl chains.[9,62,63]

Moreover, direct attachment of an alkyl Grignard reagent has been successfully fabricated onto hydrogen terminated Si(111) surfaces by direct thermal reaction with of an alkyl Grignard reagent (decylmagnesium bromide).[46]

In light of the various possible modification steps of a silicon surface, there is a substantial interest in the development of monolayers for the use in molecular electronics. One key molecule of interest is ferrocene, which has been extensively studied over the last two decades.[54] Although, there is a large number of publications on ferrocene-gold monolayers,[69-72] ferrocene also has been adsorbed onto inorganic semiconductors such as the silicon surface.[54] The presence of the band gap in silicon could allow the design of a new class of resonant tunnelling devices with possible applications in logic and low power memory.[73,74 54,57]

1.4 Ferrocene

Ferrocene is an organometallic compound, consisting of two cyclopentadienyl ligands bound on opposite sides of a central iron (II) atom ($Fe(C_5H_5)_2$). Ferrocene shows attractive electrochemical characteristics, a one electron transfer to/from ferrocene/ferrocenium which is typically rapid, because of the low reorganisation energy of the Fe(II) and Fe(III) redox states.[54,75,76]

1.4.1 Ferrocene monolayer on silicon surface

Ferrocene monolayers have been prepared with various types of silicon electrodes by the direct reaction of hydrogen-terminated silicon with ferrocenyl-alcohols,[43,77-79] vinylferrocene, [58,65,76,80-86] ethynylferrocene, [81,87-91] or ferrocenecarboxaldehyde.[58,80] A variety of other methods involved conjugation of ferrocene to pre-formed monolayers have also been demonstrated.[43,57,77-79,89,92-102] Ferrocene has also been incorporated into complex molecular structures such as DNA, using solid phase oligodeoxynucleotide synthesis.[103] These chemistries of the fabrication for ferrocenyl monolayers on silicon surface are reviewed in more detail in Chapters 3, 4 and 5.

1.4.2 Application of ferrocenyl silicon surface

The ability to tether ferrocene onto a semiconductor substrate then opens up the possibility of the development of future charge storage devices based on these monolayers that can have fast switching times and low operating voltages compared to Si/SiOx.[54]

Ferrocenyl silicon surfaces could be used as charge storage components with the bound ferrocene centre acting as the memory element. The ferrocene can be oxidised to the ferrocenium form when a positive potential is passed through the silicon. When the potential is changed this equates to the change of a bit of information from the “0” to “1” state, and the information is stored. Therefore, another potential must be applied to reduce the ferrocenium to ferrocene, which can erase the stored charge and return the device to its initial state. In this type of application, the electron is transferred from the ferrocene headgroups to the underlying conducting silicon surface by a tunneling process across the monolayer. To produce a stable and reproducible electrical response, this process must be efficient, fast, and reversible. The stability, charge density, and capacitance performances of high-quality ferrocene-terminated monolayers could

compete with those of the existing semiconductor-based memory devices, such as dynamic random access memories, DRAMs. Perhaps more importantly, the surface coverage of ferrocene allows precise control over the rate of this process. Such characteristics are relevant not only for electrocatalytic reactions but also for widening the potential applications of these assemblies to novel molecular electronic devices (e.g. chemiresistors, chemically sensitive field-effect transistors (CHEMFETs)) and redox chemistry on insulating surfaces.[54]

1.5 Objectives and structure of the present study

It is clear from previous reviews on SAMs that a project with a focus on the synthesis, preparation and characterisation of ferrocenyl silicon surface monolayers with a carbon linker between the silicon surface and the ferrocene units (Scheme 1.17), and the study of possible applications of ferrocenyl monolayers is required. The following four chapters describe the work performed to reach this goal.

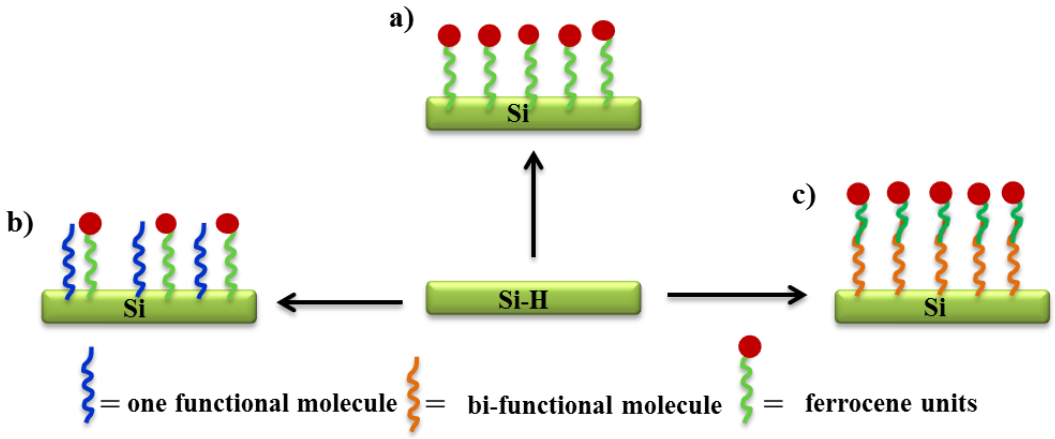

Scheme 1.17. Schematic representation of the modified silicon surfaces with ferrocene, a) pure ferrocenyl monolayer, b) mixed ferrocenyl monolayer, c) long ferrocenyl monolayer.

Chapter 2 describes the main techniques for the characterisation of ferroceneyl monolayers.

Chapter 3 deals with the study of ferrocene for use in the modification of silicon surfaces to produce pure ferrocenyl monolayers, with different linkages between the ferrocene and the silicon surface, Si-CH_2-CH_2-Fc, Si-CH=CH-Fc, Si-C≡C-Fc. An introduction to the preparation methods of these linkages, as shown in Scheme 1.17a, and their characterization is reported.

Chapter 4 provides an introduction to the preparation methods of ferrocenyl mixed monolayers, and goes on to describe the study of mixed monolayers containing a Si-CH_2-CH_2-Fc linkage with different alkyl chains. The topographic and electrochemical characterisation of theses surfaces is reported, (Scheme 1.17b).

Chapter 5 discusses the preparation methods for making longer (>C_2) ferrocene monolayers, and focusses on the study of more complex ferrocenyl monolayers on the silicon surface by two different strategies. A one-step strategy and a step-wise strategy, where a longer linkage can be produced between the ferrocene and the silicon substrate is discussed, Scheme 1.17c. Again, their topographic and electrochemical characterisation is reported.

Chapter 6 discusses possible application of the ferrocenyl silicon surfaces fabricated in Chapters 3, 4 through collaborations with other research groups.

Chapter 7 provides a brief summary of Chapters 3-5, and conclusion and further work.

.

References

1. J. C. Love, L. A. Estroff, J. K. Kriebel, R. G. Nuzzo and G. M. Whitesides, *Chemical Reviews*, 2005, **105**, 1103-1170.

2. J. J. Gooding, *Electroanalysis*, 2008, **20**, 573-582.

3. A. Vilan, O. Yaffe, A. Biller, A. Salomon, A. Kahn and D. Cahen, *Advanced Materials*, 2010, **22**, 140-159.

4. I. Willner, *Science*, 2002, **298**, 2407-2408.

5. K. L. Prime and G. M. Whitesides, *Journal of the American Chemical Society*, 1993, **115**, 10714-10721.

6. A. Ulman, Academic Press: Boston, USA, Editon edn., 1991.

7. F. Schreiber, *Progress in Surface Science*, 2000, **65**, 151-256.

8. K. B. Blodgett and I. Langmuir, *Physical Review*, 1937, **51**, 964-982.

9. S. Ciampi, J. B. Harper and J. J. Gooding, *Chemical Society Reviews*, 2010, **39**, 2158-2183.

10. S. P. Cummings, J. Savchenko and T. Ren, *Coordination Chemistry Reviews*, 2011, **255**, 1587-1602.

11. S. R. Forrest, *Chemical Reviews*, 1997, **97**, 1793-1896.

12. J. J. Gooding and S. Ciampi, *Chemical Society Reviews*, 2011, **40**, 2704-2718.

13. Y. Li and C. Z. Cai, *Chemistry-an Asian Journal*, 2011, **6**, 2592-2605.

14. J. M. Buriak, *Chemical Reviews*, 2002, **102**, 1271-1308.

15. A. Ulman, *Chemical Reviews*, 1996, **96**, 1533-1554.

16. N. Shirahata, A. Hozumi and T. Yonezawa, *Chemical Record*, 2005, **5**, 145-159.

17. S. N. Patole, PhD thesis, Newcastle Uinversity, 2004.

18. J. M. Buriak, *Chemical Communications*, 1999, 1051-1060.

19. A. B. Horn, D. A. Russell, L. J. Shorthouse and T. R. E. Simpson, *Journal of the Chemical Society-Faraday Transactions*, 1996, **92**, 4759-4762.

20. J. Mazurkiewicz, F. J. Mearns, D. Losic, L. Weeks, E. R. Waclawik, C. T. Rogers, J. G. Shapter and J. J. Gooding, *Journal of Vacuum Science & Technology B*, 2002, **20**, 2265-2270.

21. G. H. Yang, N. A. Amro, Z. B. Starkewolfe and G. Y. Liu, *Langmuir*, 2004, **20**, 3995-4003.

22. N. Garg, E. Carrasquillo-Molina and T. R. Lee, *Langmuir*, 2002, **18**, 2717-2726.

23. C. Vericat, M. E. Vela and R. C. Salvarezza, *Physical Chemistry Chemical Physics*, 2005, **7**, 3258-3268.

24. R. H. Tian, O. Seitz, M. Li, W. C. Hu, Y. J. Chabal and J. M. Gao, *Langmuir*, 2010, **26**, 4563-4566.

25. M. R. Linford and C. E. D. Chidsey, *Journal of the American Chemical Society*, 1993, **115**, 12631-12632.

26. M. R. Linford, P. Fenter, P. M. Eisenberger and C. E. D. Chidsey, *Journal of the American Chemical Society*, 1995, **117**, 3145-3155.

27. T. Strother, W. Cai, X. S. Zhao, R. J. Hamers and L. M. Smith, *Journal of the American Chemical Society*, 2000, **122**, 1205-1209.

28. A. Salomon, T. Bocking, J. Gooding and D. Cahen, *Nano Letters*, 2006, **6**, 2873-2876.

29. A. R. Pike, L. H. Lie, R. A. Eagling, L. C. Ryder, S. N. Patole, B. A. Connolly, B. R. Horrocks and A. Houlton, *Angewandte Chemie-International Edition*, 2002, **41**, 615-617.

30. L. H. Lie, S. N. Patole, A. R. Pike, L. C. Ryder, B. A. Connolly, A. D. Ward, E. M. Tuite, A. Houlton and B. R. Horrocks, *Faraday Discussions*, 2004, **125**, 235-249.

31. T. Bocking, A. Salomon, D. Cahen and J. J. Gooding, *Langmuir*, 2007, **23**, 3236-3241.

32. X. C. Zhang, S. Kumar, J. H. Chen and A. V. Teplyakov, *Surface Science*, 2009, **603**, 2445-2457.

33. S. Saliterman, *Fundamentals of BioMEMS and medical microdevices*, SPIE Press, 2006.

34. S. N. Patole, A. R. Pike, B. A. Connolly, B. R. Horrocks and A. Houlton, *Langmuir*, 2003, **19**, 5457-5463.

35. C. P. Wade and C. E. D. Chidsey, *Applied Physics Letters*, 1997, **71**, 1679-1681.

36. G. S. Higashi, R. S. Becker, Y. J. Chabal and A. J. Becker, *Applied Physics Letters*, 1991, **58**, 1656-1658.

37. H. Ubara, T. Imura and A. Hiraki, *Solid State Communications*, 1984, **50**, 673-675.

38. Y. J. Chabal, G. S. Higashi, K. Raghavachari and V. A. Burrows, *Journal of Vacuum Science & Technology a-Vacuum Surfaces and Films*, 1989, **7**, 2104-2109.

39. P. Allongue, C. H. de Villeneuve, S. Morin, R. Boukherroub and D. D. M. Wayner, *Electrochimica Acta*, 2000, **45**, 4591-4598.

40. G. S. Higashi, Y. J. Chabal, G. W. Trucks and K. Raghavachari, *Applied Physics Letters*, 1990, **56**, 656-658.

41. M. Niwano, J. Kageyama, K. Kurita, K. Kinashi, I. Takahashi and N. Miyamoto, *Journal of Applied Physics*, 1994, **76**, 2157-2163.

42. D. D. M. Wayner and R. A. Wolkow, *Journal of the Chemical Society, Perkin Transactions 2*, 2002, **0**, 23-34.

43. G. Cleland, B. R. Horrocks and A. Houlton, *Journal of the Chemical Society-Faraday Transactions*, 1995, **91**, 4001-4003.

44. H. Z. Yu, S. Morin, D. D. M. Wayner, P. Allongue and C. H. de Villeneuve, *Journal of Physical Chemistry B*, 2000, **104**, 11157-11161.

45. A. B. Sieval, V. Vleeming, H. Zuilhof and E. J. R. Sudhölter, *Langmuir*, 1999, **15**, 8288-8291.

46. R. Boukherroub, S. Morin, F. Bensebaa and D. D. M. Wayner, *Langmuir*, 1999, **15**, 3831-3835.

47. T. Strother, R. J. Hamers and L. M. Smith, *Nucleic Acids Research*, 2000, **28**, 3535-3541.

48. T. Strother, W. Cai, X. Zhao, R. J. Hamers and L. M. Smith, *Journal of the American Chemical Society*, 2000, **122**, 1205-1209.

49. D. J. Guo, S. J. Xiao, B. Xia, W. Shuai, J. Pei, Y. Pan, X. Z. You, Z. Z. Gu and Z. H. Lu, *Journal of Physical Chemistry B*, 2005, **109**, 20620-20628.

50. J. Gu, C. M. Yam, S. Li and C. Cai, *Journal of the American Chemical Society*, 2004, **126**, 8098-8099.

51. W. Liao, F. Wei, M. X. Qian and X. S. Zhao, *Sensors and Actuators B-Chemical*, 2004, **101**, 361-367.

52. L. de Smet, A. V. Pukin, Q. Y. Sun, B. J. Eves, G. P. Lopinski, G. M. Visser, H. Zuilhof and E. J. R. Sudholter, *Applied Surface Science*, 2005, **252**, 24-30.

53. Y. Yamanoi, T. Yonezawa, N. Shirahata and H. Nishihara, *Langmuir*, 2004, **20**, 1054-1056.

54. B. Fabre, *Accounts of Chemical Research*, 2010, **43**, 1509-1518.

55. J. He, S. N. Patitsas, K. F. Preston, R. A. Wolkow and D. D. M. Wayner, *Chemical Physics Letters*, 1998, **286**, 508-514.

56. H. Qi, S. Sharma, Z. H. Li, G. L. Snider, A. O. Orlov, C. S. Lent and T. P. Fehlner, *Journal of the American Chemical Society*, 2003, **125**, 15250-15259.

57. B. Fabre and F. Hauquier, *The Journal of Physical Chemistry B*, 2006, **110**, 6848-6855.

58. E. A. Dalchiele, A. Aurora, G. Bernardini, F. Cattaruzza, A. Flamini, P. Pallavicini, R. Zanoni and F. Decker, *Journal of Electroanalytical Chemistry*, 2005, **579**, 133-142.

59. C. H. de Villeneuve, J. Pinson, M. C. Bernard and P. Allongue, *The Journal of Physical Chemistry B*, 1997, **101**, 2415-2420.

60. C. Gurtner, A. W. Wun and M. Sailor, *Angewandte Chemie-International Edition*, 1999, **38**, 1966-1968.

61. E. G. Robins, M. P. Stewart and J. M. Buriak, *Chemical Communications*, 1999, 2479-2480.

62. A. Bansal, X. L. Li, I. Lauermann, N. S. Lewis, S. I. Yi and W. H. Weinberg, *Journal of the American Chemical Society*, 1996, **118**, 7225-7226.

63. L. J. Webb, D. J. Michalak, J. S. Biteen, B. S. Brunschwig, A. S. Y. Chan, D. W. Knapp, H. M. Meyer, E. J. Nemanick, M. C. Traub and N. S. Lewis, *Journal of Physical Chemistry B*, 2006, **110**, 23450-23459.

64. M. M. Sung, G. J. Kluth, O. W. Yauw and R. Maboudian, *Langmuir*, 1997, **13**, 6164-6168.

65. J. E. Bateman, R. D. Eagling, D. R. Worrall, B. R. Horrocks and A. Houlton, *Angewandte Chemie-International Edition*, 1998, **37**, 2683-2685.

66. J. M. Buriak and M. J. Allen, *Journal of the American Chemical Society*, 1998, **120**, 1339-1340.

67. J. M. Buriak, M. P. Stewart, T. W. Geders, M. J. Allen, H. C. Choi, J. Smith, D. Raftery and L. T. Canham, *Journal of the American Chemical Society*, 1999, **121**, 11491-11502.

68. N. Y. Kim and P. E. Laibinis, *Journal of the American Chemical Society*, 1998, **120**, 4516-4517.

69. T. Auletta, F. van Veggel and D. N. Reinhoudt, *Langmuir*, 2002, **18**, 1288-1293.

70. C. E. D. Chidsey, C. R. Bertozzi, T. M. Putvinski and A. M. Mujsce, *Journal of the American Chemical Society*, 1990, **112**, 4301-4306.

71. T. Kawaguchi, K. Tada and K. Shimazu, *Journal of Electroanalytical Chemistry*, 2003, **543**, 41-49.

72. S. Watcharinyanon, E. Moons and L. S. O. Johansson, *Journal of Physical Chemistry C*, 2009, **113**, 1972-1979.

73. T. Rakshit, G.-C. Liang, A. W. Ghosh and S. Datta, *Nano Letters*, 2004, **4**, 1803-1807.

74. A. Mishchenko, M. Abdualla, A. Rudnev, Y. Fu, A. R. Pike and T. Wandlowski, *Chemical Communications*, 2011, **47**, 9807-9809.

75. N. G. Tsierkezos, *Journal of Solution Chemistry*, 2007, **36**, 289-302.

76. H. Sano, M. Zhao, D. Kasahara, K. Murase, T. Ichii and H. Sugimura, *Journal of Colloid and Interface Science*, 2011, **361**, 259-269.

77. K. M. Roth, A. A. Yasseri, Z. M. Liu, R. B. Dabke, V. Malinovskii, K. H. Schweikart, L. H. Yu, H. Tiznado, F. Zaera, J. S. Lindsey, W. G. Kuhr and D. F. Bocian, *Journal of the American Chemical Society*, 2003, **125**, 505-517.

78. Q. Li, G. Mathur, M. Homsi, S. Surthi, V. Misra, V. Malinovskii, K.-H. Schweikart, L. Yu, J. S. Lindsey, Z. Liu, R. B. Dabke, A. Yasseri, D. F. Bocian and W. G. Kuhr, *Appl. Phys. Lett.*, 2002, **81**, 1494-1496.

79. Q. L. Li, G. Mathur, S. Gowda, S. Surthi, Q. Zhao, L. H. Yu, J. S. Lindsey, D. F. Bocian and V. Misra, *Advanced Materials*, 2004, **16**, 133-137.

80. N. Tajimi, H. Sano, K. Murase, K.-H. Lee and H. Sugimura, *Langmuir*, 2007, **23**, 3193-3198.

81. A. G. Marrani, F. Cattaruzza, F. Decker, P. Galloni and R. Zanoni, *Electrochimica Acta*, 2010, **55**, 5733-5740.

82. A. G. Marrani, F. Cattaruzza, F. Decker, P. Galloni and R. Zanoni, *Superlattices and Microstructures*, 2009, **46**, 40-43.

83. R. Zanoni, M. Cossi, M. F. Iozzi, F. Cattaruzza, E. A. Dalchiele, F. Decker, A. G. Marrani and M. Valori, *Superlattices and Microstructures*, 2008, **44**, 542-549.

84. P. Kruse, E. R. Johnson, G. A. DiLabio and R. A. Wolkow, *Nano Letters*, 2002, **2**, 807-810.

85. F. Decker, F. Cattaruzza, C. Coluzza, A. Flamini, A. G. Marrani, R. Zanoni and E. A. Dalchiele, *The Journal of Physical Chemistry B*, 2006, **110**, 7374-7379.

86. R. Zanoni, A. Aurora, F. Cattaruzza, C. Coluzza, E. A. Dalchiele, F. Decker, G. Di Santo, A. Flamini, L. Funari and A. G. Marrani, *Materials Science and Engineering: C*, 2006, **26**, 840-845.

87. T. Pro, J. Buckley, R. Barattin, A. Calborean, M. Gely, K. Huang, G. Delapierre, F. Duclairoir, E. Jalaguier, P. Maldivi, B. De Salvo, S. Deleonibus and G. Ghibaudo, in *Essderc 2008: Proceedings of the 38th European Solid-State Device Research Conference*, eds. S. Hall and A. Walton, Ieee, New York, Editon edn., 2008, pp. 226-229.

88. M. Cossi, M. F. Iozzi, A. G. Marrani, T. Lavecchia, P. Galloni, R. Zanoni and F. Decker, *The Journal of Physical Chemistry B*, 2006, **110**, 22961-22965.

89. K. Huang, F. Duclairoir, T. Pro, J. Buckley, G. Marchand, E. Martinez, J.-C. Marchon, B. De Salvo, G. Delapierre and F. Vinet, *Chemphyschem*, 2009, **10**, 963-971.

90. S. Ciampi, M. James, N. Darwish, E. Luais, B. Guan, J. B. Harper and J. J. Gooding, *Physical Chemistry Chemical Physics*, 2011, **13**, 15624-15632.

91. V. Aiello, N. Joo, J. Buckley, G. Nonglaton, F. Duclairoir, L. Dubois, J. C. Marchon, M. Gely, N. Chevalier and B. De Salvo, *Surface Science*, 2013, **612**, 57-62.

92. G. Riveros, S. Meneses, S. Escobar, C. Garin and B. Chornik, *Journal of the Chilean Chemical Society*, 2010, **55**, 61-66.

93. G. Riveros, G. Gonzalez and B. Chornik, *Journal of the Brazilian Chemical Society*, 2010, **21**, 25-32.

94. G. Riveros, C. Garin, S. Meneses and S. Escobar, *Molecular Crystals and Liquid Crystals*, 2010, **521**, 187-194.

95. R. D. Rohde, H. D. Agnew, W. S. Yeo, R. C. Bailey and J. R. Heath, *Journal of the American Chemical Society*, 2006, **128**, 9518-9525.

96. F. Hauquier, J. Ghilane, B. Fabre and P. Hapiot, *Journal of the American Chemical Society*, 2008, **130**, 2748-2749.

97. S. Ciampi, P. K. Eggers, G. Le Saux, M. James, J. B. Harper and J. J. Gooding, *Langmuir*, 2009, **25**, 2530-2539.

98. D. Zigah, C. Herrier, L. Scheres, M. Giesbers, B. Fabre, P. Hapiot and H. Zuilhof, *Angewandte Chemie-International Edition*, 2010, **49**, 3157-3160.

99. R. D. Eagling, J. E. Bateman, N. J. Goodwin, W. Henderson, B. R. Horrocks and A. Houlton, *Journal of the Chemical Society-Dalton Transactions*, 1998, 1273-1275.

100. A. Ng, S. Ciampi, M. James, J. B. Harper and J. J. Gooding, *Langmuir*, 2009, **25**, 13934-13941.

101. S. Ciampi, G. Le Saux, J. B. Harper and J. J. Gooding, *Electroanalysis*, 2008, **20**, 1513-1519.

102. A. G. Marrani, E. A. Dalchiele, R. Zanoni, F. Decker, F. Cattaruzza, D. Bonifazi and M. Prato, *Electrochimica Acta*, 2008, **53**, 3903-3909.

103. A. R. Pike, L. C. Ryder, B. R. Horrocks, W. Clegg, B. A. Connolly and A. Houlton, *Chemistry-a European Journal*, 2005, **11**, 344-353.

Chapter 2

Chapter 2 - Analysis Techniques

This chapter describes the main techniques for the characterisation of the ferrocenyl monolayers prepared in this project. A series of spectroscopic techniques including Fourier transform infrared (FTIR), and X-ray photoelectron spectroscopy (XPS) have been used in order to establish the chemical composition of the ferrocenyl monolayers on the silicon surface. In order to probe the physical properties of the ferrocenyl monolayers, atomic force microscopy (AFM) was used to investigate the morphology of the monolayer, whilst cyclic voltammetry (CV) was employed to study their electrical properties.

2.1 Fourier transform infrared spectroscopy [1,2]

Fourier transform infrared (FTIR) spectroscopy is a useful technique for providing chemical information regarding a sample material. This technique is a form of vibration spectroscopy that can provide intrinsic information about the functional groups within a sample. The principles of this spectroscopic technique are based upon the manner in which infrared light interacts with matter. When infrared radiation passes through a molecule, specific frequencies of the light which coincides with the natural vibrational frequency of the chemical bonds of the substance can be absorbed. This results in excitation of the molecule to higher vibration states and the difference in energy between the two vibrational states lies within the mid-infrared range.

A plot of intensity of infrared radiation as a function of energy produces a spectrum that is unique for each compound. The x-axis of the infrared spectrum is plotted with wavenumber (cm^{-1}) to measure the position of an infrared absorption band, while the y-axis is presented by either absorbance (A) or percept transmittance (%T). It should be noted that absorbance and transmittance are mathematically related to each other, and they can be converted using FTIR software from one to the other. This conversion occurs only on the y-axis and does not affect the peak position on the x-axis.

FTIR spectra show absorption bands which correspond to the frequencies of vibrations between the bonds of the atoms within the molecule. For this reason, functional groups and compounds can be identified from their FTIR spectrum as many functional groups can be recognised by their characteristic vibration frequency.

The basic components of the FTIR instrument are shown in Scheme 2.1. The Fourier transform infrared (FTIR) spectrometer consists of a light source, which emits radiation containing all IR wavelengths (e.g. 4000–400 cm^{-1}), an interferometer, a sample holder, a detector and a computer. One of the main parts of a FTIR spectrometer is an interferometer composed of a beam splitter, fixed and moveable mirrors and a drive and positioning mechanism to alter the position of the moveable mirror. The beam splitter divides the radiation beam, directing one of them to the fixed mirror and the other beam to the moveable mirror. At the beam splitter, the two reflected beams with different optical paths are recombined, producing an interference pattern, which is the sum of all the interference patterns originated by each wavelength in the beam. The interference pattern can be changed to produce a detected signal that varies with optical path difference, by systematically changing the difference in the two paths. This pattern is called an interferrogram, Using interfaced computer software, a Fourier transforms of the interferrogram produce a spectrum that can be easily interpreted, consisting of a plot of energy absorption as a function of wavenumber.

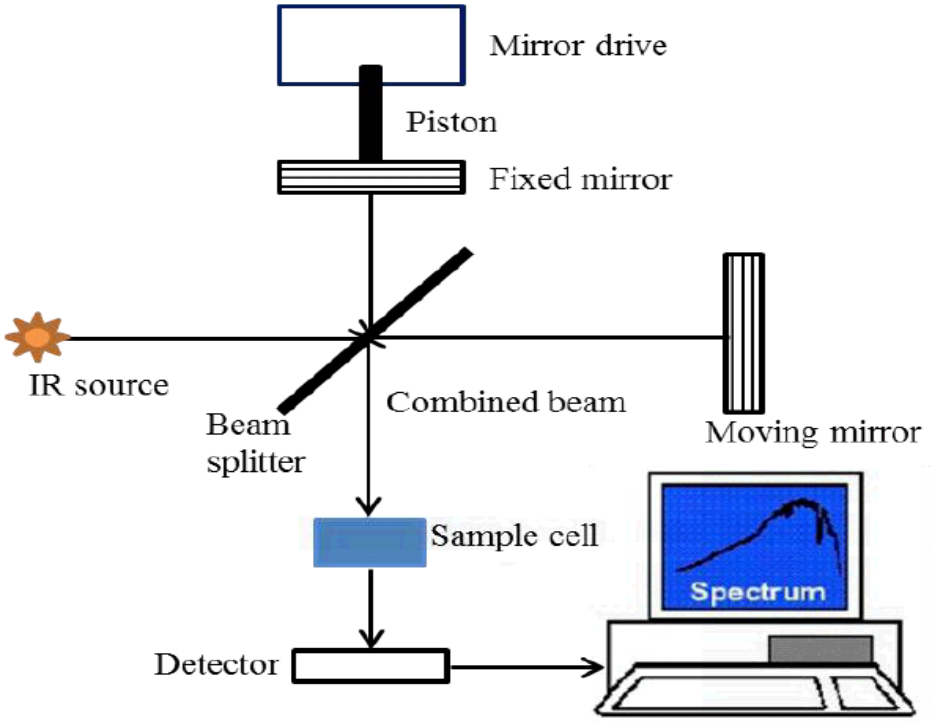

Scheme 2.1. Schematic diagram showing the main components of FTIR spectrometer.

The FTIR spectrometer simultaneously collects all the IR frequencies and for this reason it confers a major advantage over traditional dispersive spectrometers which

measure the IR frequencies individually and direct the IR light on a grating by using a monochromator.

In this thesis, FTIR was used to confirm the formation of ferrocene monolayers on silicon surfaces. It was primarily used also to characterise the different bonds between the ferrocene and silicon surfaces. All FTIR spectra were acquired using a Bio-Rad Excalibur FTS-40 spectrometer (Varian Inc., Palo Alto, CA, USA), equipped with a liquid nitrogen cooled deuterated triglycine sulphate detector, and recorded over the 600-4000 cm^{-1} range, with 128 scans, and at 4 cm^{-1} resolution.

2.2 X-ray photoelectron spectroscopy (XPS) [3-5]

XPS is a surface chemical analysis technique, also sometimes referred to as electron spectroscopy for chemical analysis (ESCA). XPS spectra are obtained by irradiating a sample with a beam of X-rays while simultaneously measuring the kinetic energy (KE) and number of electrons that escape from the top (usually < 10 nm) of the material being analysed. XPS uses ultra-high vacuum conditions ($<10^{-10}$ Torr) as shown in Scheme 2.2.

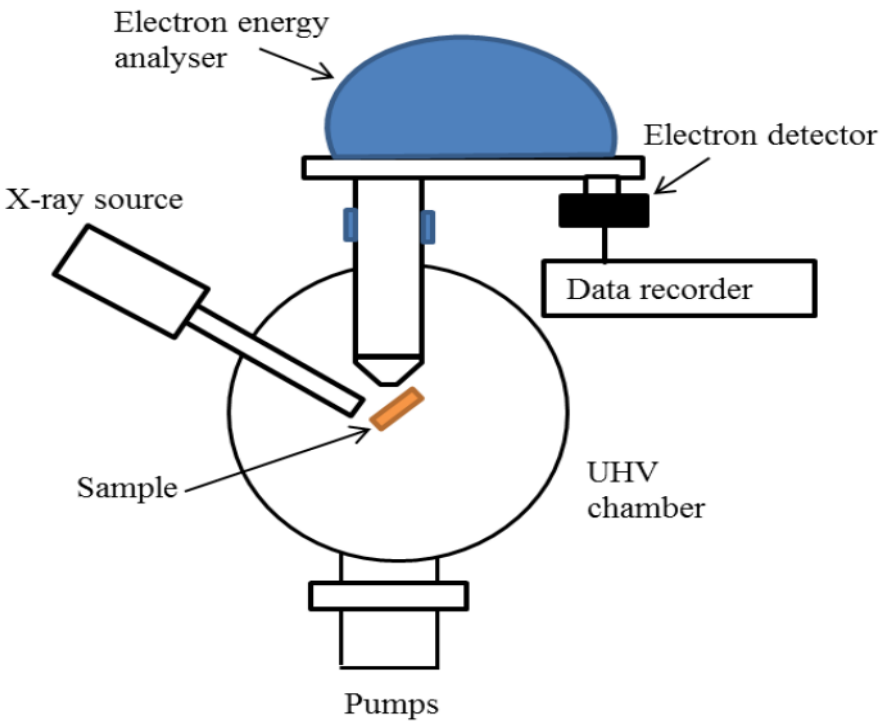

Scheme 2.2. Schematic diagram of the major components of an XPS instrument.

X-rays are produced by bombarding a metallic target (usually Al: 1486 eV, or Mg: 1254 eV) with high-energy electrons. When the incoming photons hit the sample it causes photo-ejection ionization of the electrons from the inner shell orbitals. There is certain energy between the core level electrons and the nucleus call binding energy (BE). When the electron is pulled away from the nucleus, the attraction between the electron and the nucleus decreases and the BE decreases until a point is reached when the electron will be free of the nucleus. This is the point with zero energy of attraction between the electron and the nucleus as shown in Figure 2.1.

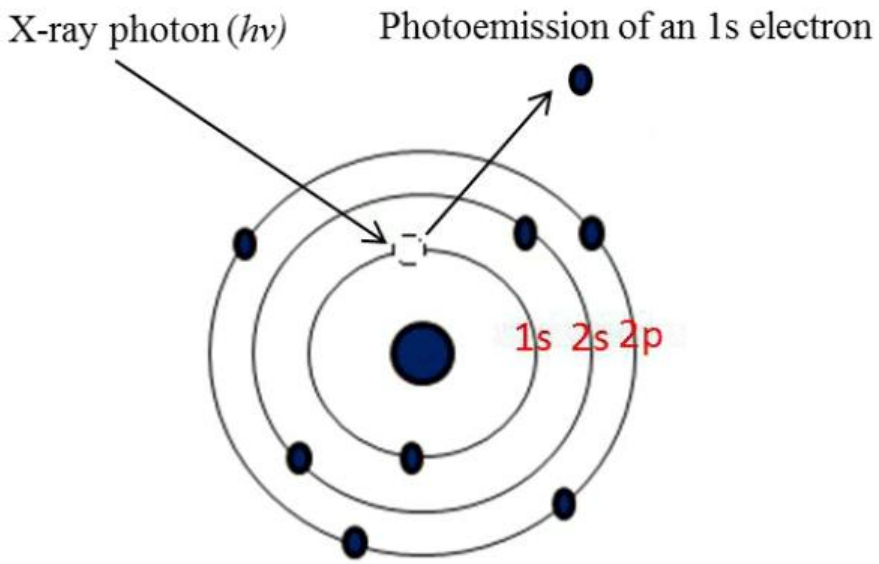

Figure 2.1. Schematic of principle of X-ray photoelectron spectroscopy.

The kinetic energy of emitted photoelectrons is described by the equation.

$E_K = h\nu - E_B - \phi$

Where, E_k is the kinetic energy of emitted electron that is measured in the XPS spectrometer, ν is Planck's constant, h is the incident frequency, E_B is the binding energy of the electron, and φ is the work function of the spectrometer.

A typical XPS spectrum is a plot of detected electrons of core level versus the binding energy of the electrons as shown in Figure 2.2. The energy of the emitted electrons depends on atomic and molecular environment from which they originated. These characteristic peaks correspond to the configuration of the electrons within the atoms and the number of detected electrons in each peak is directly related to the amount of element within the area irradiated.

The core level energy depends on the chemical state of the atom. When the element is in different chemical state, e.g. oxidation state, its corresponding energy level will be different, thus giving out photoelectrons at slightly different energies. The energy shift is the so-called "chemical shift". The chemical shift in binding energy correlates with the overall charge on the atom and with the presence of any chemical bonding. This can be interpreted by XPS data to give information of a chemical nature of the sample such as the oxidation state of the atom, number and type of surrounding atoms, and the electronegativity of atoms.

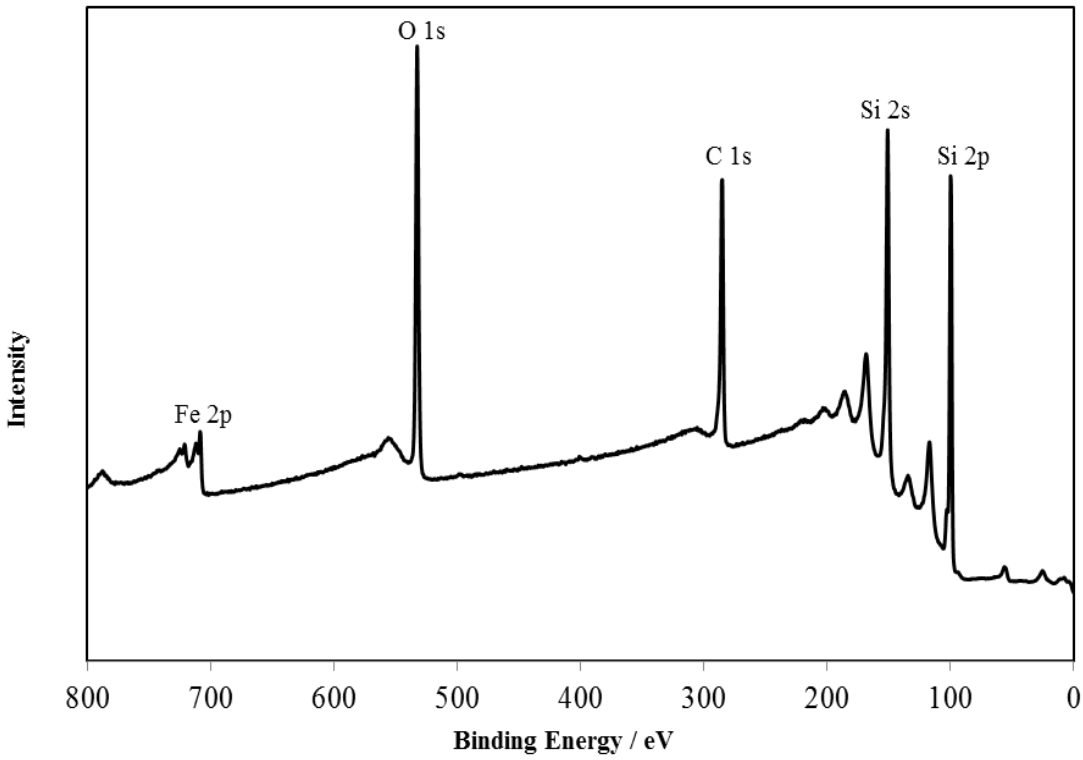

Figure 2.2. Survey XPS spectrum of ethylferrocene monolayer on silicon.

In this thesis, all XPS were carried out using a Thermo Scientific K-Alpha X-ray photoelectron spectrometer (Thermo Electron Corp., East Grinstead, UK), equipped with an Al Kα X-ray source (1486.6 eV) with a variable spot size of 20–400 μm. A take-off angle of 90˚ was used during data acquisition. Data analysis was carried out using CasaXPS software (Casa Software Ltd.).

2.3 Atomic force microscopy [6,7]

Atomic force microscopy (AFM) or scanning force microscopy (SFM) is a very high-resolution type of scanning probe microscopy. It is classically used for mapping surface

topographies. The general description of the AFM process, is to use a sharpened tip with long typically < 5 μm and diameter < 15 nm, mounted at one end of cantilever upon which a laser beam is focused, to track over the sample surface features.

Forces between the tip and the sample surface cause the cantilever to deflect and a detector measures the cantilever deflection as the tip is scanned over the sample. Changes in the tip height (z) are related to the force on the tip and stiffness of the cantilever of the cantilever via Hooke's law (F= kz), where k is the spring constant and the measured cantilever deflections allow a computer to generate a map of surface topography (Scheme 2.3).

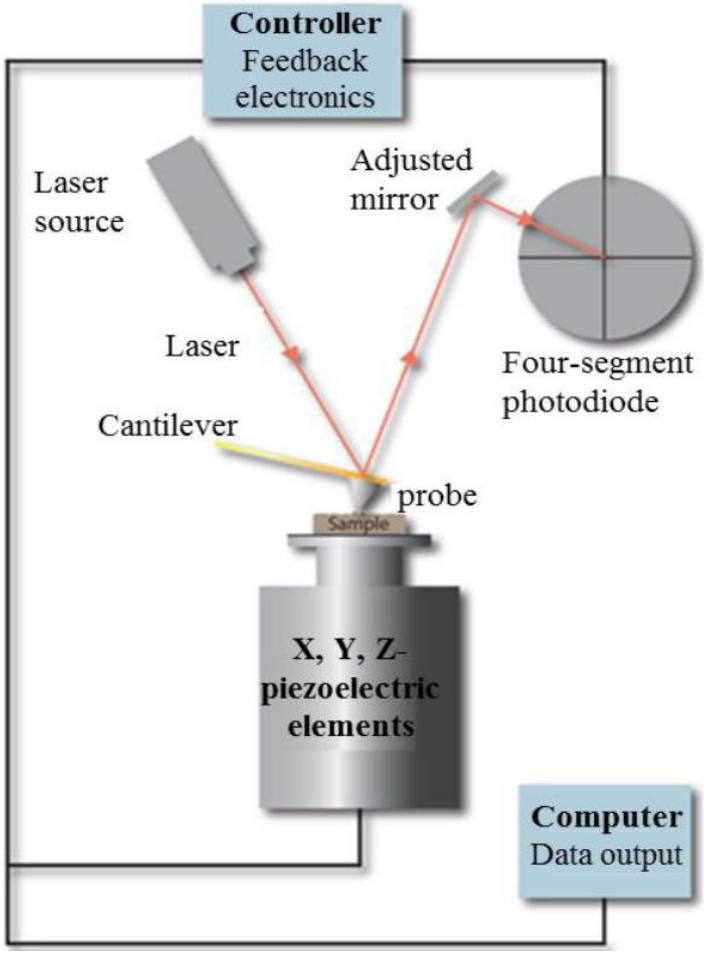

Scheme 2.3. Schematic diagram of the major components of atomic force microscopy (AFM).

The AFM can work in two modes, tapping and contact mode. In tapping mode AFM topography scans, the tip oscillates near the sample surface. The amplitude of the cantilever oscillation is a few tens of nanometres on the sample, which ensures that the

tip does not get stuck in the thin layer see Figure 2.3a. The sample in tapping mode is less likely to be damaged by the tip.

In contact mode, the AFM probe remains in close contact with sample as the scanning proceeds see Figure 2.3b. The probe-sample interaction in contact mode is dominated by repulsive forces. The force between the tip and the surface is kept constant during scanning by maintaining a constant deflection. Contact mode AFM imaging can cause damage to soft samples such as organic and biological materials, due to high forces exerted by the tip on the samples.

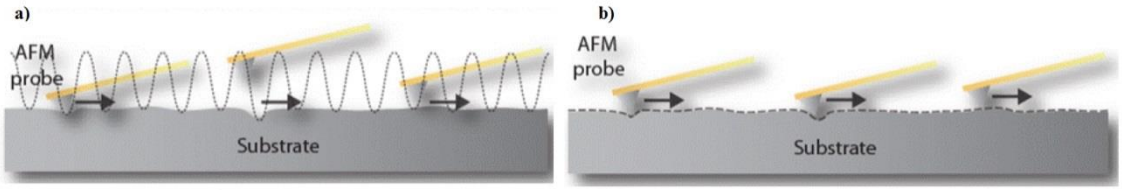

Figure 2.3. Schematic diagram showing (a) tapping mode and (b) contact mode operation of AFM techniques.

In this work, topographical AFM data was acquired using Tapping Mode^{TM} were performed in air on a Multimode Nanoscope IIIa (Veeco Instruments Inc., Metrology Group, Santa Barbara, CA, USA). Etched Si AFM probes (TESP model, n-doped Si cantilevers, $f0$ = 230–280 kHz, spring constant = 20–80 N m-1, Veeco Instruments Inc., Metrology Group). Data acquisition was carried out using Nanoscope version 5.12b36 software (Veeco Instruments Inc., Digital Instruments).

2.4 The composition of electrochemical cell [8,9]

Electrochemical cells with low resistance can be investigated successfully using only two electrodes. However, at high cell resistance the three-electrode cell is preferred for electrochemical analysis, where using a reference electrode, a working electrode, and a counter electrode. The working electrode is the most interesting electrode, where the reaction between electroactive species in solution and the electrode surface takes place. The potential is applied between the reference electrode and the working electrode and the resultant current is measured between the working electrode and the counter electrode. These data are then plotted as current (i) vs. potential (E). The second electrode of the electrochemical cell is the reference electrode in which the potential must remain as a constant value over the experiment duration, even with passing of the

current across the reference electrode. Therefore, any changes in the electrochemical cell can be attributed to the processes occurring on the working electrode (either observed or controlled potential). The reference electrode should also be reversible and have a stable potential, which may be calculated from the Nernst equation. There are many standard reference electrodes such as the standard hydrogen electrode (SHE) which is set by convention equal to 0.00 V, and standard silver chloride electrode (0.222V vs. SHE at 25 °C) and saturated calomel electrode SCE (0.242V vs. SHE at 25 °C).

The third electrode in the electrochemical cell is the counter electrode; usually it can be platinum, tungsten or any inert wire. Since in two-electrodes cells the current flows between both electrodes (working and reference), this may affect the potential of the reference electrode and consequently the cell potential, because the reference electrode serves simultaneously as auxiliary and reference electrode. In order to overcome such a problem a counter electrode should be used, and then the current will flow between working and counter electrodes instead of working and reference electrodes.

The correlation between the potential and concentrations of electroactive species can be mathematically expressed by the Nernst equation:

$$E=E^{\phi} + \frac{RT}{nF} \ln \frac{[O]}{[R]} \qquad \text{.....(2.1)}$$

Where E is cell potential (V), Eϕ is standard electrode potential (V), R is the gas constant (8.3145 J mol^{-1} K^{-1}), F is Faraday's constant (1F= 96,485.3 C mol-1), [O] is the activity of oxidized species and [R] is the activity of reduced species.

As current passes through the cell Fe^{3+} is converted to Fe^{2+} at the electrode interface. Therefore, the depletion of Fe^{3+} at the electrode is quicker than diffusion from bulk solution. This means that, the Faradic current is dependent on both electrode kinetic and mass transport.

2.4.1 Electrode Kinetic

Electrode kinetics are related to rate the electron transfer process (k_0) between the electrode and solution. There are some parameters which can disturb the electron transfer at the solution-electrode interface, such as electrode material, adsorbed species, multiple and consecutive electron transfer steps. If a high kinetic barrier occurs, this must be overcome by applying extra potential called overpotential, at this point the k_0

<< k_d. For example, for reduction of ferric ions to occur at the electrode, a free energy barrier must be overcome for electron to leave the working electrode. Therefore, by varying the working electrode potential, the free energy of its available electrons can be influenced, making reduction at the interface more or less favourable.

2.4.2 Mass transport

The reactant must be transferred from the bulk solution to the interface to allow electrolysis to take place at an electrode. After reaction has occurred the molecule must diffuse away from the surface to allow for other molecules to be transported into electrode. It should notice that, there are three modes of mass transport, which convection, diffusion and migration as shown in Figure 2.4.

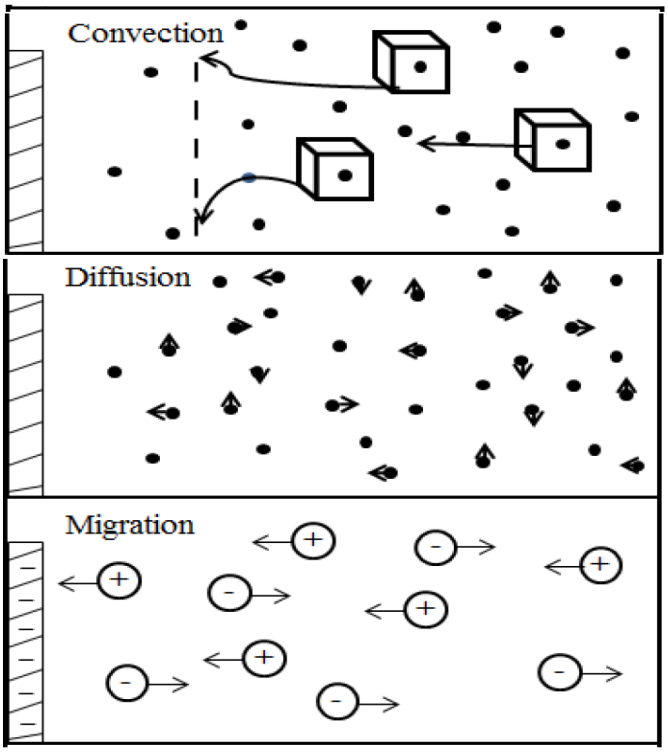

Figure 2.4. The three modes of mass transport, convection, diffusion and migration.

(a) Convection:

Convection can be defined as the movement of material by movement of the liquid. It may be caused by one of two initially or forced convection. Initially convection is natural convection which can occur either thermal gradients or/ and density differences in solution caused by electrolysis. Whereas forced convection could occur by stirring, gas bubbling or vibration of the electrolyte.

(b) Diffusion:

Diffusion can occur for species that are either changed and uncharged. It is defined as spontaneous movement of analyte species to the electrode surface under concentration gradient where chemical change has taken place. At the electrode surface the reaction which occurs is where the concentration of [O] starts to reduce with time in the region adjacent to the electrode surface. Whereas, the concentration of [R] starts to develop with time. Hence, in order to maintain current flow during the experiment, O will diffuse toward the electrode, and R will diffuse away from the electrode or vice versa for an anodic reaction.

(c) Migration:

Unlike diffusion, migration is a movement of just charged species to the electrode surface by electrostatic force. The mechanism by which electrical charges pass through the electrolyte can be ascribed to the migration. However, such a mode of mass transport is uncommon for the analyte because the inert electrolyte screens the charge on the electrode and there is no electrical field outside the double layer (few nm).

2.4.3 Diffusional transport in electrolysis

In consider this equation: $Fe^{3+} + e^{-} \rightarrow Fe^{2+}$

In the presence of excess electrolyte and without stirring, only diffusion of Fe^{3+} through the solution down a concentration gradient may take place. Initially, the system contains Fe^{3+} at the interface and in the bulk solution. When a potential is applied to system, the Fe^{3+} moves to electrode causing concentration gradient of Fe^{3+} near to electrode (as no remain Fe^{3+} near to electrode) while the concentration of Fe^{3+} remains the same in bulk solution. In other words, the concentration of Fe^{3+} is different near to electrode area and in bulk solution. The area near to electrode called the diffusion layer, where the concentration gradients are essentially linear. Figure 2.5 show the increase in diffusion layer using a concentration profile at set times in an electrolysis experiment.

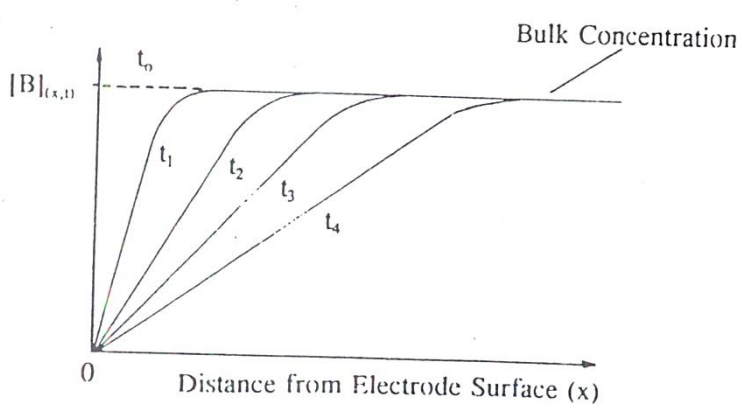

Figure 2.5. Concentration profile of Fe^{3+} at an electrode *vs* time in an electrolysis experiment.

The diffusion layer grows until the reduction of Fe^{3+} to Fe^{2+} during electrolysis reaction has taken place. However, the diffusion layer is limited by natural convection, which has some control over the final diffusion layer size at the electrode, and thus the speed at which constant layer thickness is obtained.

Therefore, diffusion and convection can affect the transport of redox species to the electrode, which produces larger current than observed for pure diffusion.

2.4.4 Cyclic voltammetry

Cyclic voltammetry is one of the most widely used methods in inorganic, physical and biological area for study of fundamental oxidation and redaction processes. However, in general, it is widely used for qualitative information on electron transfer processes, from the relationship between current and voltage observed in an electrochemical process.

Initially, in cyclic voltammetry the working electrode is immersed in an unstirred solution, which containing some electroactive species. A potential is applied to the working electrode ($E_{initial}$), and is scanned to a predetermined limit (E_1), then at this potential the voltage is reserved and returns to a second predetermined limit (E_2). The potential-time waveform is based on sweeping the potential at a constant rate between initial and final potentials which is known as the forward scan. Then the potential can be swept back to the initial potential in the backward scan. This is called an excitation signal, a linear potential scan with a triangular waveform as shown in Figure 2.6.

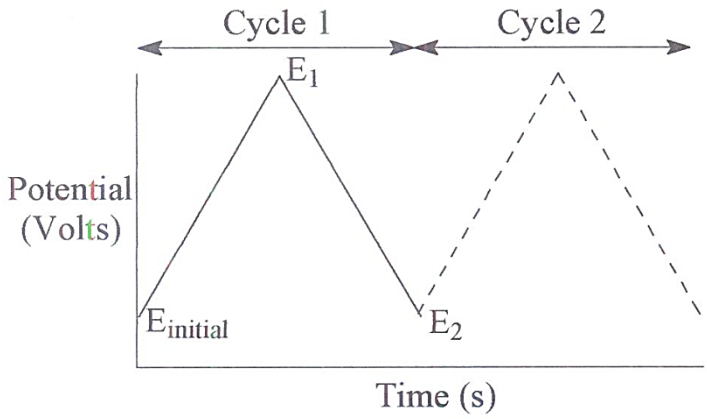

Figure 2.6. Excitation signal in CV in triangle waveform.

The potential starts at ($E_{initial}$) where no reaction occurs and scans to a second potential (E_1). When the potential reaches E_1 either reduction/or oxidation can be take place at the electrode surface as shown in Figure 2.7. Then the potential is reversed to E_2. The current is proportional to the concentration gradient at the electrode surface. The repeating CV for many cycles can give information on the stability of the electroactive species and also the rate of electron transfer and molecular mechanisms.

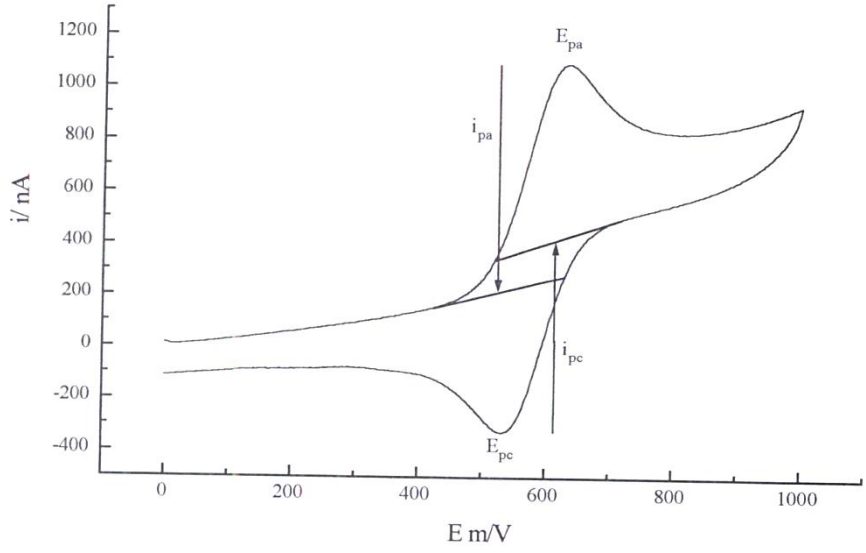

Figure 2.7. Cyclic volatammogram for ferrocene derivative.

Figure 2.7 shows an example CV for a ferrocene derivative. The potential ($E_{initial}$) is sufficiently positive enough to oxidize the ferrocene, and the anodic current (i_{pa}) is observed. The current increases rapidly until all electroactive species near to the electrode area have been oxidized which causes the peak. The peak begins to decline as the oxidation process is limited by diffusional transport to the electrode interface. At the

switching potential, the potential is reversed and the negative scan starts, which continues until the potential is negative enough to reduce all the recently oxidized species. The reduction process gives a cathodic wave (i_{pc}) when the reduction process becomes mass transport limited.

2.4.5 Cyclic voltammetry applied to surface bound specie

When chemical species are attached to a surface, reversible electron transfer can be recorded. The oxidation/reduction process of surface bound ferrocene are:

$$1: Fe^{2+} \Leftrightarrow Fe^{3+} + e^{-}$$
$$2: Fe^{3+} + e^{-} \Leftrightarrow Fe^{2+}$$

The potential starts from zero ($E_{initial}$) and increases until it becomes positive enough to oxidise the ferrocene (Fe^{2+}) at which point an anodic current is observed. The current continues to increase until all the ferrocene (Fe^{2+}) is oxidised to ferrocenium (Fe^{3+}), then the current decays back to zero. After that the potential is scanned until it reaches switching potential where it is reversed. The potential is scanned until it is sufficiently negative to reduce the surface bound Fe^{3+}, the peak increases until all the Fe^{3+} is reduced to Fe^{2+}. The ideal CV of an electroactive speices bound to a surface is shown in Figure 2.8.

Where there is no effect of diffusion, as the reaction is controlled only by electron transfer kinetics, the areas under both peaks are equal. This area gives the amount of charge required to carry out the electrochemical process, which gives the amount of material bonded to the surface.

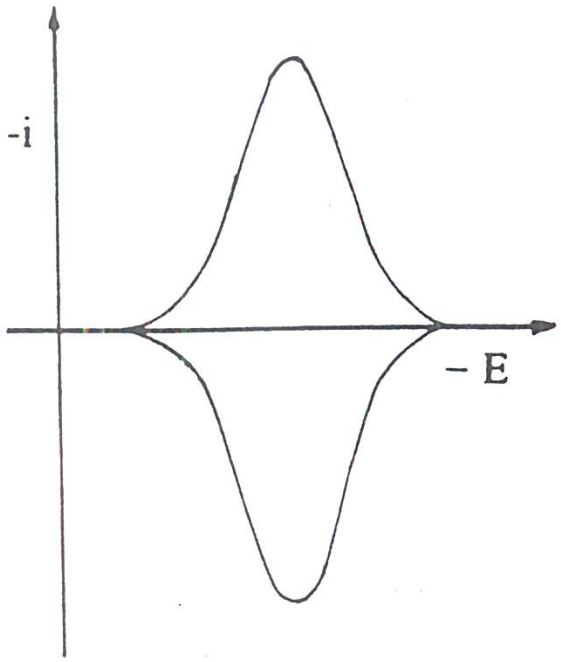

Figure 2.8. CV for reversible one-electron couple bound to a surface.

In this study, electrochemical measurements for ferrocenyl silicon monolayers were carried out in an all-glass three-electrode cell with Ag or Ag/AgCl wire reference electrode, a platinum/palladium wire as counter electrode, where silicon surface is the working electrode. CV in most of cases were recorded in aqueous 0.1 KCl electrolyte against a Ag/AgCl wire reference electrode and a platinum wire was used as the counter electrode using an Ivium CompactStat potentiostat. Silicon electrodes were created by sealing silicon chips in a teflon holder with a circular section of 3.85 mm diameter exposed to light. A screw cap allowed replacement of the silicon chip, and a Vitron O-ring was used to create a seal between the screw cap and the silicon surface. The teflon cell was held within a glass cell and the exposed electrode surface aimed at a quartz window in the side of the glass cell see Scheme 2.4. The light source was placed against this window and used to illuminate the silicon electrode during CV experimental.

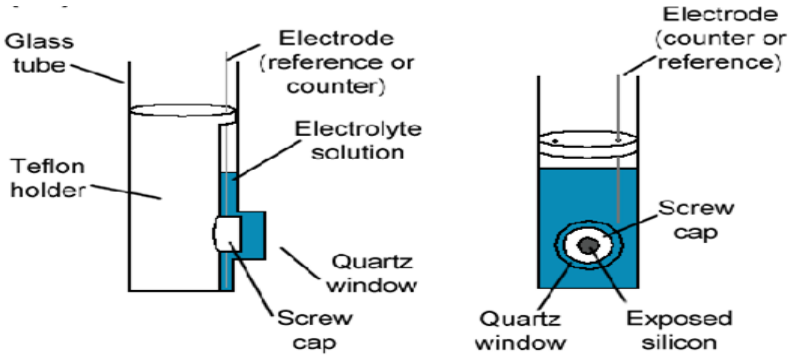

Scheme 2.4. A diagram of the Teflon cell employed in the CV experimental . Light from the Modulight source is directed through the quartz window onto the wetted electrode surface.

References

1. Silverstein, R.M.W., Francis X.; Kiemle, David J, *Spectrometric Identification of Organic Compounds*. Edition, Editor. 2005, John Wiley & Sons.

2. Smith, B.C., *Fundamentals of Fourier Transform Infrared Spectroscopy*, Second Edition. 2011: Taylor & Francis.

3. Smith, G.C., *Surface analysis by electron spectroscopy: measurement and interpretation.* 1994: Plenum Press.

4. Vickerman, J.C., *Surface analysis: the principal techniques*. 1997, Chichester, England John Wiley.

5. Watts, J. F. Wolstenholme, J. *An Introduction to Surface Analysis by XPS and AES.* 2008. Chichester, England John Wiley & Sons ltd..

6. Rugar, D. and P. Hansma, *Atomic force microscopy*. *Physics Today*, 1990. 43(10).

7. Yao, N. and Z.L. Wang, *Handbook of Microscopy for Nanotechnology*. 2005, Springer London, Limited.

8. Allen J. Bard and L.R. Faulkner, *Electrochemical Methods Fundamental and Application.* 2001, Vol. Second Edition.: *John Wiley*.

9. Greef R., R. Peat, D. Pletcher, L. M. Petre, and J. Robinson, *Instrumental Methods in Electrochemistry*. 1985, *New York: Chichester*.

Chapter 3

Part of this chapter is based on the publication:

A. Mishchenko, M. Abdualla, A. Rudnev, Y. Fu, A. R. Pike and T. Wandlowski, "Electrochemical scanning tunnelling spectroscopy of a ferrocene-modified n-Si(111)-surface: electrolyte gating and ambipolar FET behaviour" *Chem. Commun.*, 2011, **47**, 9807-9809.

Chapter 3 -Ferrocenyl silicon surfaces; synthesis and characterisation

In the introductory chapter, the attractive electrochemical characteristics of ferrocene and the facile routes to the chemical modification of silicon electrodes were discussed. There has been an intense effort to fabricate and understand the electrochemical properties of ferrocenyl modified silicon surfaces.[1-16] This Chapter foucses on the fabrication of ferrocenyl monolayers with three different -C_2- linkages C-C, C=C, C≡C between the silicon and redox group. Studies into the stability and electrochemical properties are reported.[1]

3.1 Introduction

In order to fabricate suitable ferrocenyl silicon surfaces for device integration, the chemistry of the modification step needs to be highly reproducible. A key parameter that requires fine control is the coverage of the silicon surface with ferrocene molecules. In previous work, a large range of ferrocenyl coverages have been reported, varying from 3.5×10^{-12} to 2.8×10^{-9} mol cm^{-2}.[1,3,5,6,10,14-16] These results suggest that there is over a thousand fold difference in coverage between the lowest and highest surfaces investigated. This discrepancy appears to be due to the different procedures employed or the nature of the linkages used to produce the monolayer. Therefore, one aspect of obtaining highly reproducible surfaces that needs consideration, chemistry and the solvent used in the modification step.[3,17] There are three main methods for the activation of the hydrosilylation reaction. The methods that have been previously used to modify a silicon surface are: thermal activation, light irradiation and catalyst activation, where the reaction proceed via a radical mechanism.[18]

Sano and co-workers investigated different hydrosilylation activation methods and different solvents with low concentrations of vinylferrocene to form an ethylferrocene monolayer on a silicon hydride surface.[3] They reported mesitylene and *n*-decane with the thermal activation method and the visible light irradiation method.[3] They found that activation by light formed high quality monolayers, and also that *n*-decane was better than mesitylene as a solvent, due to *n*-decane being a superior solvent for suppressing particulate deposition.[3] Therefore, this chapter investigates other ways to improve the monolayer stability and the reproducibility of the synthetic procedures.

This Chapter investigates three different synthetic methods to produce three different linkages (sp^3, sp^2, and sp linkage) between the silicon surface and the ferrocene, as shown in Scheme 3.1. After synthesis, investigations into how each of these approaches affects the total coverage of ferrocene, and how reproducible each method is, are explained. The different methods used to produce three different linkages are (a) a thermal method to fabricate an ethyl-linked ferrocene silicon **EFc** (Scheme 3.1a), (b) a room temperature method to fabricate a vinyl-linked ferrocene silicon **VFc** (Scheme 3.1b), and (c) a nucleophilic substitution method to fabricate ethynyl-linked ferrocene Silicon **EnFc** (Scheme 3.1c).

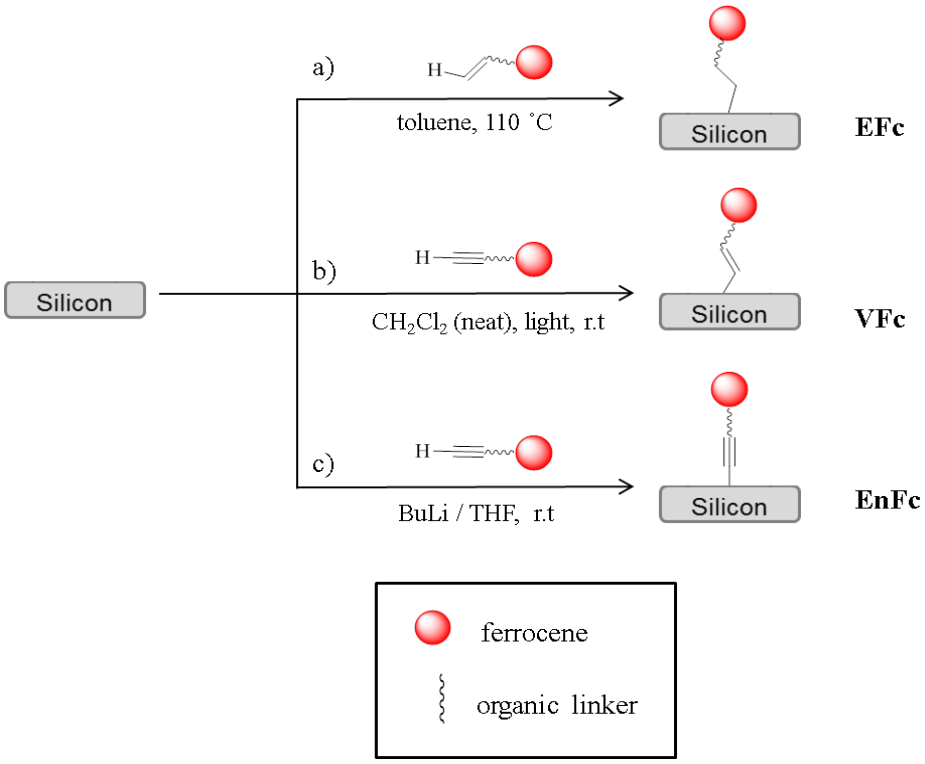

Scheme 3.1. Schematic representation of the three routes employed to generate ferrocene modified silicon surfaces with different linkages, a) modified silicon surface with ferrocene to generate ethyl linkage **EFc**, b) modified silicon surface with ferrocene to generate vinyl linkage **VFc**, c) modified silicon surface with ferrocene to generate ethynyl linkage **EnFc**.

The following results are representative of many experiments performed on each surface fabricated. The key data is presented and highlights some of the key findings.

3.2 Results and Discussion

In order to reproducibly fabricate ferrocenyl monolayers on a silicon substrate, there are two main considerations. The first is the preparation of the silicon surface before the modification and the second is the modification step itself. These two processes are

discussed here for the fabrication of **EFc**, **VFc**, and **EnFc** surfaces. This Chapter also details the characteristion of these ferrocenyl surface by atomic force microscopy (AFM), X-ray photoelectron spectroscopy (XPS), and cyclic voltammetry (CV). Some DFT calculations are included to support these findings.

3.2.1 Cleaning and etching silicon surface

The silicon surface was prepared for modification according to the literature precedence,[19,20] Scheme 3.2. The cleaning of the silicon surface involves an initial wash with organic solvents (trichloroethylene, acetone, 2-propanol) in order of increasing hydrophilicity/polarity and ends with a water wash. This ensures that any organic material is removed from the surface. This is followed by soaking the wafer in piranha solution (H_2SO_4/H_2O_2) to oxidize the surface and give a uniform oxide layer. An etching step follows using 40% ammonium fluoride solution to remove the silicon oxide and leave a silicon hydride surface, which is atomically flat, as shown in Scheme 3.2.

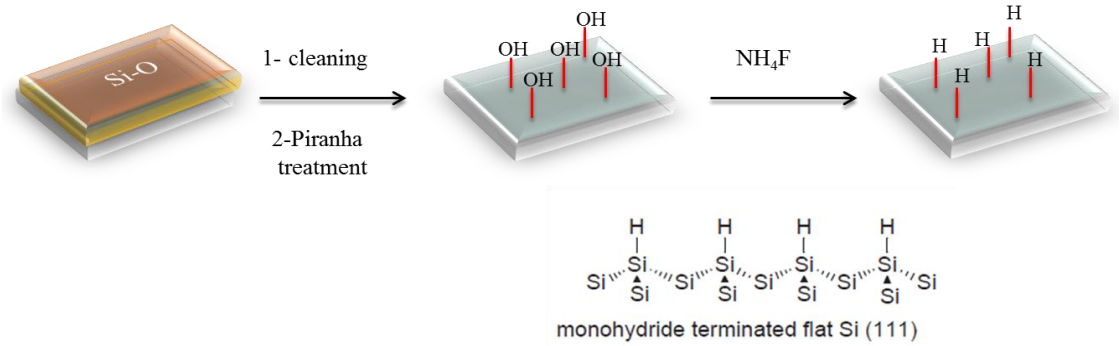

Scheme 3.2. Etching steps of flat silicon surface n-type Si(111), starting with cleaning and then followed by NH_4F etching.

3.2.2 Modification step

The hydride silicon surface was modified with ferrocene derivatives to give three surfaces with sp^3, sp^2, and sp linked monolayers as shown in Scheme 3.3.

Ethylferrocene silicon **EFc** (sp^3 linkage) was prepared by the reaction between vinylferrocene and a silicon hydride surface using thermal activation of the surface in toluene at high temperature 110 ˚C via a hydrosilylation mechanism.[14] Other groups have used mesitylene,[10] and *n*-decane[3], as well as toluene as solvents for the hydrosilylation reaction.[14] However to assess a single reaction condition, toluene was chosen as the solvent for all thermally activated surface modifications.

Vinylferrocene silicon **VFc (**sp^2 linkage) was prepared by reaction between the silicon hydride surface and ethynylferrocene, at room temperature in neat DCM under ambient illumination for overnight. A vinylferrocene monolayer was previously produced by mild photochemical (white light) grafting by another group,[16] and also in the presence of a Lewis acid.[6]

Finally, an ethynylferrocene silicon surface **EnFc (**sp linkage) was produced by the reaction between silicon hydride surface and ethynylferrocene. A nucleophilic substitution reaction was used by an acetylide anion using butyl lithium.[6]

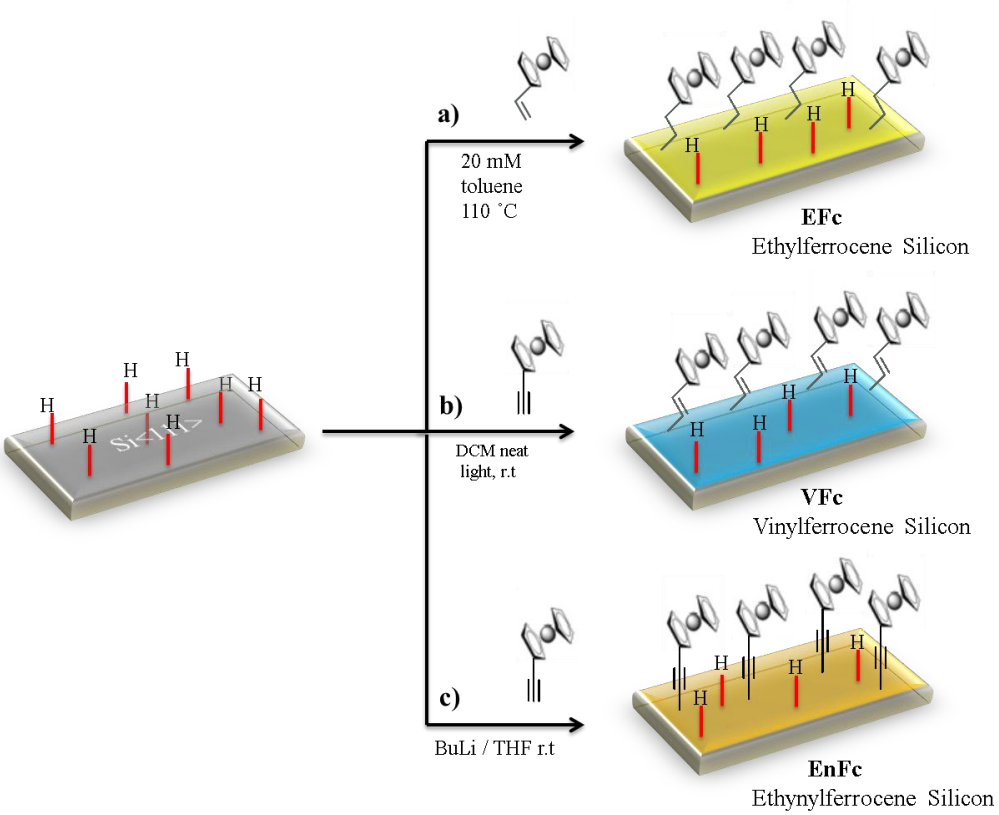

Scheme 3.3. Ferrocene monolayers on silicon surface were formed with three different linkages involving sp^3, sp^2 and sp hybridised carbons. a) **EFc** refers to the monolayer formed by thermal reaction of vinylferrocene with Si-H. b)**VFc** refers to the monolayer formed by reaction of ethynylferrocene with Si-H. c) **EnFc** refers to the monolayer formed by reaction of ethynylferrocene in THF with Si-H.

3.2.3 Characterisation by FTIR spectroscopy

FTIR is a convenient spectroscopic method that can be used to quickly determine the chemical functionality of the modified silicon surfaces and to confirm the different linkages between the ferrocene and silicon surface. Silicon is largely transparent to FTIR and so can simply be used as a support for monolayer studies by IR. However, in

order to follow the modification steps by FTIR an increased surface area is required as a single monolayer is insufficient for detection by FTIR. Therefore, instead of the atomically flat etched silicon, porous silicon (PS) is required to monitor the surface by FTIR. PS provides a vastly superior surface area and therefore a much larger amount of material can be analysed by FTIR. PS was made similar to the literature methods,[21] as shown in Scheme 3.4.

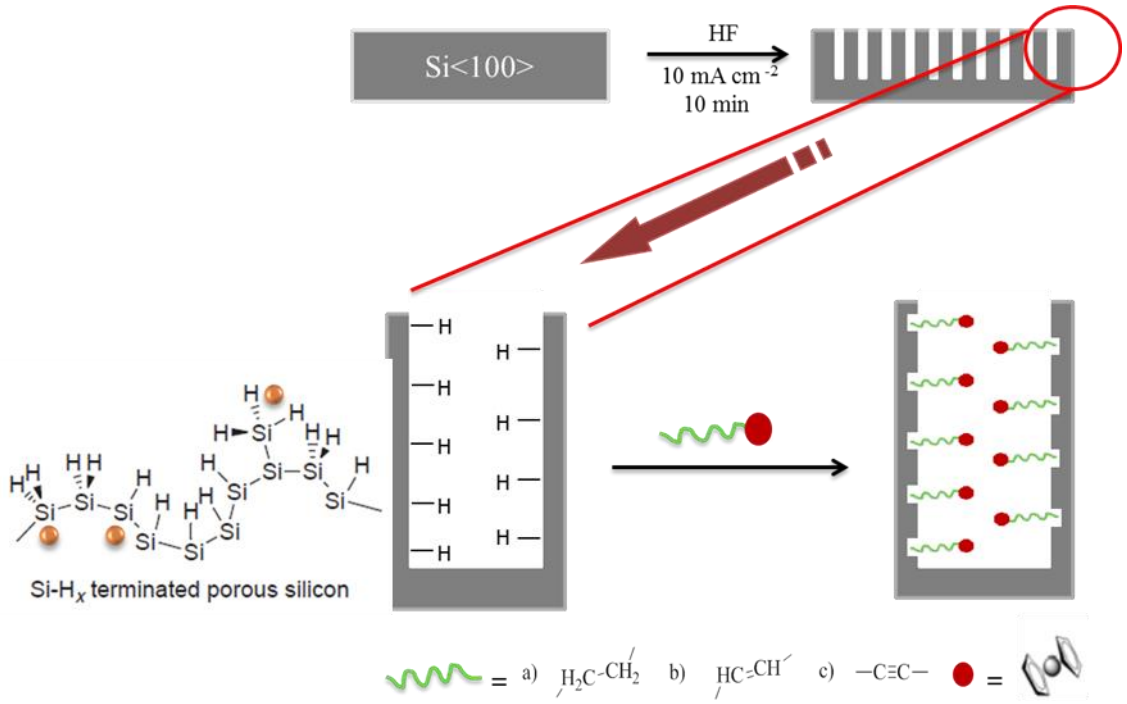

Scheme 3.4. Schematic representation of electrochemical etching of Si(100) with HF to produce porous silicon (PS). PS followed by formation of three different ferrocene linkages **EFc**, **VFc**, and **EnFc** the same method used with flat silicon hydride.

The alkylation of the porous silicon surface with ferrocene derivatives was then followed by FTIR, to produce the three different surfaces, **EFc**, **VFc**, and **EnFc**. The surface modification conditions were kept exactly the same as those used for the modification of single-crystal silicon as shown in Scheme 3.3.

In general, FTIR spectra of freshly prepared porous silicon shows three relatively strong bands at 2088, 2112 and 2140 cm^{-1} due to the three Si-H, SiH_2, and SiH_3 surface species respectively.[22,23] In addition, a strong band at 915 cm^{-1} appears due to the Si-H_2 scissors mode,[14] and Si-H bending at 660 cm^{-1}. After alkylation, the Si-H stretches are observed as less intense and unstructured bands due to alkylation and heterogeneous broadening.[14] The presence of a mode at 2250 cm^{-1} due to O-Si-H in **EFc** (Figure 3.1) and **VFc** (Figure 3.2) suggests a small amount of oxidation of those surfaces.[23] This is

typical for PS treated with polar solvents,[21] and is probably not observed for **EnFc** (Figure 3.3) because of the extreme reactivity of BuLi towards trace water and the polar solvent, THF, employed.

Figure 3.1 shows the FTIR spectra of hydrogen-terminated PS, vinylferrocene, and the **EFc** surface. After alkylation of PS, the FTIR spectrum no longer shows the C=C stretching mode peak of the vinylferrocene at 1620 cm^{-1}, which indicates a change of hybridisation of the vinyl carbon atoms (sp^2 to sp^3) and confirms chemisorption of vinylferrocene on the silicon surface. New peaks appear at 2952, 2921 and 2852 cm^{-1}, which can be attributed to asymmetric/symmetric methylene stretches the of the ethyl linkage. The other new peak at 3096 cm^{-1} may be attributed to C-H stretches within the ferrocene ring. However, the silicon surface is not completely covered by ethylferrocene as the Si-H band is still relatively sharp and two of the three peaks are still identifiable at 2083 cm^{-1} and 2107 cm^{-1}. It is known that upon alkylation of Si-H surfaces the three Si-H stretch modes tend to broaden and merge into one peak.[14]

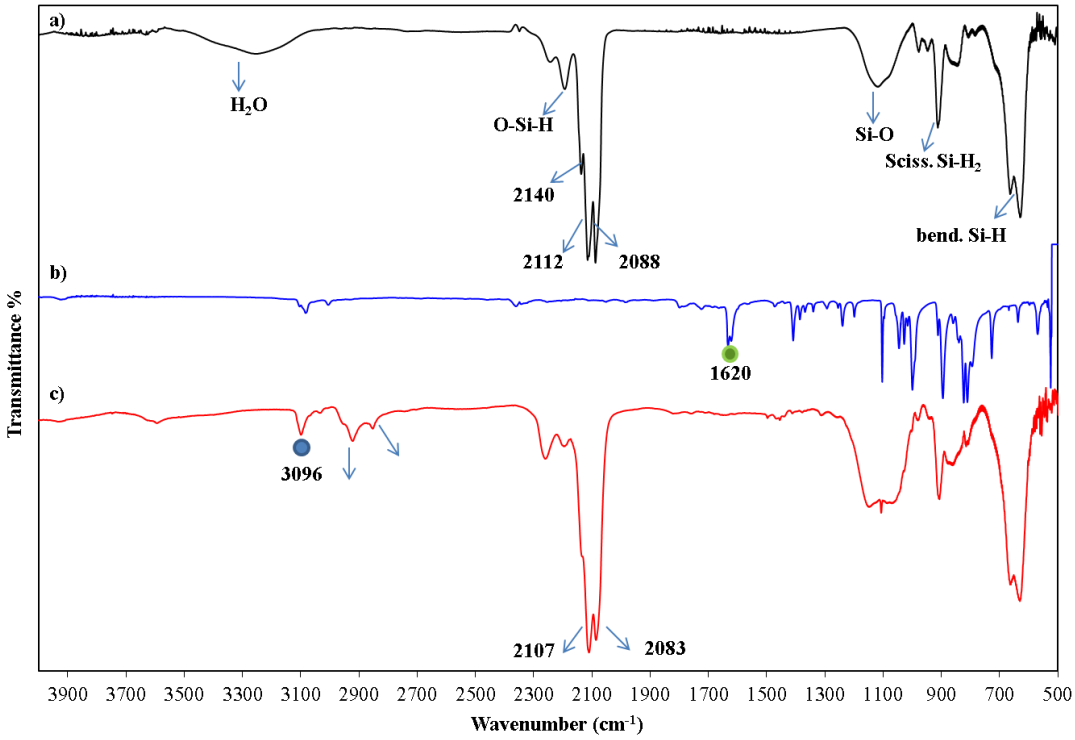

Figure 3.1. FTIR spectra of a) porous Si-H surface, b) vinylferrocene, and c) **EFc** surface.

The FTIR spectra of PS-H, ethnylferrocene, and **VFc** surfaces are shown in Figure 3.2. The PS-H surface was alkylated with ethynylferrocene in dry condition with neat DCM and the reaction was monitored with time. After 3 hours the surface was washed with

DCM and an FTIR spectrum was recorded; Figure 3.2c. There were no major differences to the starting PS-H spectrum, Figure 3.2a, indicating that after 3 hours the silicon hydride surface is not significantly alkylated. The three Si-H peaks remain largely unchanged. However, the FTIR spectrum of a surface that was left to react overnight shows the Si-H peak starting to broaden to two peaks at 2083cm^{-1} and 2105 cm^{-1}. A new peak at 3096 cm^{-1} was noticed, which can be attributed to C-H stretches present in the ferrocene ring. Interestingly, the peak at around 3328 cm^{-1} in the spectrum of ethynylferrocene is not seen in the spectrum of the **VFc** surface, as the terminal alkynyl proton *v* (≡C-H) has reacted with the Si-H surface.[24,25] This also indicates that there is no physisorbed and unreacted ethynylferrocene on the silicon wafer, confirming that the surface cleaning steps after reaction are performed thoroughly. A new peak at 1581 cm^{-1} can be attributed to Si-C=C stretch,[26,27] which further supports the formation of the desired **VFc** surface.

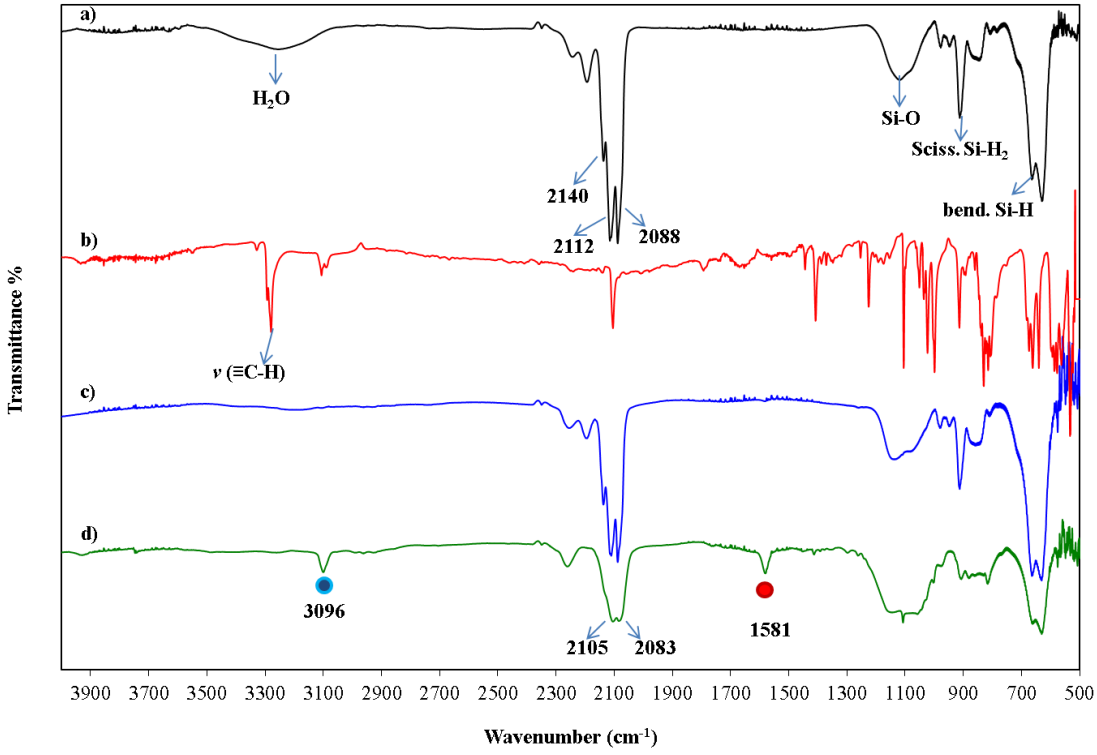

Figure 3.2. FTIR spectra of a) porous Si-H surface, b) ethynylferrocene, c) **VFc** surface alkylated for 3 h, d) **VFc** surface alkylated for overnight.

The FTIR spectra in Figure 3.3 show a comparison of the monolayer composition of PS-H, ethnylferrocene, and the **EnFc** surface. It is clear that the PS-H surface has been alkylated by ethynylferrocene as the PS-H peaks now appear as a single broad band centred around 2082 cm^{-1}. A new peak at 3096 cm^{-1} can be attributed to C-H stretches

of ferrocene ring. A new peak also appears at 2140 cm^{-1} similar to the Si-C≡C -mode seen in various alkynyl-linked monolayers previously report.[24] The absence of the peak due to the alkynyl terminal *v* (≡C-H) at around 3328 cm^{-1} confirms chemisorption of **EnFc** onto the silicon surface.[24,32]

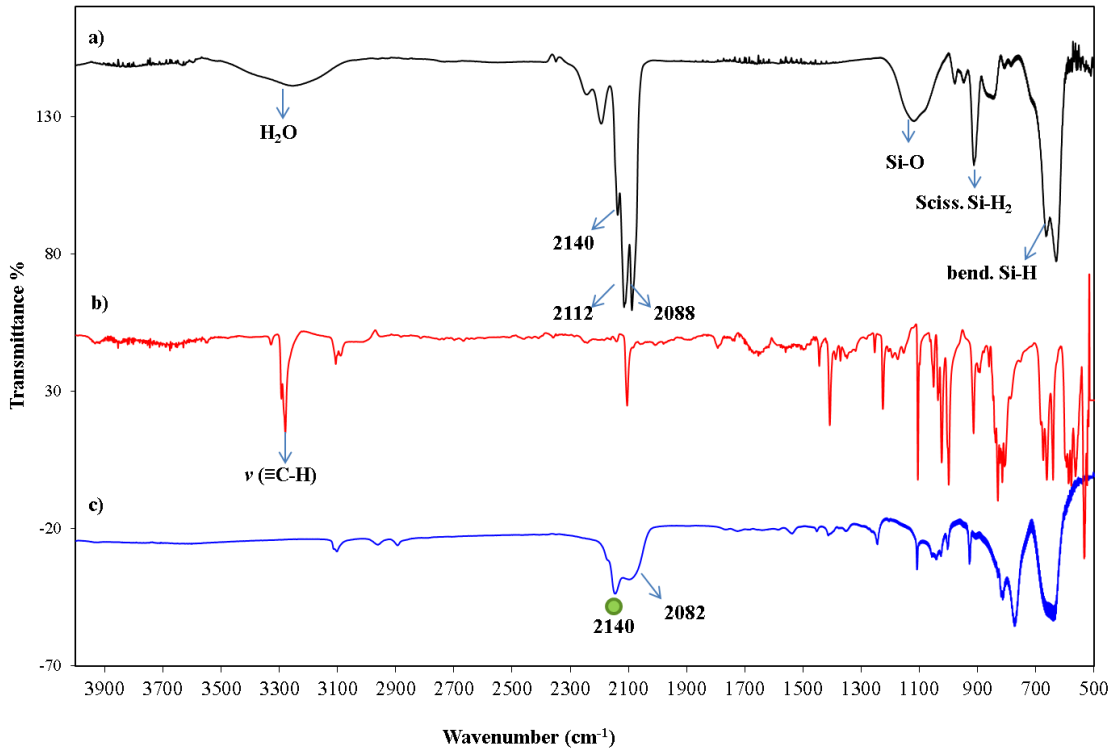

Figure 3.3. FTIR spectra of a) porous Si-H surface, b) ethynylferrocene, and c) **EnFc** surface.

FTIR characterisation can confirm the difference between the linkages of the silicon bound monolayers **EFc, VFc**, and **EnFc,** which contain single, double, and triple bonds respectively. These studies were by necessity performed on porous silicon surfaces, however atomically flat Si(111) substrates are required to produce ferrocenyl monolayers on silicon surfaces that can be easily characterised electrochemically and by AFM. The (111) orientation of the silicon crystal provides an atomically flat monohydride Si-H terminated surface after etching in 40% aq NH_4F (Scheme 3.2).[11] Densely packed alkyl monolayers can be produced on the monohydride-terminated surface Si(111) and many reports of the synthesis and characterisation of ferrocenyl surfaces are found in the literature.[1]

3.2.4 Characterization by atomic force microscopy

Figure 3.4 shows the AFM images obtained of n-Si (111) wafers before and after modification with the ferrocene derivatives. AFM images of the modified surfaces

(Figure 3.4) show some differences in the topography between these surfaces. However in general, a relatively smooth surface was observed. The root mean square (rms) roughness of the surfaces (Si-H, **EFc**, **VFc**, and **EnFc**) were recorded over an area of $0.5 \times 0.5\ \mu m^2$ in each AFM image using the Nanoscope AFM software package. The AFM images from a freshly prepared silicon hydride surface show the typical step/terrace structure, as seen in Figure 3.4a. The silicon hydride roughness is around 0.19 nm. In general, the roughness of these four surfaces were comparable, **VFc** was the most similar in roughness to the unmodified **Si-H** surface, whereas the roughness of **EFc** and **EnFc** were similar to each other and slightly higher than **Si-H** and **VFc** (see Table 3.1).

Surface	**Si-H**	**EFc**	**VFc**	**EnFc**
rms	0.19 nm	0.21 nm	0.19 nm	0.22 nm

Table 3.1. The rms roughness recorded over an area of average $0.5 \times 0.5\ \mu m^2$ for the Si-H, **EFc**, **VFc**, and **EnFc** surfaces. These values are an average value determined from several different measurements taken on the same surface.

In addition, triangular features were observed on the Si-H surface, which can be attributed to oxidation of the silicon as the AFM measurement was carried out in ambient conditions.[5] The three different ferrocenyl surfaces, **EFc**, **VFc**, and **EnFc** also show similar surface features although there is some evidence of possible physisorbed material lying on top of the regular monolayers as irregular protrusions. AFM of **VFc** (Figure 3.4c) clearly shows multiple step/terrace features, more so than **EFc** and **EnFc** Figure 3.4b and Figure 3.4d respectively.

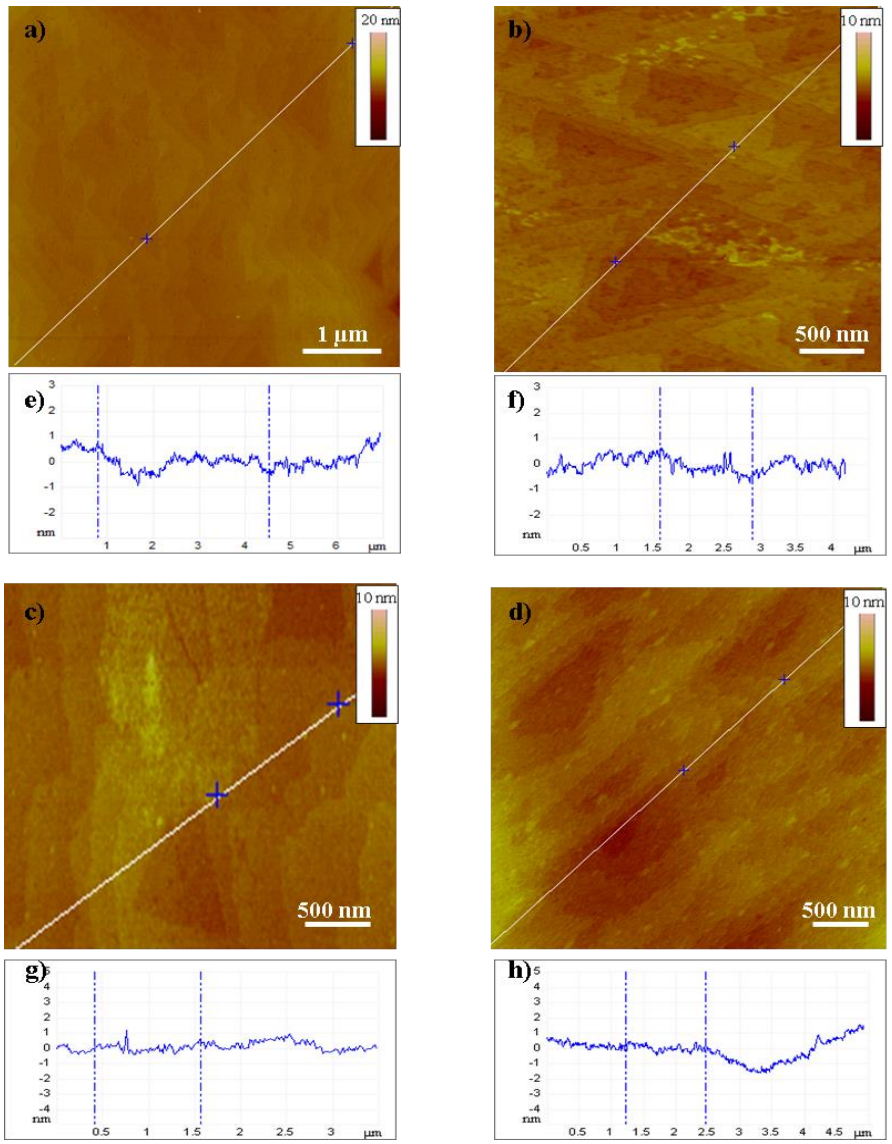

Figure 3.4. AFM tapping image from a) n-Si(111)-H, b) **EFc** surface, c) **VFc** surface, and d) **EnFc** surface, with scale bar insert in image. Corresponding linear cross-section profiles analysis (e, f, g, and h) taken along the marked segments for AFM image (a, b, c, and d) respectively.

The AFM images shown here are representative of each surface, where multiple areas within the same sample and multiple samples for the same surface type were analysed. In all cases, there were no major differences in roughness between different samples and different areas within the same sample.

In conclusion, these AFM studies on the ferrocenyl-modified surfaces **EFc**, **VFc** and **EnFc** indicate that in all cases the different linkages between the silicon and the monolayer result in surfaces which are stable to imaging and retain some of the topography of the silicon hydride surface. This suggests that in each case the surface is a simple covalently bound monolayer. The slight differences in morphology and

roughness of these surfaces may be due to the quality of the monolayer packing determined by the nature of the linkage and the alkylation method employed. However, the appearance of triangular features on the surface does indicate some surface degradation due to silicon oxidation, which may occur during AFM measurement, as this was observed on both the fresh silicon hydride surface and after SAM formation. It is also clear that the surfaces fabricated by the three different alkylation methods are also relatively free from physisorbed contaminants, very little excess material remains on the surfaces after the post-synthesis washing steps. Therefore, attention turned to the characterisation of the monolayer composition, and studies by X-ray photoelectron spectroscopy were performed.

3.2.5 Characterisation by X-ray photoelectron spectroscopy

XPS was used to characterise the presence, abundance and chemical state of the ferrocene derivatives within the silicon bound monolayers **EFc**, **VFc** and **EnFc**. There have been many previous studies on just these types of systems and XPS is a key method for their elemental analysis.[3,6,13,28]

The XPS survey spectra (Figure 3.5) of Si-H, **EFc**, **VFc** and **EnFc** all indicate characteristic peaks from the silicon substrate itself (Si 2p) and from the C 1s, O 1s, and Fe 2p core levels of the surface-attached ferrocene molecules. After monolayer formation, the Fe 2p peak is clearly present, indicating that the ferrocenyl monolayers were strongly absorbed on the Si-H surface. These monolayers were stable under repeated washing with organic solvents and sonication indicating that the ferrocene molecules are not physisorbed but chemisorbed on the surface. Therefore, the XPS analyses discussed here are of the covalently bound monolayers and not excess material adhered to the surface.

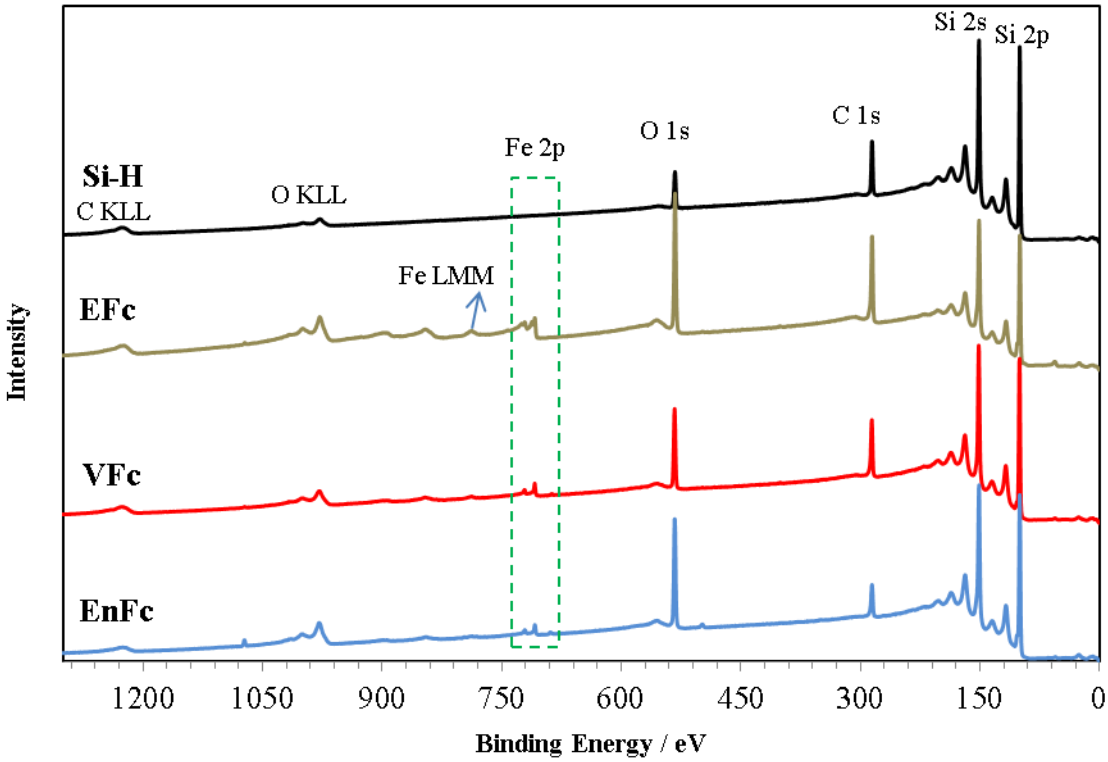

Figure 3.5. XPS survey spectra of Si-H, **EFc**, **VFc**, and **EnFc** surfaces.

The high resolution spectra of Fe 2p, Figure 3.6, shows that the iron is present in two oxidation states, Fe(II) and Fe(III). Fe 2p fitting typically can be complex, but a basic/simple fit was used here to highlight the two different types present.

The presence of Fe 2p signals approximately at 708 eV (Fe $2p_{3/2}$) and 721 eV (Fe $2p_{1/2}$) can be contributed to Fe(II) from the ferrocene ring. Whilst a second component, at higher binding energy around 711 eV (Fe $2p_{3/2}$) and 724 eV (Fe $2p_{1/2}$), arises from a proportion of Fe species being in the ferrocenium state. The oxidation of Fe(II) to Fe(III) has been reported for similar monolayers (vinylferrocene monolayer) during SAM formation.[10] The possible reason for the oxidation is that the potential of the O_2/H_2O redox couple is slightly more positive than the potential of the ferrocenium/ferrocene couple, meaning any remaining oxygen in the reaction solution would oxidise the ferrocenyl groups.[10] It could be also depend on the reaction time.[10] Additional features in the Fe 2p spectrum (Figure 3.6) are attributed to shake up satellite peaks of Fe(II) ≈715eV (Fe $2p_{3/2}$) and ≈728 eV (Fe $2p_{1/2}$), and also of the Fe(III) (≈719 eV (Fe $2p_{3/2}$), and ≈732 eV (Fe $2p_{1/2}$)). These findings are consistent with previous literature reports.[3,5,6,10,12,13,28]

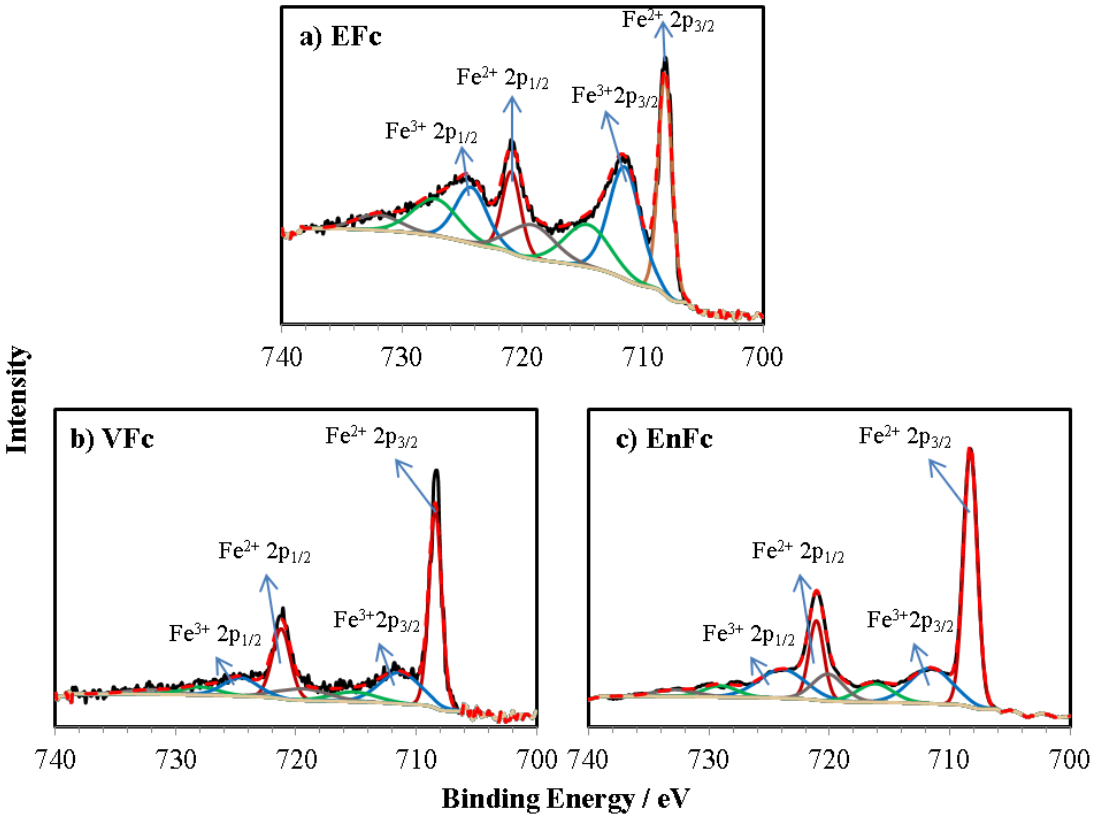

Figure 3.6. XPS spectra of the Fe 2p regions for a) **EFc**, b) **VFc**, c) and **EnFc**. Experimental spectra are shown in black, while curve-fit separated components are shown in red dash.

It is possible to gauge the extent of surface coverage and oxidation by comparing the XPS peak areas of Fe/Si, C/Fe and also Fe(II)/Fe(III). The ratios of the peak areas between these pairs of atoms were calculated by CasaXPS software (Table 3.2). The atomic ratio of Fe/Si was nearly five times higher for **EFc** (0.05) compared to either **EnFc** (0.011) or **VFc** (0.013) (Table 3.2). Although it is not possible to draw an exact surface coverage from these numbers, it is apparent that the **EFc** surface does contain more ferrocene groups than either the **EnFc** or **VFc** surfaces. These ratios lie in good comparison to other previous literature reports, where the Fe/Si ratio varies from 0.008 to 0.06.[6,28]

The Fe(II)/Fe(III) ratio can be used to understand the extent of oxidation of the ferrocenyl monolayer. The expectation would be that the Fe(II) signal would dominate the spectra with some evidence of oxidation by trace oxygen species during alkylation. However, in the case of the **EFc** monolayer the Fe(II)/Fe(III) ratio of 0.72 shows that considerable oxidation, ca. 30%, of the ferrocene unit has occurred (Table 3.2). This may be explained by increased oxidation due to the higher temperature (110˚C) used in the preparation of **EFc**, Figure 3.7, compared to the ambient conditions used in the

preparation of the other surfaces. In an earlier report an **EFc** surface prepared by a Grignard reaction resulted in a Fe(II)/Fe(III) ratio of 1.8, which highlights that the method of surface preparation has a considerable effect on the monolayer composition. Both **VFc** and **EnFc** indicated ratios for Fe(II)/Fe(III) of 1.94 and 1.64 respectively which are in good comparison to previous studies.[6]

Surface	**Fe (II)** $2p_{3/2}$, $2p_{1/2}$ **eV**	**Fe (III)** $2p_{3/2}$, $2p_{1/2}$ **eV**	**Fe/Si**	**C/Fe**	**Fe(II) / Fe(III)**
EFc	708.1, 720.8	711.4, 724.6	0.050	13.0	0.72
VFc	708.4, 721.2	711.3, 724.6	0.013	25.8	1.94
EnFc	708.3, 721.1	711.5, 723.9	0.011	20.6	1.64

Table 3.2. Values of binding energy for relative atomic ratios for **EFc, VFc**, and **EnFc** the atomic ratios calculated by CasaXPS software.

The atomic ratios of Fe/Si and C/Fe for the **EFc** surface were 0.050 and 13.0 respectively. The C/Fe value approximates to the expected stoichiometry of ethylferrocene ($C_{12}H_{13}Fe$) bound to the silicon surface, indicating that the carbon skeleton from vinylferrocene is incorporated into the **EFc** surface. This ratio was similar to that previously reported from XPS studies carried out on an ethylferrocene monolayer, where the ratios of Fe/Si and C/Fe were 0.06 and 12 respectively.[28] However, the Fe/Si ratio for **VFc** and **EnFc** were similar to each other, but somewhat smaller than for **EFc**, 0.013 and 0.011 respectively. Furthermore, the C/Fe ratio for **VFc** and **EnFc** were again similar to each other, but substantially larger than for **EFc**, 25.8 and 20.6 respectively. These findings indicate that the **VFc** and **EnFc** surfaces are clearly more contaminated with carbon species than the **EFc** surface. This may be due to the high temperature in preparation of **EFc,** which led to efficient of cleaning the surfaces during reaction. Whereas, the room temperature reaction used in the preparation of **VFc** and **EnFc** surfaces may lead to chemical contamination by physisorbed material on the surface.

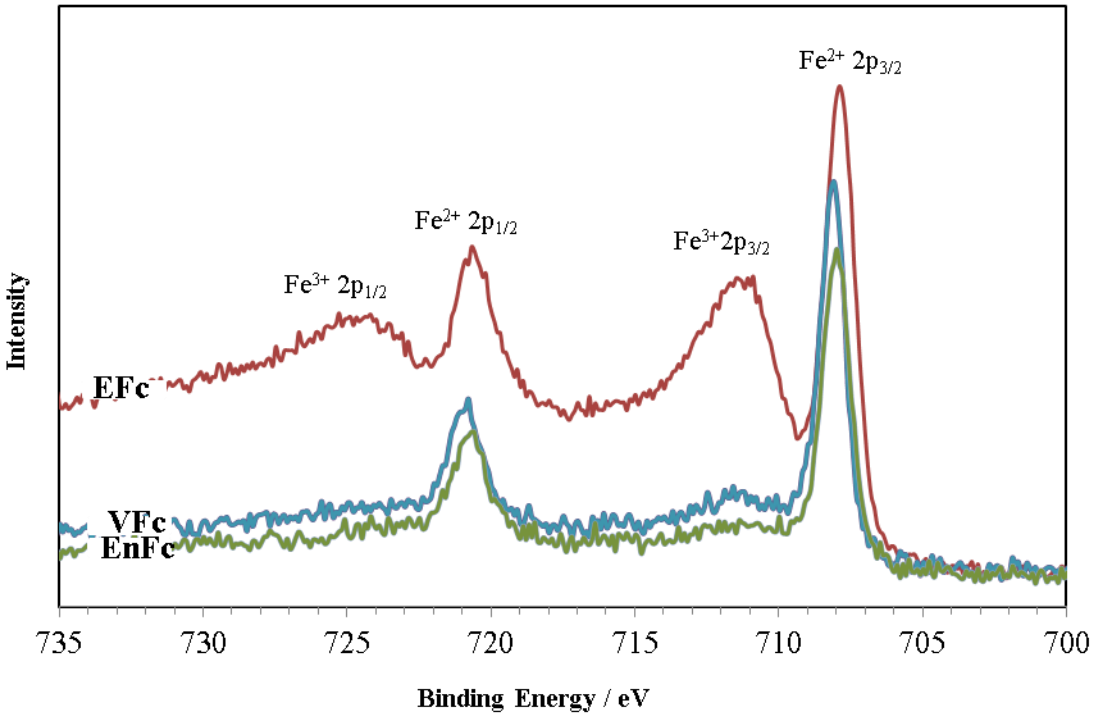

Figure 3.7. XPS comparison of iron for **EFc**, **VFc**, and **EnFc** surfaces.

The next area of the XPS survey scan to be discussed was that of the Si region. The high-resolution spectra for the Si-H and **EFc**, **VFc** and **EnFc** surfaces are shown in Figure 3.8. It clearly appears that the silicon hydride surface (Figure 3.8a) is free of silicon oxide (103 eV) as there are only two components at 99.6 eV and 100 eV, which can be attributed to Si $2p_{3/2}$ of the bulk silicon and the Si-H surface respectively. However, the Si-H surface was unlike the modified surfaces, which all showed an additional peak at 103 eV, due to oxidation of the silicon. This finding confirmed that the oxidation of silicon surface occurred during the chemical modification step, in agreement with other previous literature report.[5,29] It is conceivable that oxidation could also occur after modification, but before XPS characterisation, since the modified surfaces were not stored in inert atmospheric conditions during transfer to the XPS equipment.[5]

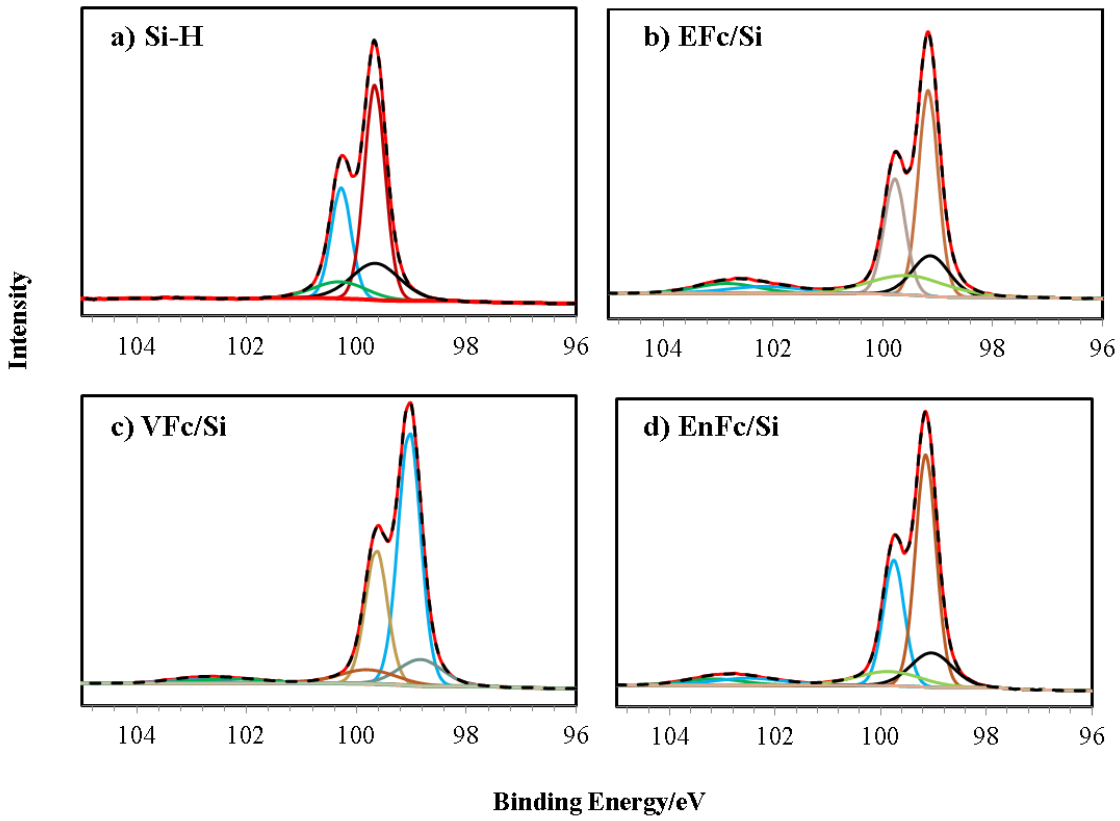

Figure 3.8. XPS of Si 2p for silicon hydride surface and after alkylation to give three different **EFc**, **VFc** and **EnFc** surfaces.

Curve fitting of the modified silicon surface Si 2p doublet can be split to three different environments at binding energies of 99.6 eV, 100 eV and 102.8 eV corresponding to Si $2p_{3/2}$ component. The 99.6 eV can be assigned to the Si $2p_{3/2}$ of bulk silicon, whereas the component at 100 eV can be attributed to the terminal Si atoms as bonded to either Si–C/Si-H.[13] Furthermore, the component of binding energy 102.8 eV can be attributed to silicon oxide. Here, the shift of 3.5-4 eV from the bulk Si signal, depends on the thickness of the oxide layer.[13] Other peaks at 100.2 eV, 100.6 eV, and 103.5 eV correspond to the $2p_{1/2}$ levels.[5]

For further information about these monolayers, high-resolution XPS spectra of the C1s region was fitted in a similar way as to the previous discussion on the Si 2p region. The fitting of the C 1s spectrum can be complicated, due to contamination from carbon containing species.[30,31] However, in a recent literature report by Zuilhof's group, the XPS interpretation of carbon containing monolayers on silicon provided an understanding of the nature of the silicon-carbon linkage.[27,32] According to Zuilhof *et al*, the difference between the linkages (Si-C-C, Si-C=C) can be observed from the fitting of the C 1s in the XPS spectrum, primarily from the 285 eV and 283.8 eV peaks

respectively.[32,33] Here, the fitting of XPS also shows there is small peak at 283.2 eV for the **VFc** surface, which can be attributed to Si-C=C.[32,33] Likewise the **EnFc** surface, also has a small peak at 283.6 eV which is attributed to Si-C≡C. Whereas in the case of **EFc**, the peak for Si-C is very close to the methylene component (285 eV) suggesting that the Si-C-C bond is fully saturated.

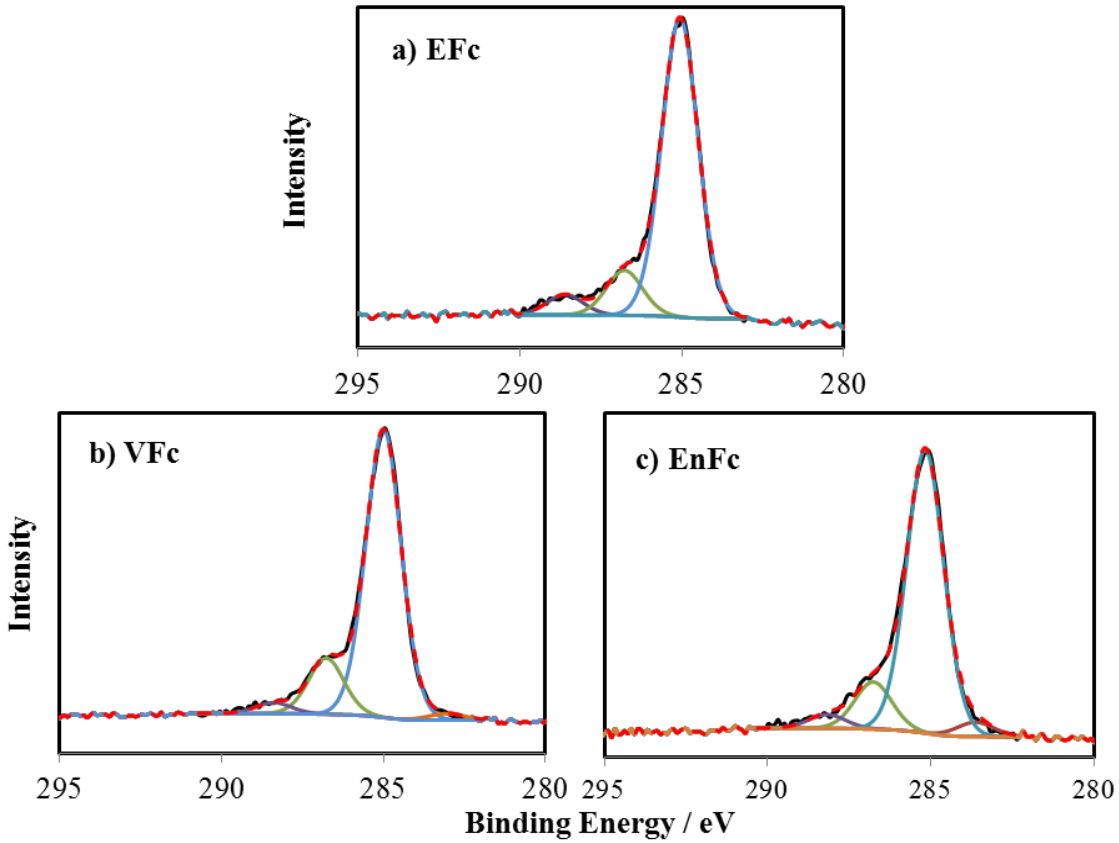

Figure 3.9. XPS spectra of the C 1s regions for the a) **EFc**, b) **VFc**, c) and **EnFc** surfaces. Experimental spectra are shown in black line, while curve-fit separated components are shown in red dash.

The large peak in all three surfaces at 285 eV can be attributed to the carbon atoms of the ferrocene ring as well as any hydrocarbon contaminants.[11,33] The two smaller peaks at 286.6 eV and 288.3 eV can be attributed to contamination by adventitious carbon species, which could come from solvents used in the washing step, such as acetone.

3.2.6 Characterisation by cyclic voltammetry

As discussed in the introductory chapter, ferrocene has several attractive electrochemical properties. For example, its electron-transfer rate is fast due the low reorganisation energy, and the ferrocene and ferrocenium redox states are chemically stable.[1,3,34] Therefore, ferrocene can be used to electrochemically monitor subtle

changes in the local molecular environment. In particular, cyclic voltammetry has been extensively used to investigate localised changes in solvent, electrode modifications and molecular connectivity.

Although, most of previous work on ferrocenyl monolayers at Si has employed highly doped p-type Si electrodes, n-type electrodes were used here for the photoelectrochemical measurements discussed in Chapter 6.

3.2.6.1 CV of vinylferrocene and ethynylferrocene

The synthesis of **EFc**, **VFc** and **EnFc** required the reaction of an unsaturated ferrocenyl compound with a silicon hydride surface under different reaction conditions as shown in Scheme 3.3. Both vinylferrocene and ethynylferrocene were used as reagents in this study. The electrochemical properties of ferrocene itself are well known,[34] and the effects of an additional unsaturated linkage (C=C, or C≡C) on the cyclopentadienyl ring have been reported.[35] Here, the cyclic voltammetry of vinylferrocene and ethynylferrocene were firstly studied as standards for the investigations into the redox behaviour of **EFc**, **VFc** and **EnFc**. The cyclic voltammogram of vinylferrocene exhibited a formal reversible redox response of 326 mV versus a Ag wire at 0.1 V s^{-1} in acetonitrile. The anodic and cathodic peaks for vinylferrocene were located at 348 and 303 mV respectively giving a peak separation of 45 mV, see Figure 3.10. Under the same conditions, ethynylferrocene exhibited a formal reversible redox response at 460 mV, anodic and cathodic peaks for at 495 mV and 425 mV respectively giving a peak separation of 70 mV as shown in Figure 3.10. The anodic and cathodic peaks of ferrocene are reported to be located 1020 mV and 926 mV at 0.1 V s^{-1} in acetonitrile, giving a peak separation of 94 mV and a formal redox response of 973 mV.[34]

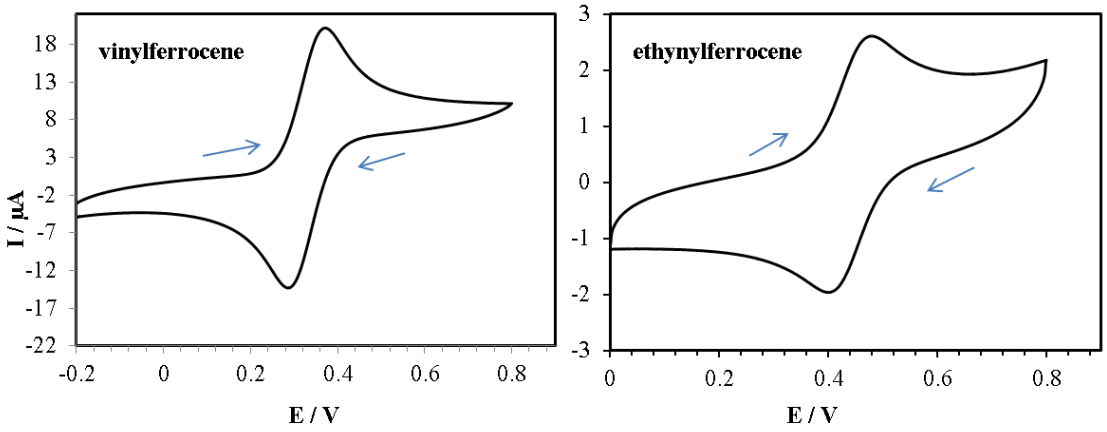

Figure 3.10. Cyclic voltammograms of vinylferrocene and ethynylferrocene recorded in $LiClO_4$ (0.1 M) CH_3CN at a scan rate of 0.1 V s^{-1} and under ambient using gold, tungsten and silver wires, as working, counter and quasi reference electrodes respectively. Arrows indicate the scan direction.

3.2.6.2 CV of ferrocene bound to silicon surface

When electroactive chemical compounds are covalently bound to a silicon surface, there are several fundamental differences in the shape of the CV compared to the same compound recorded in solution. Firstly, the redox response is generally more symmetrical and sharper and there should be no or little peak separation. The charges associated with anodic and cathodic processes also are equal. Moreover, the peak current increases linearly with increasing scan rate, *v*, see insert in Figure 3.11. CV recorded in solution exhibit a peak current that is proportional to the square root of the scan rate, $v^{½}$. These properties can be clearly seen in the cyclic voltammograms of **EFc** as shown in Figure 3.11. For example the anodic peaks currents at 180 mV, 201 mV and 227 mV for scan rates of 25 mV s^{-1}, 50 mV s^{-1}, and 100 mV s^{-1} respectively. The anodic and cathodic peaks were 222 mV 155 mV for 0.1 V s^{-1} to give expected surface separation 67 mV. [45]

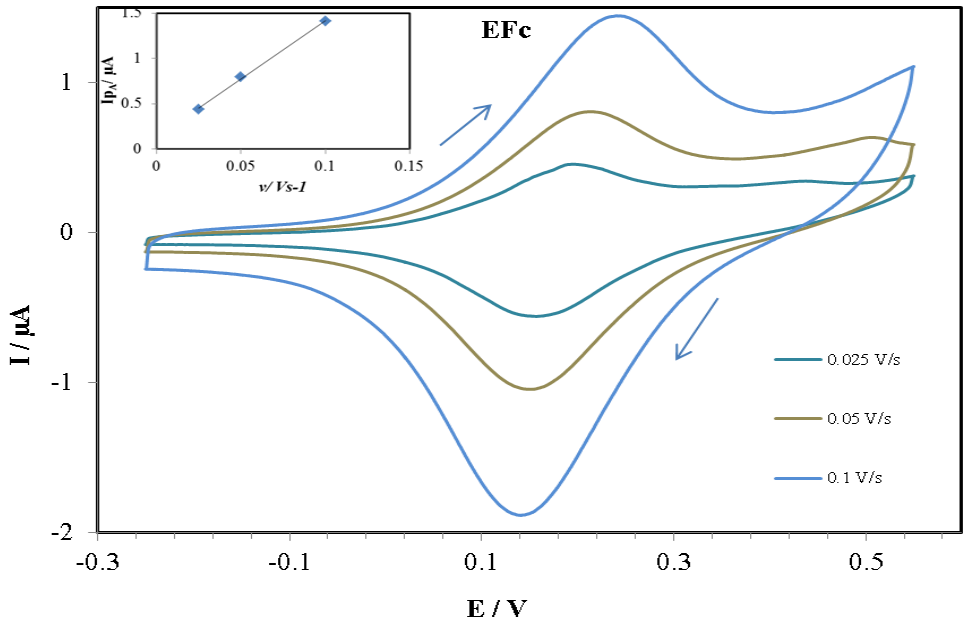

Figure 3.11. Cyclic voltammograms of **EFc** at different scan rates. The experiments were performed in MeCN (0.1 M $LiClO_4$) using Ag as the reference electrode. Arrows indicate the scan direction. Insert is dependencies of the oxidation peak current on scan rate.

3.2.6.3 CV of EFc, VFc, and EnFc surfaces in water

Cyclic voltammograms of **EFc**, **VFc** and **EnFc** surfaces, (Figure 3.12), were recorded in aqueous electrolyte (0.1 M KCl) at a scan rate of 1 V s^{-1} under illumination by white light 425-600 nm from a Modulight source. A control surface, comprising of an undecyl surface, **UND,** is also presented which shows mainly capacitive behaviour, but there is evidence of a reversible surface state at -250 mV and the onset of Si oxidation at 100 mV. A clear, chemically-reversible wave is observed for the ferrocene moieties of the **EFc** and **VFc** surfaces as shown in Figure 3.12b and Figure 3.12c. However, the behaviour of the **EnFc** surface is very different; the CV was unstable under repeated cycling and some ferrocene was lost after the first cycle, Figure 3.12d. The **EnFc** surface also shows more evidence of Si oxidation, which is partly due to the more positive potential range and partly due to loss of ferrocene from the monolayer. However, both **EFc** and **VFc** surfaces were stable to repeated cycling.

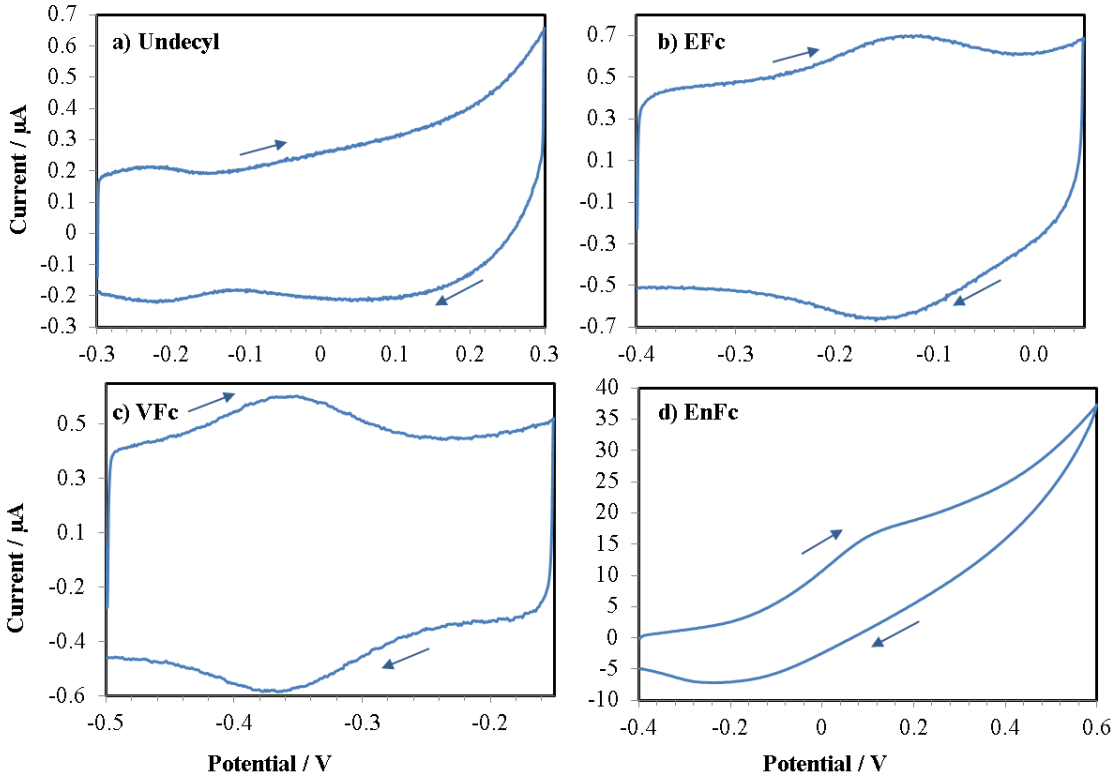

Figure 3.12. Cyclic voltammograms recorded of **UND**, **EFc**, **VFc**, and **EnFc**. The voltammograms were recorded in 0.1M aqueous KCl at a scan rate of 1 V s^{-1} and under illumination by 425-600 nm light. Potentials are measured against a Ag/AgCl wire reference electrode. Arrows indicate the scan direction.

Figure 3.12 shows that the anodic peaks of the **EFc** and **VFc** surfaces are broader than 91 mV, with FWHMs of about 130 mV and 110 mV respectively. The usual explanation for such behaviour is that the ideal wave shape assumes no lateral interactions between the redox groups in the monolayer, whereas the positive charges produced upon oxidation of ferrocene to ferrocenium would be expected to repel each other and cause the wave to broaden as higher potentials are required to overcome the repulsion.[10,28] Another possibility is that there is a distribution of electrode potentials for ferrocenes in the monolayer, because of heterogeneities in the local environments.

Surface	ΔE_p (mV)	E_p^A	E_p^C	$E^{\circ\prime}$ (mV)	FWHMs(mV)	coverage/mol cm $^{-2}$
EFc	10	-138	-148	-143	130	1.8×10^{-12}
VFc	2	-312	-314	-313	110	1.9×10^{-12}

Table 3.3. The electrochemical properties of modified silicon surfaces **EFc**, and **VFc** in aqueous KCl at a scan rate of 1 V s^{-1}.

3.2.6.4 CV of EFc, VFc, and EnFc in acetonitrile

Because the **EnFc** was unstable in aqueous solution, CV was also carried out in acetonitrile. The redox activities of the ferrocene monolayers **EFc**, **VFc**, and **EnFc** were also recorded at different scan rates in acetonitrile as shown in Figure 3.13

The anodic and cathodic peaks for **EFc** were located at 223 mV and 149 mV, for **VFc** at -86 mV and -75 mV and for **EnFc** at 60 mV and 73 mV versus Ag in 0.1 M $LiClO_4$ in MeCN at scan rate 0.1 V s^{-1}. The peak separation was outside the expected surface behaviour for **EFc** (74 mV) and then within for both **VFc** (11 mV) and **EnFc** (13 mV). The surfaces exhibited a formal reversible redox response at 186 mV for **EFc**, -81 mV for **VFc**, and 67 mV for **EnFc**. The potential of the cathodic peak shifted to a more negative value with increasing scan rate, whereas, the potential of the anodic peak potential shifted to more a positive value. This shift may be due to the IR drop through the electrical contact on the back of the silicon,[10] either resistance surface 1-12 Ω cm so silicon not high conductive or could be from solution. These monolayers were stable for many cycles. The CV of the **EnFc** monolayer also was stable compared with the CV previously recorded in an aqueous electrolyte (Figure 3.12). The dependencies of the oxidation peak current on scan rate are displayed in Figure 3.13. Linear relationships were observed as a function of *v*, which confirm the ferrocene is chemically bound to silicon surface.[13] Figure 3.13 shows that the CV anodic peaks of **EFc**, **VFc** and **EnFc** are broader than 91 mV, with FWHMs of about 178 mV, 140 mV and 142 mV, respectively.

Surface	E_p^A	E_p^C	ΔE_p (mV)	$E^{\circ'}$(mV)	FWHMs(mV)	coverage/ mol cm $^{-2}$
EFc	223	149	74	186	178	1.3×10^{-10}
VFc	-86	-75	11	-81	140	2.7×10^{-11}
EnFc	60	73	13	67	70	5.4×10^{-11}

Table 3.4. The electrochemical properties of modifier silicon surface **EFc**, **VFc** and **EnFc** in acetonitrile CV at 0.1 V s^{-1}.

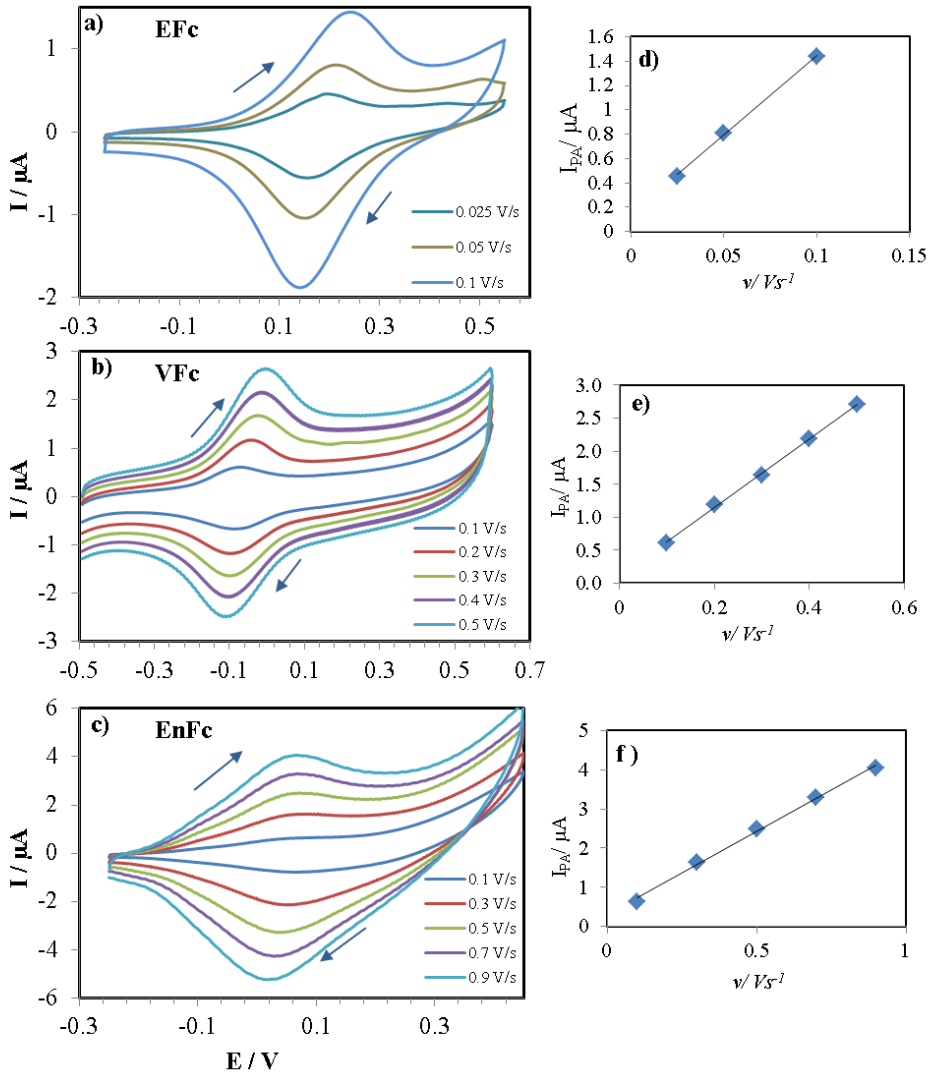

Figure 3.13. Cyclic voltammograms for monolayers a) **EFc**, b) **VFc**, and c) **EnFc** at different scan rates. The linear dependency of peak current on scan rate is shown (d, e, and f) respectively. The experiments were performed in 0.1 M $LiClO_4$/MeCN using Ag as the reference electrode. Arrows indicate the scan direction

3.2.6.5 Surface coverage

The surface coverage of ferrocene for each monolayer type was determined using the expression $Q= nFA\Gamma$. Q is the amount of charge passed by the adsorbed layer (C), and is determined by the integrated area under each reduction or oxidation peak as highlighted in Figure 3.14. *n is* the number of electrons involved in the electron-transfer process (*n=1 for ferrocene)*, F is the Faraday constant (6,485.3365 C mol^{-1}), Γ the monolayer coverage in moles of adsorbed ferrocene per cm^2, and A is the electrode surface area (which in the example below is equal to 0.28 cm^2). The coverage of ferrocene monolayer on the silicon surface was estimated by integration of the area under the anodic peak in each CV by using software within CHI760B Electrochemical Workstation. Surface coverage data is tabulated in Table 3.4, which presents the highest surface coverage obtained from many samples. For example, the coverage for **EFc** surface was estimated in this study to range from 3.5×10^{-12} mol cm^{-2} to 1.3×10^{-10} mol cm^{-2}.[2]

The following calculation was performed to estimate the surface coverage,

$$\text{e.g } Q= nFA\Gamma$$

$$3.65\times10^{-6}\,(\text{C}) = 1\times96485(\text{C/mol}) \times 0.28\,(\text{cm}^{-2})\Gamma$$

$$\Gamma = 3.65\times10^{-6} / 1\times96485\times 0.28$$

$$\Gamma = 1.35\times 10^{-10}\ mol\ cm^{-2}$$

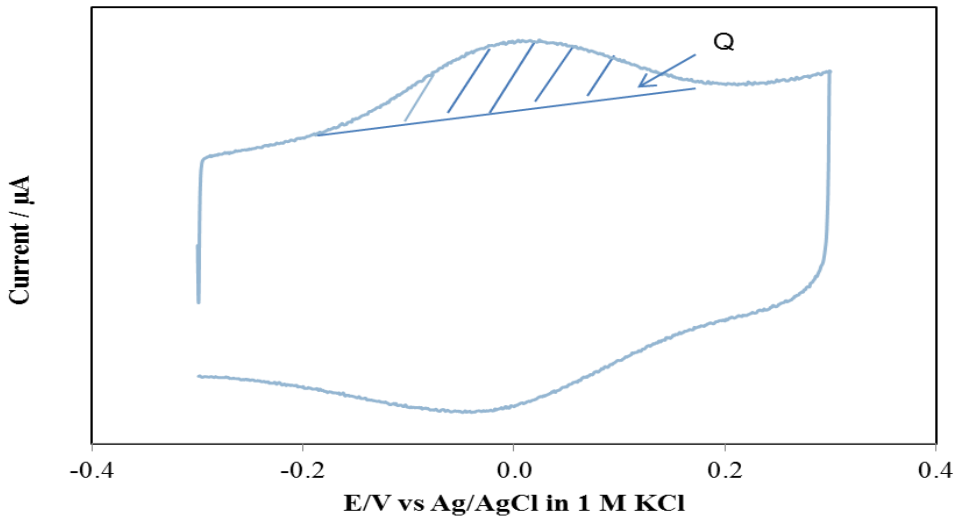

Figure 3.14. Cyclic voltammograms recorded at monolayer coated n-Si(111) to show the charge Q.

Therefore, the surface **EFc** has 1.35×10^{-10} mol of ferrocene every square centimeter. This is not near to the theorectical coverage which can be estimated if the ferrocene moieties are considered as spheres with a projection diameter of 6.6 Å.[36,37] 100% coverage of ferrocene is impossible since the distance between silicon hydride sites on silicon surface is only 3.8 Å.[38] Consequently, a defect-free monolayer will not be produced by compounds which have a molecular radius larger than about 2 Å.[11,38,39] For example, a completely passivated surface by methyl group (2 Å) has been reported,[38] whereas longer alkyl chain (> C_2H_4) cannot give complete passivation due to van der Waals interactions between methylene units of adjacent alkyl chain see Figure 3.15.[38]

Therefore, the maximum theoretical coverage of ferrocene can be calculated by:

Ferrocene molecule has area = πr^2 which is $(3.14 \times (3.3\times10^{-8})^2) = 3.4\times10^{-15}$ cm^2

Therefore, every 1 cm^2 of silicon surface can be covered by 2.9×10^{14} ferrocene molecules which mean 5×10^{-10} mol cm^{-2} of ferrocene close packing was assumed to limited to 90% coverage.[36]

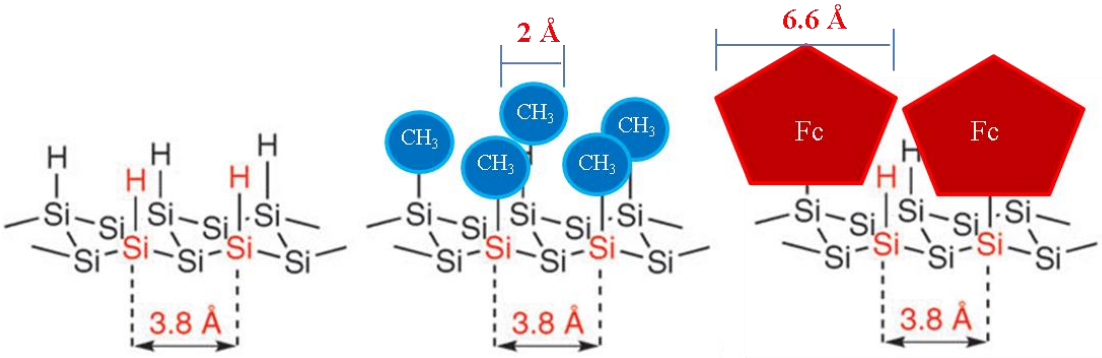

Figure 3.15. Cartoon figure show the distance between Si-Si sites and how methyl monolayer can be complete coverage whereas in case of ferrocene monolayer 100% coverage is impossible.

Therefore, maximum theorectical coverage is $0.9\times5\times10^{-10}$ mol cm^{-2} = 4.5×10^{-10} mol cm^{-2} as assumed in a previous report. [2,36]

Coverage = coverage calculated from CV / theorectical maximum

Coverage = 1.3 x 10^{-10} / 4.5 x 10^{-10} = 29 %

The CV for the **EFc** surface in this study shows that the peak-to-peak separations and the formal potentials increase linearly with an increase in **EFc** coverage.[2] CV has been recorded for **EFc** in aqueous 0.1 M $HClO_4$ against a palladium wire as reference electrode.[2] The investigation by CV for different **EFc** samples indicated that formal potential is shifted to higher positive potential with increasing surface coverage, as shown in Figure 3.16a, b. In addition, the peak separation also increases which is paralleled by an increase in the FWHM of the anodic and cathodic redox peaks. This could be due to repulsive lateral interactions within ferrocene units in the **EFc** surface, where this increase became clearer with higher surface coverage. The shape of the anodic and cathodic redox peaks also become more distorted as the surface coverage increase from 1% to 29 % as shown in Figure 3.16a. This is due to the heterogeneity of the local environment around the ferrocene species and to dominating repulsive interactions at higher coverages.[2]

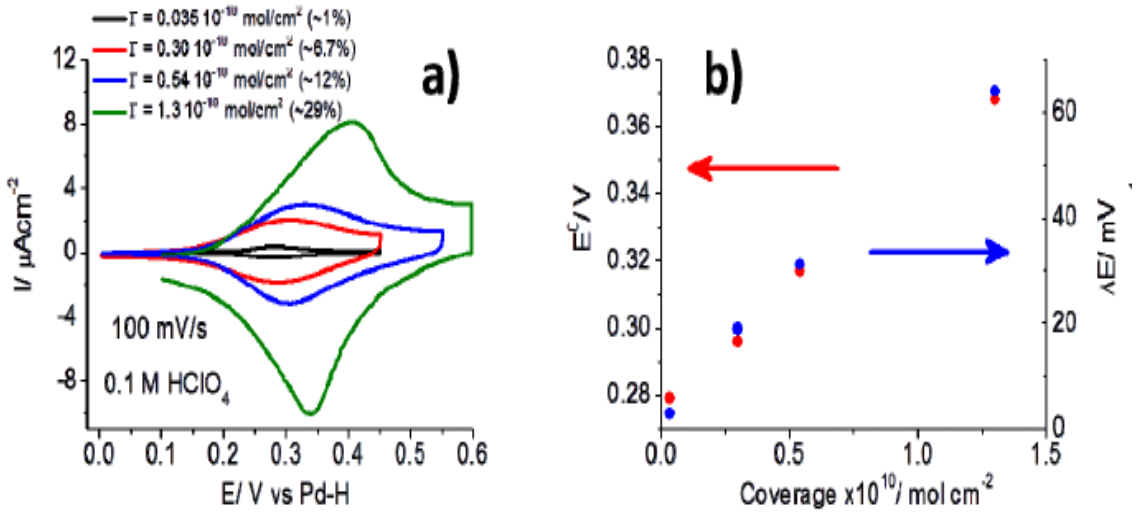

Figure 3.16. a) Comparison of cyclic voltammograms for different coverage's of **EFc** surface on Si(111) surfaces. b) Formal potentials E^0 and peak-to-peak separations ΔE at 100 mV s^{-1} as functions of the **EFc** coverage.[2]

In conclusion, CV gives more details about the stability of the monolayers **EFc**, **VFc**, and **EnFc** in different solvent systems. In addition, reproducible monolayers were difficult to achieve because different samples of the same surface type give different coverage values. The surface coverage calculated in aqueous solvent is generally lower than acetonitrile. For example, in aqueous solvent the coverage was estimated to be 1.8×10^{-12} mol cm^{-2} and 1.9×10^{-12} mol cm^{-2} for **EFc** and **VFc** respectively. Whereas, the surface coverage in acetonitrile was estimated to be from 3.5×10^{-12} mol cm^{-2} to 1.3×10^{-10} mol cm^{-2} for the **EFc** surface, and from 3.5×10^{-12} mol cm^{-2} to

2.7×10^{-11} mol cm^{-2} for the **VFc** surface, and from 3.5×10^{-12} mol cm^{-2} to 5.4×10^{-11} mol cm^{-2} for the **EnFc** surface. The coverage was higher for **EFc** surface compared than **VFc** and **EnFc** surfaces. However, the highest coverage obtained here for all surfaces **EFc, VFc**, and **EnFc** were higher than the coverages in the previous report.[6] In an earlier report, the **EFc** surface was prepared by a Grignard reaction resulting in a low coverage of 6.7×10^{-12} mol cm^{-2}, compared with the **EFc** surface, 1.3×10^{-10} mol cm^{-2}, in this study. The reason for this could be due to the different method used in preparation of the **EFc** surface.[6] In the case of the **VFc** surface there was a small difference in coverage between a previous study, 3.4×10^{-11} mol cm^{-2}, and in this study 2.7×10^{-11} mol cm^{-2}.[6] Previously, the **VFc** surface was prepared by a Lewis acid catalyst method and here prepared under room temperature and ambient light. Interesting in the case of the **EnFc** surface the same preparation method was used a butyl lithium catalyst. The coverage of the **EnFc** surface reported in a previous study, 3.1×10^{-11} mol cm^{-2}, was less than this study, 5.4×10^{-11} mol cm^{-2}.[6] The percentage of the coverage is shown in Figure 3.17, **EFc** 1-29%, **VFc** 1-6 % and **EnFc** 1-12%. The difference in coverage could be due to the method that was used for modification or to how the ferrocene molecules pack on the silicon surface.

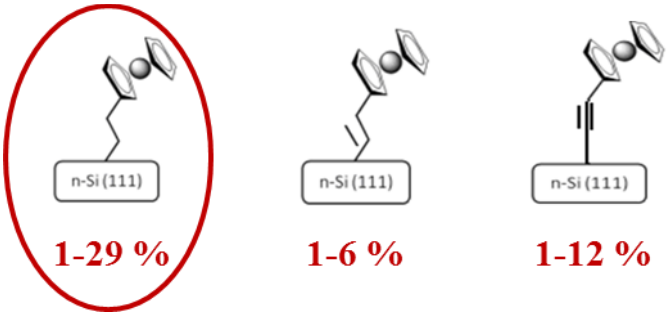

Figure 3.17. The percentage coverage of three different linkages, **EFc**, **VFc** and **EnFc**.

3.2.7 Molecular Modelling

In light of the conclusions from the electrochemical studies, the molecular geometries for the modified ferrocenyl surfaces were modelled by DFT calculations. The optimised geometries of molecular cluster models for **EFc**, **VFc**, and **EnFc** surfaces where calculated using the B3LYP functional, 6-31G* basis set and pseudopotentials as implemented in Spartan 04 (Wavefunction Inc, CA, USA). The modelling (Figure 3.18) studied the distance between the iron and the silicon surface, because this distance can play a role in electron transfer between ferrocene and silicon, and it also may determine how easily the silicon surface near the ferrocene group is oxidised or hydrolysed.

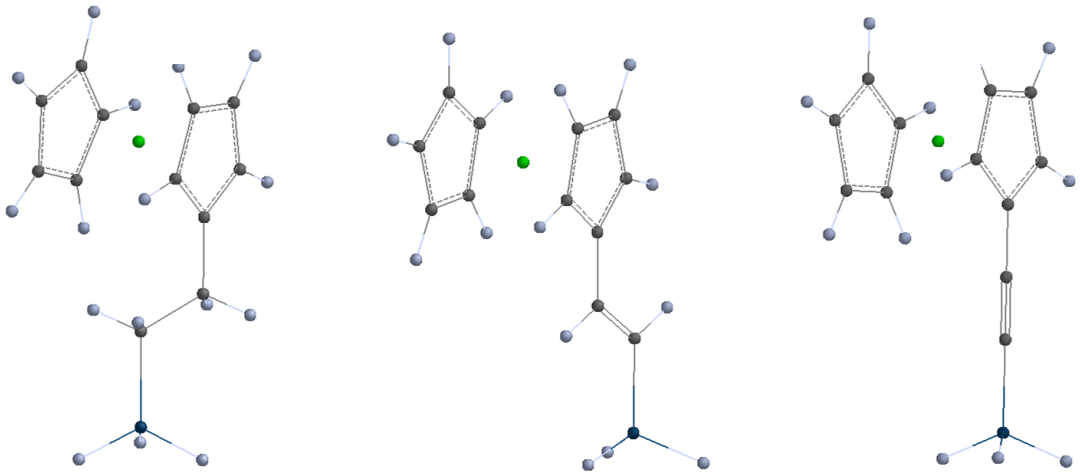

Figure 3.18. Optimised geometries of the molecular models at B3LYP/6-31G(d) using the built-in pseudopotential for Fe in Spartan 04 (Wavefunction Inc., CA, USA), a) H_3Si-$(CH_2)_2$-Fc (**EFc** surface); b) H_3Si-(HC=CH)-Fc (**VFc** surface); and c) H_3Si-(C≡C)-Fc (**EnFc** surface).

The distances between the central iron atom of the ferrocene moiety and the silicon atom was calculated, Table 3.5. This distance is of interest as it is approximately equal to the distance an electron must travel if the electron transfer reaction occurs via tunnelling. The optimised structures are shown in Figure 3.18. Although, the difference in Fe-Si distance is only 0.03 nm, the trend correlates with the observed ease of oxidation of the ferrocene. From the geometry of monolayers seen in Figure 3.18 there is more space round **EnFc** linkage and therefore access to a neighbouring silicon atom is more feasible leading to an increased opportunity for oxidation to occur.

Model	**Distance between the central iron and the silicon atom / nm**
H_3Si-$(CH_2)_2$-Fc, **EFc** surface	0.5628
H_3Si-(HC=CH)-Fc, **VFc** surface	0.5773
H_3Si-(C≡C)-Fc, **EnFc** surface	0.5911

Table 3.5. Fe-Si distances determined from the molecular models.

3.3 Conclusions

The ferrocene monolayers **EFc**, **VFc**, and **EnFc** have been successful prepared, with three different linkages Si-CH_2-CH_2-Fc, Si-CH=CH-Fc, and Si-C≡C-Fc, respectively. These monolayers on porous silicon were characterised chemically by FTIR to observe the different linkages between Si-ferrocene. XPS characterisation provided further confirmation of chemisorbed monolayers of ferrocene on each silicon surface. AFM

showed that these monolayers were stable during AFM measurement. An estimate of the ferrocene coverage on these monolayers in acetonitrile were calculated from CV, which gave surface coverage values of 3.5×10^{-12} mol cm^{-2} to 1.3×10^{-10} mol cm^{-2} for **EFc**, 3.5×10^{-12} mol cm^{-2} to 2.7×10^{-11} mol cm^{-2} for **VFc,** and 3.5×10^{-12} mol cm^{-2} to 5.4×10^{-11} mol cm^{-2} for **EnFc**. The reproducibility of these monolayers was not easy to control. The reason could be due to the multistep preparation of the modified sample. It could be due to the etching step or the alkylation step. In the etching step the surface may not have been etched properly, either the NH_4F solution was not fully degassed, or there may have been some oxygen remaining in the ferrocenyl alkylation solution which could oxidise the surface and so affect the surface coverage. However, the highest coverage was reported for the **EFc** surface. This could be due to the method of preparation, where the thermal activation protocol was used to produce this surface. It could be that the higher temperature helped more ferrocenes to react with the surface compared with the room temperature methods used to produce both the **VFc** and **EnFc** surfaces.

Therefore, due to the low reproducibility of the surfaces prepared here in Chapter 3, the next Chapter investigates the fabrication of a mixed monolayer in a way to improve the reproducibility of the thermal activation approach. Studies into how to control the spatial resolution of the ferrocene on the silicon surface are also reported.

Experimental

Materials

All reagents were obtained from Sigma-Aldrich, except anhydrous toluene and anhydrous THF which were obtained from Acros Organic. Aqueous ammonium fluoride solution (Fluka, purum 40% in H_2O). Silicon wafer (n-Si(111) P-doped, 525 μm thickness, 1-12 Ω cm, 100 mm, single-side polished, miscut angle <0.1^o) and (p-Si(100) B-doped, 525 micron thickness, 1-10 Ω cm, single-side polished, miscut angle <0.5^o) was purchased from Compart Technology (Cambridge, UK). Water of nominal resistivity 18 MΩ cm was obtained using a Barnstead Nanopure^{TM} purification train.

FTIR

Transmission FTIR spectra were recorded on a Bio-Rad Excalibur FTS-40 (Varian Inc., Palo Alto, CA) with an MCT detector. The spectral resolution was 2 cm^{-1} and 128 scans were averaged. Porous Si chips were used in all FTIR spectra reported.

AFM

AFM images in Tapping Mode^{TM} were performed in air on a Multimode Nanoscope IIIa (Veeco Instruments Inc., Metrology Group, Santa Barbara,CA) using TESP probes (n-doped Si cantilevers, Veeco Instruments Inc., Metrology Group), with a resonant frequency of 238-293 kHz, and a spring constant of 20-80 N m^{-1}. Data acquisition was carried out using Nanoscope version 5.12b36 software (Digital Instruments).

XPS

Spectra were acquired on a Thermo-Fisher Scientific K-Alpha instrument. This uses monochromated Al X-rays (1486.6 eV) and the spot size was 400 μm. The pass energy was used 200 eV for survey scans and 20 eV for narrow scans. The instrument contains Cu, Ag and Au samples which we used to calibrate the instrument for energy and intensity. Spectra were fitted with a combination of components represented by Gaussian-Lorentzian convolutions and a Shirley background using the CasaXPS software (Casa Software Ltd, UK). The ratios between the atoms in these mixed monolayers were calculated by CasaXPS software.

Cyclic voltammetry

Cyclic voltammograms were recorded using different conditions,

CV of ferrocene derivatives were recorded using 0.5 mg ethynylferrocene, or vinylferrocene dissolved in 2 mL of 0.1 M lithium perchlorate in acetonitrile with gold as working electrode, tungsten and silver wires were used as counter and reference electrodes, respectively. Cyclic voltammograms were then recorded at a scan rate of 0.1 V s^{-1}.

CV on silicon surfaces was recorded using two different systems. In 0.1 M $LiClO_4$/MeCN as electrolyte with an Ag wire quasi-reference electrode, and tungsten/platinum wire as counter electrode (on a CH Instruments 700B potentiostat). An Ivium ModuLight LED light source was used to provide white light to the silicon surface during cyclic voltammetry with electrode diameter 6.6 mm. CV was recorded by small teflon cell was fixed on top of the modified Si substrate with a Vitron O-ring attached to it, some of acetonitrile recorded on teflon cell with a diameter of 3.85 mm exposed to light.

Also, CV were recorded in aqueous 0.1 KCl electrolyte against a Ag/AgCl wire reference electrode and a platinum wire was used as the counter electrode using Ivium CompactStat potentiostat. Silicon electrodes were created by sealing silicon chips in a teflon holder with a circular section of 3.85 mm diameter exposed to light. A screw cap allowed replacement of the silicon chip, and a Vitron O-ring was used to create a seal between the screw cap and the silicon surface. The teflon cell was held within a glass cell and the exposed electrode surface aimed at a quartz window in the side of the glass cell see Scheme 2.4 (Chapter 2). The light source was placed against this window and used to illuminate the silicon electrode during CV experimental.

Electrochemical measurements were carried out in an all-glass three-electrode cell with Ag or Ag/AgCl wire reference electrode, a platinum/palladium wire as counter electrode, where silicon surface is the working electrode. The aqueous 0.1 M $HClO_4$, or 0.1 M $LiClO_4$ in MeCN was chosen as supporting electrolyte. The ~1 x 1 cm^2 silicon surface is sealed in by a Vitron O-ring in Teflon cell, the ohmic contact to the back of the Si chip was made via an In/Ga eutectic and a copper wire. (Some CV figures were filtered by simple moving average over 15 points).

Preparation of modified Si-surfaces, EFc, VFc and EnFc

To modify the silicon surface, two steps are required, preparation silicon hydride surface and then alkylation with ferrocene to form the redox active monolayer.

Preparation of hydrogen-terminated porous silicon

Si wafer (p-Si(100) 1-10 Ohm cm) was cut into 1 cm^2 square pieces. Electrical contact to the back of the chips was made by abrading the back-side, rinsing with acetone and inserting into the PTFE cell in which the chip is pressed against a Cu foil and Cu connecting wire. The wetted area of the chip is defined by an O-ring seal on the polished face. The electrolyte was a 1:1 v/v solution of 48 % aqueous HF: absolute ethanol. A constant current density of 12.7 mA cm^{-2} was applied for 10 min was applied using a source-meter (model 2601, Keithley, Reading, UK; cell diameter of wetted area = 1 cm, current = 10 mA). The chips were then washed in water, dried under a stream of dry N_2 and used immediately for further monolayer preparation experiments.

Preparation of flat Si-surfaces

The following steps were performed to produce flat and clean modified silicon electrodes literature review,[19,20] as shown in Scheme 3.2.

i) Silicon surface cleaning

A Si <111> orientated low miscut angle wafer was cut into small squares of ca. 1 cm^2. These were cleaned with trichloroethylene by boiling vigorously for 20 min. The chips were subsequently transferred to a vial containing acetone CH_3OH at room temperature for 5 min. This was repeated with 2-propanol, soaking for 5 min. Finally, the sample was transferred to Nanopure water and soaked for 5 min.

ii) Preparation of uniform oxide layers:

The chips were transferred from Nanopure water into a freshly prepared piranha solution (1:4) (2 ml 30% H_2O_2, Sigma Aldrich, *Trace*SELECT®, and 8 ml 96% H_2SO_4) and left for 20 min. The preparation of the piranha solution is an exothermic reaction, and heat is evolved. However, upon cooling down, the chip-containing solution was heated gently on a hotplate. The chips were rinsed thoroughly with Nanopure water, and then stored in fresh Nanopure water until etching.

iii) Wet etching:

A home-built Teflon cell (Figure 3.19) and plunger were rinsed thoroughly with Nanopure water to remove impurities. The trough was then half-filled with aqueous ammonium fluoride solution (Fluka, purum 40% in H_2O), and the chips were placed in a holder with the plunger raised so that the chips are seated at the top of the cell. The chips are mounted in such a way that the polished side is facing inwards in a vertical position. The cell lid was then screwed down securely, and an argon flow was introduced into the ammonium fluoride solution for 1 - 2 h.

Then the argon inlet line was lifted out of the solution to create an argon blanket above the cell before the plunger is pressed down to lower the chips into the deoxygenated ammonium fluoride solution to etch for 15 min see Figure 3.19. The chips were lifted out of the etching solution by raising the plunger and rinsed thoroughly with Nanopure water to remove any ammonium fluoride. Finally, any excess water was removed by placing the chip edges onto dry filter paper and blowing under a gentle stream of nitrogen, before they are quickly transferred to the appropriate reflux solution. After etching, the H-terminated chips were again rinsed with water, quickly dried with a nitrogen stream and immediately used for monolayer preparation.

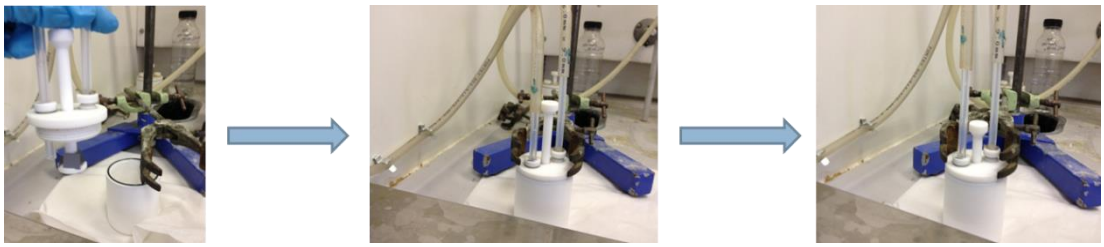

Figure 3.19. Etching steps of flat silicon surface by ammonium fluoride solution.

Caution: hydrofluoric acid, ammonium fluoride and Piranha solution are hazardous materials. These chemicals should only be handled by trained personnel using appropriate personal protective measures. Wastes from these procedures should only be disposed of by approved procedures.

Formation of ethylferrocene monolayer EFc

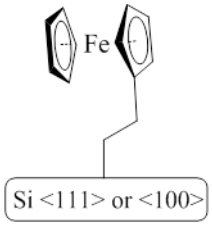

EFc

Freshly etched porous Si or Si(111)-H chips were alkylated in 20 mM of vinylferrocene (42.4 mg) in toluene (10 mL) by refluxing at 110 °C in a Schlenk flask on a glass vacuum line under nitrogen for overnight. Young's taps were used to avoid contamination of the surfaces by grease residues. Finally, the excess physisorbed vinylferrocene was removed by rinsing with DCM. [14]

Formation of vinylferrocene monolayer VFc

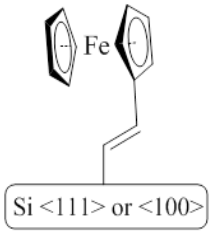

VFc

Freshly etched porous Si or Si(111)-H chips were transferred to a small Schlenk flask under a nitrogen atmosphere. A droplet containing 10 mg of ethynylferrocene in ~100 μL DCM was placed on the porous Si face or the polished face (Si(111)-H) of the chips. The reaction was left at room temperature under ambient illumination for overnight. Finally, the excess physisorbed ethynylferrocene was removed by rinsing with DCM.

Formation of ethynylferrocene monolayer EnFc

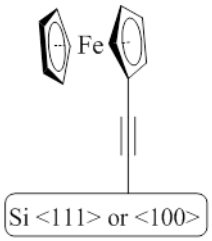

EnFc

A modified version of a previous procedure (THF was used in place of diethylether) was followed.[6] Ethynylferrocene (55 mg, 0.26 mmol) was dissolved in 5 mL of THF in a dry round-bottom flask, 0.15 mL of 1.6 M butyl lithium (n-BuLi, 2.4×10^{-4} mol, Aldrich) in hexane was added rapidly and the solution was stirred for 15 min under a N_2 atmosphere to allow for the formation of lithium ferrocenylethynylide. Next, freshly-etched silicon hydride chips were immersed in the solution and the reaction was left overnight with stirring at room temperature. The chips were removed and cleaned with eight sonication cycles: 5 min each, in 1% TFA in diethyl ether (2×10 mL), diethyl ether (2×10 mL), 4% TFA in CH_2Cl_2 (2× 10 mL), CH_2Cl_2 (2×10 mL), and then dried in a stream of N_2.

Formation of undecyl monolayer

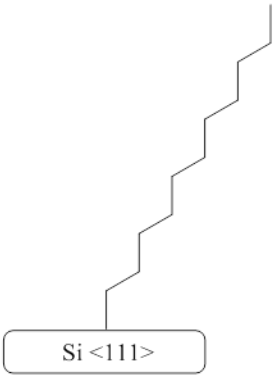

UND

Freshly etched Si(111)-H chips were alkylated in 20 mM of undecene in toluene by refluxing at 110 °C in a Schlenk flask on a glass vacuum line under nitrogen overnight to generate the undecyl monolayer **UND**. Finally, the excess physisorbed of undecene was removed by rinsing with DCM.

References

1. B. Fabre, *Accounts of Chemical Research*, 2010, **43**, 1509-1518.

2. A. Mishchenko, M. Abdualla, A. Rudnev, Y. Fu, A. R. Pike and T. Wandlowski, *Chemical Communications*, 2011, **47**, 9807-9809.

3. H. Sano, M. Zhao, D. Kasahara, K. Murase, T. Ichii and H. Sugimura, *Journal of Colloid and Interface Science*, 2011, **361**, 259-269.

4. A. A. E. A. Dalchiele, G. Bernardini, F. Cattaruzza, A. Flamini, P. Pallavicini, R. Zanoni and F. Decker, *Journal of Electroanalytical Chemistry*, 2005, **579**, 133-142.

5. G. Riveros, G. Gonzalez and B. Chornik, *Journal of the Brazilian Chemical Society*, 2010, **21**, 25-32.

6. A. G. Marrani, F. Cattaruzza, F. Decker, P. Galloni and R. Zanoni, *Electrochimica Acta*, 2010, **55**, 5733-5740.

7. K. Huang, F. Duclairoir, T. Pro, J. Buckley, G. Marchand, E. Martinez, J.-C. Marchon, B. De Salvo, G. Delapierre and F. Vinet, *Chemphyschem*, 2009, **10**, 963-971.

8. A. G. Marrani, E. A. Dalchiele, R. Zanoni, F. Decker, F. Cattaruzza, D. Bonifazi and M. Prato, *Electrochimica Acta*, 2008, **53**, 3903-3909.

9. S. Ciampi, G. Le Saux, J. B. Harper and J. J. Gooding, *Electroanalysis*, 2008, **20**, 1513-1519.

10. N. Tajimi, H. Sano, K. Murase, K.-H. Lee and H. Sugimura, *Langmuir*, 2007, **23**, 3193-3198.

11. B. Fabre and F. Hauquier, *The Journal of Physical Chemistry B*, 2006, **110**, 6848-6855.

12. F. Decker, F. Cattaruzza, C. Coluzza, A. Flamini, A. G. Marrani, R. Zanoni and E. A. Dalchiele, *The Journal of Physical Chemistry B*, 2006, **110**, 7374-7379.

13. R. Zanoni, F. Cattaruzza, C. Coluzza, E. A. Dalchiele, F. Decker, G. Di Santo, A. Flamini, L. Funari and A. G. Marrani, *Surface Science*, 2005, **575**, 260-272.

14. J. E. Bateman, R. D. Eagling, D. R. Worrall, B. R. Horrocks and A. Houlton, *Angewandte Chemie-International Edition*, 1998, **37**, 2683-2685.

15. A. G. Marrani, F. Cattaruzza, F. Decker, P. Galloni and R. Zanoni, *Superlattices and Microstructures*, 2009, **46**, 40-43.

16. R. Zanoni, M. Cossi, M. F. Iozzi, F. Cattaruzza, E. A. Dalchiele, F. Decker, A. G. Marrani and M. Valori, *Superlattices and Microstructures*, 2008, **44**, 542-549.

17. M. Herrera, T. Ichii, K. Murase and H. Sugimura, *Chemistry Letters*, 2012, **41**, 1188-1190.

18. J. M. Buriak, *Chemical Reviews*, 2002, **102**, 1271-1308.

19. S. N. Patole, A. R. Pike, B. A. Connolly, B. R. Horrocks and A. Houlton, *Langmuir*, 2003, **19**, 5457-5463.

20. L. H. Lie, S. N. Patole, A. R. Pike, L. C. Ryder, B. A. Connolly, A. D. Ward, E. M. Tuite, A. Houlton and B. R. Horrocks, *Faraday Discussions*, 2004, **125**, 235-249.

21. J. E. Bateman, R. D. Eagling, B. R. Horrocks, A. Houlton and D. R. Worrall, *Chemical Communications*, 1997, 2275-2276.

22. J. H. Song and M. J. Sailor, *Journal of the American Chemical Society*, 1998, **120**, 2376-2381.

23. P. Gupta, A. C. Dillon, A. S. Bracker and S. M. George, *Surface Science*, 1991, **245**, 360-372.

24. E. G. Robins, M. P. Stewart and J. M. Buriak, *Chemical Communications*, 1999, 2479-2480.

25. J. Hannant, J. H. Hedley, J. Pate, A. Walli, S. A. F. Al-Said, M. A. Galindo, B. A. Connolly, B. R. Horrocks, A. Houlton and A. R. Pike, *Chemical Communications*, 2010, **46**, 5870-5872.

26. M. P. Stewart and J. M. Buriak, *Angewandte Chemie-International Edition*, 1998, **37**, 3257-3260.

27. L. Scheres, M. Giesbers and H. Zuilhof, *Langmuir*, 2010, **26**, 10924-10929.

28. R. Zanoni, A. Aurora, F. Cattaruzza, C. Coluzza, E. A. Dalchiele, F. Decker, G. Di Santo, A. Flamini, L. Funari and A. G. Marrani, *Materials Science and Engineering: C*, 2006, **26**, 840-845.

29. G. Riveros, S. Meneses, S. Escobar, C. Garin and B. Chornik, *Journal of the Chilean Chemical Society*, 2010, **55**, 61-66.

30. B. R. Weinberger, G. G. Peterson, T. C. Eschrich and H. A. Krasinski, *Journal of Applied Physics*, 1986, **60**, 3232-3234.

31. J. Terry, M. R. Linford, C. Wigren, R. Y. Cao, P. Pianetta and C. E. D. Chidsey, *Applied Physics Letters*, 1997, **71**, 1056-1058.

32. L. Scheres, M. Giesbers and H. Zuilhof, *Langmuir*, 2010, **26**, 4790-4795.

33. D. Zigah, C. Herrier, L. Scheres, M. Giesbers, B. Fabre, P. Hapiot and H. Zuilhof, *Angewandte Chemie-International Edition*, 2010, **49**, 3157-3160.

34. N. G. Tsierkezos, *Journal of Solution Chemistry*, 2007, **36**, 289-302.

35. A. R. Pike, PhD thesis, Newcastle University, 2001.

36. K. Seo, I. C. Jeon and D. J. Yoo, *Langmuir*, 2004, **20**, 4147-4154.

37. C. E. D. Chidsey, C. R. Bertozzi, T. M. Putvinski and A. M. Mujsce, *Journal of the American Chemical Society*, 1990, **112**, 4301-4306.

38. S. Ciampi, J. B. Harper and J. J. Gooding, *Chemical Society Reviews*, 2010, **39**, 2158-2183.

39. S. Ciampi, T. Böcking, K. A. Kilian, M. James, J. B. Harper and J. J. Gooding, *Langmuir*, 2007, **23**, 9320-9329.

Chapter 4

Chapter 4 - Modified silicon surface with mixed monolayer of ferrocene

In the previous chapter, ferrocenyl modified silicon surfaces, with different C_2-linkages (C-C, C=C and C≡C) were fabricated and electronically characterised. The thermal method gave the best coverage for the **EFc** surface with the CH_2-CH_2 linkage. However, using the methodology and procedures described in Chapter 3, it was not easy to reproduce monolayers of the same quality and surface coverage.

Therefore, this Chapter will explore the current state of the art on the fabrication of mixed monolayers and then describe investigations into mixed ferrocenyl monolayer synthesis, as a way to improve reproducibility and also to control the spatial separation of ferrocene units within the monolayer. Thus, mixtures of vinylferrocene with different alkenes were chosen to produce mixed monolayers on silicon in a one-pot reaction, as shown in Scheme 4.1b, in a similar way to the production of 100% ferrocenyl monolayers, Scheme 4.1a, as described in Chapter 3.

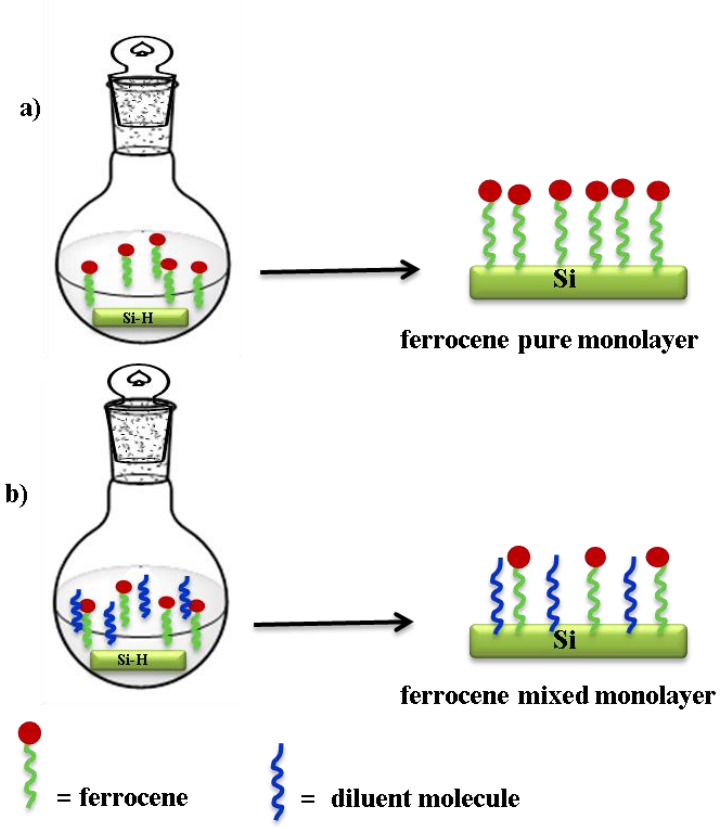

Scheme 4.1. Fabrication of ferrocenyl surfaces from two different solutions, a) ferrocene pure solution as described in Chapter 3, and b) ferrocene mixed solution with different simple alkenes to produce mixed monolayers, this method will be used in this Chapter.

In the above approach, a range of alkenes (hexene C_6H_{12}, octene C_8H_{16}, decene $C_{10}H_{20}$, and undecene $C_{11}H_{22}$) were used with vinylferrocene in a mixture for the alkylation of a silicon hydride surface. A thermal activation hydrosilylation method was used (110 ˚C in toluene as solvent) as described in Chapter 3. These alkenes have different lengths and boiling points, which may affect the rate of reaction, the packing of the monolayers, and hence the relative surface coverage of the ferrocenyl group. It has been reported that the C_8 alkyl (or longer) gold monolayer can packed closely.[1]

4.1 Introduction

A considerable amount of literature has been published on the fabrication of ferrocene mixed monolayers on gold.[2-7] However, far too little attention has been given to investigating the synthesis of mixed ferrocenyl monolayers on silicon surfaces.[8-12] Mixed monolayers can also be seen as a way to separate ferrocene units across a surface with good order.[12]

There are two possible approaches for the preparation of ferrocenyl mixed monolayers at a silicon surface, one involves multiple synthetic steps at the surface (Scheme 4.2a), and the other is a straightforward one-step reaction (Scheme 4.2b).

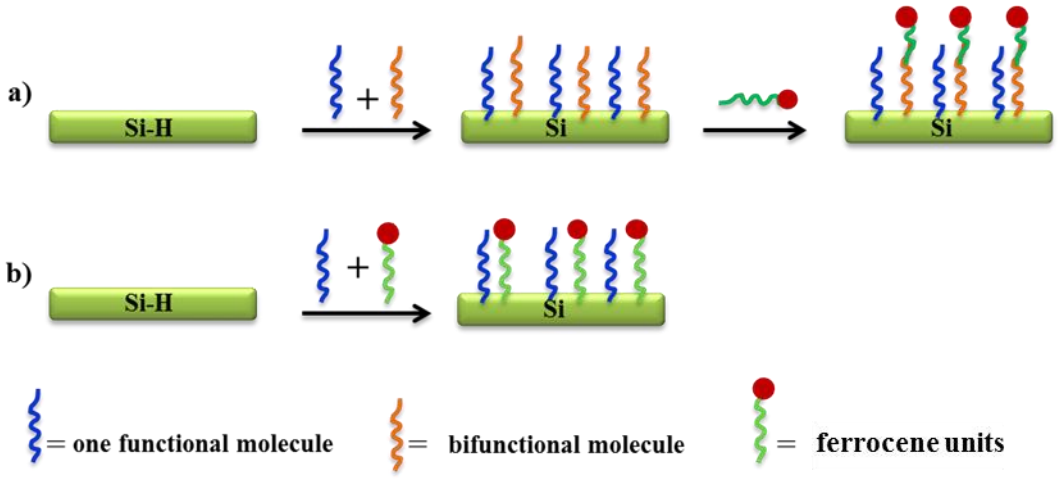

Scheme 4.2. Fabrication of ferrocene mixed monolayer by two different preparation, a) ferrocene units attached after multiple steps reaction and b) ferrocene mixed monolayer attached to silicon surface by one-step reaction.

For the preparation of ferrocenyl mixed monolayers both approaches, the multiple step[8,9,11] and the one-step reaction.[10,13] as described in Scheme 4.2, have been reported. The following sections discuss these two approaches.

4.1.1 Multiple step preparation of ferrocene mixed monolayer on silicon surface

In the multiple-step approach, Scheme 4.2a, a mixture of a bifunctional molecule and a monofunctionl alkene is used to alkylate a silicon surface to produce a mixed monolayer. One group of the bifunctional molecule must be able to react with the silicon hydride, ie an alkene, whereas, the other terminus bears a second reactive group that can be used for subsequent functionalization. This terminal reactive group can b used to later attach ferrocene units through one or more additional steps. Most of the previous work on the fabrication of mixed ferrocenyl monolayers reported methodologies based on this approach, and it is described in more detail in the following paragraphs.[8,9,11] It has been reported that a ferrocenyl monolayer attached through the multistep approach results in better packing of the ferrocenyl monolayer than through the one-step reaction.[8] This is due to the sterical hindrance of the ω-substituted alkene.[8] This could be due to two reasons, the multistep reaction method usually uses milder conditions compared with the one-step reaction, such as aminolysis.[8]

Fabre reported that the concentration of ferrocene on the silicon surface can be roughly controlled by dilution of the ferrocene in the alkylation solution.[12] For example, the coverage of ferrocene units in a ferrocenyl/decyl mixed monolayer can be approximately controlled by the ratio of ethyl undecylenate/decene in the reaction solution, where the ethyl undecylenate is later converted to contain a ferrocene terminal group, as depicted in Scheme 4.3.[8] This mixed monolayer undergoes several treatments before the mixed ferrocenyl surface is formed. First, treatment with *t*-BuOK followed by HCl produces a carboxyl terminal group. Subsequently, *N*-hydroxysuccinimide reacts with the carboxyl group to activate the monolayer. Finally, 2-aminoethylferrocenyl-methylether was introduced through carbodiimide coupling to yield the ferrocene mixed monolayer.[8]

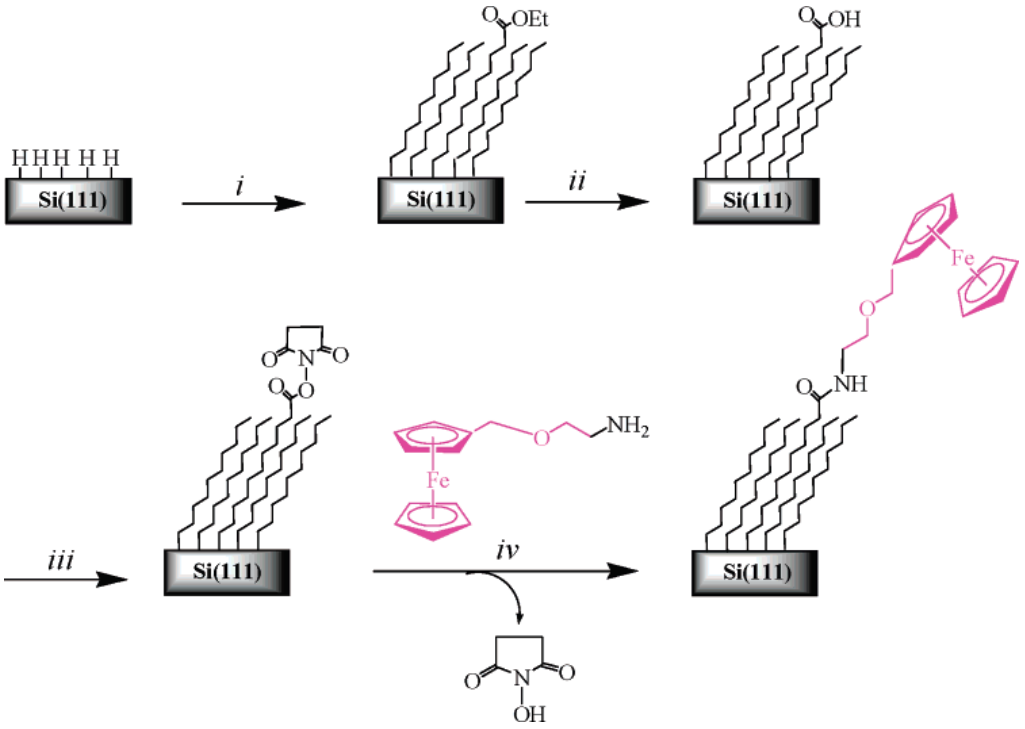

Scheme 4.3. Ferrocenyl mixed monolayers was prepared by multistep reaction (*i*) mixture of ethyl undecylenate and 1-decene, 120 °C, 20 h; (*ii*) DMF/0.25 M *t*-BuOK, rt, 10 min, then 1 M HCl, rt, 10 min; (*iii*) 0.1 M aq. NHS + 0.2 M aq. EDC, rt, 2 h; (*i*V) CH_2Cl_2/0.05 M **1**, rt, 3 h.[8]

In addition, a mixed acid fluoride/methyl-terminated monolayer has been fabricated by the thermal reaction of a silicon hydride with mixture of 10-undecynoyl fluoride/dodecyne, followed by reaction with 2-aminoethylferrocenylmethylether using carbodiimide coupling.[11] The ferrocenyl mixed monolayer is shown in Scheme 4.4.

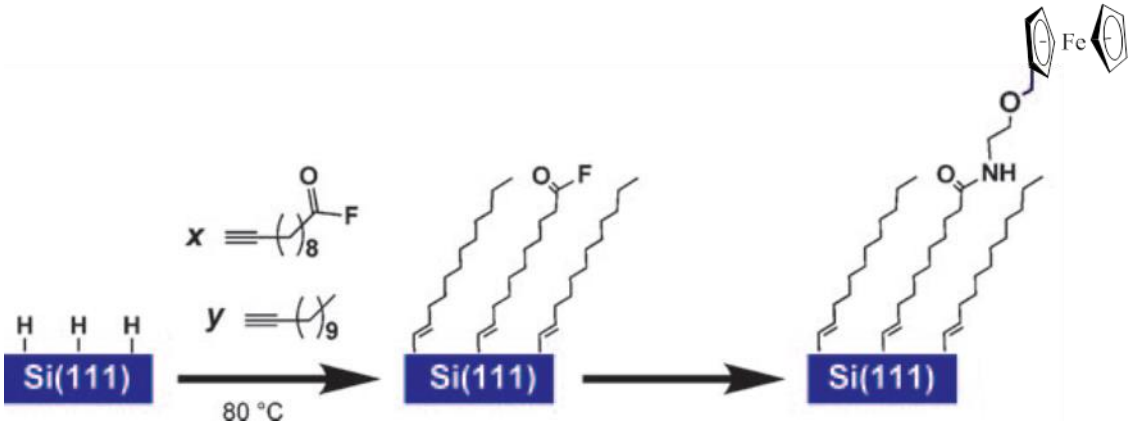

Scheme 4.4. Preparation of the ferrocene-terminated mixed monolayers on n-type Si(111) surfaces using multistep reaction.[11]

Furthermore, Gooding and co-workers have used click chemistry to produce a mixed ferrocene monolayer by a step-wise approach.[9,14] They described the modification of a silicon surface in two steps including the click reaction with an azido ferrocene. A hydrosilylation reaction carried out using a mixed alkyne solution of 1-heptyne and

1,8-nonadiyne, yielded a terminal acetylene which could then be further functionalised via the click reaction with an azido-ferrocene to produce the ferrocenyl mixed monolayer, shown in Scheme 4.5.[9]

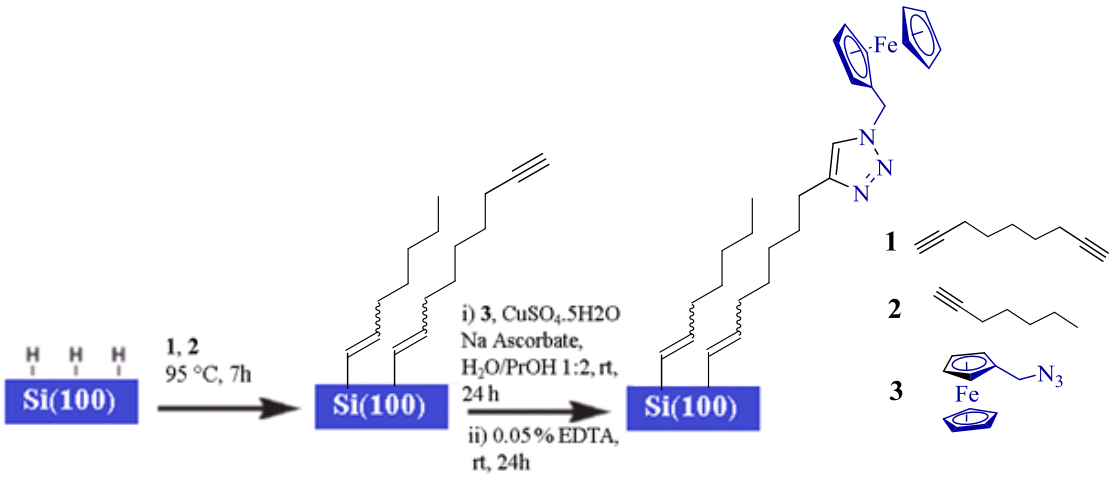

Scheme 4.5. Hydride-terminated Si(100) surfaces were reacted with different molar mixtures of alkynes **1** and **2** (mole fraction of diyne **1** was either 0.5, 0.1, or 0.05. Followed by reaction with ferrocene azide using Cu(I)-catalysis.[9]

The multistep approach for the fabrication of diluted ferrocene monolayers on silicon has not been explored to the extent of other SAM systems on silicon. The three ferrocenyl surfaces in Scheme 4.6 are taken from key reports in the literature that have utilized this method. However, the single step approach, previously summarised in Scheme 4.2b, has an even smaller precedent for the production on mixed ferrocenyl monolayers on silicon. The following section outlines the current state of the art in this area.

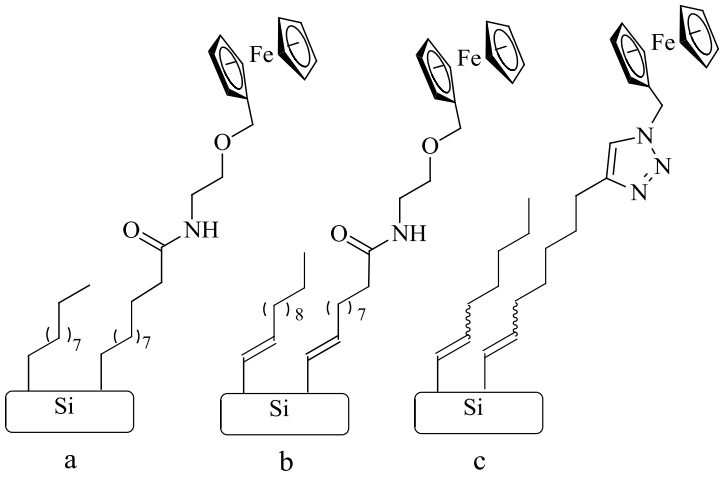

Scheme 4.6. Ferrocenyl mixed monolayer silicon modified surface produce by multiple steps preparation. (a),[8] (b)[11] and (c).[9]

4.1.2 One step preparation of ferrocene mixed monolayer on silicon surface

Several studies have produced mixed monolayers on silicon surfaces using a single chemical modification step.[15,16] However, there are only a few previous reports on ferrocene mixed monolayers fabricated using the one-step reaction approach,[10,13,17] shown in Scheme 4.2b. In general, a mixture containing a modified ferrocene and a spacer molecule is used to alkylate a silicon hydride surface to produce a mixed ferrocene monolayer, where the ferrocenes are separated by the spacer molecules. Therefore, this section investigates the preparation of different ferrocenyl/alkyl mixed monolayers using the one-pot reaction approach.

In one example, a mixed monolayer has been fabricated from a ferrocene/porphyrin mixture to alkylate a silicon hydride surface, Scheme 4.7a.[13] In another example, a ferrocenyl mixed monolayer was prepared from a mixture of 4-biphenylmethanol and 4-ferrocenylbenzyl alcohol, Scheme 4.7b.[10,17]

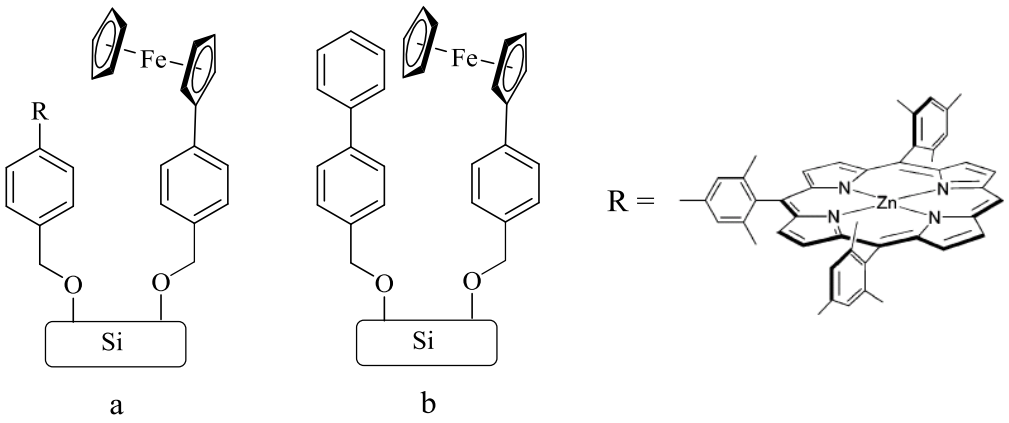

Scheme 4.7. Mixed ferrocenyl monolayer silicon modified surface produce by one-step preparation. (a)[13] and (b).[10,17]

In light of these reports, this Chapter describes the preparation and characterisation of ferrocenyl mixed monolayers via the one-pot reaction or single chemical modification approach.

Here the choice of ferrocene unit was vinylferrocene, and the modification step was the thermally activated hydrosilylation reaction at a silicon hydride surface. The thermal activation method was used as this method gave the highest monolayer coverage during the studies described in Chapter 3. A range of different alkenes were used as the spacer molecules, and the ratio of vinylferrocene and simple alkene was varied to investigate the reproducibility of these mixed monolayers. In addition, this allows for investigations

into the possibility of control over the separation of the ferrocene molecules in the monolayer through different ratios of vinylferrocene/alkene in the reaction solution. Alternative methods were not explored but may have some potential for future investigations.

4.2 Results and Discussion

In order to fabricate ferrocenyl mixed monolayers on silicon surfaces, a freshly prepared Si-H surface was placed in a 50:50 mol:mol mixture of vinylferrocene/alkene (1-hexene C_6H_{12}, 1-octene C_8H_{16}, 1-decene $C_{10}H_{20}$, and 1-undecene $C_{11}H_{22}$) in toluene and reacted at 110 ˚C overnight. This is the same method as described previously in Chapter 3 to generate the simple **EFc** surface. The mixed monolayers produced are **EFc/C$_6$**, **EFc/C$_8$**, **EFc/C$_{10}$**, and **EFc/C$_{11}$**, prepared from mixtures of vinylferrocene/hexene, vinylferrocene/octene, vinylferrocene/decene, and vinylferrocene/undecene respectively, see Scheme 4.8.

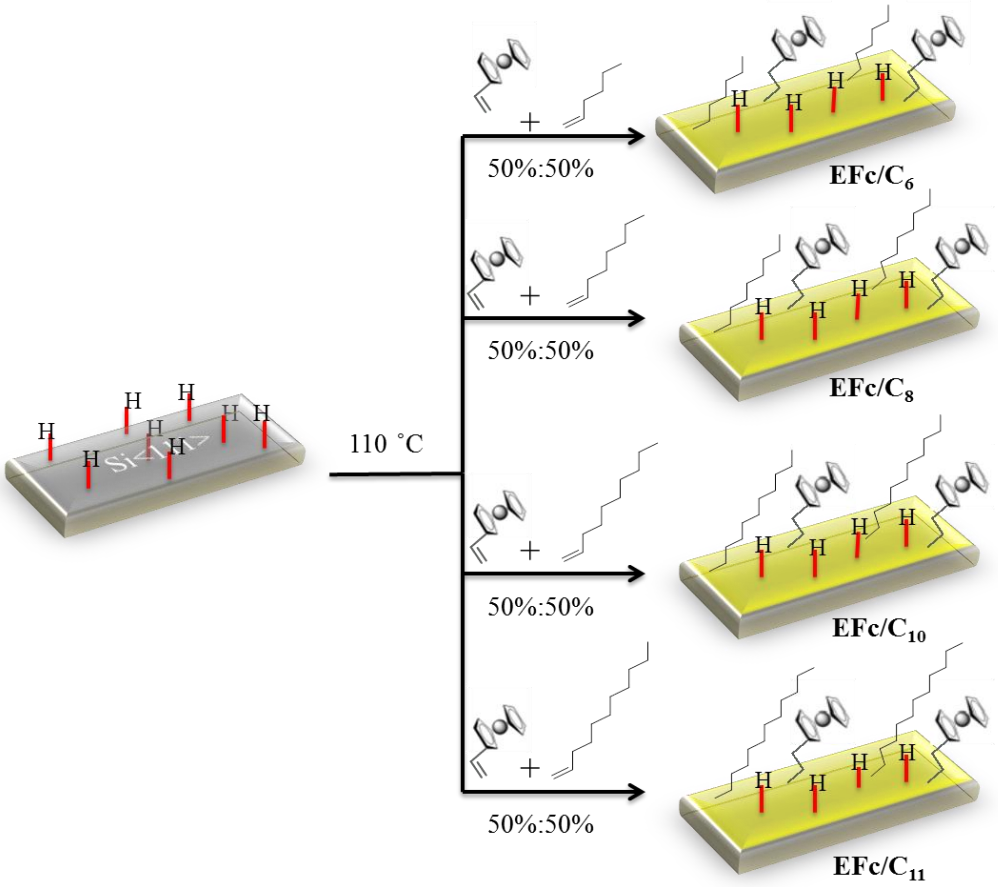

Scheme 4.8. Schematic representation of the formation of mixed ferrocenyl/alkyl monolayers on silicon. **EFC/C$_6$**, **EFC/C$_8$**, **EFC/C$_{10}$**, and **EFC/C$_{11}$**.

The boiling points of these alkenes vary considerably, hexene 60-66 ˚C, octene 122-123 ˚C, decene 166.5-173.5 ˚C, and undecene 192-193 ˚C. The difference in boiling point may affect the kinetics of the hydrosilylation reaction for the attachment of the spacer units and so affect the packing of the ferrocene units within these monolayers. In this case, hexene may produce a relatively poorly packed monolayer, as most of the hexene in the reaction vessel will be as a vapour due to its low boiling point. Additionally, the shorter chain alkenes will not pack so well due to reduced hydrophobic affects within the shorter CH_2 chains.

In this study, the ratio of 50:50 mol:mol, vinylferrocene/alkene was investigated first for all four spacer molecules, followed by a single study of the more diluted ferrocenyl monolayers with octene only.

4.3 Characterisation of 50:50 mixed monolayers

In order to assess the quality of these monolayers AFM, and XPS were performed. In addition, CV was used to record the surface coverage of ferrocene within these monolayers

4.3.1 Characterisation by atomic force microscopy

The AFM images obtained from mixed monolayers surfaces show a difference in the topography. Previous work used AFM to look at the topography of modified silicon surfaces and the underlying terrace/step structure that is expected from etched silicon. It is also possible to use the AFM imaging software (the Nanoscope AFM software) to measure the root-mean-square (rms) roughness of the surfaces to give an indication of the homogeneity of the monolayers.[8,11]

AFM images of the 50:50 **EFc**/(**C_6**, **C_8**, **C_{10}** and **C_{11}**) surfaces (Figure 4.1) show some minor differences in their topography. In general, 50:50 **EFc/alkene** surfaces are relatively clean and the expected terrace/step topology can be clearly seen, Figure 4.1. However, such terrace/step structure cannot be clearly identified in AFM images of **EFc/C_6** (Figure 4.1a).

Here the roughness of the 50:50 mixed monolayers **EFc**/(**C_6**, **C_8**, **C_{10}** and **C_{11}**) is less rough than has been previously described for ferrocene mixed monolayers.[8,11] It has been previously reported that the roughness of long chain ferrocenyl/decyl and long chain ferrocenyl/undecyl mixed monolayers are ca. 3.5 Å (0.35 nm),[8,11] which is more

than the roughness of the 50:50 mixed monolayers in this study, **EFc/C$_6$**, **EFc/C$_8$**, **EFc/C$_{10}$**, and **EFc/C$_{11}$**, which were 0.28 nm, 0.23 nm, 0.22 nm and 0.19 nm respectively, see Table 4.1.

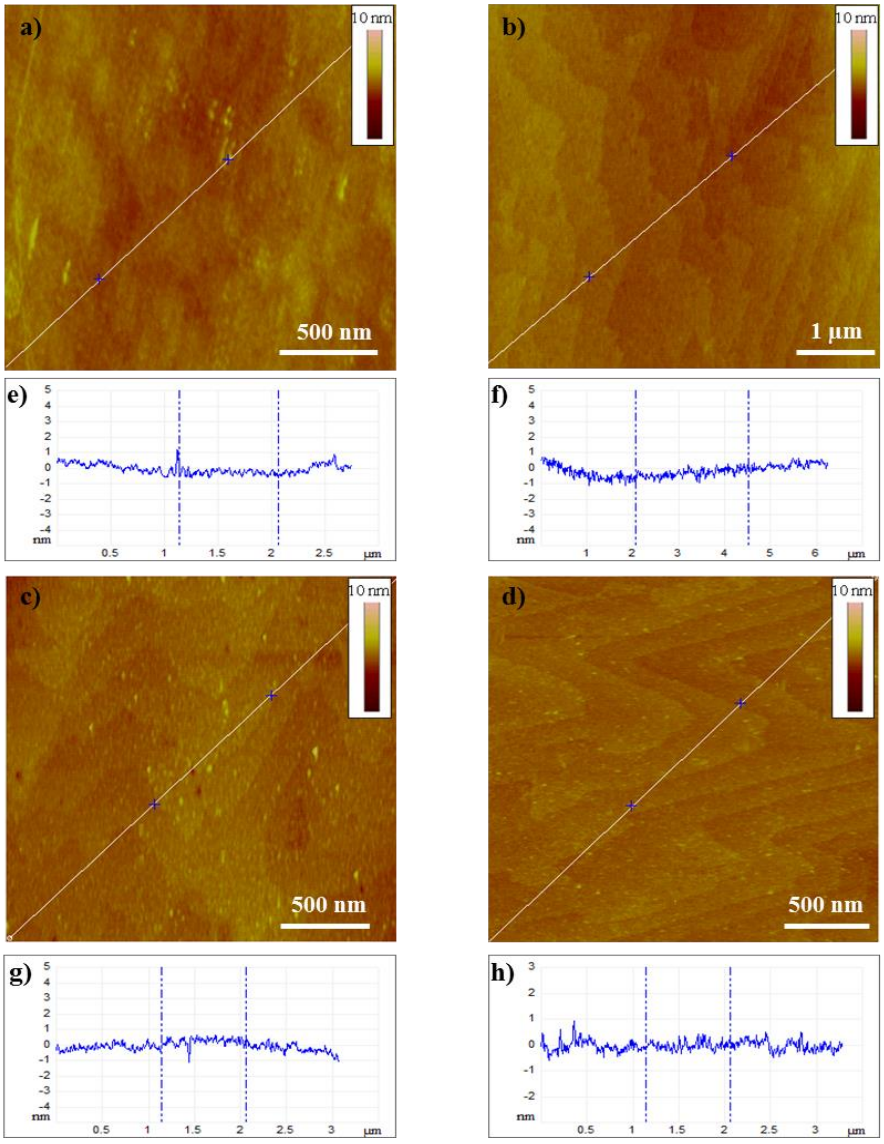

Figure 4.1. AFM tapping image from 50:50 mixed monolayers. (a) **EFc/C$_6$**; (b) **EFc/C$_8$**; (c) **EFc/C$_{10}$** and (d) **EFc/C$_{11}$**. Corresponding linear cross-section profiles (e, f, g, and h) were taken along the marked segments of AFM images (a, b, c, and d), respectively.

The roughness measurements from the AFM image revealed that the **EFc/C$_{11}$** (0.19 nm) has a similar roughness to **VFc** and Si-H surfaces (0.19 nm) in Chapter 3. This could be due to good packing of C_{11} with vinylferrocene. The roughness of **EFc/C$_8$** (0.23 nm) and **EFc/C$_{10}$** (0.22 nm) were similar and were also close to the roughness of the 100% **EFc** surface perpared in Chapter 3. This could also be due to the good packing of C_8 and C_{10} with vinylferrocene. Whereas, the roughness of **EFc/C$_6$** is noticeably more rough

(0.28 nm), as shown in Table 4.1, because as reported, short alkyl chains do not pack well when the alkyl chain is less than eight units long.[1]

Surface:	**EFc/C_6**	**EFc/C_8**	**EFc/C_{10}**	**EFc/C_{11}**
rms	0.28	0.23	0.22	0.19

Table 4.1. The rms roughness recorded over an area of average 0.5 × 0.5 μm^2 for the 50:50 mixed monolayer **EFc/C_6**, **EFc/C_8**, **EFc/C_{10}**, and **EFc/C_{11}** surfaces. These values an average value determined from several different measurement.

AFM studies on these mixed 50:50 monolayers showed that, these surfaces were stable during imaging. Although, they were similar in their topography, **EFc/C_6** has a slightly higher roughness compared to the 100% ferrocenyl monolayers studied in Chapter 3.

4.3.2 Characterisation by X-ray photoelectron spectroscopy

XPS was used to help confirm the formation of the mixed monolayer (ferrocenyl/alkyl) on the silicon substrate.[8,11] Figure 4.2 shows the survey spectrum of four different mixed 50:50 ratio monolayers of **EFc/C_6**, **EFc/C_8**, **EFc/C_{10}**, and **EFc/C_{11}**. The spectra show characteristic peaks from the silicon substrate itself (Si 2s, Si 2p) and from the C 1s, O 1s, and Fe 2p core levels of the surface attached ferrocene/alkene molecules.

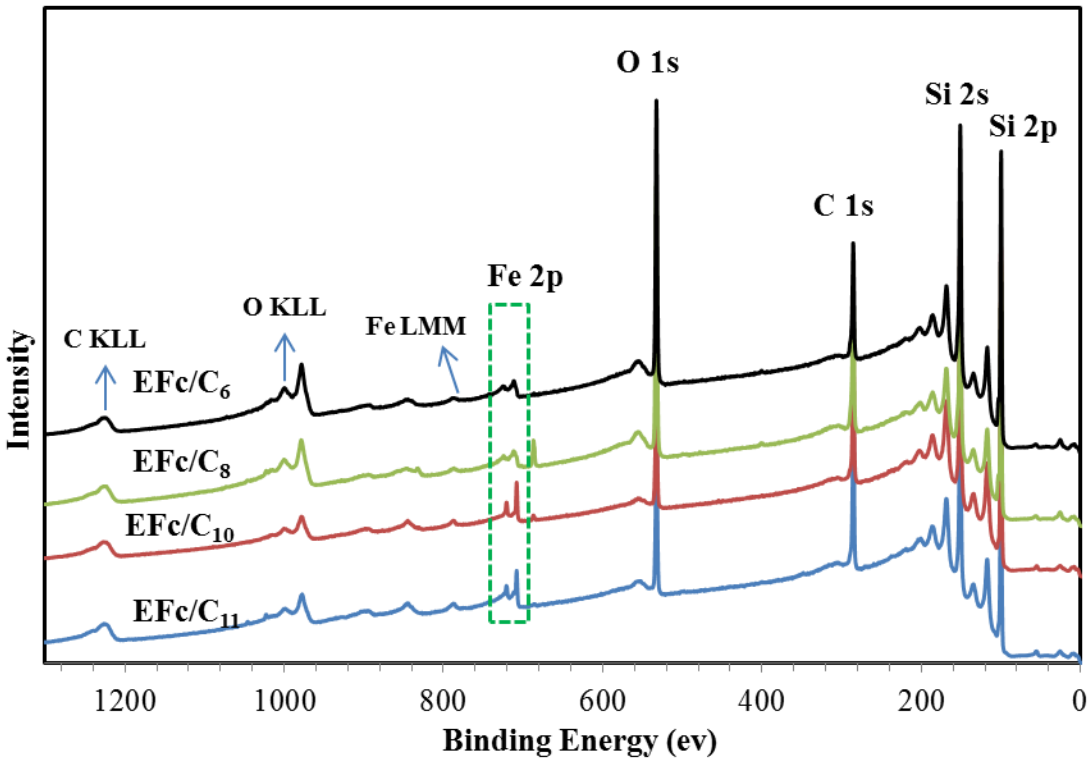

Figure 4.2. Survey X-ray photoelectron spectra of the ethylferrocenyl/alkyl mixed monolayers (50:50) prepared.

The high resolution spectra of the Fe 2p region shows that the iron is present in two oxidation states, Fe(II) and Fe(III). As has been mentioned in Chapter 3, the fitting of Fe 2p can be complex, but here a simple fitting was used to highlight the two different types of iron present.

Figure 4.3 shows the fitting of the Fe 2p core level for the four different 50:50 mixed monolayers. Curve fitting indicated the presence of two iron components, Fe(II) and Fe(III), in each case. The presence of a Fe 2p signal at 707.9 eV (Fe $2p_{3/2}$) and 720.6 eV (Fe $2p_{1/2}$) can be contributed to Fe(II) from the ferrocene ring. Whereas, the second component at higher binding energy, 711 eV (Fe $2p_{3/2}$) and 724 eV (Fe $2p_{1/2}$) arises from a proportion of the Fe species being in the Fe(III) ferrocenium state, as shown in Table 4.2.[18] The oxidation of Fe(II) to Fe(III) has also been presented for other ferrocenyl/alkyl mixed monolayers.[8] Fe(II) is the dominant species in both the **EFc/C$_6$** and **EFc/C$_8$** surfaces see Table 4.2, whereas, Fe(II) is less abundant when compared to the Fe(III) species on both of the **EFc/C$_{10}$** and **EFc/C$_{11}$** surfaces, see Table 4.2. In Chapter 3 it was proposed that the increase in intensity of Fe(III) may be due to the high temperature of thermal reaction conditions was used to prepare **EFc**, compared to the milder room temperature conditions used for both **VFc** and **EnFc** (see Chapter 3).

However, these current studies suggest that temperature is not the only reason for increased oxidation of Fe(II) to Fe(III). A high intensity of Fe(III) was observed for longer alkyl chain mixed monolayers, as seen in **EFc/C$_{10}$** and **EFc/C$_{11}$**, In this case, it could be due to more competition between the vinylferrocene and the alkene, either C_{10} or $C_{11,}$ to react with the silicon surface. This could be a result of the slower reaction kinetics of the vinylferrocene and so increasing the chance for any oxygen species in the solvent oxidising the silicon surface and also the ferrocene to ferrocenium. It could also be that the longer alkenes, C_{10} and C_{11}, react with the silicon surface to form a more stable well-packed monolayer which hinders the vinylferrocene to react with the silicon. Long alkyl chains of more than C_8 are known to form stable monolayers with good packing on gold.[1] Therefore, C_{10} and C_{11} monolayers on silicon could have denser molecular packing which could prevent the vinylferrocene reaching the silicon surface. Other reasons for oxidation of ferrocene to ferrocenium may be due to residual oxygen in the system, thus oxidising the ferrocenyl groups, as the potential of the O_2/H_2O redox couple being slightly more positive than the ferrocenium/ferrocene.[18,19]

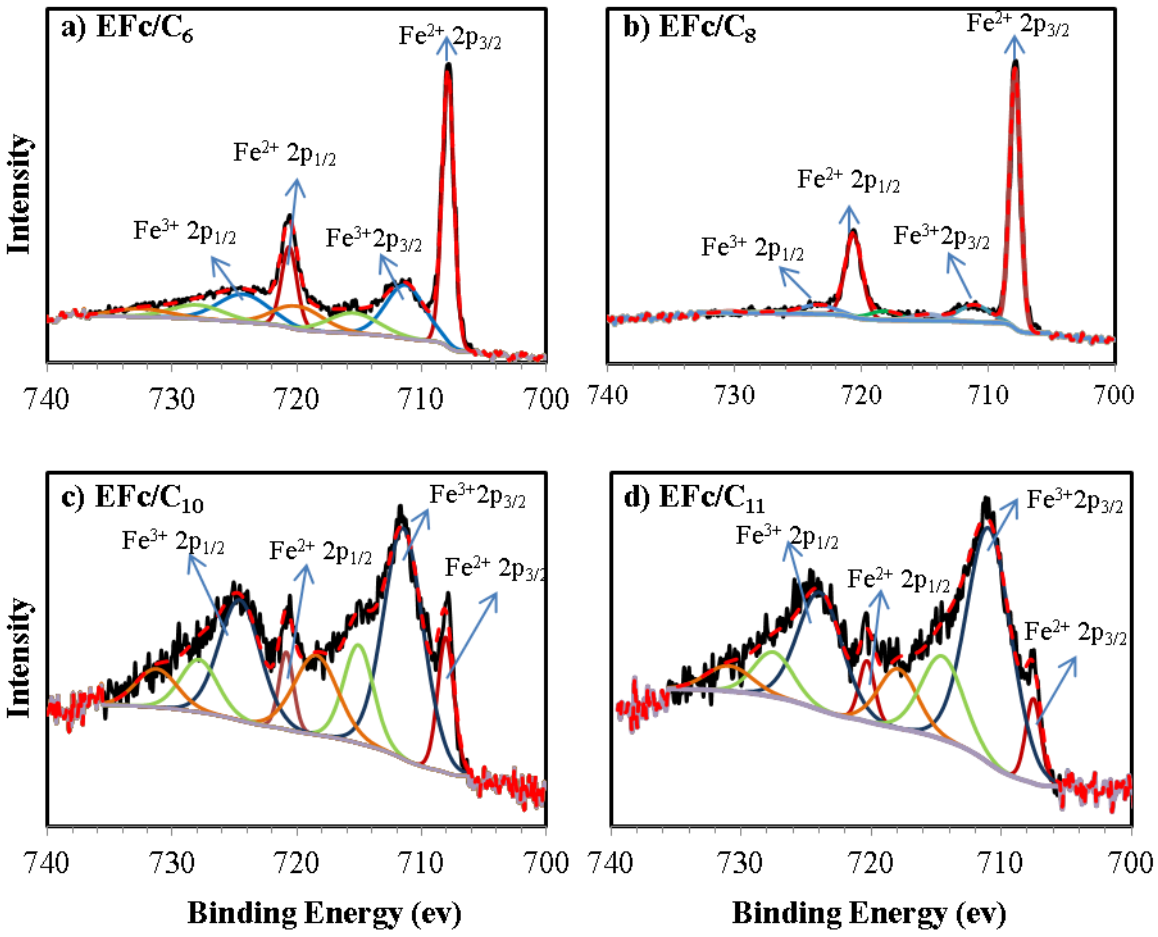

Figure 4.3. XPS spectra of the Fe 2p regions of 50:50 % of a) **EFc/C$_6$**, b) **EFc/C$_8$**, c) **EFc/C$_{10}$** and d) **EFc/C$_{11}$**. Experimental spectra are shown in black line, while curve-fit separated

components are shown in red dash. c) **EFc/C$_{10}$** and d) **EFc/C$_{11}$** are much noisier and reduced signal from less ferrocene.

It can also be observed from the XPS data that the oxidation of the silicon surface in the **EFc/C$_{10}$** and **EFc/C$_{11}$** systems is more substantial compared to the **EFc/C$_6$** and **EFc/C$_8$** surfaces. The Si 2p XPS spectra show a high intensity silicon oxide peak (103 eV) for these monolayers (Figure 4.4). Other components in the Fe 2p spectrum (Figure 4.3) are attributed to shake up satellites of Fe(II) ≈ 715.6 eV (Fe 2p$_{3/2}$) and ≈728 eV (Fe 2p$_{1/2}$)), and shake up satellites of the Fe(III) (≈719 eV (Fe 2p$_{3/2}$), ≈732 eV (Fe 2p$_{1/2}$)).

The atomic ratios of Fe/Si were similar for all mixed monolayers, and the same for both **EFc/C$_{10}$** and **EFc/C$_{11}$** monolayers (Table 4.2). The atomic ratio of C/Fe was higher than the theoretical calculation attributed to the surface, which is most likely due to contamination arising from the surrounding organics in the environment during handling. However, the C/Fe value of the **EFc/C$_{11}$** surface was the same as the expected theoretical calculation for this monolayer, see Table 4.2. It could simply be that the **EFc/C$_{11}$** surface was cleaned thoroughly and that no fingerprint residues or organic contaminants were on the silicon surface.

Surface	**Fe(II)**	**Fe(III)**	**Fe/Si**	**C/Fe**		**Fe(II)/Fe(III)**
	2p$_{3/2}$, 2p$_{1/2}$	**2p$_{3/2}$, 2p$_{1/2}$**		Theor.	Exp.	
EFc/C$_6$	707.9, 720.6	711.3, 724.3	0.029	18	21	1.20
EFc/C$_8$	707.9, 720.6	711.0, 724.5	0.025	20	23	3.80
EFc/C$_{10}$	708.0, 720.8	711.4, 724.6	0.021	22	30	0.34
EFc/C$_{11}$	707.8, 720.5	711.0, 724.8	0.021	23	23	0.83

Table 4.2. Values of binding energy for relative atomic ratios for **EFc/C$_6$**, **EFc/C$_8$**, **EFc/C$_{10}$** and **EFc/C$_{11}$**. The atomic ratios calculated by CasaXPS software.

A simple curve fitting of the Si 2p doublet can be split into three different environments (Figure 4.4a-d). A high intensity component at binding energy 99.6 eV can be attributed to the Si 2p$_{3/2}$ of the bulk silicon and the Si-C bond.[8] Whereas, the component at 100 eV can be assigned to the Si 2p$_{3/2}$ of the Si-H bond. Additionally, the component at binding energy 102.6 eV can be attributed to the Si 2p$_{3/2}$ of silicon oxide.[20] Other peaks at 100.2 eV, 100.6 eV, and 103.5 eV correspond to the 2p$_{1/2}$ levels.[21,22]

As described in Chapter 3, the oxidation of the silicon surface occurs either during or after the modification step, which is in agreement with other previous literature reports.[23,24] It could also occur during the transfer of the samples for XPS characterisation as the samples were not kept in a controlled environment after the reaction and during transfer to the XPS.

It can be clearly seen that, the Si 2p signal (103 eV) from the silicon oxide is more intense in the **EFc/C$_{10}$** and **EFc/C$_{11}$** samples than **EFc/C$_6$** and **EFc/C$_8$** monolayers see Figure 4.4c and Figure 4.4d. The difference in length of the alkyl chain, as already discussed, could be the reason for more oxidation of the silicon in the **EFc/C$_{10}$** and **EFc/C$_{11}$** surfaces.

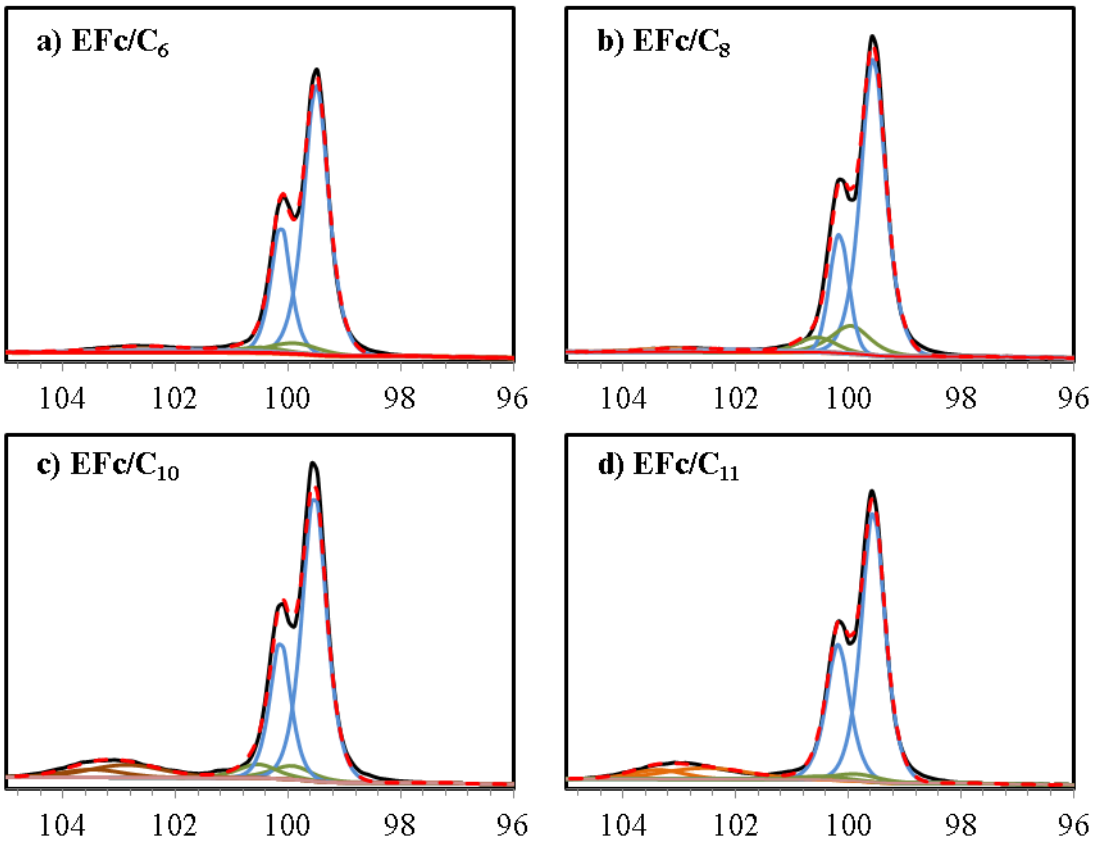

Figure 4.4. XPS of Si 2p for 50:50 mixed monolayer of a) EFc/C$_6$, b) EFc/C$_8$, c) EFc/C$_{10}$, and d) EFc/C$_{11}$ surface.

4.3.3 Characterisation by cyclic voltammetry

CV was carried out in both aqueous and organic electrolyte solutions as several arrangements of electrochemical characterisation were performed. Photoelectrochemical experiments, described later in Chapter 6, were performed using a water based system due to the nature of the cell employed.

In Chapter 3, the broad shape of the CV for 100% ferrocene monolayers, was explained due to the repulsive interactions between nearby ferrocenes. Therefore, to observe voltammograms with wave-shapes closer to the ideal case, the 50:50 mixed monolayers were electrochemically investigated by CV. The CV of different mixed monolayers were also studied in order to control the separation of ferrocene units across the silicon surface and to investigate methods to improve the reproducibility of these surfaces. It is clear that, from the cyclic voltammograms of 50:50 **EFc/C$_6$**, **EFc/C$_8$** and **EFc/C$_{10}$** in aqueous electrolytes, the wave-shapes become less ideal upon dilution of the ferrocenes with the alkyl groups as shown in Figure 4.5. FWHMs of the mixed 50:50 monolayers are 145 mV, 154 mV, and 143 mV for **EFc/C$_6$**, **EFc/C$_8$** and **EFc/C$_{10}$**, respectively, compared to 130 mV for the equivalent 100% **EFc** monolayer. The anodic and cathodic waves are now no longer the same shape, especially in the case of 50:50 **EFc/C$_{10}$**, which may indicate that counter anion transport into the monolayer to maintain neutrality is becoming an important factor.

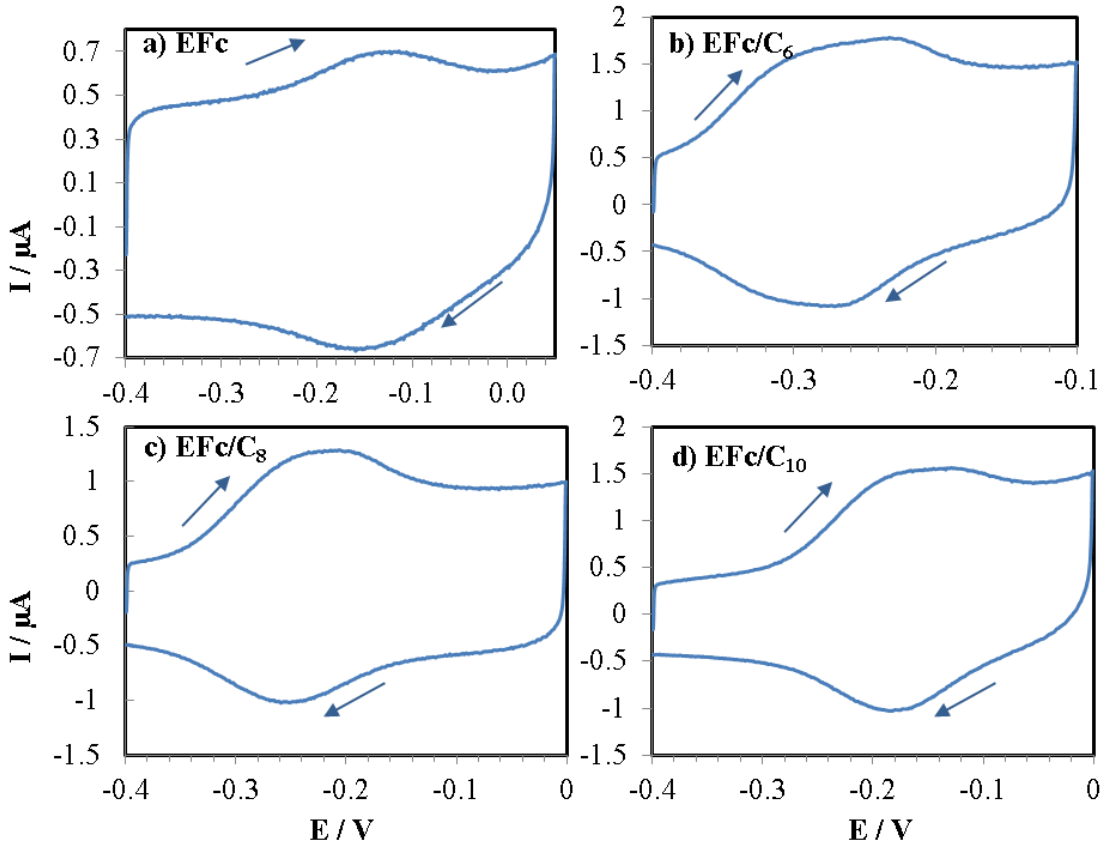

Figure 4.5. Cyclic voltammograms recorded at monolayer coated n-Si(111). a) **EFc** surface, b) 50:50 **EFc/C$_6$** surface, c) 50:50 **EFc/C$_8$** surface and d) 50:50 **EFc/C$_{10}$** surface are shown. The voltammograms were recorded in aqueous 0.1 M KCl at a scan rate of 1 V s^{-1} and under illumination. Potentials are measured against a Ag/AgCl wire reference electrode. Arrows indicate the scan direction.

The **EFc/C$_6$** monolayer exhibited a formal reversible redox response at -265 mV. The anodic and cathodic peaks were at -259 mV and -271 mV respectively giving a peak separation of 12 mV. The anodic and cathodic peaks were located at -223 mV and -244 mV for **EFc/C$_8$**, with a peak separation of 21 mV, and a formal reversible redox response of -234 mV. Whereas, the formal reversible redox potential of **EFc/C$_{10}$** was recorded at -265 mV. Where the anodic peak was at -172 mV and the cathodic peak was at -168 mV giving a peak separation of 9 mV. The peak separation of **EFc/C$_6$**, **EFc/C$_8$** and **EFc/C$_{10}$** surfaces were as expected (< 59/n mV) for surface confined redox behaviour.[8]

Surface	E_p^A	E_p^C	ΔE_p (mV)	$E^{\circ'}$ (mV)	FWHMs (mV)	coverage/ mol cm $^{-2}$
EFc	-138	-148	10	-143	130	1.8×10^{-12}
EFc/C$_6$	-259	-271	12	-265[a]	145	1.04×10^{-11}
EFc/C$_8$	-223	-244	21	-234	154	9.5×10^{-12}
EFc/C$_{10}$	-163	-172	9	-168	143	1.57×10^{-11} [b]

Table 4.3. The electrochemical properties of modifier silicon surface **EFc** surface and 50:50 of **EFc/C$_6$**, **EFc/C$_8$**, and **EFc/C$_{10}$** in aqueous solution at scan rate 1 V s^{-1}. [a] estimated value due to high waves distorted in the CV. [b] The distorted shape of the CV and the onset of silicon oxidation near $E^{\circ'}$ for this monolayer which may the value is inaccurate.

The CV of the 50:50 mixed monolayers **EFc/C$_6$**, **EFc/C$_8$**, **EFc/C$_{10}$** and **EFc/C$_{11}$** were also recorded in an acetonitrile electrolyte solution (0.1 M $LiClO_4$) versus sliver wire reference electrode at 0.5 V s^{-1} scan rate, see Figure 4.6.

The formal reversible redox response of the **EFc/C$_6$** surface was 33 mV, where the anodic and cathodic peaks were 59 mV and 7 mV respectively, with a peak separation of 52 mV as shown in Figure 4.6a. The **EFc/C$_8$** surface showed a formal reversible redox response at -57 mV, with the anodic and cathodic peaks at -32 mV and -72 mV and a peak separation of 40 mV, Figure 4.6b. There was a small peak separation, 29 mV, recorded for the **EFc/C$_{10}$** surface with anodic and cathodic peaks located at -32 mV and -61 mV giving a formal reversible redox response at -47 mV, see Figure 4.6c. It is clear that there is more than one reduction wave on the **EFc/C$_{10}$** surface. The reason could be due to different environments of the ferrocene on the silicon surface. Also the peak separation for **EFc/C$_{11}$** surface was outside the expected surface behaviour, 180 mV. The **EFc/C$_{11}$** surface exhibited a formal reversible redox response of 194 mV,

with the anodic and cathodic peaks of 284 mV and 104 mV, see Figure 4.6d. This separation may be due to the IR drop through the electrical contact on the back of the silicon.[18]

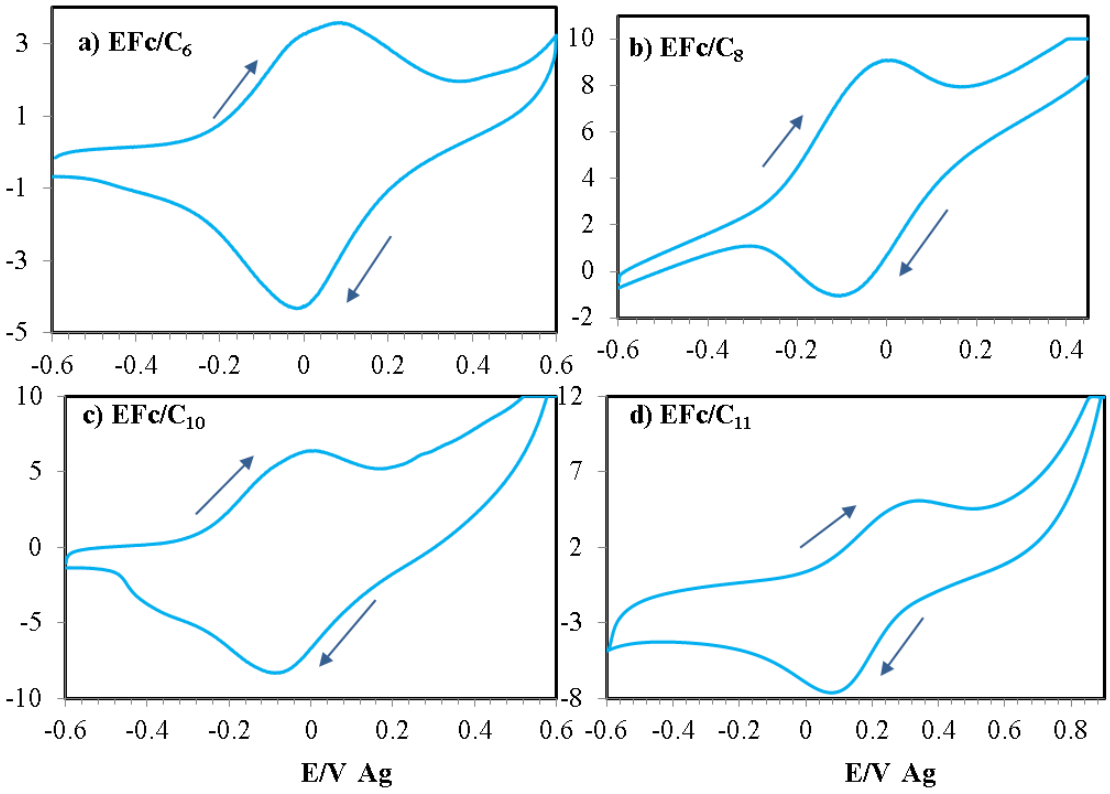

Figure 4.6. Cyclic voltammograms recorded at monolayer coated n-Si(111). Monolayers of 50:50 a) **EFc/C$_6$**, b) **EFc/C$_8$** c) **EFc/C$_{10}$** and d) **EFc/C$_{11}$** are shown. The voltammograms were recorded in (0.1 M $LiClO_4$) CH_3CN at 0.5 V s^{-1} scan rate and under illumination. Potentials are measured against a Ag wire reference electrode. Arrows indicate the scan direction.

Surface	E_p^A	E_p^C	ΔE_p (mV)	$E^{\circ'}$ (mV)	FWHMs (mV)	coverage mol cm $^{-2}$
EFc/C$_6$	59	7	52	33	115	3.49×10^{-11}
EFc/C$_8$	-32	-72	40	-57	66	4.0×10^{-11}
EFc/C$_{10}$	-32	-61	29	-47	160	3.63×10^{-11}
EFc/C$_{11}$	284	104	180	194	269	3.06×10^{-11}

Table 4.4. The electrochemical properties of modifier silicon surface 50:50 of **EFc/C$_6$**, **EFc/C$_8$** **EFc/C$_{10}$** and **EFc/C$_{10}$** in acetonitrile solution at scan rate 0.5 V s^{-1}

Figure 4.7 compares the CV of the 50:50 **EFc/C$_8$** surface in two different electrolyte solvents, aqueous and acetonitrile. In aqueous solvent, the anodic and cathodic peaks were located at -223 mV and -244 mV respectively giving a peak separation of 21 mV,

as shown in Figure 4.7a. However, in acetonitrile the anodic peak was at -32 mV and the cathodic peak at -72 mV to give a peak separation of 40 mV see Figure 4.7b. The larger peak separation an acetronitrile over water is expected as result of the increased resistance due to the lower polarity of the organic solvent. The difference in peak separation reported for the 50:50 **EFc/C$_8$** surface could be due to the IR drop across the solvent or the electrical contact on the back of the silicon.[18] However, it could also be due to a difference in the coverage between these surfaces. In Chapter 3, the **EFc** surface showed an increase in peak separation with increasing surface coverage.[25] The peak separation is also known to increase with increasing scan rate, so here for the aqueous system the scan rate was 0.8 V s^{-1} compared to 1 V s^{-1} for the acetonitrile system, which may contribute to the small difference observed. The 50:50 **EFc/C$_8$** surface in aqueous electrolyte exhibited a formal redox response at -234 mV versus Ag/AgCl reference electrode, whereas, in acetonitrile electrolyte versus a sliver wire reference electrode this surface has a formal redox response of -57 mV. The differences in the electrochemical set up, solvents and reference electrodes could fully explain the observed difference of nearly 200 mV in the formal redox potentials of the same surface under the two conditions.

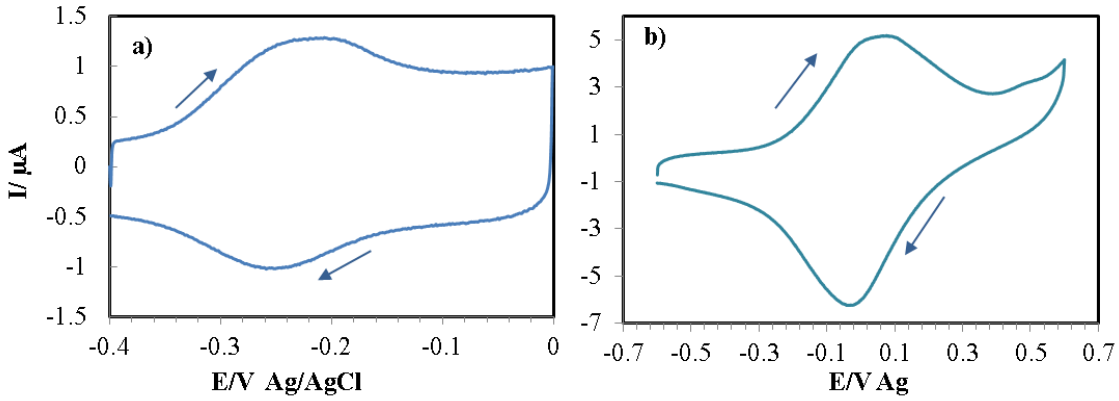

Figure 4.7. Cyclic voltammograms recorded at 50:50 **EFc/C$_8$** monolayer coated n-Si(111). a) in aqueous 0.1 M KCl at a scan rate of 1 V s^{-1} against a Ag/AgCl wire reference electrode, and b) in 0.1M, $LiClO_4$, CH_3CN at scan rate 0.8 V s^{-1} against a Ag wire reference electrode, and both under illumination. Arrows indicate the scan direction.

The coverage of the 50:50 mixed monolayers in aqueous electrolyte appear higher, 1.04×10^{-11} mol cm^{-2}, than the coverage of the pure monolayer recorded in Chapter 3, 1.8×10^{-12} mol cm^{-2} for the same electrolyte, see Table 4.3. The reason for that could be much less ferrocene is lost from the surface upon immersion in an aqueous electrolyte for such mixed monolayers compared with a pure monolayer. Increased stability of

mixed monolayers has been reported by previous workers to show that there are fewer defects and a smaller opportunity for oxidation of the surface.[12]

In addition, the coverage of ferrocene in the 50:50 mixed monolayers as recorded in acetonitrile, Table 4.4, appears higher than the 50:50 mixed monolayers recorded in aqueous electrolyte, Table 4.3. This observation could be due to a difference in the amount of ferrocene that is removed from the surface during the CV measurement. In an aqueous electrolyte, oxidation of the silicon is more likely and the ferrocene monolayer more susceptible to oxidative degradation than the relatively stable situation when in the organic acetonitrile environment. The ferrocenyl coverage data tabulated in Table 4.4 is from the samples with the maximum observed coverage. In most cases, the surface coverage of each surface type varied between different samples all prepared in the same way. In addition, the reproducibility of 50:50 **EFc/C$_6$**, **EFc/C$_8$**, **EFc/C$_{10}$** and **EFc/C$_{11}$** was not easy to achieve. The **EFc/C$_8$** surface was the most reproducible surface, which over many samples, gave a consistent surface coverage between 3.5×10^{-11} mol cm^{-2} and 4.0×10^{-11} mol cm^{-2}, see Appendix. Therefore, the **EFc/C$_8$** surface was chosen to study how dilution of the ferrocenes in the monolayer could be used to control the separation of the redox centres on the silicon electrode.

Consequently, a range of diluted ferrocenyl monolayers based on the **EFc/C$_8$** system were prepared by decreasing the ratio of vinylferrocene to 1-octene in the alkylation solution, vinylferrocene: 1-octene 20:80 mol:mol, 10:90 mol:mol, 1:99 mol:mol and 0:100 mol:mol, to give the following surfaces 20:80 **EFc/C$_8$**, 10:90 **EFc/C$_8$**, 1:99 **EFc/C$_8$** and 100 **OCT**, respectively.

4.4 Characterisation of more dilute EFc/C$_8$ surfaces

These monolayers were characterised using AFM, XPS and CV. The characterisation of more dilute monolayers started with AFM to assess the quality of these monolayers, and was followed by XPS to confirm attachment of the vinylferrocene and alkene to the silicon surface. Finally, CV was performed to study the stability of these monolayers and to measure the surface coverage.

4.4.1 Characterization by atomic force microscopy for dilute EFc/C$_8$ surfaces

AFM images of the mixed monolayer **EFc/C$_8$** surfaces with different ratios of octene in the alkylation solution 80; 90; 99; and 100 % are shown in Figure 4.8. AFM of these

surfaces show some minor differences in their topography but they are relatively clean and the terrace/step topology can be observed. These monolayers were also stable during AFM imaging and could be imaged multiple times.

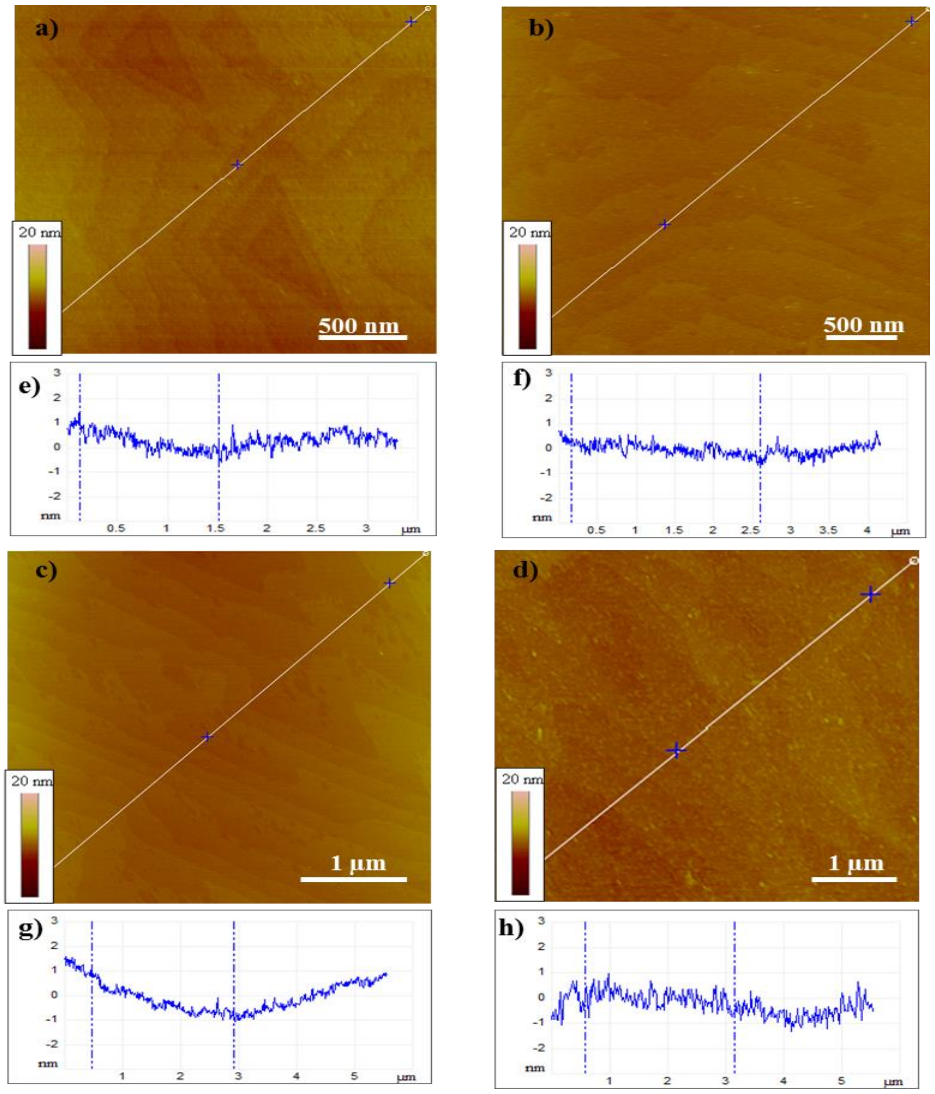

Figure 4.8. AFM tapping image from **EFc/C$_8$** mixed monolayers with different ratio. (a) 20:80; (b) 10:90; (c) 1:99 and (d) 0:100. Corresponding linear cross-section profiles (e, f, g, and h) were taken along the marked segments of AFM images (a, b, c, and d) respectively.

The roughness of these surfaces is tabulated in Table 4.5. It seems that the roughness of the dilute **EFc/C$_8$** mixed monolayer decreases with decreasing number of ferrocene units in the monolayer. In other words, when the vinylferrocene ratio in the alkylation solution is reduced, the roughness also decreases as shown in Table 4.5. For example, as the vinylferrocene ratio decreases from 50%, 20%, 10% to 1% the roughness decreases from 0.23 nm, 0.22 nm, 0.21 nm to 0.18 nm. This is could be due to the difference in packing between vinylferrocene and octene regions on silicon surface. Nevertheless, for the 100% pure octyl monolayer, **OCT**, the observed roughness is very different,

0.35 nm, which suggests that this surface did not form as expected or was not cleaned thoroughly. However, the roughness of the pure ethylferrocene monolayer, **EFc**, is 0.19 nm, (Chapter 3) which matches the expectations seen here.

The roughness of the mixed **EFc/C_8** surface is less than the roughness reported for the ferrocene terminated/dodecenyl monolayer, where 10% and 50% of ferrocene gave roughness values of 0.33 nm and 0.34 nm respectively.[11] This could be due to the fact that the lengths of the components within the mixed monolayer in this study is more comparable. The chain lengths of C_6, C_8 C_{10}, C_{11} are 0.79 nm, 0.80 nm, 1.31 nm, 1.45 nm, respectively, compared to the ferrocene-Si distance of **EFc** (0.72 nm).

Ratio of EFc/C_8	**50:50**	**20:80**	**10:90**	**1:99**	**0:100**
rms (nm)	0.23	0.22	0.21	0.18	0.35

Table 4.5. The rms roughness recorded over an area of average 0.5×0.5 μm^2 for the mixed monolayer **EFc/C_8** surfaces with different ratio. These values an average value determined from several different measurement.

The different ratios of the dilute mixed monolayers, 20:80, 10:90, and 1:99 of **EFc/C_8** had roughness values between 0.18 nm to 0.23 nm. The difference in morphology and roughness of these surfaces may be due to the way the monolayer packs depending on the spatial separation of the ferrocene units within the alkyl monolayer. Increasing the alkyl dilution of the **EFc/C_8** mixed monolayer shows clear terrace/step topology in the AFM images which supports the expected close packing of these mixed monolayers.

4.4.2 Characterisation by X-ray photoelectron spectroscopy for more dilute EFc/C_8 surfaces

After the successful characterisation of the 50:50 **EFc/alkyl** surface, the more diluted surfaces of **EFc/C_8** were also characterised by XPS. The survey spectra of **EFc/C_8** (20:80, 10:90, 1:99) all indicate characteristic peaks from the silicon substrate itself (Si 2p) and from the C 1s, O 1s, and Fe 2p core levels of the surface attached ferrocene molecules as shown in Figure 4.9. However, the Fe peaks were too small to observe clearly in the survey spectra, but the high-resolution spectrum shows the presence of Fe on the surface in all cases, see Figure 4.10. Ferrocene molecules are chemisorbed onto the silicon surface, as confirmed by the stability of these monolayers under sonication and repeated washing with organic solvents.

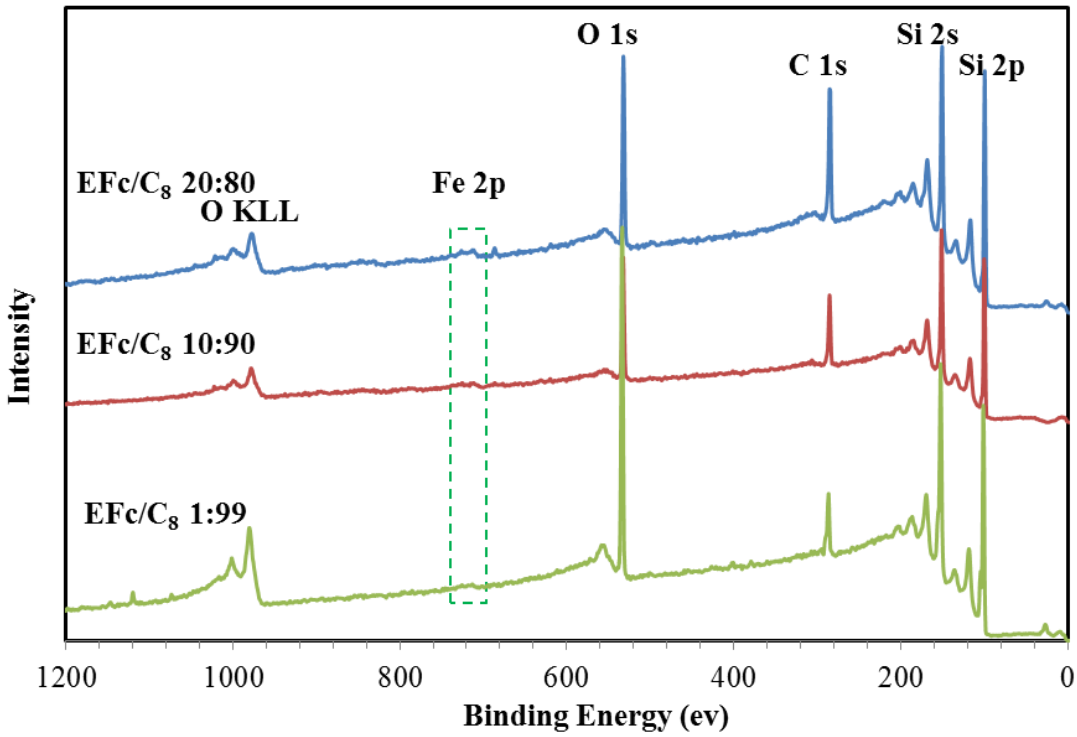

Figure 4.9. Survey X-ray photoelectron spectra of the **EFc/C$_8$** mixed monolayers with different ratio prepared.

To get more information about the oxidation state of Fe 2p, a simple fitting was applied to the high resolution spectra, Figure 4.10. The fitting shows that the iron is present in two oxidation states, Fe(II) and Fe(III). The presence of Fe 2p signals at 708 eV (Fe $2p_{3/2}$) and 720 eV (Fe $2p_{1/2}$) can be contributed to Fe(II) from the ferrocene ring. Whilst the second component, at higher binding energy 710.9 eV (Fe $2p_{3/2}$) and 723.7 eV (Fe $2p_{1/2}$), arises from a proportion of Fe species being in the ferrocenium state. Additional features in the Fe 2p spectrum (Figure 4.10) Fe(II) ≈ 715 eV (Fe $2p_{3/2}$) and ≈728 eV (Fe $2p_{1/2}$)), and the Fe(III) (≈718 eV (Fe $2p_{3/2}$), ≈732 eV (Fe $2p_{1/2}$)) are attributed to shake up satellite peaks. These findings are consistent with previous literature reports and earlier studies.[18]

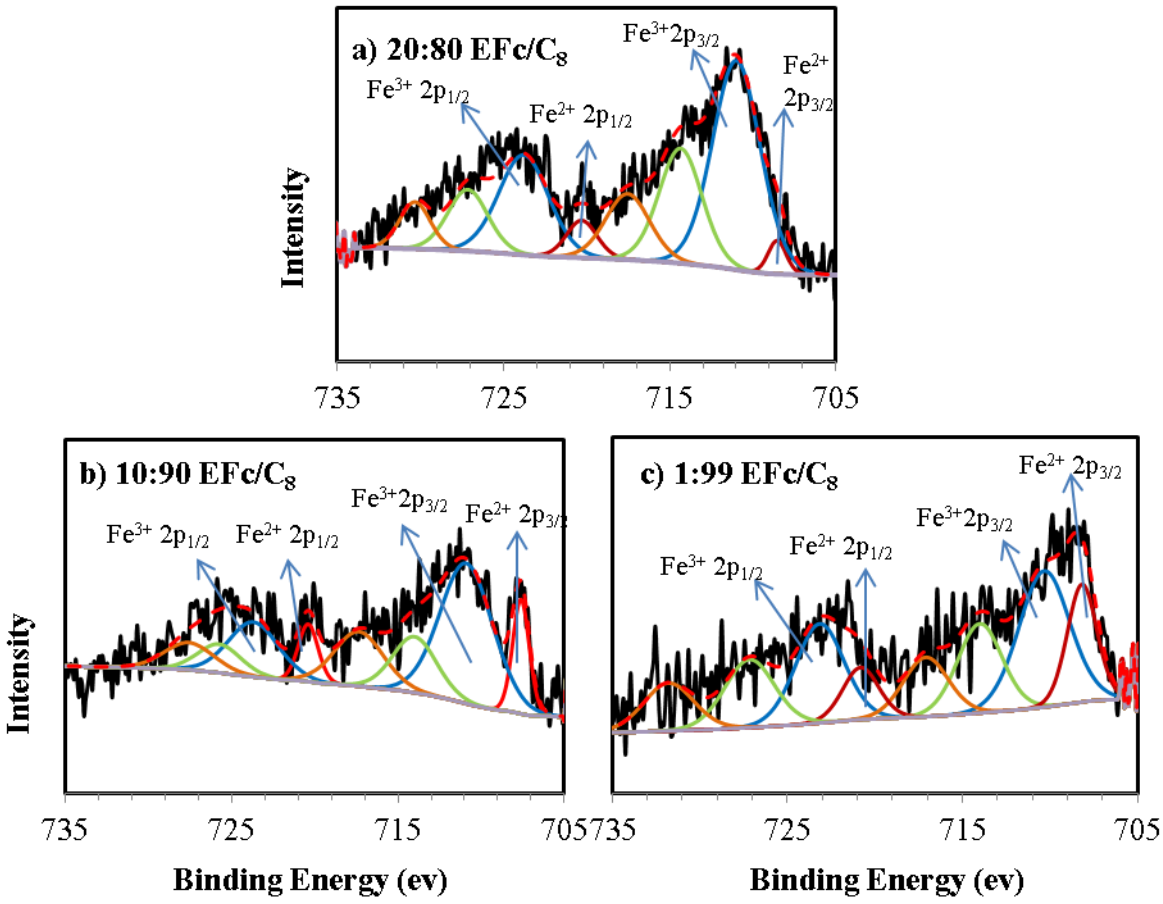

Figure 4.10. XPS spectra of the Fe 2p regions for a) 20:80 **EFc/C$_8$**, b) 10:90 **EFc/C$_8$** and c) 1:99 **EFc/C$_8$** Experimental spectra are shown in black, while curve-fit separated components are shown in red dash. Spectra are much noisier and signal reduced because less ferrocene.

It is possible to gauge the extent of surface coverage and oxidation by comparing the XPS peak areas of Fe/Si, C/Fe and also Fe(II)/Fe(III). The ratios of the peak areas between these pairs of atoms were calculated by Casa XPS software, see Table 4.6.

EFc/C$_8$ ratio	**Fe(II)** **2 p$_{3/2}$, 2p$_{1/2}$ eV**	**Fe(III)** **2 p$_{3/2}$, 2p$_{1/2}$ eV**	**Fe/Si**	**C/Fe**	**Fe(II)/Fe(III)**
20:80	708.5, 720.3	710.9, 723.8	0.011	60	0.11
10:90	708, 720.4	710.9, 723.7	0.009	41	0.30
1:99	708.4, 720.2	710.9, 723.6	0.0045	55	0.45

Table 4.6. Values of binding energy for relative atomic ratios for **EFc/C$_8$** monolayer prepared with ratio between vinylferrocene/octene in the solution (20:80, 10:90, and 99:1).the atomic ratios calculated by CasaXPS software.

The atomic ratio of Fe/Si in 20:80 **EFc/C$_8$** (0.011) was nearly five times lower compared to the **EFc** surface (0.05, from XPS study in Chapter 3), also this ratio was nearly 2.7 times lower than the Fe/Si ratio of 50:50 **EFc/C$_8$** studied in this chapter (Table 4.2). It is apparent that the **EFc** surface does contain more ferrocene groups than the 50:50 **EFc/C$_8$** (0.025), 20:80 **EFc/C$_8$** (0.011), 10:90 **EFc/C$_8$** (0.009), and 1:99 **EFc/C$_8$** (0.0045) surfaces, see Figure 4.11.

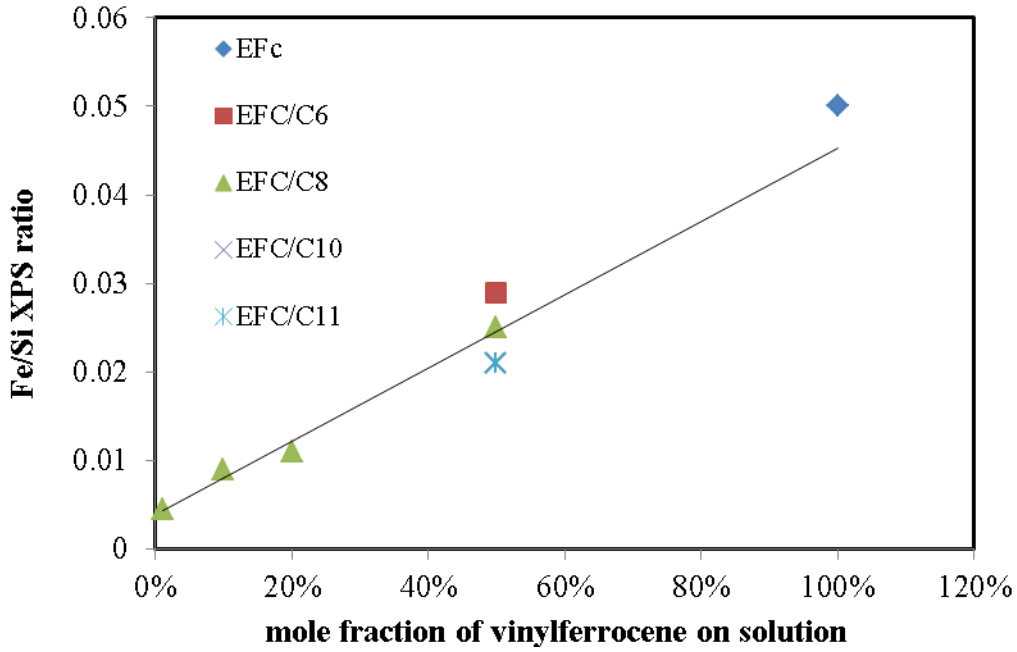

Figure 4.11. Fe/Si XPS ratio with pure ferrocene on **EFc** surface, and also different mixed monolayers 50:50 **EFc/C$_6$**, **EFc/C$_8$**, **EFc/C$_{10}$** and **EFc/C$_{11}$**. Followed by more dilution vinylferrocene on surface **EFc/C$_8$**.

The Fe(II)/Fe(III) ratio can be used to compare which oxidation state dominates within the surface bound ferrocene units. The expectation would be that the Fe(II) signal would dominate the spectra, but expectedly in the more dilute monolayer the Fe(III) signal is the dominant species (Figure 4.10 and Table 4.6). This could be due to the difficulty in the formation of a close-packed vinylferrocene monolayer on these surfaces, allowing any trace of oxygen access to the ferrocene to then be oxidised to ferrocenium.

The C/Fe value in the dilute monolayer **EFc/C$_8$** is higher than expected, which may be due to the fact that the sample was left in ambient conditions for more than a month before being analysed by XPS. In the case of the 1:99 **EFc/C$_8$** sample, it was left for longer than 6 months before analysis was performed, as shown in Table 4.6. However, this finding indicated that there is more contamination with carbon species when the proportion of vinylferrocene increases in the solution, see Table 4.6. There is

competition between vinylferrocene and octene in the alkylation solution to react with the Si-H surface and if more ferrocene reacts it leaves more areas of silicon hydride unreacted due to the size of the ferrocene unit and its relatively poor packing. This therefore means that the proportion of octene that can react with the surface is more than the expected ratio from the alkylation solution.

4.4.3 Characterisation by cyclic voltammetry for more dilute EFc/C_8 surfaces

CV of the different **EFc/C_8** surfaces were recorded to investigate the possibility of controlling the separation of ferrocene units on silicon surface through the ratio of vinylferrocene and octene within the alkylation solution. Figure 4.12 shows the CV of the dilute **EFc/C_8** mixed monolayer recorded in 0.1 M $LiClO_4$ in acetonitrile at 0.5 V s^{-1}. The 20:80 **EFc/C_8** surface presents a formal reversible redox response at 35 mV versus a Ag wire reference electrode at 0.5 V s^{-1}, where the anodic peak is located at 138 mV and the cathodic peak at -68 mV, giving a peak separation of 206 mV, as shown in Figure 4.12a. Furthermore, the 90:10 **EFc/C_8** surface indicates both the anodic and cathodic peaks were located at 64 mV and 38 mV, with a small peak separation of 26 mV, and a formal reversible redox response at 51 mV, Figure 4.12b. In addition to that, the more dilute **EFc/C_8** surface, 1:99, presented an anodic peak at -418 mV and a cathodic peak at -377 mV to give a peak separation of 41 mV, and a formal reversible redox potential of -398 mV, as shown in Figure 4.12c, and Table 4.7.

The peak separation of 10:90 and 1:99 **EFc/C_8** surfaces were as expected for surface confined redox behaviour < 59/n mV.[8] Whereas, a much larger peak separation, outside the range expected for a surface bound species was reported for the 20:80 **EFc/C_8** surface, 206 mV.

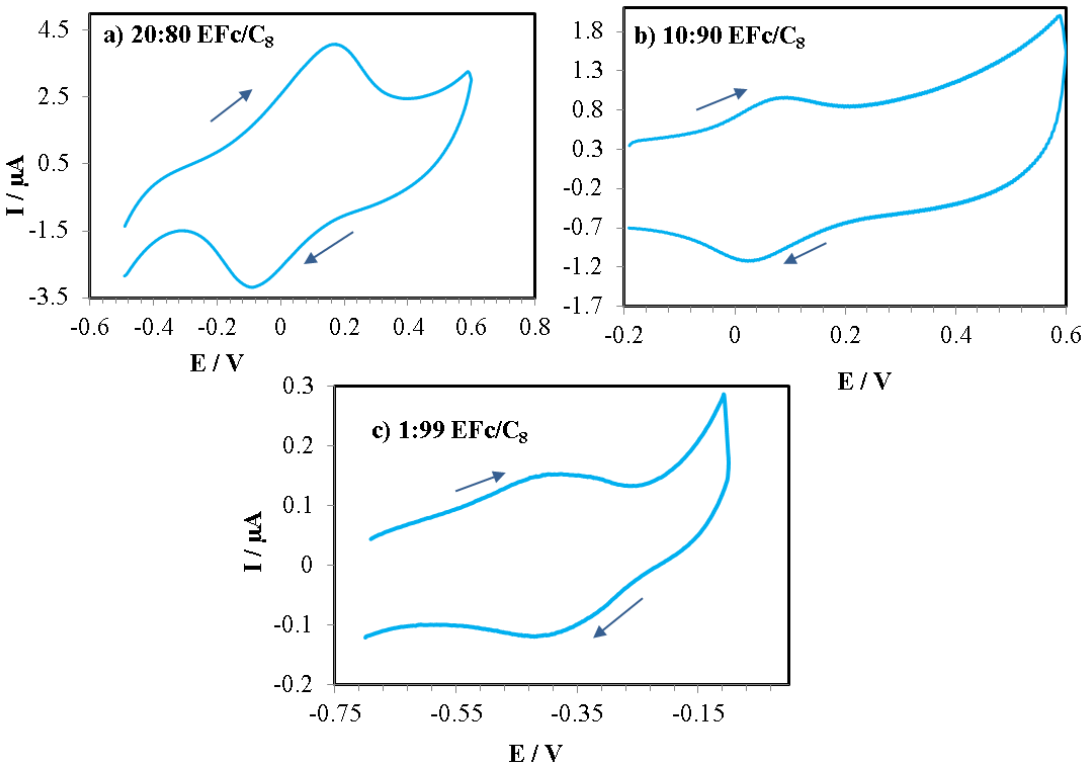

Figure 4.12. Cyclic voltammograms recorded at monolayer coated n-Si(111). Monolayers consisting of ethylferrocenyl (EFc) chains diluted with octyl giving surfaces a) 80:20 **EFc/C$_8$**, b) 90:10 **EFc/C$_8$** and c) 1:99 **EFc/C$_8$** are shown. The voltammograms were recorded in (0.1 M, $LiClO_4$) CH_3CN at 0.5 V s^{-1} scan rate and under illumination. Potentials are measured against a Ag wire as reference electrode. Arrows indicate the scan direction.

The CV data recorded in acetonitrile were used to calculate the surface coverage of ferrocene within the dilute mixed **EFc/C$_8$** monolayers, Table 4.7. There is a consistent decrease in the ferrocene coverage on the silicon surface as the mole fraction of ferrocene in the alkylation solution decreases. For example, by decreasing the mole fraction of ferrocene in the alkylation solution from 20% to 1% the coverage decreases from 3.03×10^{-11} mol cm $^{-2}$ to 7.95×10^{-13} mol cm $^{-2}$, a difference of nearly 40 times, which is twice the difference in relative ferrocene concentrations.

Dilute EFc/C$_8$	ΔE_p (mV)	E_p^A	E_p^C	E° (mV)	coverage mol cm $^{-2}$
20:80	206	138	-68	35	3.03×10^{-11}
10:90	26	64	38	51	1.84×10^{-12}
1:99	41	-418	-377	-398	7.95×10^{-13}

Table 4.7.The electrochemical properties of more dilution **EFc/C$_8$** modified silicon surface in acetonitrile solution at scan rate 0.5 V s^{-1}.

The ferrocenyl surface coverage, as calculated from the peak areas of the anodic peaks in CV of the mixed **EFc/C$_8$** monolayers, may not depend linearly on the ratio of ferrocene/alkene in the alkylation solution. However, the plot of surface coverage against mole fraction of ferrocene in the alkylation solution, Figure 4.13, suggest that in fact this may be the case, if errors associated with the data collection are accounted for. This result is in agreement with previous work where Fabre found that the coverage of ferrocene in *n*-decyl/ferrocene-terminated monolayers showed a non-linear correlation and were not significantly dependent on the composition of the ferrocene/alkene mixture.[8] In that work, the surface was modified in a multi-step approach and increased steric effects during the reaction were cited as the reason behind this observation. However, by using a simplified, one-pot, mixed alkene/ferrocene hydrosilylation approach, controlling the separation of ferrocene units across the silicon surface may be possible.

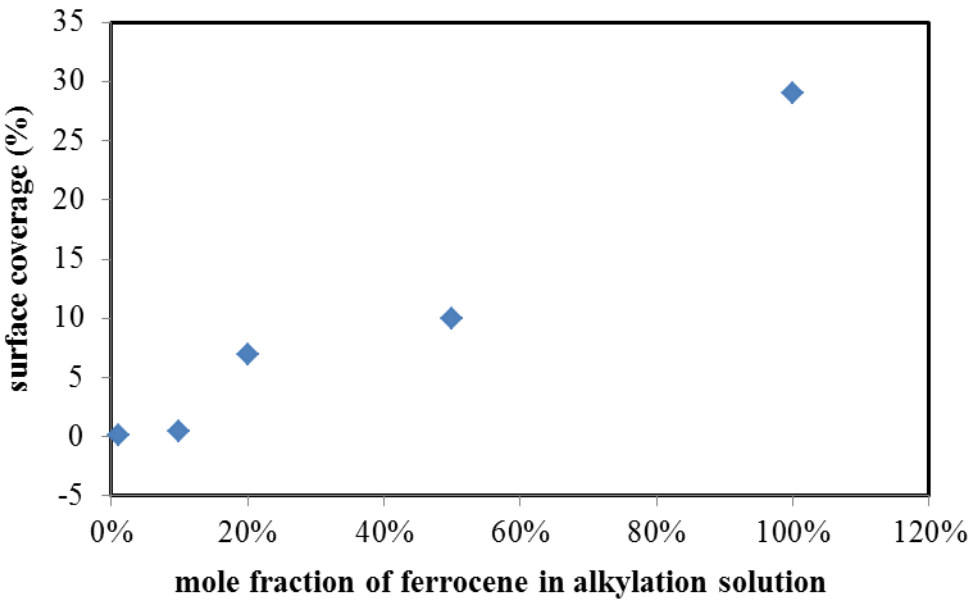

Figure 4.13. Variation of the surface coverage of ferrocene in mixed **EFc/C$_8$** monolayers with molar fraction of vinylferrocene in the initial alkene mixture.

4.5 Conclusion

Hydrogen terminated Si(111) single crystal was modified with a 50:50 mol:mol mixture of vinylferrocene and one of several simple alkenes, 1-hexene C_6H_{12}, 1-octene C_8H_{16}, 1-decene $C_{10}H_{20}$, or 1-undecene $C_{11}H_{22}$. The resulting four mixed ferrocenyl/alkyl monolayers were **EFc/C$_6$**, **EFc/C$_8$**, **EFc/C$_{10}$**, and **EFc/C$_{11}$**. These monolayers were characterised using AFM, XPS and CV. AFM showed these monolayers were stable

during imaging and retained the underlying silicon step-terrace structure. Moreover, the surface roughness data were largely similar except in the case of the **EFc/C$_6$** surface where increase in roughness compared to the 100% ferrocenyl monolayer was observed. XPS characterisation confirmed that the vinylferrocene/alkene components were attached to the silicon surface, due to element peaks of the Si 2s, Si 2p, C 1s, and Fe 2p core levels. Cyclic voltammograms of the mixed 50:50 monolayers, **EFc/C$_6$**, **EFc/C$_8$**, **EFc/C$_{10}$** and **EFc/C$_{11}$** were analysed in two different electrolytes, water and acetonitrile. The estimated ferrocenyl surface coverage depended on which solvent/electrolyte system was used. The higher coverage was observed in acetonitrile, and this could be because these surfaces are more stable in acetonitrile than aqueous electrolyte. In aqueous electrolyte some ferrocene may be lost from the surface during the CV measurement due to oxidation of the silicon surface. The estimated surface coverage of ferrocene ranged from 9.5×10^{-12} mol cm^{-2} to 1.57×10^{-11} mol cm^{-2} in aqueous electrolyte. Whereas, the estimated coverage in acetonitrile ranged from 3.06×10^{-11} mol cm^{-2} for the **EFc/C$_{11}$** surface to 4.0×10^{-11} mol cm^{-2} for the **EFc/C$_8$** surface. In these studies, the CV data from the **EFc/C$_8$** surface proved to be the most reproducible. The coverage of **EFc/C$_8$** surface gave consistent values between 3.5×10^{-11} mol cm^{-2} and 4.0×10^{-11} mol cm^{-2} over many samples.

Therefore, the **EFc/C$_8$** surface was chosen to prepare various diluted ferrocenyl monolayers in order the control the ferrocene separation on the silicon surface. Dilute **EFc/C$_8$** surfaces which ranged from 20:80, 10:90 and 1:99, in the vinylferrocene:octene alkylation solution were successfully papered. These dilute monolayers were stable under AFM imaging, and the surface roughness of these dilute monolayers decreased with decreasing percentage of ferrocene in the reaction solution. In addition, XPS characterisation confirmed the attachment of ethylferrocenyl/alkyl on the silicon surface due to the Si 2s, Si 2p, C 1s, and Fe 2p core level peaks appearing in survey spectrum. An interesting result from the XPS study was that the ratio of Fe/Si increased approximately with increasing mole fraction of vinylferrocene in the alkylation solution. The cyclic voltammetry was also carried out in order to estimate the surface coverage electrochemically and to explore the separation of ferrocene units on the silicon surface. From the CV data, the coverage of different dilute mixed monolayers **EFc/C$_8$** were 3.03×10^{-11} mol cm^{-2}, 1.84×10^{-12} mol cm^{-2} and 7.95×10^{-13} mol cm^{-2} for 20:80, 10:90 and 1:99 **EFc/C$_8$** surfaces respectively. It could be possible to control the spatial separation of the ferrocene units on the silicon surface, as the coverage of the mixed **EFc/C$_8$**

monolayers were found to depend on the surface mole fraction of vinylferrocene in the initial alkylation solution.

4.6 Experimental

Materials

All reagents were obtained from Sigma-Aldrich, except anhydrous toluene and anhydrous THF which were obtained from Acros Organics, aqueous ammonium fluoride solution (Fluka, purum 40% in H_2O). Silicon wafer (n-Si(111) P-doped, 525 μm thickness, 1-12 Ohm cm, single-side polished, miscut angle <0.1^o). Water of nominal resistivity 18 MΩ cm was obtained using a Barnstead Nanopure^{TM} purification train.

Details of AFM, XPS, and CV specification were explained in Chapter 3.

Preparation of mixed monolayer modified Si-surfaces, EFc/C_6, EFc/C_8, EFc/C_{10} and EFc/C_{11}

The preparation of these mixed monolayers can be produced by two steps, preparation of flat Si-surfaces (see experimental in Chapter 3), then followed by modification with mixed alkylation solution to produce mixed monolayers.

Formation of EFc/alkyl mixed monolayers

Freshly etched Si(111)-H chips were alkylated in 20 mM (50:50 mol:mol) of vinylferrocene/ 1-(hexene, octene, decene, or undecene) in toluene by refluxing at 110 °C in a Schlenk flask on a glass vacuum line under nitrogen overnight. Young's taps were used to avoid contamination of the surfaces by grease residues. Finally, the excess physisorbed vinylferrocene/alkene were removed by rinsing with DCM. In some experiments to prepared mixed monolayers, a portion of the vinylferrocene was replaced by different portion of octene (20:80 mol:mol, 10:90 mol:mol or 1:99 mol:mol) to prepare different mixed monolayers of **EFc/C_8**, with the total concentration of alkene fixed at 20 mM.

Formation of octyl monolayer, OCT

Freshly etched Si(111)-H chips were alkylated in 20 mM of 1-octene in toluene by refluxing at 110 °C in a Schlenk flask on a glass vacuum line under nitrogen overnight to generate pure octyl monolayer **OCT**. Finally, the excess physisorbed octene was removed by rinsing with DCM.

References

1. A. Lio, D. H. Charych and M. Salmeron, *Journal of Physical Chemistry B*, 1997, **101**, 3800-3805.

2. M. Y. Ho, P. Li, P. Estrela, S. Goodchild and P. Migliorato, *Journal of Physical Chemistry B*, 2010, **114**, 10661-10665.

3. S. Watcharinyanon, E. Moons and L. S. O. Johansson, *Journal of Physical Chemistry C*, 2009, **113**, 1972-1979.

4. L. Mueller-Meskamp, B. Luessem, S. Karthaeuser, M. Homberger, U. Simon and R. Waser, in *Proceedings of the International Conference on Nanoscience and Technology*, eds. E. Meyer, M. Hegner, C. Gerber and H. J. Guntherodt, Editon edn., 2007, vol. 61, pp. 852-855.

5. R. C. Chambers, C. E. Inman and J. E. Hutchison, *Langmuir*, 2005, **21**, 4615-4621.

6. T. Kawaguchi, K. Tada and K. Shimazu, *Journal of Electroanalytical Chemistry*, 2003, **543**, 41-49.

7. T. Auletta, F. van Veggel and D. N. Reinhoudt, *Langmuir*, 2002, **18**, 1288-1293.

8. B. Fabre and F. Hauquier, *The Journal of Physical Chemistry B*, 2006, **110**, 6848-6855.

9. S. Ciampi, P. K. Eggers, G. Le Saux, M. James, J. B. Harper and J. J. Gooding, *Langmuir*, 2009, **25**, 2530-2539.

10. K. M. Roth, A. A. Yasseri, Z. M. Liu, R. B. Dabke, V. Malinovskii, K. H. Schweikart, L. H. Yu, H. Tiznado, F. Zaera, J. S. Lindsey, W. G. Kuhr and D. F. Bocian, *Journal of the American Chemical Society*, 2003, **125**, 505-517.

11. D. Zigah, C. Herrier, L. Scheres, M. Giesbers, B. Fabre, P. Hapiot and H. Zuilhof, *Angewandte Chemie-International Edition*, 2010, **49**, 3157-3160.

12. B. Fabre, *Accounts of Chemical Research*, 2010, **43**, 1509-1518.

13. Q. L. Li, G. Mathur, S. Gowda, S. Surthi, Q. Zhao, L. H. Yu, J. S. Lindsey, D. F. Bocian and V. Misra, *Advanced Materials*, 2004, **16**, 133-137.

14. A. Ng, S. Ciampi, M. James, J. B. Harper and J. J. Gooding, *Langmuir*, 2009, **25**, 13934-13941.

15. Y. J. Liu, N. M. Navasero and H. Z. Yu, *Langmuir*, 2004, **20**, 4039-4050.

16. C. Rogero, B. T. Chaffey, E. Mateo-Marti, J. M. Sobrado, B. R. Horrocks, A. Houlton, J. H. Lakey, C. Briones and J. A. Martin-Gago, *Journal of Physical Chemistry C*, 2008, **112**, 9308-9314.

17. Q. Li, G. Mathur, M. Homsi, S. Surthi, V. Misra, V. Malinovskii, K.-H. Schweikart, L. Yu, J. S. Lindsey, Z. Liu, R. B. Dabke, A. Yasseri, D. F. Bocian and W. G. Kuhr, *Appl. Phys. Lett.*, 2002, **81**, 1494-1496.

18. N. Tajimi, H. Sano, K. Murase, K.-H. Lee and H. Sugimura, *Langmuir*, 2007, **23**, 3193-3198.

19. M. Lu, T. He and J. M. Tour, *Chemistry of Materials*, 2008, **20**, 7352-7355.

20. R. Zanoni, F. Cattaruzza, C. Coluzza, E. A. Dalchiele, F. Decker, G. Di Santo, A. Flamini, L. Funari and A. G. Marrani, *Surface Science*, 2005, **575**, 260-272.

21. A. G. Marrani, F. Cattaruzza, F. Decker, P. Galloni and R. Zanoni, *Electrochimica Acta*, 2010, **55**, 5733-5740.

22. G. Riveros, C. Garin, S. Meneses and S. Escobar, *Molecular Crystals and Liquid Crystals*, 2010, **521**, 187-194.

23. G. Riveros, G. Gonzalez and B. Chornik, *Journal of the Brazilian Chemical Society*, 2010, **21**, 25-32.

24. G. Riveros, S. Meneses, S. Escobar, C. Garin and B. Chornik, *Journal of the Chilean Chemical Society*, 2010, **55**, 61-66.

25. A. Mishchenko, M. Abdualla, A. Rudnev, Y. Fu, A. R. Pike and T. Wandlowski, *Chemical Communications*, 2011, **47**, 9807-9809.

Chapter 5

Chapter 5 - Towards conjugated ferrocenes tethered to silicon

In the previous chapter, different dilutions monolayers of ethylferrocenyl with simple alkyl chains yielded mixed monolayers (**Fc/C_6**, or **Fc/C_8**, or **Fc/C_{10}**, or **Fc/C_{11}**) were fabricated and electronically characterised.

Therefore, in this chapter, efforts to build longer chain linkages (> C_2) between the ferrocene and silicon surface are first described. Then investigations into how the linkage type and length affects the electron transfer between the ferrocene and the silicon surface are detailed. Longer alkyl chain linkages between the ferrocene and silicon surface can be synthesised in two ways, as shown in Scheme 5.1.

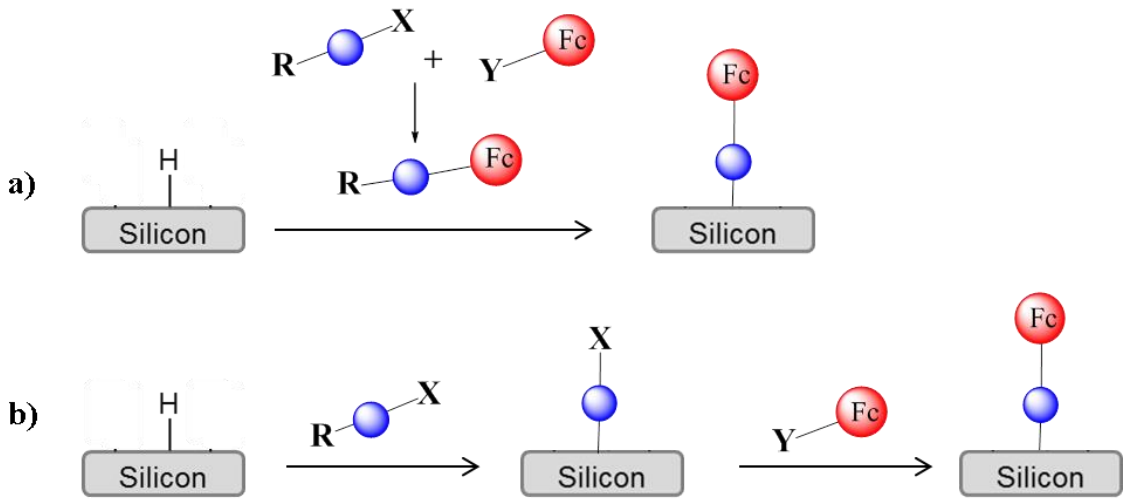

Scheme 5.1. Fabrication of ferrocene modified silicon surfaces by two approaches: a) pre-synthesis of tethered ferrocene followed by attachment to a silicon surface, b) step-wise building via alkylation of the silicon surface with a linker followed by addition of ferrocene.

In one approach (Scheme 5.1a) a ferrocenyl group with an extended tether is first synthesised, which is then attached as a complete unit to the silicon surface. An alternative strategy is to build up in a stepwise fashion from the silicon surface via a series of surface confined reactions, Scheme 5.1b. The alkyl linkage provides a molecular interconnect between the silicon substrate and ferrocene and could afford control over the electron transfer kinetics. The linker is required to possess a surface-reactive head group to alkylate the silicon hydride surface, R. Also, it must have a terminal end group to introduce other chemical functionalities, X, as shown in Scheme 5.1b. In our instance, the coupling with ferrocene involves the Sonogashira cross coupling reaction to from a new C-C bond. One advantage of step-wise reactions

performed on a solid substrate is the ease of purification simply by washing the surface with appropriate solvents to remove unreacted material and any side products.

5.1 Introduction

Although SAMs on silicon surfaces have been extensively studied,[1-3] there has been a recent effort in the development of more complex surface bound structures.[4-7]

5.1.1 Advantage and disadvantage of one-step and step-wise strategy

As already mentioned there are two principal methods for producing complex modified silicon surfaces. In the one-step strategy, hydrogen-terminated silicon surfaces can be alkylated with a range of pre-synthesised functional moieties bearing terminal groups reactive to an Si-H surface, such as: 1-alkenes,[8-14] 1-alkynes,[12-21] 1-alcohols,[22,23] and 1-aldehydes.[9,23] In the step-wise strategy, the Si-H surface is alkylated with a bifunctional molecule, one group reacts with the Si-H surface in the same was as in Strategy 1 as shown in Scheme 5.1b, and the other bears a second reactive group for subsequent functionalization e.g. alcohols,[5,6] acids,[24] amines, [25] halides,[26] or esters.[24] This terminal reactive group can be converted to more complex organic or bioorganic extended structures. However, the step-wise method is more popular for the fabrication of complex surfaces because this modular approach provides increased diversification during building and is attractive due to the simplified purification processes after each addition. The ease of building and the richness of commercially available chemicals that can be attached to the surface makes this route relatively straightforward.[19,24] A step-wise strategy has been previously used to attach several biological compounds, for example, DNA, [5,6,25] proteins,[7] and enzymes.[27] Moreover, the purification of these monolayers are easy, by washing the surface with suitable solvents. Nevertheless, the main drawback of this strategy is a strong dependence on the efficiency and reliability of the particular coupling approach used and any eventual protection/deprotection steps involved.[19,24] In addition, step-wise reactions often exhibit a decrease in the typical yield due to the sterically confined nature of surface reactions. It is well known that typical yields are below 50 % for the initial silicon hydride surface alkylation step. Any subsequent coupling reaction in a step-wise approach may also fail and so present some unreacted starting martial after each coupling reaction.[12] In contrast, a large range of different pre-synthesised and purified compounds can be immobilized by the one-step strategy. Despite its advantage and efficacy, the one-step strategy suffers from several

major drawbacks. The first disadvantage of the one-step strategy is that the synthesis of these compounds is more challenging, and in particular purification can prove to be more difficult. Another disadvantage of the one-step strategy is the difficulty to produce close packed monolayers because of the large footprint of these pre-synthesised compounds.[12,19] The distance between close-packed molecules in a monolayer on silicon is 3.8 Å and therefore a defect-free monolayer will not be produced by compounds which have a molecular radius larger than about 2 Å.[2,19,24] In addition, a monolayer produced from ω-substituted 1-alkenes will be less ordered when the ω-substituent is sterically hindered. A bulky terminal group dominates the close packing effects of the alkyl chain,[2] whereas in the step-wise approach, each component in the coupling reactions makes well-ordered monolayers due to their smaller size.[19,24,28]

5.1.2 Step-wise approach

There are many methods that use a step-wise approach to generate SAMs. The following section describes some examples.

5.1.2.1 Click chemistry

Click chemistry is a widely used method to quickly produce complex compounds, since it was first reported in 2001 by Sharpless and co-workers.[29] More recently, click chemistry has been successfully used to functionalise silicon surfaces.[18,19,30] In principle, surface-bound alkynes in the presence of a Cu(I) catalyst can undergo the Huisgen 1,3-dipolar cycloaddition reaction with compounds bearing the azide group. Click chemistry of acetylene-terminated monolayers on silicon has been studied by various research groups.[18,19,30] The reaction between a silicon hydride surface and di-alkynyl compounds such as 1,8-nonadiyne[18,19] or 1,6-heptadiyne[30] have been reported. For example, Ciampi and co-workers reported that, 1,8-nonadiyne gave a tethered C_9-monolayer with terminal alkyne groups exposed for further modification. This was followed by click reaction with a range of azides, such as 4-azidophenacyl bromide, 1-azidobutane, 2-azido-1,4-dimethoxbenzene, and 11-azido-3,6,9-trioxaundecan-1-ol. In general, these two-step reactions gave well-ordered surfaces in good yield (36 to 80 %) as shown in Scheme 5.2.[18,19]

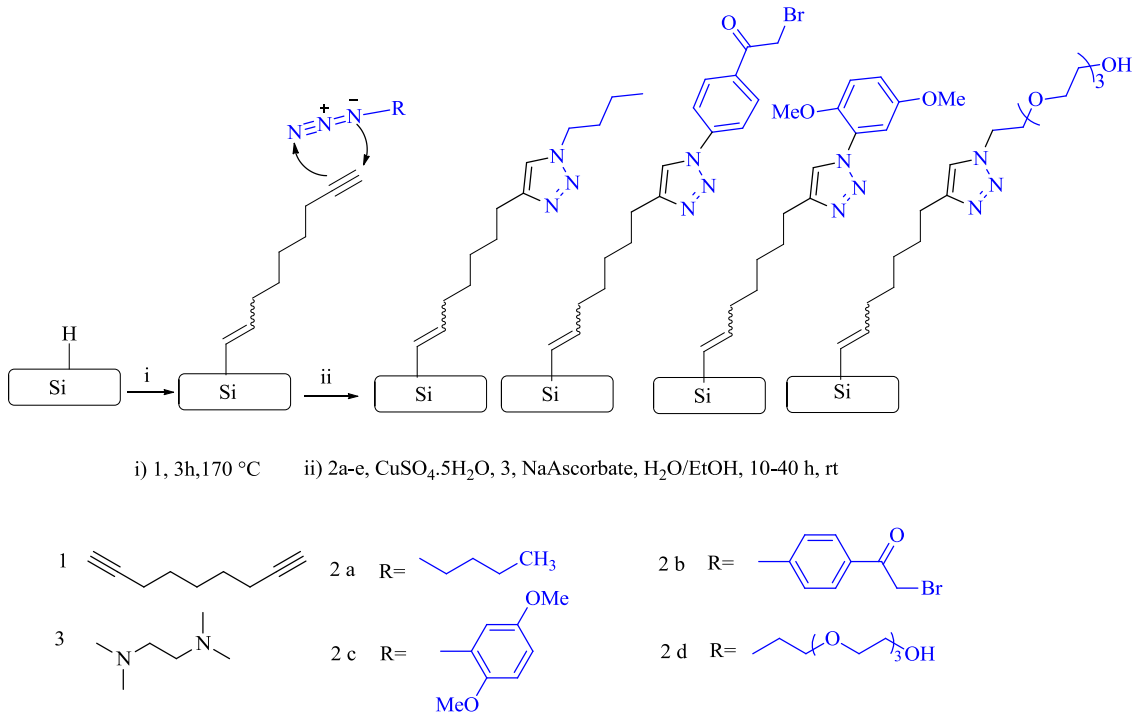

Scheme 5.2 The preparation of a monolayer presenting an alkyne functionality (i) was followed by ligand-assisted click reactions with substituted azido species (ii).

5.1.2.2 Sonogashira cross coupling reaction

A second method for catalysed coupling for surface modification is the Sonogashira reaction. However, far too little attention has been given to the Sonogashira cross coupling reaction to fabricate functional silicon surfaces. Sonogashira coupling has been widely exploited in organic synthetic chemistry,[31,32] and recently it has been used in solid-phase surface chemistry.[10,11,33] Traditionally, Sonogashira coupling reaction is the palladium-catalysed coupling between an aryl or vinyl halide compound and a terminal alkyne (sp^2 and sp) to generate a C≡C bond.[10,11,33] On a silicon surface, the Sonogashira coupling reaction has been performed in the presence of a palladium catalyst under either microwave or thermal conditions.[10,11,33] The microwave-assisted reaction employed mild conditions, which have been found to give high yields over short reaction times.[10,33] The reaction under thermal conditions requires a high temperature and extended reaction times.[11] Although, the microwave method was reported with the high yield, the thermal method will be used in this Chapter. Because the coverage of the thermal method reported in Chapter 3 gave the highest coverage, therefore, the thermal method was the chosen approach for mixed monolayer fabrication in Chapter 4 and will be used again in this Chapter to build long chain ferrocene monolayers.

There are two possible approaches to utilising the Sonogashira reaction at a surface, see Scheme 5.3. The first approach (Scheme 5.3a) makes use of an aryl/vinyl halide to modify the silicon surface, A1; this is then followed by coupling with a terminal alkyne to give the final surface A2. The second approach (Scheme 5.3b) makes use of a terminal alkyne to modify the silicon surface first, B1 then this modifed surface is coupled with the aryl/vinyl halide to give the desired surface, B2. Although both these methods are possible, reports in the literature only describe the first approach.[10,11,33] This seems logical given that the first alkylation step generally involves the formation of a Si-C bond with an alkene or alkyne group. Therefore, to generate an alkynyl terminated surface a diyne or equivalent (an ω-alkynyl, -alkene, -alcohol, -amine etc) is required with the alkyne group protected to prevent reaction at both ends with the silicon hydride surface. Overall, the generation of the alkyne surface followed by Sonogashira coupling, route (b), requires additional protection and deprotection steps and so becomes less attractive.

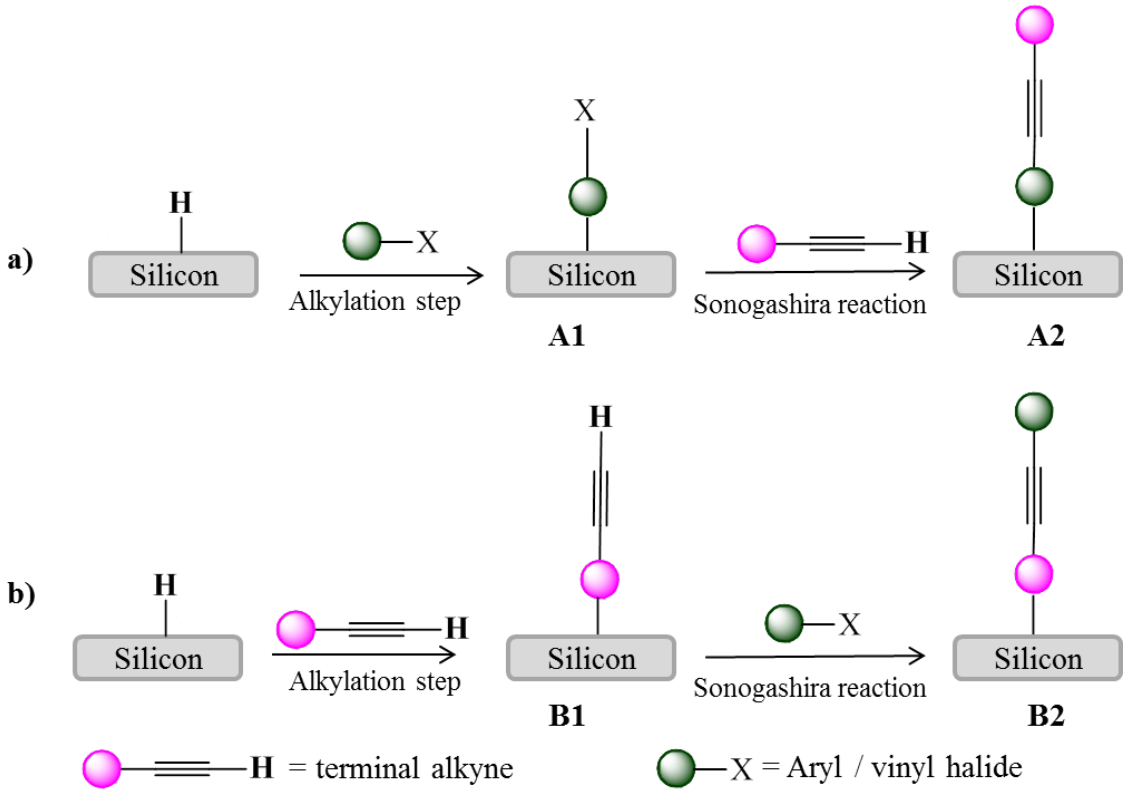

Scheme 5.3. Fabrication of modified silicon surfaces via Sonogashira coupling reactions by two approaches: a) modified silicon surface with aryl/vinyl halide (X) followed by coupling with terminal alkyne, b) modified silicon surface with terminal alkyne followed by coupling with aryl/vinyl halide (X).

The aryl/vinyl halide group used in the Sonogashira coupling on silicon surfaces is in most cases an iodine compound. The iodine containing monolayer is a better choice

than the bromine monolayer for Sonogashira coupling due to two main reasons. Firstly, the bromine derivative is less reactive than its iodine equivalent in a Sonogashira coupling reaction.[10] Moreover, bromine monolayers can form radicals more easily than the iodine equivalent and so could react with the silicon surface directly to form bromine-silicon bonds.[10] At present, three key studies in the literature discuss the modification of aryl-halide functionalised silicon surfaces by the Sonogashira coupling.[10,11,33] In one example, iodophenyl-terminated silicon (111) monolayers were formed by reaction between silicon hydride with 1-(allyloxy)-4-iodobenzene, see Scheme 5.4. Subsequently, conjugated molecules such as 1-ethynyl-4-fluorobenzene or 1-chloro-4-ethynylbenzene were coupled by the Sonogashira reaction at 60 ˚C for 4 h.[11]

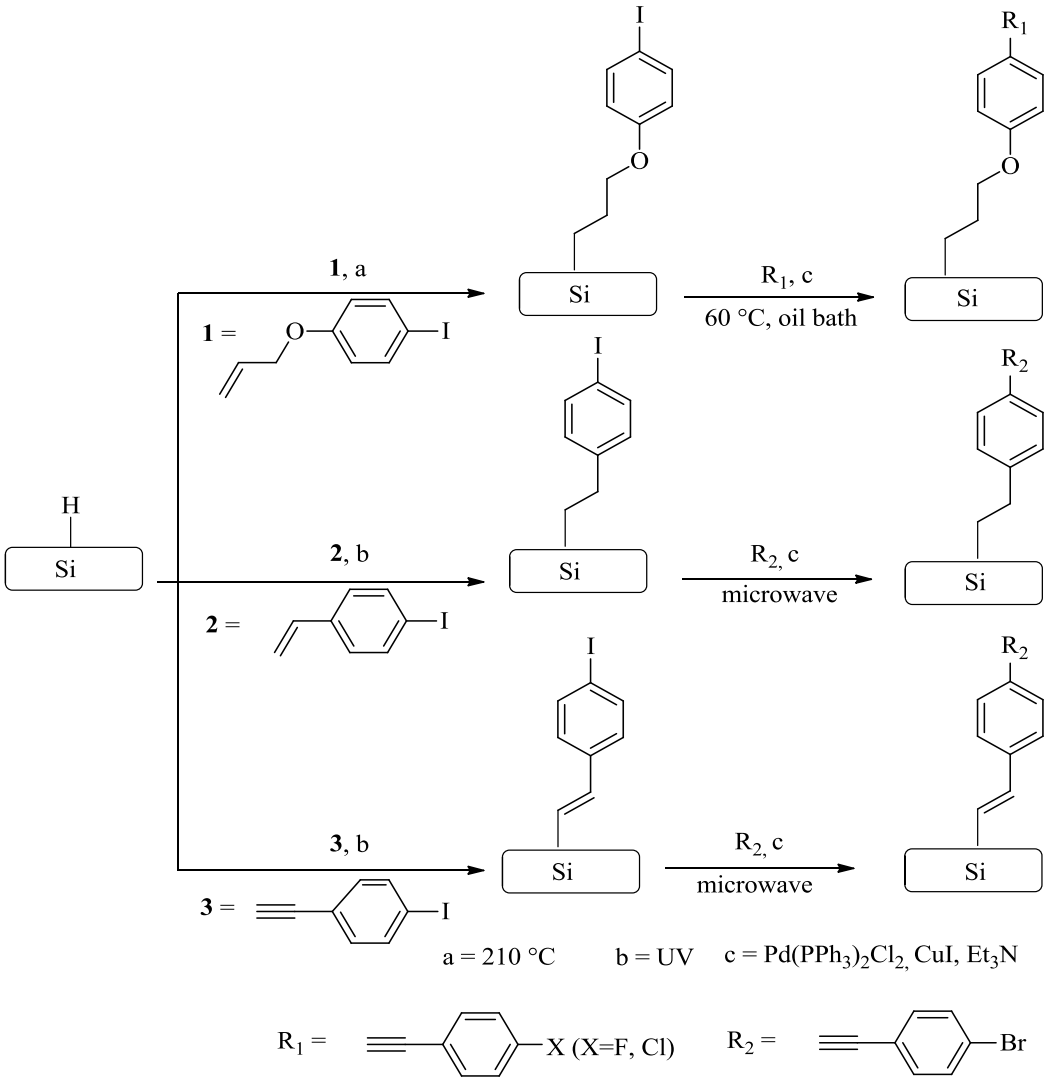

Scheme 5.4. The modification of silicon surfaces with iodo derivatives **1**, **2** and **3** by two methods, thermal (a), and UV (b), these were followed by Sonogashira coupling with R_1 and R_2 under thermal and microwave conditions respectively.

XPS analysis of the surfaces found that the yield of coupling the surface with 1-ethynyl-4-fluorobenzene was higher than the coupling with 1-chloro-4-ethynylbenzene, as seen

by a comparison of the I 3d peak before and after reaction. In other words, XPS spectra show the disappearance of the I 3d signal and the appearance of a new peak for F 1s, in the case of coupling with 1-ethynyl-4-fluorobenzene. Whereas, in the case of coupling with 1-chloro-4-ethynylbenzene, the XPS spectra show some remaining I 3d signal, which suggests that there is incomplete coupling during the reaction.[11] Moreover, in a second example, 4-bromophenylacetylene was covalently conjugated to an iodostyrene monolayer on a Si(111) surface in a microwave reactor at 40 °C (Scheme 5.4).[10] XPS studies indicated that the coupling of 4-iodostyrene with 4-bromophenylacetylene was not complete even after 2 h reaction times. In an additional study, Lin and co-workers reported the fabrication of a fully conjugated monolayer on silicon via mild microwave-assisted UV irradiation. p-(4-iodophenyl)acetylene was first immobilized on Si(111) surfaces, then subsequently coupled with p-(4-bromophenyl)acetylene. In this approach they reported an improved yield of 90 % after 2 h, (Scheme 5.4).[33] The third report was carried out by a group using the more conventional thermal method.[11]

These limited reports on Sonogashira coupling reactions to modify silicon surfaces focus on the development of a new synthetic strategy to assemble monolayers using the Pd-catalysed reaction to form an extended monolayer through a new C≡C bond. However, in each case, the reported surfaces were not investigated for further functionality. There is no report of ferrocenyl-modified silicon surfaces fabricated by the Sonogashira coupling reaction.

5.1.3 Step-wise approach used to generate ferrocenyl monolayer

Although ferrocenyl silicon surfaces have been reported in depth since the 1990s, there still is a growing interest in the routes to their fabrication and their complex electrochemical behaviour.[28] Commercially available vinylferrocene and ferrocene carboxaldehyde have been used to modify silicon surfaces by Decker and co-workers in a one-pot reaction.[8,9,34,35] In addition, longer alkyl chains of ferrocene have also been reported on silicon surfaces as monolayers formed by step-wise reactions. For example, a propylferrocene modified silicon surface was synthesised by white light activated hydrosilylation reaction between silicon hydride and allyl bromide. This was followed by another step using monolithioferrocene to couple to the terminal bromine as shown in Scheme 5.5a.[26]

Click chemistry was used to fabricate longer alkyl chains between the ferrocene and the silicon surface.[15-17,20,36] Ciampi *et al.* successfully reported a step-wise reaction on a

silicon (100) wafer in 2008.[16] This report described the modification of a silicon surface in two steps including the click reaction. A hydrosilylation reaction carried out between 1,8-nonadiyne and a silicon hydride surface was followed by the click reaction with an azido-ferrocene, see Scheme 5.5b.[16] Moreover, Ng and co-workers have also reported the synthesis of a covalent bond between azido-ferrocene and non-1-yne-8-ene via the 1,3-Huisgen cycloaddition click reaction see Scheme 5.5c.[15] Furthermore, two different research groups have synthesised C_{11}-azido ferrocene modified surfaces by a three steps approach. Initially, 11-halogen-1-undecene was used to produce a halogen terminated monolayer, this was followed by conversion of the halogen to an azide group and finally the click reaction with ethynylferrocene was performed,[20,36] as shown in Scheme 5.5d.

An alternative successful route was achieved by using a 1,3-diyne to generate a C_{11}-ferrocenyl linked silicon surface. Again two reaction steps were carried out, firstly, 1,8-nonadiyne was attached to the silicon surface and then followed by a acetylenic coupling reaction with ethynylferrocene (Scheme 5.5e).[17] Interestingly, a four-step reaction has also been successfully demonstrated, long ferrocenyl monolayers on silicon, both pure and mixed were fabricated by carbodiimide chemistry. An amine-substituted ferrocene derivative was used to assemble carboxylic acid monolayers via a stepwise reaction,[24] see Scheme 5.5f.

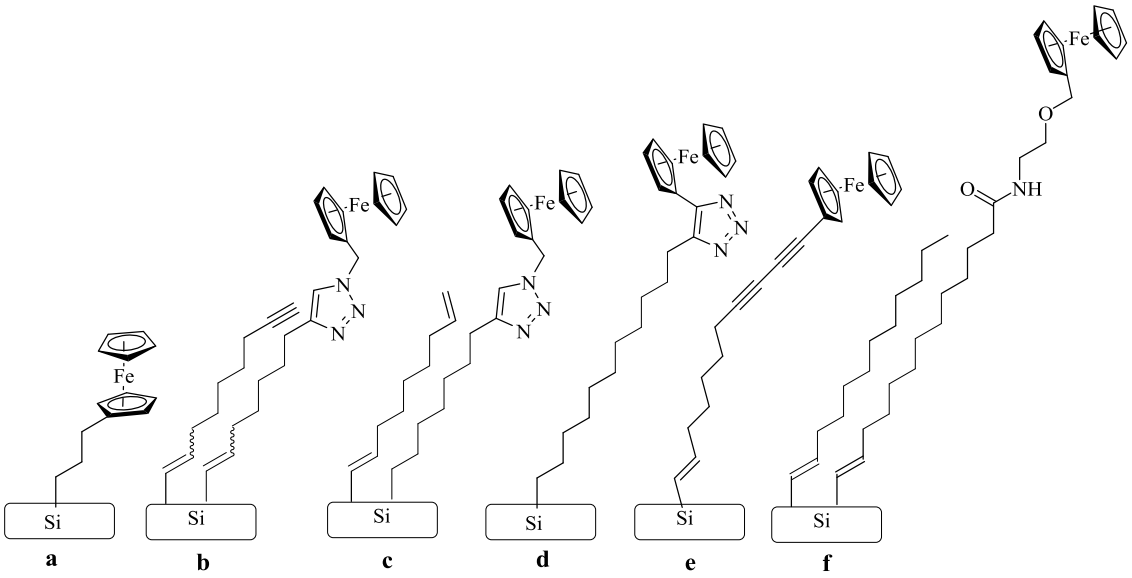

Scheme 5.5. Ferrocenyl silicon modified surface produce by step-wise strategy.

In light of these recent reports, this chapter will investigate the synthesis of fully conjugated alkyl chain linkages between ferrocenes and silicon surfaces. The linkage will be based on 1-alkynes because they have been found to be more reactive than

1-alkenes to form stable closely packed monolayers on silicon.[14,15,37] Also, it has been reported that the synthesis of conjugated electroactive molecules is problematic.[26]

Therefore, this chapter will describe the fabrication of fully conjugated electrochemically active ferrocene monolayers on silicon surfaces by hydrosilaylation chemistry. The approach taken involves two different strategies; a one-step strategy and a step-wise strategy. In both cases, 1-alkynes were used as the functional group to alkylate the silicon surface. Firstly, a conjugated ferrocenyl moiety (either 1-(but-1-en-3-yne)ferrocene or 5-iodo-3-ethyl-2-ethynylthiophene was synthesised, purified and characterised and then attached to the silicon surface in one-step. In the second step-wise strategy, 5-iodo-3-ethyl-2-ethynylthiophene was attached to the silicon surface before coupling with ethynylferrocene via the Sonogashira reaction**.**

5.2 Results and Discussion

Despite the range of possible chemistries for the covalent attachment of monolayers onto a silicon substrate,[14,15,20] in this work the alkyl ferrocenyl chain (linkage longer C_2) was immobilized by a thermal route via the hydrosilylation reaction. This is because thermal route gave the best coverage compared with the room temperature and nucleophilic substitution by acetylide anion approaches described in Chapter 2. In Chapter 3, mixed monolayers were also fabricated by the thermal route and again this was the method chosen to produce the extended ferrocenyl surfaces described in this Chapter. In order to fabricate a conjugated linkage between the silicon electrode and the ferrocene reported group two different routes were investigated. First, as outlined in Scheme 5.1a, the molecular synthesis of a ferrocene bearing an extended tether 1-(but-1-en-3-yne)ferrocene is then followed by the attachment of the complete unit to the silicon in a single surface reaction. Second, the silicon surface is modified with a compound that has two terminal active groups, a bifunctional interconnect molecule, (5-iodo-3-ethyl-2-ethynylthiophene). One active group (alkyne) reacts with the silicon to alkylate the surface and the other (iodothiophene) allows for further modification via the Sonogashira reaction to incorporate the ferrocene. The following section describes the synthesis of a ferrocene moiety bearing a long conjugated alkyl chain and its reaction with a silicon hydride surface. In addition, the synthesis of an iodothiphene unit bearing an alkyne group, its reaction with a silicon surface, and its subsequent coupling with ethynylferrocene are described.

5.2.1 Synthesis 1-(but-1-en-3-yne)ferrocene, 2.

1-(but-3-en-1-yn-1-trimethylsilane)ferrocene, **1** was synthesised from ferrocene carboxaldehyde according to the procedure reported by Lin and co-worker.[38] Purification proved difficult and the pure TMS protected compound **1** was isolated in 31% yield after column chromatography, see Scheme 5.6.

The TMS protecting group of (3-trimethylsilyl-2-propynyl)triphenyl phosphonium bromide is required to avoid removal of the terminal acetylene hydrogen instead of the desired deprotonation of the carbon to the triphenyl phosphonium bromide group. Compound **1** was deprotected with tetrabutylammonium fluoride in 1.0 M THF.

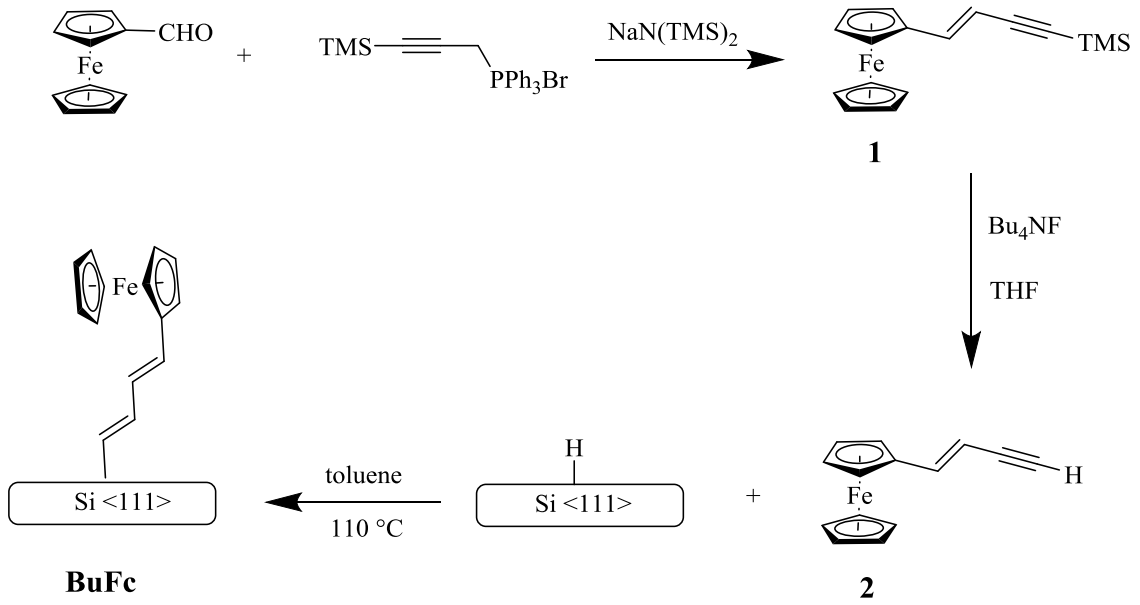

Scheme 5.6. Synthesis and deprotection of 1-(but-3-en-1-yn-1-trimethylsilane)ferrocene, and formation of modified silicon surface **BuFc** surface by alkylation Si-H with compound 2 in toluene overnight.

Compounds **1** and **2** were fully characterised by ^{1}H NMR, ^{13}C NMR spectroscopy and ESI-MS, see experimental section. The ^{1}H NMR in $CDCl_3$ shows that compound **2** exhibits a vinyl proton signal at 6.84, and 5.73 ppm with a *J*(HH) coupling constant of 16.1 Hz, which is comparable to the vinylic protons of vinylferrocene (15.6 Hz) and indicative of trans geometry.[38] The purified **2** was a brown oil that was then used for the fabrication of the ferrocene silicon surfaces, **BuFc,** according to the methods discussed below.

5.2.2 Fabrication of 1-(but-3-en-1-yn)ferrocene modified silicon surface, BuFc.

Single crystal silicon was prepared according to procedure outlined in Chapter 2.[39,40] Compound **2** was attached to the hydrogen-terminated silicon surface by thermal alkylation in toluene at reflux overnight.[41] The modified silicon surface **BuFc** is designed to provide an extended conjugated linkage between the bulk silicon and the ferrocene group, where the terminal alkynyl group of **2** is reduced during hydrosilylation to provide a Si-CH_2=CH_2- linkage.[16,19,20] Surface **BuFc** was characterised by AFM, XPS and was also investigated electrochemically by CV.

5.2.3 Synthesis of 5-iodo-3-ethyl-2-ethynylthiophene, 4

Compound **3,** see Scheme 5.7, was previously synthesised by a former PhD student as part of a different project.[42] The alkynyl group was once again protected by TMS and had to be removed before the reaction with silicon could be attempted. In this case, the simple removal of the TMS group by potassium carbonate in methanol was completed in high yield (80 %) to give pure compound **4**, as outlined in Scheme 5.7. Compound **4** was characterised ^{1}H NMR spectroscopy, ^{13}C NMR spectroscopy and ESI-MS spectroscopy, see experimental section.

5.2.4 Synthesis of thiophene-ferrocene silicon surface, TpFc

Whereas the fabrication of surface **BuFc** only requires one surface reaction (alkylation of Si-H with **2**), the route towards the fabrication of surface **TpFc** involved two surface reactions. The first step requires reaction between **4** and freshly etched silicon hydride surface to give the thiophene surface **Tp**. The second step is a Sonogashira cross-coupling reaction between **Tp** and ethynylferocene in the presence of Pd as catalyst to produce surface **TpFc**.[11,31] The silicon modified surfaces **Tp** and **TpFc** were characterised by AFM, XPS and for surface **TpFc** electrochemically investigated by CV.

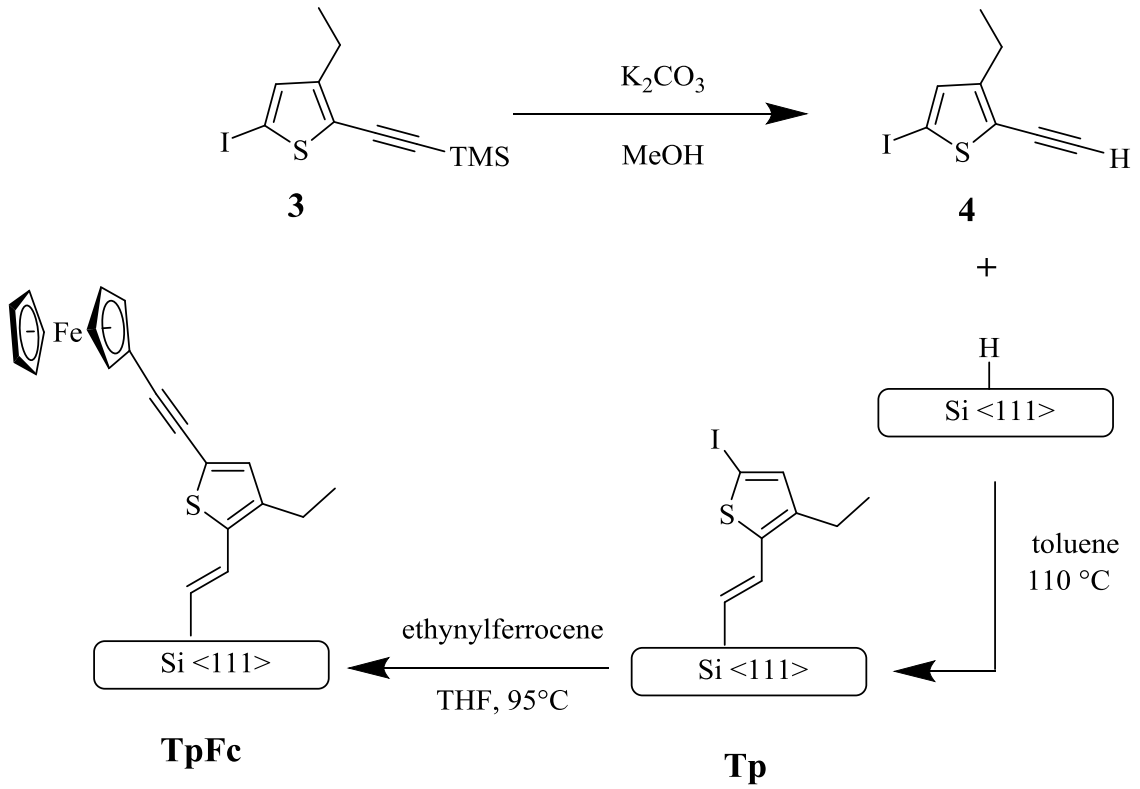

Scheme 5.7. Deprotection of 5-iodo-3-ethyl-2-ethynylthiophene **4,** compound **4** was used as a linkage to modify silicon surface by thermal hydrosilylation to give **Tp** surface. **Tp** surface was coupled with ethynylferrrocene by Sonogashira reaction (copper (I) iodide, tetrakis(triphenylphosphine)palladium(0) and diisopropylamine at 95˚C) to give **TpFc**.

5.2.5 Characterisation by atomic force microscopy

The AFM images obtained from a silicon sample before and after modification with **2** and **4** and coupling of **Tp** with ethynylferrocene to give surfaces **BuFc**, **Tp** and **TpFc**, respectively, are shown in Figure 5.1.

AFM images of the modified surfaces show some minor differences in their topography. The AFM of a fresh silicon hydride surface (Figure 5.1a) clearly shows the terrace and step edges in a triangular pattern which is attributed to oxidation of the silicon as the AFM measurement was carried out in atmospheric conditions.[26] The AFM image of **BuFc** (Figure 5.1b) shows a dirty surface but careful inspection reveals feint indications of the underlying silicon terraces. It is also possible that these large irregular protrusions are caused by polymerisation of the conjugated ferrocene on the surface. On the other hand, the **Tp** surface was relatively clean and the expected terrace/step topology can be clearly seen, Figure 5.1c. After performing the Sonogashira reaction at the surface, coupling with ethynylferrecene to give the **TpFc** surface, once again the AFM image

shows the terrace and step edge structures and was clean as seen in Figure 5.1d. This was surprising as the Pd catalyst and other ligands used in the coupling reaction to produce the **TpFc** surface could be expected to contaminate the surface.

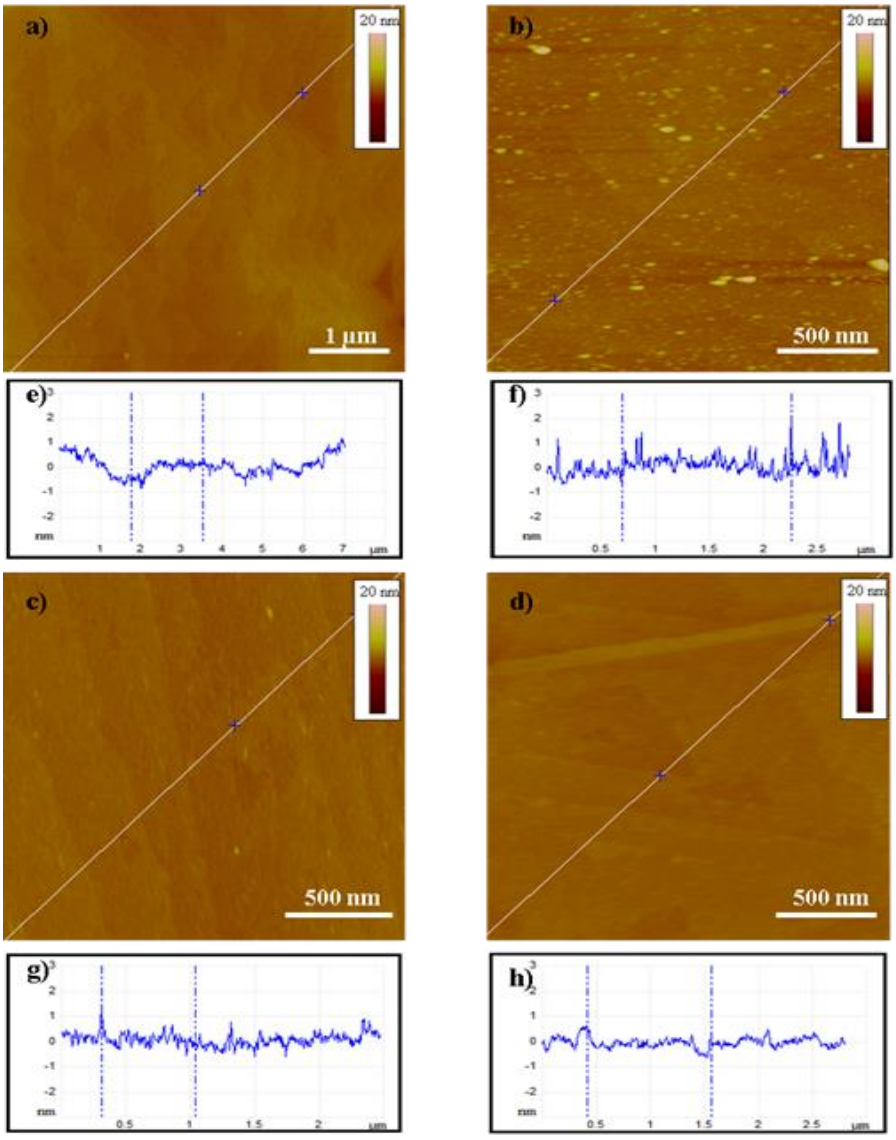

Figure 5.1. AFM tapping images of n-**Si(111)-H** (a), **BuFc** (b), **Tp** (c), and **TpFc** (d). Corresponding linear cross-section profile analysis are shown in e, f, g, and h and were taken along the marked segments for the AFM image a, b, c, and d respectively.

The roughness of these surfaces were measured using the NanoScope AFM software. Surfaces **Tp** and **TpFc** are more homogeneous than surface **BuFc** as shown in Table 5.1, as expected from simple inspection of the AFM images. The highest recorded surface roughness of surface **BuFc** is twice that of the other surfaces and this data supports the belief that the extended conjugated alkyl linkage is likely to polymerise at raised temperatures and so form aggregates on the surface during thermal hydrosilylation.

Surfaces **Tp** and **TpFc** however, have similar roughness data to the silicon hydride surface and suggests that homogenous monolayer formation has been achieved.

Surface	**Si-H**	**BuFc**	**Tp**	**TpFc**
rms (nm)	0.19	0.40	0.20	0. 19

Table 5.1. The rms roughness recorded over an area of average 0.5×0.5 μm^2 for the monolayers Si-H, **BuFc**, **Tp**, and **TpFc** surfaces. These values an average value determined from several different measurement.

5.2.6 Characterisation by X-ray photoelectron spectroscopy

The silicon surface reactions illustrated in Scheme 5.6 and Scheme 5.7 were verified by X-ray photoelectron spectroscopy and the chemical changes were monitored after each step.

The XPS of the **BuFc** monolayer was carried out to determine the elemental composition of the modified silicon surface. The survey spectrum in Figure 5.2 shows characteristic peaks from the silicon substrate itself (Si 2s, Si 2p) and from the C 1s, O 1s, and Fe 2p core levels of the surface attached ferrocene molecule.

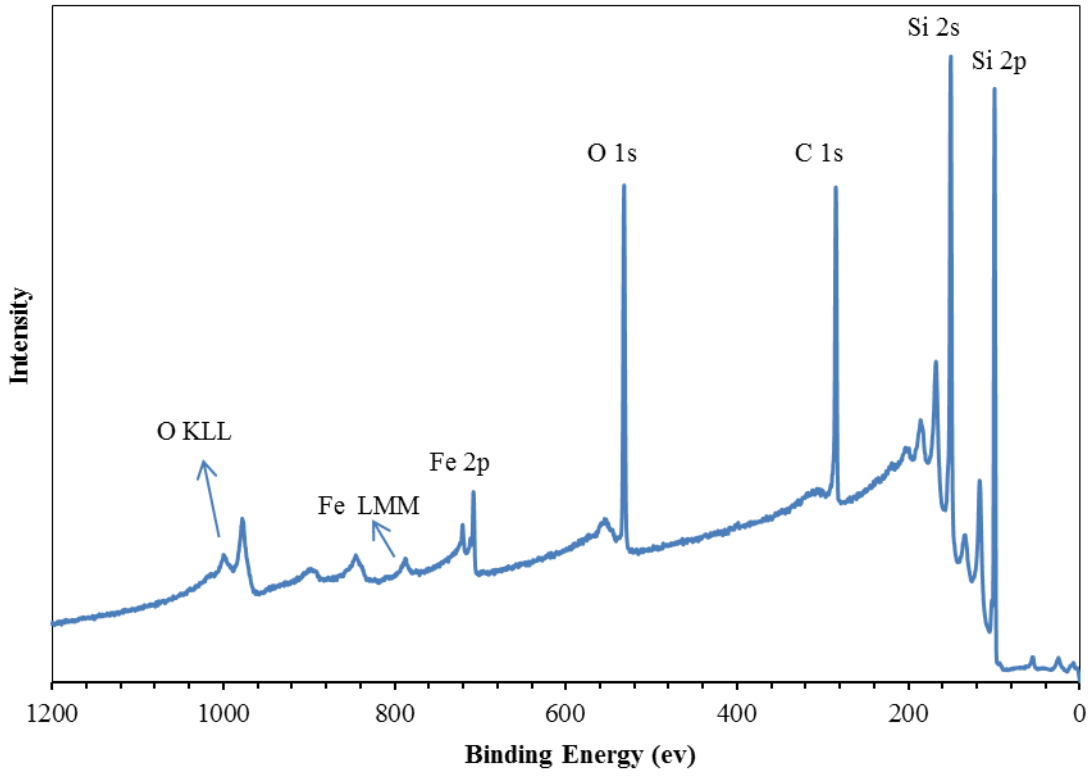

Figure 5.2. Survey X-ray photoelectron spectrum of the BuFc surface.

The high resolution Fe 2p peak (Figure 5.3a) shows that Fe is present in two oxidation states, (II) and (III). The Fe(II) component peaks are more dominant than the Fe(III) peaks even though the reaction proceeded for over 20 h. This is contrary to the findings in a previous report,[43] where for the reaction of vinylferrocene with a hydrogen-terminated Si(111) substrate, the intensity of the Fe(II) peak is only higher than the Fe(III) peak up to reaction times of 10 h. The decrease in intensity of the Fe(II) peak is due to oxidation to Fe(III) over extended reaction times.[43] Here, the **BuFc** monolayer shows that the intensity of the Fe(II) peak is considerably greater that the Fe(III) peak. This suggests that even after a reaction time between 15-20 h, there is considerably less oxidation than in previous reports,[43] as shown in Table 2. Curve fitting of the Fe 2p peaks was set to separate the two expected ions Fe(II) and Fe(III), and the calculation indicated a total of eight components. The presence of the Fe 2p doublet at 708.0 eV (Fe $2p_{3/2}$) and 720.8 eV (Fe $2p_{1/2}$) can be attributed to the ferrocenyl Fe(II).[25,40-42] Whereas, Fe(III), the ferrocenium salt, was also evident from the additional doublet observed with binding energy at 711.3 eV (Fe $2p_{3/2}$) and 723.9 eV (Fe $2p_{1/2}$).[26,43-45] The reason for oxidation is likely to be due to the fact that the potential of the O_2/H_2O redox couple is slightly more positive than the potential of the ferrocinium/ferrocene couple, and any remaining oxygen in the reaction could therefore oxidize the ferrocenyl groups.[43,46] The remaining doublet peaks 715.0 eV (Fe $2p_{3/2}$) and 727.8 eV (Fe $2p_{1/2}$) are attributed to shake up satellites of Fe(II), and shake up satellites of the Fe(III) appear at 718.3 eV (Fe $2p_{3/2}$), 731.0 eV (Fe $2p_{1/2}$). These finding are consistent with previous literature reports.[26,43-45]

The high resolution C 1s signal can be decomposed into five components as shown in Figure 5.3b, a small components at 283.3 can be assigned to Si-*C*=C.[37] The large peak at 285 eV can be attributed to the carbon atoms of the butylferrocene and any hydrocarbon contamination.[24,47] Other component at 286.1, 287.2 and 288.7 eV can be attributed to contamination of carbon species during washing and cleaning steps.

The high-resolution spectrum of the Si 2p peak was fited with doublet of Si $2p_{3/2}$ and $2p_{1/2}$ as shown in Figure 5.3c. Curve fitting of Si 2p can be split to three different environments, of binding energies 99.4 eV, 99.7 eV and 102.8 eV corresponding to Si $2p_{3/2}$, bulk Si atoms, the Si–C bond and silicon oxide respectively. Other peaks correspond to $2p_{1/2}$ levels.[44,48]

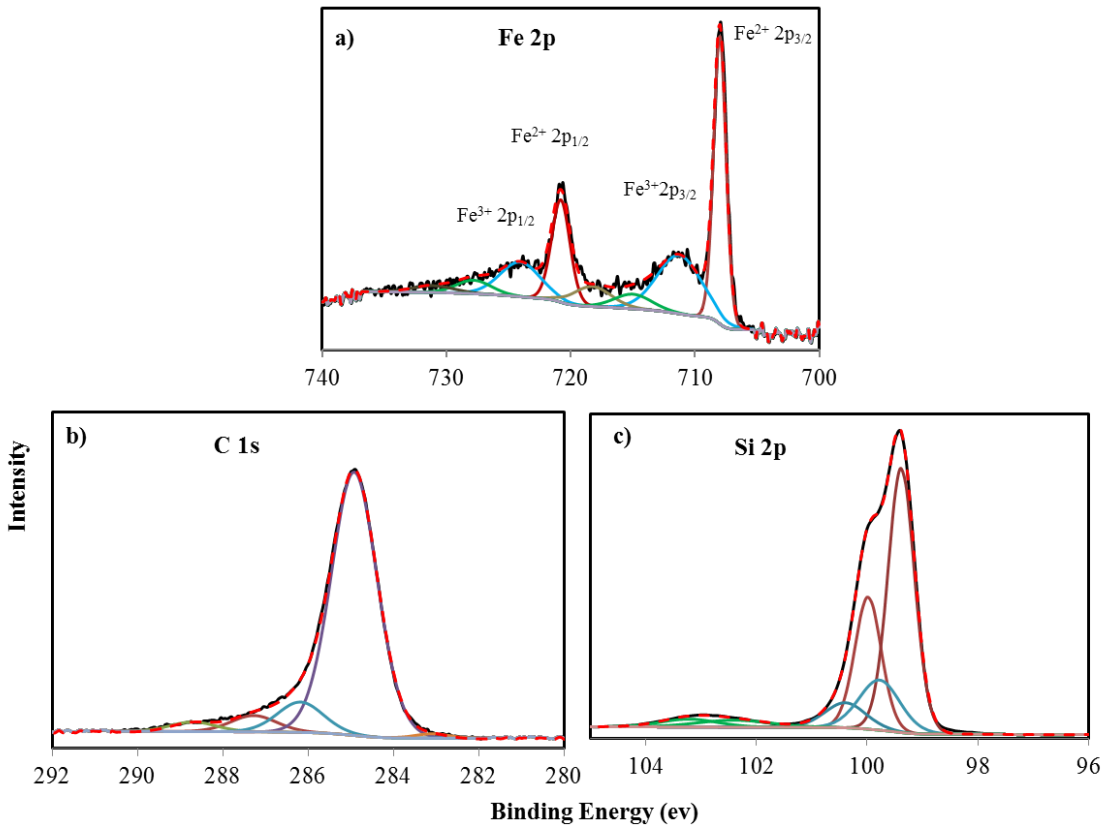

Figure 5.3 XPS of the **BuFc** surface a) Fe 2p region, b) C 1s regions and c) Si 2p regions for the experimental spectra are shown in black line, while curve-fit separated components are shown in red dash.

The alternative two-step strategy towards silicon modification was also monitored by XPS after each surface reaction. Figure 5.4 shows a comparison of the XPS survey spectra of (a) silicon surface modified with **4**, to give **Tp** and (b) surface **Tp** after Sonogashira coupling with ethynylferrocene to give **TpFc**. Both XPS spectra clearly show Si 1s, Si 2p and C 1s signals. It was confirmed that the silicon hydride surface has been alkylated with 5-iodo-3-ethyl-2-ethynylthiophene (**4**) due to the appearance of two peaks from the I 3d component in the XPS spectra (Figure 5.4a) between 619.4-631 eV. There is also the S 2s signal from the thiophene at 230 eV. The present finding is in reasonable agreement with other research which found the appearance of a I 3d signal at 619.3 eV and 630.8 eV, when a hydrogen–terminated silicon surface was alkylated with 1-(allyloxy)-4-iodobenzene.[11] Sonogashira coupling of ethynylferrocene with the **Tp** surface gave the **TpFc** surface. The most interesting finding in the survey scan was the appearance of a new peak, corresponding to Fe between 707 and 725 eV as shown in Figure 5.4b. This suggests the incorporation of the ethynylferrocene into the monolayer. Another important finding was that the XPS spectrum showed a major reduction, and in some instances total loss in the intensity of the I 3d signal. This suggests that the iodo-

thiophene has reacted fully (or sometimes depending on the particular surface studied, only partially reacted) with ethynylferrocene during the Sonogashira coupling. Previous reports of Sonogashira reactions monitored by only indicated the partial replacement of the iodine from the monolayer.[10,11]

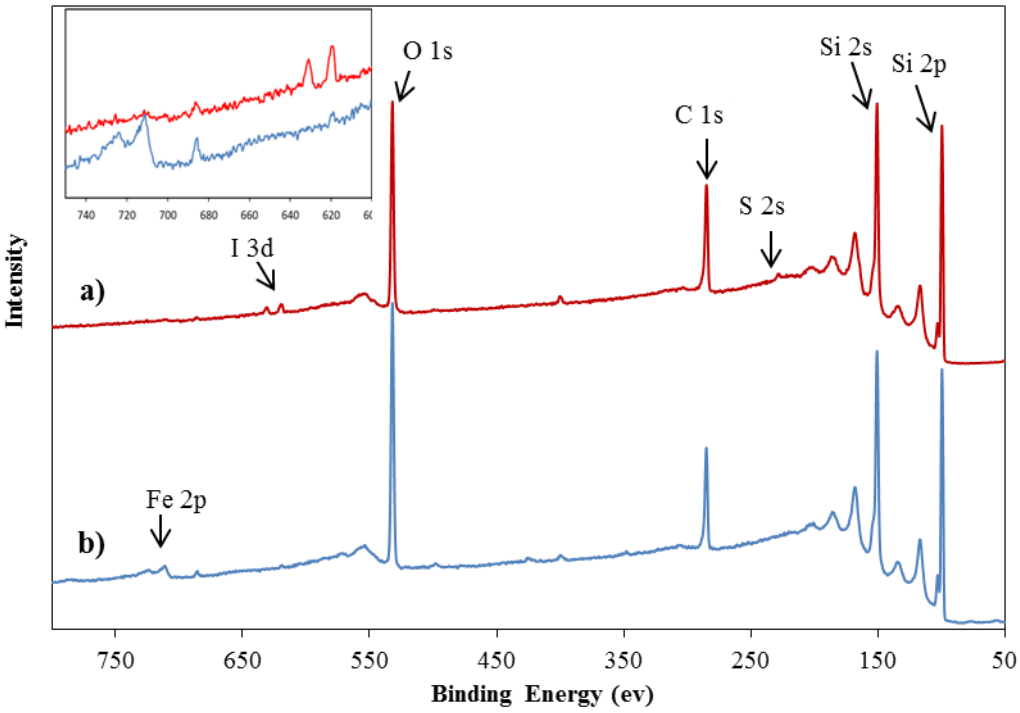

Figure 5.4. Survey X-ray photoelectron spectra of the a) **Tp** surface and b) **TpFc** surface.

Details about the oxidation state of these components were taken from the high-resolution spectrum of the I 3d signal (Figure 5.5).

The high-resolution I 2d peak (Figure 5.5a) shows that iodine is present in two oxidation state. Curve fitting of I 2d showed doublet peaks at 619.8, and 630.9 eV, attributed to I $3d_{5/2}$ and I $3d_{3/2}$ respectively. The present finding is reasonable agreement with other iodoaromatic monolayers, such as 1-(allyloxy)-4-iodobenzene[11] and iodostyrene[10] monolayers, which should appearance of a I 3d signal appear at 619.3 and 630.8 eV.[11]

The high-resolution spectrum of the C 1s single of the **Tp** surface, can be split into five components at 283.3, 285, 286.4, 287.7 and 289.0 eV, see Figure 5.5b. The small component at 283.3 eV can be assigned to Si-C=C,[37] Whereas, the large peak at 285 eV can be attributed to the carbon atoms of the thiophene and hydrocarbon contamination.[24,47] The peak at 287.2 eV can be attributed to C-S in thiophene.[49] Other

components at 286.1 eV and 288.7 eV can be attributed to contamination of carbon species or solvent during washing and cleaning steps.

Curve fitting of Si 2p peaks from the **Tp** surface, Figure 5.5c, can be split into three different oxidation states, at binding energies of 99.4 eV, 99.7 eV and 102.8 eV corresponds to Si $2p_{3/2}$, corresponding to bulk Si atoms, the Si–C bond and silicon oxide, respectively. Other peaks correspond to the $2p_{1/2}$ levels. This is slightly shifted compared to than previous literature reports.[44,48]

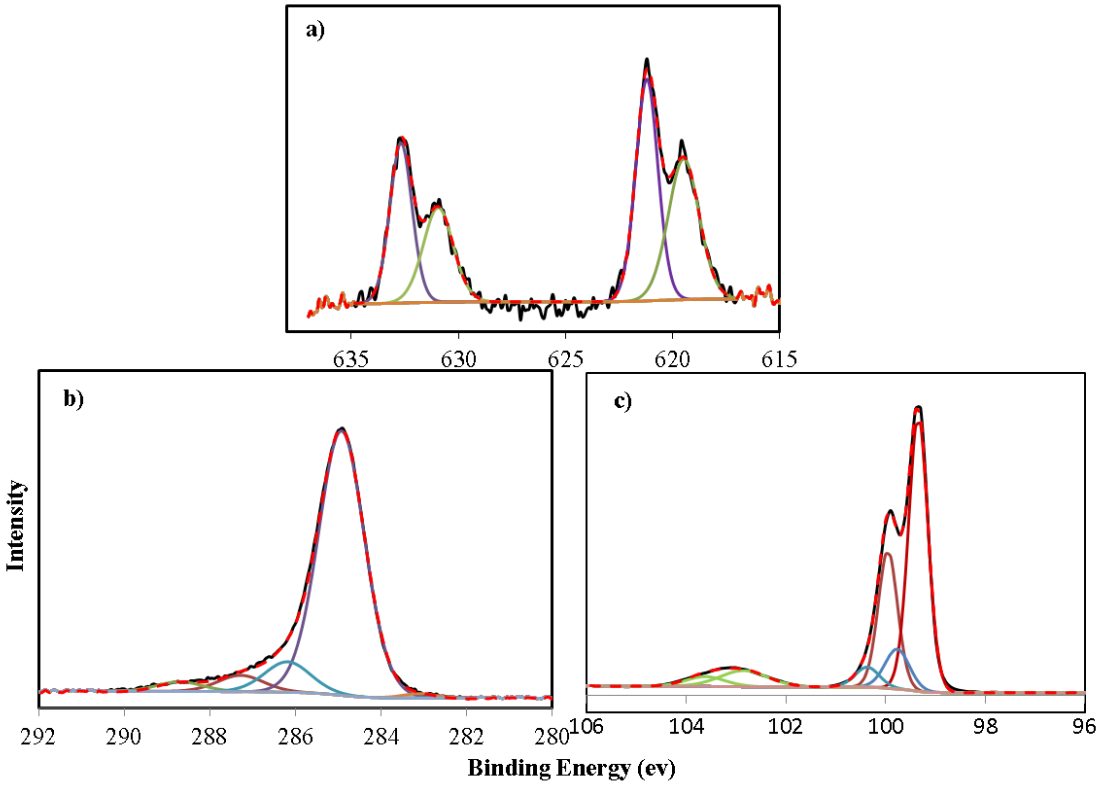

Figure 5.5. XPS of the **Tp** a) I 3d region, and b) C 1s regions and c) silicon region for **Tp** surface the experimental spectra are shown in black line, while curve-fit separated components are shown in red dash.

After Sonogashira coupling reaction of the **Tp** surface with ethynylferrocene, the **TpFc** surface was analysed by XPS. The high-resolution spectra of the Fe 2p region for partially and fully modified **TpFc** surfaces was examined, see Figure 5.6a,b respectively. The fitting suggests two chemical states corresponding to Fe(II) and Fe(III) in both cases. The Fe $2p_{3/2}$ and Fe $2p_{1/2}$ signals for both reactions are around 708 eV and 721 eV are due to the Fe(II) from the ferrocene. Likewise the Fe(III) doublet also presented for both reactions around 711.5 eV and 722.4 eV which were attributed to Fe $2p_{3/2}$ and Fe $2p_{1/2}$ respectively.[26,43-45] However, their relative abundances are dependent

of the completeness of the substitution during the Sonogashira reaction. The Fe(III) signals could be from the corresponding ferrocenium salt. The reason for oxidation could be due to residual oxygen in the reaction solvent.[43,46] Other peaks are attributed to shake up satellite signals and these findings are consistent with previous literature reports. [26,43-45]

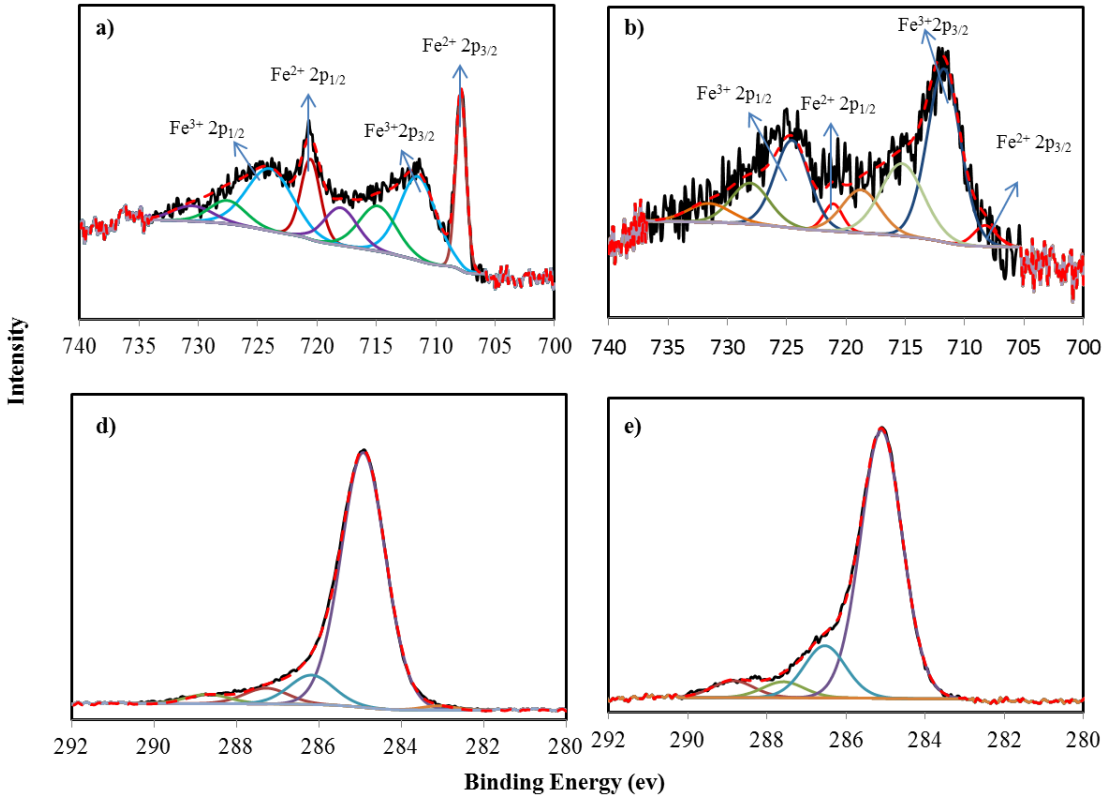

Figure 5.6. XPS of surface **TpFc** a) Fe 2p region for partial Sonogashira reaction with ethynylferrocene, b) Fe 2p region for complete Sonogashira reaction with ethynylferrocene reaction, c) Si 2p region for **TpFc**, and d) C 1s regions for **TpFc**. Experimental spectra are shown in black line, while curve-fit separated components are shown in red dash.

The main difference between the high-resolution fitting of the partially and fully reacted **TpFc** surfaces is in the ratio between Fe(II) and Fe(III). Figure 5.6a shows that the Fe(II) intensity is higher than Fe(III). Whereas Figure 5.6b shows that the intensity of Fe(III) is higher than Fe(II). This may be due to differences in the surfaces studied, as in the case of incomplete Sonogashira coupling most of the observed iron is in the Fe(II) form. However when the Sonogashira coupling was 100% effective the major iron component was from Fe(III). This suggests that in the complete Sonogashira coupling, Fe(II) is oxidised to Fe(III). It could be due to solvent was used in Sonogashira coupling, THF, has effect on oxidation of Fe(II) to Fe(III).[50]

Moreover, curve fitting of the high-resolution spectra of C1s of the **TpFc** surface shows five components at 283.3, 285, 286.2, 287.2 and 288.8 eV, see Figure 5.6d-e. A small component at 283.3 can be assigned to Si-C=C.[37] The large peak at 285 eV can be attributed to the carbon atoms of the thiophene-ferrocene and also hydrocarbon contamination.[24,47] Whereas, the peak at 287.2 eV can be attributed to *C*-S in thiophene.[49] Other components at 286.2 eV and 288.8 eV can be attributed to contamination from carbon species during washing and cleaning steps.

Surface	Fe(II) (eV) $2p_{3/2}$, $2p_{1/2}$	Fe(III) (eV) $2p_{3/2}$, $2p_{1/2}$	Fe/Si	C/Fe	Fe(II) /Fe(III)
BuFc	708.0, 720.8	711.3, 723.9	0.025	21	1.54
TpFc partial	707.8, 720.5	711.7, 724.5	0.012	21	0.61
TpFc complete	708.2, 721.9	711.5, 723.9	0.015	26	0.50

Table 5.2. Values of binding energy for relative atomic ratios for the **BuFc** surface and both partial and fully modified **TpFc** surfaces.

The XPS data shown in Figure 5.4 were collected at normal emission. Additional data can also be collected at grazing emission, where the electrons detected have escaped from much shallow depths, therefore increasing the surface sensitivity. By comparing spectra under these two conditions, one can draw information about the relative depth of chemical species in a surface. This is achieved by a stratification plot as demonstrated in Figure 5.7 generated from the wide-scan XPS spectra. This plot presents the relative depth of each species as the centre of a grey box, and the relative intensity (i.e. amount) of the species is given by the area of the box. The plot in Figure 5.7 simply shows the substitution of the iodo group on the **Tp** surface with the ferrocene group on the **TpFc** surface, seen by the change in iodine and iron peak intensities. Angle-resolved XPS studies presented in Figure 5.7 also show that the ferrocene group is found deeper towards the surface than the iodo group after Sonogashira coupling. This is unexpected and could be due to the ferrocene being bent towards the silicon surface. Relative amounts of these materials are also found to be similar for surfaces **Tp** and **TpFc**.

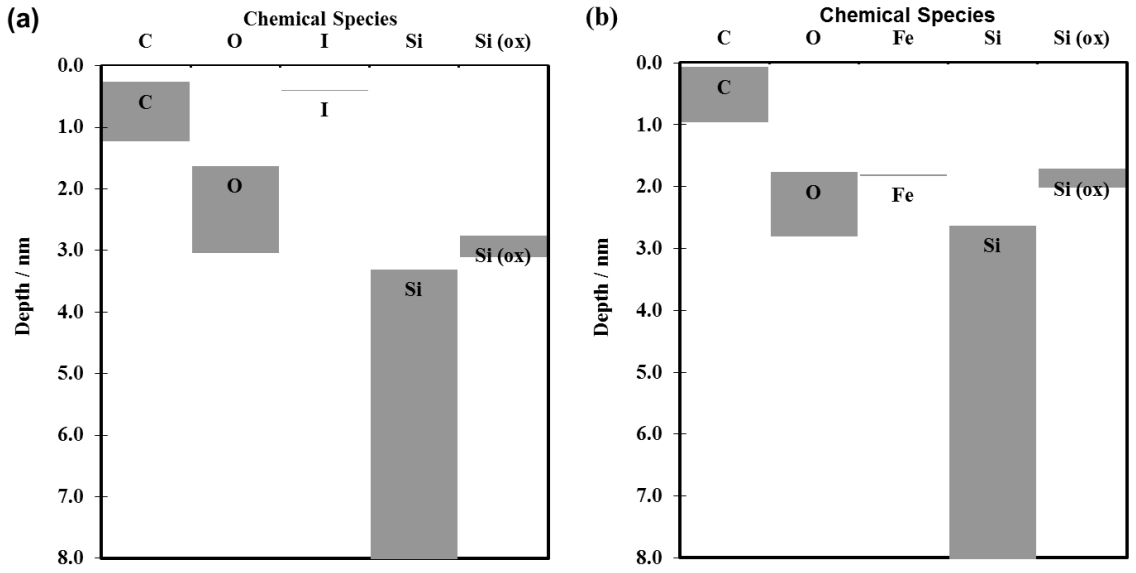

Figure 5.7. Stratification plots generated from ARXPS data of (a) the **TP** surface (b) the **TPFc** surface. The depth of the boxes in the plots indicate the average depth at which the chemical signal was detected, while the area of the boxes indicates the relative quantity of the chemical species.

In comparison to the **BuFc** surface, the observed ferrocene content for both **TpFc** surfaces appears to be considerably less after the two-step modification approach. The atomic ratio of Fe/Si for **BuFc** was twice that of **TpFc**. This is summarised in Table 5.2 and is not unexpected due to the disruption in the packing of the monolayer over two modification steps (supported by CV in next session). Naturally the fully coupled **TpFc** surface shows a higher Fe/Si ratio than the partial coupled surface. In addition, the ratio of Fe(II) to Fe(III) is higher for **BuFc,** over the two-step modified surfaces. In a comparison between the partial and fully Sonogashira coupled surface, the Fe(II) component is higher than Fe(III) for the partial coupling, but the Fe(III) component is higher than Fe(II) for the fully coupled surface. The expected atomic ratio of C/Fe for theses surfaces is 14, and 20 for **BuFc** and **TpFc** respectively. The values obtained from the XPS studies however show an increase in this ratio which again is likely to be due to additional surface contamination by carbon containing species.

5.2.7 Characterisation by cyclic voltammetry

CVs of **BuFc** and **TpFc** were recorded using 0.1 M $LiClO_4$ in acetonitrile as an electrolyte solution and sliver and tungsten wires as reference and counter electrodes respectively. Figure 5.8 shows the voltammetric response of a silicon surface modified with compound **2**, **BuFc,** with a formal redox potential of 59 mV, other key parameters are summarised in Table 5.3.

The peak separation between the anodic, 137 mV, and cathodic, -20 mV peaks for the **BuFc** surface was 157 mV at 1 V s^{-1} (see Figure 5.8). Although this peak separation is unexpected, it is less than other reported values. For a propyl ferrocene modified silicon surface, peak separations of 150 mV and 210 mV for scan rates of 0.25 V s^{-1} and 0.1 V s^{-1} respectively were reported.[26] The big separation also could be due to the IR drop across the electrical contact on the back of the silicon.[43]

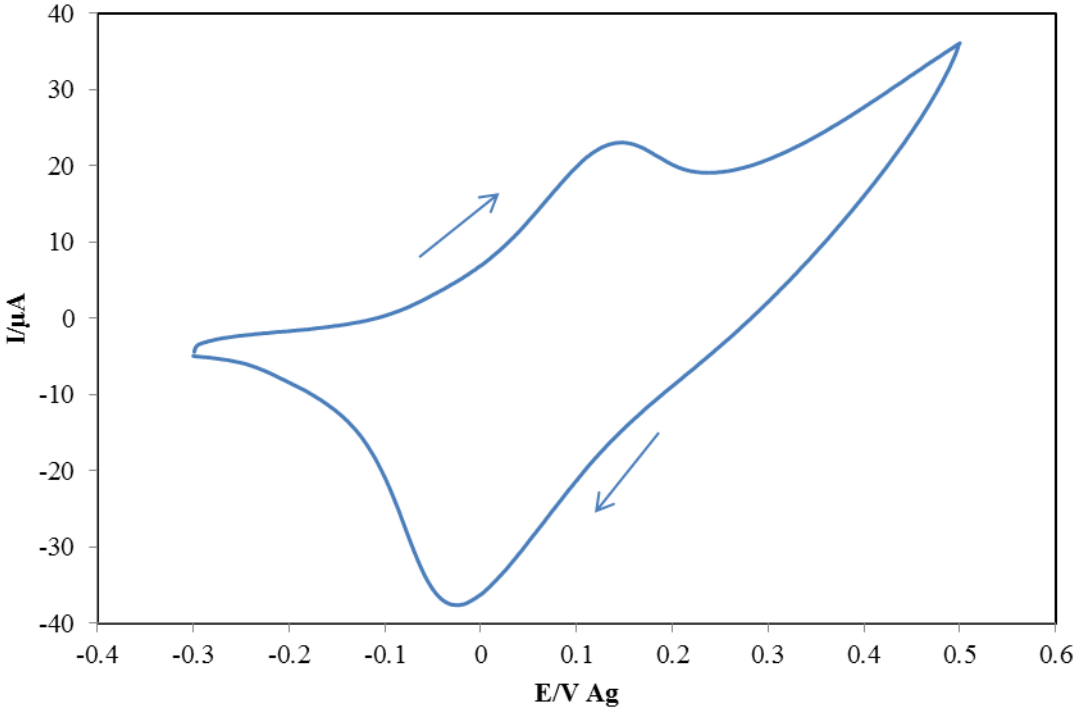

Figure 5.8. CVs recorded using a modified silicon surfaces **BuFc** as the working electrode. The silicon electrode was immersed in acetonitrile containing 0.1 M $LiCLO_4$ under illumination during the recording of the voltammogram at scan rate 1V s^{-1}. Arrows indicate the scan direction.

As the CV was recorded under illumination and the acetonitrile electrolyte was not fully dry and may have oxygen present in the solution, oxidation of the silicon surface can be expected, as seen by the rising background at positive potentials, see Figure 5.8. Integration of the anodic peak from the voltammogram gave an estimation of the ferrocenyl surface coverage to be 6.25×10^{-11} mol cm^{-2}. However, the integration of the cathodic peak from the same voltammogram gave an estimation of the surface coverage to be 2.23×10^{-10} mol cm^{-2} (theoretical calculation explained in chapter 3), see Table 5.3. The difference between the coverage obtained from the anodic and cathodic peaks (the unsymmetrical shape of the CV) is likely to be due to the effect the variation in light intensity has on the oxidation peak through the n-type silicon substrate.

The redox behaviour of **BuFc** was recorded at different scan rates see Figure 5.9. These voltammograms show an increasing anodic current as the scan rate increases. The insert in Figure 5.9 confirms that this relationship is linear and indicates that the ferrocene has been attached to the silicon surface and is stable. The separation between the oxidation and reduction potentials (ΔE_p) increases as the scan rate increases. This scan-rate dependence of the peak separation can be explained by a slower electron-transfer rate from the redox centre to the silicon substrate through the longer linker. Indeed, the presence of this linker hampers the electron transfer and when the scan rate is increased, it becomes too fast for the electrons to overcome the linker tunnel barrier and therefore higher potentials are required for electron transfer to occur at an appreciable rate.[20] It could have a contribution from the IR drop across the electrical contact on the back of the silicon.[43]

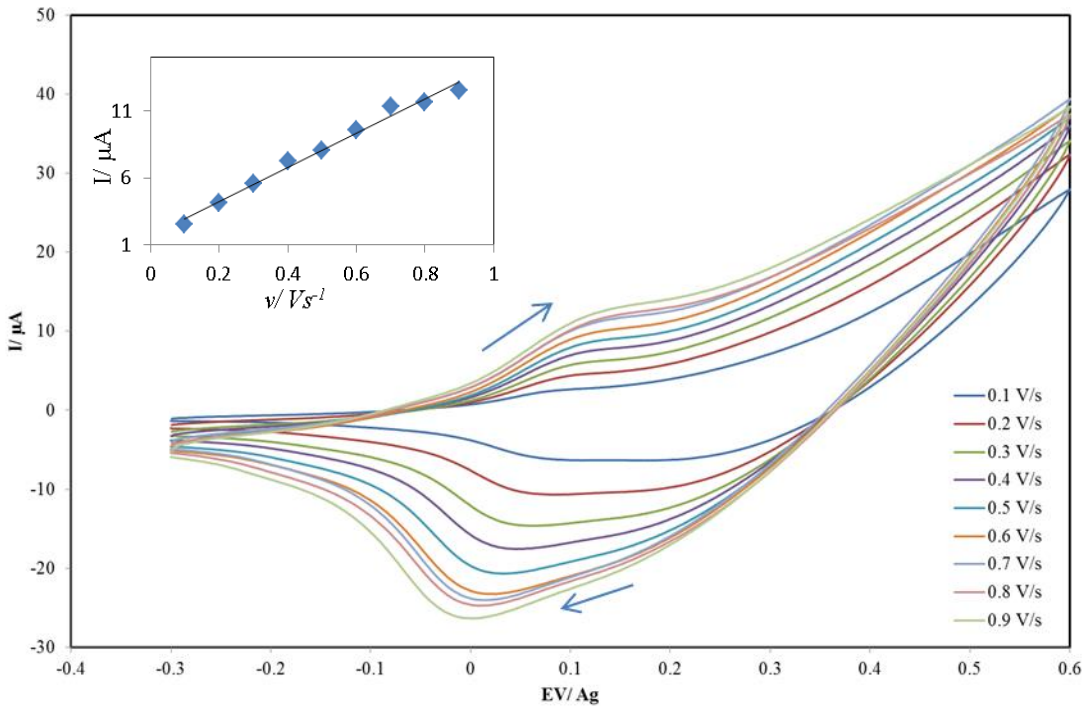

Figure 5.9. CVs recorded using modified silicon **BuFc** as the working electrode. The silicon electrode was immersed in acetonitrile containing 0.1 M $LiCLO_4$ under illumination during the recording of the voltammogram at different scan rate. The linear dependency of peak current on scan rate is shown as insets. Arrows indicate the scan direction.

Figure 5.10 shows the voltammetric response of the modified silicon surface **TpFc** under the same conditions. The CV was recorded only at a scan rate of 1 V s^{-1} due to the difficulty in recording data at low scan rates. Similarly, the **TpFc** monolayer exhibited a formal reversible redox response at 58 mV versus silver at 1 V s^{-1}. The anodic and

cathodic peaks were are 119 mV and -4 mV respectively giving a peak separation of 123 mV.

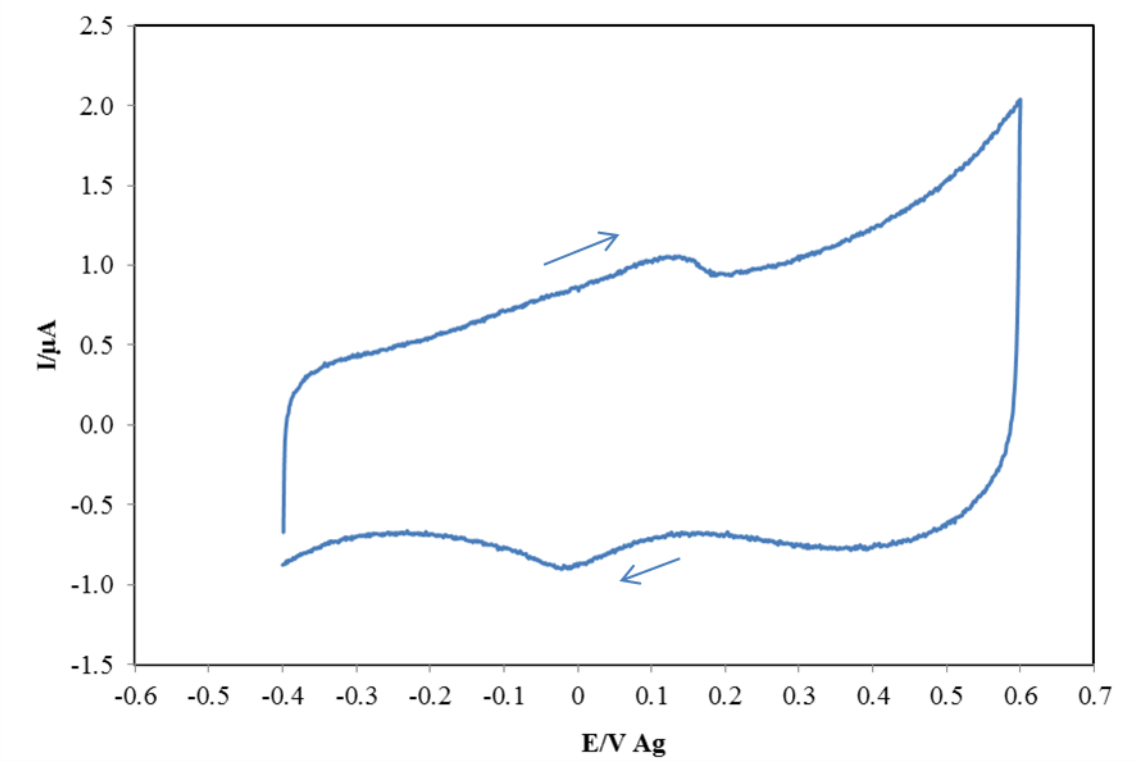

Figure 5.10. CVs recorded using modified silicon **TpFc** as the working electrode. The silicon electrode was immersed in acetonitrile containing 0.1 M $LiClO_4$ under illumination during the recording of the voltammogram at scan rate 1V s^{-1}. Arrows indicate the scan direction.

Surface	ΔE_p (mV)	E_p^A	E_p^C	E° (mV)	coverage/mole cm $^{-2}$
BuFc	159	137	-20	58.5	Oxd 6.25×10^{-11} Red 2.23×10^{-10}
TpFc	123	119	-4	57.5	7.2×10^{-12}

Table 5.3. The electrochemical properties of modifier silicon surface **BuFc** and **TpFc**.

The surface coverage data obtained from CV show that the one-step reaction (**BuFc** surface) yields higher ferrocene coverage than the step-wise reaction (**TpFc** surface). This may be due to not all of the silicon hydride sites being alkylated with thiophene, as it is impossible to get 100% coverage for thiophene derivative which have a diameter > 4.8 Å, as discussed in Chapter 3.[2,19,24] The second reaction, coupling with ethynylferrocene, is also unlikely to yield 100% modification and so it is expected that the overall coverage will be significantly reduced. It could also be due to the fact that

the ferrocene bends towards the silicon surface, as suggested by XPS, which could effect in the packing of monolayer.

5.3 Conclusions

In this chapter, efforts to build longer conjugated linkages (> C_2) between the ferrocene and silicon surface were successfully prepared, by synthesis of two different linkages 1-(but-1-en-3-yne)ferrocene and (5-iodo-3-ethyl-2-ethynylthiophene). 1-(but-1-en-3-yne)ferrocene was attached as a complete unit to the silicon surface in one step to give the **BuFc** surface. Whereas, a bifunctional interconnect molecule, (5-iodo-3-ethyl-2-ethynylthiophene) was reacted with the silicon hydride substrate to alkylate the surface and then was followed with further modification via the Sonogashira reaction to incorporate ferrocene to give **TpFc** surface. Then these surfaces (**BuFc, TpFc)** were characterised by AFM, XPS and CV. One-step reaction (**BuFc**) showed better coverage than the two-step reaction (**TpFc**). The ferrocenyl coverage of **BuFc** surface was 6.25×10^{-11} mol cm^{-2}, whereas the coverage of **TpFc** surface was 7.2×10^{-12} mol cm^{-2}.

5.4 Experimental

Materials and Methods

All reagents were obtained from Sigma-Aldrich, except anhydrous toluene and anhydrous THF, which were obtained from Acros Organics, aqueous ammonium fluoride solution (Fluka, purum 40% in H_2O). Silicon wafer (n-Si(111) P-doped, 525 µm thickness, 1-12 Ω cm, single-side polished, miscut angle <0.1^o). Reactions were performed under nitrogen using standard Schlenk techniques.

^{1}H NMR and ^{13}C NMR were performed on a JEOL ECS 400 spectrometer. AFM, XPS normal, and CV parameters are as stated in Chapter 3.

XPS of stratification analysis was performed on an AXIS Nova (Kratos Analytical) utilising monochromatic AlKα X-rays (1486.6 eV) operating at 15 kV with 15 mA emission (225 W). Data was collected at two emission angles, 0 and 67.5 degrees, with a pass energy of 80 eV in electrostatic lens mode. Charge neutralisation was used throughout the analysis. Stratification plots were generated using the ARCtick spread sheet (National Physical Laboratory).

1-(but-3-en-1-yn-1-trimethylsilane)ferrocene

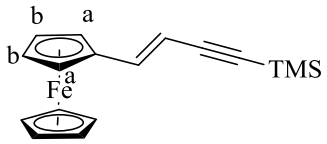

1

Compound **1** was prepared according to literature method.[38]

To a slurry of (3-trimethylsilyl-2-propynyl)triphenyl phosphonium bromide (5 g, 1.1 mmol) in anhydrous THF (20 ml) was added a 2.0 M THF solution of sodium bis(trimethylsilyl)amide (0.7 ml, 1.4 mmol) at ambient temperature. and stirred for 30 min, and then a solution of the ferrocenecarboxaldehyde (0.2 g, 0.9 mmol) in THF (10 ml) was added slowly. The solution was stirred for another 2 hr under an atmosphere of nitrogen, the water (50 ml) was added and then two layers were separated. The aqueous layer was extracted with diethyl ether (3 x 30 mL). The organic layer

washed twice with a saturated aqueous solution of sodium chloride (10 mL), dried over Na_2SO_4, filtered, and the solvent was removed under vacuum to give a brown oil. The crude product was purified by column chromatography (silica gel, 95:5 hexane: ethylacetate) to give dark brown oil **1** (99 mg, 31 %).

^{1}H NMR (400MHz, $CDCl_3$): δ 6.79 (1H, d, *J* = 16.1 Hz, Fc*CH*=CH), 5.76 (1H, d, *J* = 16.1 Hz, FcCH=*CH*), 4.35 (2H, app. t, *J* = 1.8 Hz, CH_a) 4.28 (2H, app. t, *J*=1.8 Hz, CH_b), 4.14 (5H, s, C_5H_5), 0.21 (9H, s, $SiMe_3$). ^{13}C NMR (100 MHz, $CDCl_3$): δ 141.9 (Fc*C*H=CH), 104.8 (FcCH=*C*H), 94.7, 81.5, 69.7, 69.4, 67.0, 0.12 ($SiMe_3$). HRMS (ESI, m/z): calculated for $C_{17}H_{21}SiFe$ [M+H] 309.0650, found 309.0659.

1-(but-1-en-3-yne)ferrocene

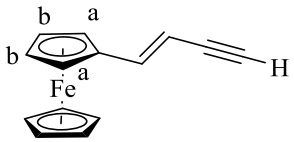

2

Deprotection of compound **1** to give compound **2** was prepared according to literature method.[38]

Compound **1** (40 mg, 0.129 mmol) was dissolved in THF (5 ml). Then 1.0 M THF solution of n-Bu_4NF (0.14 ml, 0.14 mmol) was added to the solution slowly with stirring. The reaction was left to stir for 2 h. The solvent was removed and the crude product was purified by column chromatography 95:5 hexane: ethylacetatet to give dark brown oil **2**, (12 mg, 40 %).

^{1}H NMR (400 MHz, $CDCl_3$): δ 6.84 (1H, d, *J* = 16.1 Hz, Fc*CH*=CH), 5.73 (1H, d, *J* = 16.1 Hz, FcCH=*CH*), 4.38 (2H, s, CH_a), 4.30 (s, 2H, CH_b), 4.15 (s, 5H, C_5H_5), 3.00 (1H, d, *J* = 2.3, ≡*CH*). ^{13}C NMR (100 MHz, $CDCl_3$): δ 142.5 (Fc*C*H=CH), 103.4 (FcCH=*C*H), 83.7, 81.2, 69.8, 69.5, 67.1 (C_5H_5, C_5H_4). HRMS (ESI, m/z): calculated for $C_{14}H_{12}Fe$ $[M]^+$ 236.0289, found 236.0272.

1-(but-1,3-dien)ferrocene monolayer

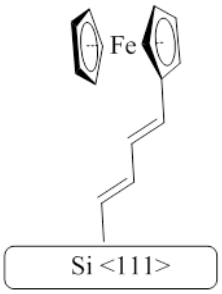

BuFc

A fresh wafer of flat silicon hydride surface (preparation in Chapter 3) was added to a anhydrous solution of compound **2** (4.7 mg, 20 µmol) in toluene (10 mL) and the reaction mixture was refluxed at 110 °C for overnight. The alkylated surface was washed with DCM and dried under a stream of nitrogen.

5-iodo-3-ethyl-2-(trimethylsilyl)ethynyl)thiophene

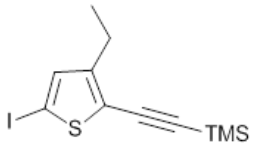

3

5-iodo-3-ethyl-2-((trimethylsilyl)ethynyl)thiophene was synthesised by Donald Lawrie.[42]

To a solution of diisopropylamine (8.5 mL, 60 mmol) in diethylether (50 mL) at -78 °C was added n-butyllithium (32.0 mL, 54.4 mmol (1.7 M in pentane)). The mixture was warmed up to 0 °C for 30 minutes and then re-cooled down to -78 °C. 3-ethyl-2-((trimethylsilyl)rthyynyl)thiophene (5.75 g, 27.5 mmol) in diethylether (50 mL) at room temperature was added dropwise and the solution was warmed up again to 0 °C for 10 minutes and then re-cooled to -78 °C. A solution of iodine (15.26 g, 60 mmol) in diethylether (75 mL) was cooled down to -78 °C before being added via cannula to initial solution. The mixture was allowed to room temperature and then stirred for 16 hours before being quenched by the addition of water (250 mL). The aqueous layer was extracted with diethylether (3 x 100 mL) and the organic extracts were combined and washed with brine (250 mL) and aqueous sodium thiosulphate (250 mL). The organic layer was dried over magnesium sulphate, filtered and evaporated on a rotary evaporator.

The crude product was purified by column chromatography (silica gel, hexane) to give yellow oil that darkens (7.63 g, 83 %).

^{1}H NMR (400 MHz, $CDCl_3$): δ 7.00 (1H, s, $CH_{thiophene}$), 2.48 (2H, q, J = 7.6 Hz, CH_2), 1.19 (3H, t, J = 7.6 Hz, CH_3), 0.24 (9H, s, $SiMe_3$). ^{13}C NMR (125 MHz, $CDCl_3$): δ 137.5 ($CH_{thiophene}$), 151.4, 124.0, 102.9, 95.9, 76.7, 22.7 (CH_2), 14.5 (CH_3), 0.13 ($SiMe_3$). HRMS (ESI, m/z): calculated for C_8H_7SI [M+H] 334.9787, found 334.9753.

5-iodo-3-ethyl-2-ethynylthiophene

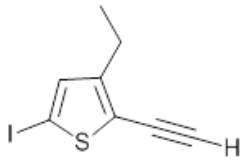

4

The 5-iodo-3-ethyl-2-(trimethylsilyl)ethynyl)thiophene **3** (350 mg, 1.04 mmol) was dissolved in methanol (20 mL) with potassium carbonate (570 mg, 4.16 mmol). The solution was stirred overnight at room temperature. The reaction mixture was poured into water (100 mL). The product was extracted from the aqueous layer with DCM (3 x 50 mL). The organic layer was separated and dried with $MgSO_4$ and concentrated to give a yellow oil (218 mg, 80 %).

^{1}H NMR (400 MHz, $CDCl_3$): δ 7.02 (1H, s, $CH_{thiophene}$), 3.50 (1H, s, C≡CH), 2.70 (2H, q, J = 7.6 Hz, CH_2), 1.21 (t, 3H, J = 7.6 Hz, CH_3).^{13}C NMR (100 MHz, $CDCl_3$): δ 137.4($CH_{thiophene}$), 84.9 (C≡*C*H), 151.8, 122.6, 75.3, 74.3, 22.4 (CH_2), 14.5 (CH_3). HRMS (ESI, m/z): calculated for C_8H_7SI [M+H] 262.9391, found 262.9390.

5-iodo-3-ethyl-2-vinylthiophene monolayer

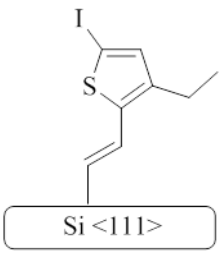

Tp

A fresh wafer of flat silicon hydride surface was added to a degassed solution of 5-iodo-3-ethyl-2-ethynylthiophene **4** (5.2 mg, 20 µmol) in toluene (10 mL) and the reaction mixture was refluxed at 110 ˚C for overnight. The alkylated surface was washed with DCM and dried under a stream of nitrogen.

4-ethyl-2-(-1-ferrocenylethynyl)-5-vinyl-thiophene monolayer

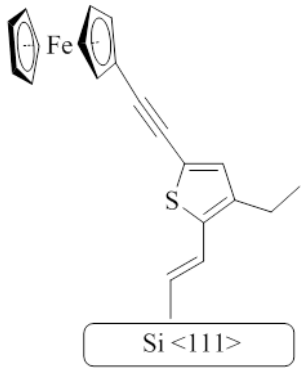

TpFc

Modified silicon wafer **Tp** was immersed to solution of ethynylferrocene (4.2 mg, 20 µmol) in anhydrous THF (10 mL). Copper (I) iodide (96 mg, 0.5 mmol), tetrakis(triphenylphosphine)palladium(0) (0.15 µg, 1 nmol) and diisopropylamine (100 µL) were added and the reaction mixture was refluxed at 95˚C for overnight. After cooling, the alkylated surface was washed with DCM and dried under a stream of nitrogen.

References

1. J. M. Buriak, *Chemical Reviews*, 2002, **102**, 1271-1308.

2. S. Ciampi, J. B. Harper and J. J. Gooding, *Chemical Society Reviews*, 2010, **39**, 2158-2183.

3. S. P. Cummings, J. Savchenko and T. Ren, *Coordination Chemistry Reviews*, 2011, **255**, 1587-1602.

4. J. J. Gooding and S. Ciampi, *Chemical Society Reviews*, 2011, **40**, 2704-2718.

5. J. Escorihuela, M. J. Banuls, R. Puchades and A. Maquieira, *Chemical Communications*, 2012, **48**, 2116-2118.

6. A. R. Pike, L. H. Lie, R. A. Eagling, L. C. Ryder, S. N. Patole, B. A. Connolly, B. R. Horrocks and A. Houlton, *Angewandte Chemie-International Edition*, 2002, **41**, 615-617.

7. J. Gu, C. M. Yam, S. Li and C. Cai, *Journal of the American Chemical Society*, 2004, **126**, 8098-8099.

8. R. Zanoni, A. Aurora, F. Cattaruzza, C. Coluzza, E. A. Dalchiele, F. Decker, G. Di Santo, A. Flamini, L. Funari and A. G. Marrani, *Materials Science and Engineering: C*, 2006, **26**, 840-845.

9. E. A. Dalchiele, A. Aurora, G. Bernardini, F. Cattaruzza, A. Flamini, P. Pallavicini, R. Zanoni and F. Decker, *Journal of Electroanalytical Chemistry*, 2005, **579**, 133-142.

10. A. Boe, S. Nguyen and J.-H. Kim, *Nanoscape*, 2008, **5**, 125-135.

11. M. Qu, Y. Zhang, J. He, X. Cao and J. Zhang, *Applied Surface Science*, 2008, **255**, 2608-2612.

12. M. P. Stewart and J. M. Buriak, *Angewandte Chemie-International Edition*, 1998, **37**, 3257-3260.

13. J. M. Buriak, M. P. Stewart, T. W. Geders, M. J. Allen, H. C. Choi, J. Smith, D. Raftery and L. T. Canham, *Journal of the American Chemical Society*, 1999, **121**, 11491-11502.

14. L. Scheres, M. Giesbers and H. Zuilhof, *Langmuir*, 2010, **26**, 10924-10929.

15. A. Ng, S. Ciampi, M. James, J. B. Harper and J. J. Gooding, *Langmuir*, 2009, **25**, 13934-13941.

16. S. Ciampi, G. Le Saux, J. B. Harper and J. J. Gooding, *Electroanalysis*, 2008, **20**, 1513-1519.

17. S. Ciampi, M. James, N. Darwish, E. Luais, B. Guan, J. B. Harper and J. J. Gooding, *Physical Chemistry Chemical Physics*, 2011, **13**, 15624-15632.

18. S. Ciampi, T. Böcking, K. A. Kilian, J. B. Harper and J. J. Gooding, *Langmuir*, 2008, **24**, 5888-5892.

19. S. Ciampi, T. Böcking, K. A. Kilian, M. James, J. B. Harper and J. J. Gooding, *Langmuir*, 2007, **23**, 9320-9329.

20. K. Huang, F. Duclairoir, T. Pro, J. Buckley, G. Marchand, E. Martinez, J.-C. Marchon, B. De Salvo, G. Delapierre and F. Vinet, *Chemphyschem*, 2009, **10**, 963-971.

21. E. G. Robins, M. P. Stewart and J. M. Buriak, *Chemical Communications*, 1999, 2479-2480.

22. G. Cleland, B. R. Horrocks and A. Houlton, *Journal of the Chemical Society-Faraday Transactions*, 1995, **91**, 4001-4003.

23. R. Boukherroub, S. Morin, P. Sharpe, D. D. M. Wayner and P. Allongue, *Langmuir*, 2000, **16**, 7429-7434.

24. B. Fabre and F. Hauquier, *The Journal of Physical Chemistry B*, 2006, **110**, 6848-6855.

25. X. C. Zhang, S. Kumar, J. H. Chen and A. V. Teplyakov, *Surface Science*, 2009, **603**, 2445-2457.

26. G. Riveros, G. Gonzalez and B. Chornik, *Journal of the Brazilian Chemical Society*, 2010, **21**, 25-32.

27. S. E. Létant, B. R. Hart, S. R. Kane, M. Z. Hadi, S. J. Shields and J. G. Reynolds, *Advanced Materials*, 2004, **16**, 689-693.

28. B. Fabre, *Accounts of Chemical Research*, 2010, **43**, 1509-1518.

29. H. C. Kolb, M. G. Finn and K. B. Sharpless, *Angewandte Chemie-International Edition*, 2001, **40**, 2004-2021.

30. L. Britcher, T. J. Barnes, H. J. Griesser and C. A. Prestidge, *Langmuir*, 2008, **24**, 7625-7627.

31. K. Sonogashira, Y. Tohda and N. Hagihara, *Tetrahedron Letters*, 1975, **16**, 4467-4470.

32. K. Sonogashira, *Journal of Organometallic Chemistry*, 2002, **653**, 46-49.

33. J.-C. Lin, J.-H. Kim, J. A. Kellar, M. C. Hersam, S. T. Nguyen and M. J. Bedzyk, *Langmuir*, 2010, **26**, 3771-3773.

34. R. Zanoni, F. Cattaruzza, C. Coluzza, E. A. Dalchiele, F. Decker, G. Di Santo, A. Flamini, L. Funari and A. G. Marrani, *Surface Science*, 2005, **575**, 260-272.

35. F. Decker, F. Cattaruzza, C. Coluzza, A. Flamini, A. G. Marrani, R. Zanoni and E. A. Dalchiele, *The Journal of Physical Chemistry B*, 2006, **110**, 7374-7379.

36. A. G. Marrani, E. A. Dalchiele, R. Zanoni, F. Decker, F. Cattaruzza, D. Bonifazi and M. Prato, *Electrochimica Acta*, 2008, **53**, 3903-3909.

37. L. Scheres, M. Giesbers and H. Zuilhof, *Langmuir*, 2010, **26**, 4790-4795.

38. F. Liu, X. H. Wu, J. L. Xia, S. Jin, G. A. Yu and S. H. Liu, *Journal of Organometallic Chemistry*, 2010, **695**, 809-815.

39. L. H. Lie, S. N. Patole, A. R. Pike, L. C. Ryder, B. A. Connolly, A. D. Ward, E. M. Tuite, A. Houlton and B. R. Horrocks, *Faraday Discussions*, 2004, **125**, 235-249.

40. S. N. Patole, A. R. Pike, B. A. Connolly, B. R. Horrocks and A. Houlton, *Langmuir*, 2003, **19**, 5457-5463.

41. J. E. Bateman, R. D. Eagling, D. R. Worrall, B. R. Horrocks and A. Houlton, *Angewandte Chemie-International Edition*, 1998, **37**, 2683-2685.

42. D. J. Lawrie, PhD thesis, Newcastle Uinversity, 2004.

43. N. Tajimi, H. Sano, K. Murase, K.-H. Lee and H. Sugimura, *Langmuir*, 2007, **23**, 3193-3198.

44. A. G. Marrani, F. Cattaruzza, F. Decker, P. Galloni and R. Zanoni, *Electrochimica Acta*, 2010, **55**, 5733-5740.

45. H. Sano, M. Zhao, D. Kasahara, K. Murase, T. Ichii and H. Sugimura, *Journal of Colloid and Interface Science*, 2011, **361**, 259-269.

46. M. Lu, T. He and J. M. Tour, *Chemistry of Materials*, 2008, **20**, 7352-7355.

47. D. Zigah, C. Herrier, L. Scheres, M. Giesbers, B. Fabre, P. Hapiot and H. Zuilhof, *Angewandte Chemie-International Edition*, 2010, **49**, 3157-3160.

48. G. Riveros, C. Garin, S. Meneses and S. Escobar, *Molecular Crystals and Liquid Crystals*, 2010, **521**, 187-194.

49. M. A. C. Campos, J. M. J. Paulusse and H. Zuilhof, *Chemical Communications*, 2010, **46**, 5512-5514.

50. M. Herrera, T. Ichii, K. Murase and H. Sugimura, *Chemistry Letters*, 2012, **41**, 1188-1190.

Chapter 6

Part of this chapter is based on the publication:

A. Mishchenko, M. Abdualla, A. Rudnev, Y. Fu, A. R. Pike and T. Wandlowski, "Electrochemical scanning tunnelling spectroscopy of a ferrocene-modified n-Si(111)-surface: electrolyte gating and ambipolar FET behaviour" *Chem. Commun.*, 2011, **47**, 9807-9809.

Chapter 6 - Future prospects

In light of the work described in the preceding three chapters, it was reported that the ferrocene modified surfaces could have possible applications in charge storage and memory devices.[1] The following sections detail some of the collaborative work performed to investigate these possibilities using the surfaces previously described.

6.1 Electrochemical scanning tunnelling spectroscopy of a ferrocene-modified n-Si(111)-surface, EFc

The following experiments were performed jointly with Thomas Wandlowski group (Department of Chemistry and Biochemistry, University of Bern) using **EFc** (Chapter 3) and **OCT** surfaces (Chapter 4).

Addressing the local redox properties of Fc–Si heterojunctions represents an important approach to understand better the scalability of devices where ferrocene monolayers on silicon surfaces have potential applications in charge storage and communication devices.[2] In particular, in situ scanning tunnelling microscopy (STM) and spectroscopy (STS) studies provide invaluable information about the local electrochemical properties of individual ferrocene moieties chemically attached to a silicon surface. STS studies were performed in an electrochemical environment to characterise ferrocene–silicon hybrid devices based on the **EFc** surface fabricated in the work described in Chapter 3, to demonstrate redox-mediated enhancement of the tunnelling current. Therefore, two surfaces were studied in this work: ethylferrocene, **EFc**, and octenyl surface, **OCT**.

Error! Reference source not found.a, shows an in situ STM image of the **EFc** sample. he bias voltage was kept at 0.5 V as lower positive voltages immediately lead to a loss of feedback control, and negative voltages destroyed the tip due to hydrogen evolution. When the substrate potential *Es* approaches the formal potential of ferrocene, bright raised areas are visible (Figure 6.1a). These features can be attributed to the enhanced conductance of the ferrocene species when substrate and tip Fermi levels approach the redox level (HOMO) of the ferrocene molecules on the surface. The variation in contrast remains stable, even when the substrate *Es* is made more positive as compared to the formal redox potential of ferrocene. It also disappears upon scanning the *Es* back into the stability range of the reduced ferrocene moiety. This behaviour was not observed for the non-redox-active surface, **OCT,** as shown in Figure 6.1b.

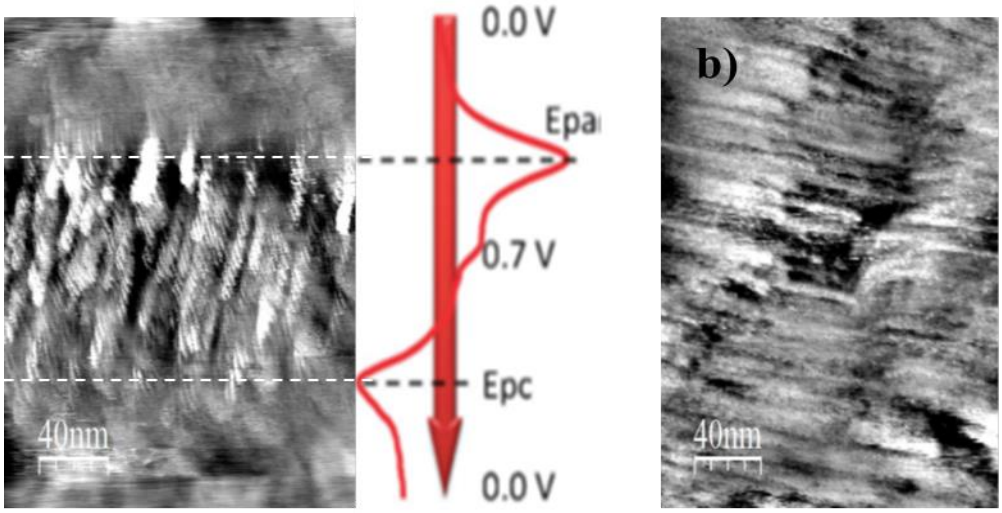

Figure 6.1. In situ STM image (200 - 90 nm) of a (a) **EFc** sample during a potential cycle from *Es* = 0.0 V to 0.7 V and back to 0.0 V at 5 mV s^{-1} and (b) **OCT** sample. The bias voltage V_{bias} was kept at 0.5 V. The substrate electrochemical current is plotted on the right side of panel a for guidance. E_p^A and E_p^c are the anodic and cathodic peak potentials of the ferrocene redox process.[1]

Constant-bias in situ STS was used to explore this observance in more detail. The potentials of both working electrodes (tip and substrate) are changed in tandem, ensuring that the bias voltage is kept constant. Typical results obtained for the **EFc** (red) and **OCT** (blue) surfaces are illustrated in Figure 6.2 . The data demonstrate an increase in the tunnelling current flowing through the tip for the electrochemically active ferrocene sample in **EFc**. Reference experiments with insulating adlayer of the **OCT** sample did not show this effect (blue traces in Figure 6.2). The number of **EFc** molecules contributing to the detected current in the nanoscale STM-type junction is estimated to be 2 to 3. This estimation was based on the exponential dependence of the tunnelling current on distance, the tip apex radius being <5 nm and an **EFc** surface coverage of 29%.

Redox-assisted enhancement of tunnelling currents has been reported before for a variety of molecules bound to metal electrodes.[3, 4] However, the work here on a redox-molecule enhanced response in a nanoscale tunnelling junction between silicon electrode modified with a covalently attached functional molecule (ferrocene) and a metal (gold) STM tip at an electrochemical solid/liquid interface is the first of its kind.

Enhancement of the tunnelling current in metal|molecule|metal tunnelling junctions is seen when both substrate and tip potentials approach the formal potential of the redox process under study. Plots of the tunnelling current *vs*. substrate potential in tunnelling

junctions formed at metal substrates are often bell-shaped, with the maximum occurring close to the formal potential of the redox group.[5] In the case of **EFc**, the tunnelling current rises steeply with an onset potential near to that for the oxidation of the ferrocene.

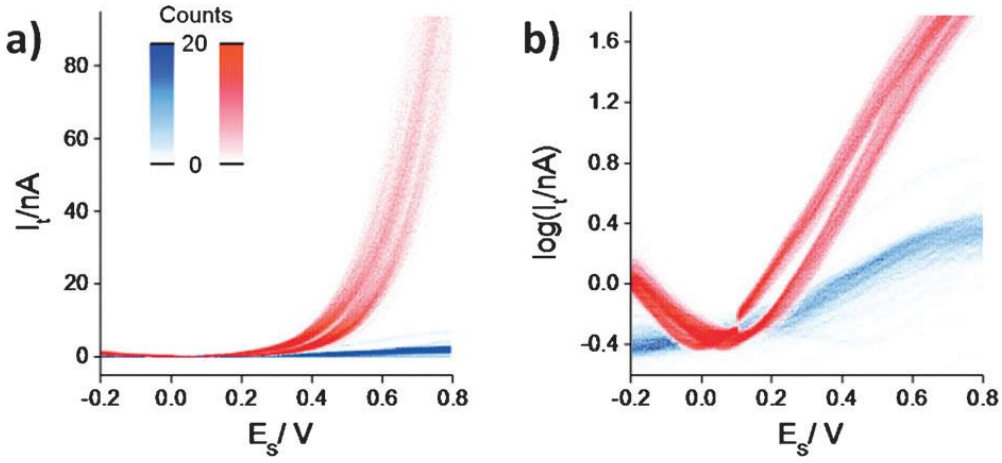

Figure 6.2. In situ STS measurements of **EFc** (red traces) and **OCT** (blue traces) in linear (a) and semi-logarithmic (b) representation. The bias voltage V_{bias} was kept at 0.5 V and 500 individual spectra were plotted together in each 2D intensity graph.

Control experiments with **OCT** samples demonstrated clearly the absence of enhancement for the non-redox active monolayers (blue traces in Figure 6.2a and b). This comparison shows that the immobilised ferrocenes act as dopant centres on the surface of the n-Si(111) electrode. The logarithm of the tunnelling current is plotted against the substrate potential, see Figure 6.2b. The shape of this curve resembles a plot of the drain-source current, the gate voltage of an ambipolar field effect transistor (FET) such as that reported for other devices.[6, 7] The oxidised ferrocenium is responsible for the enhancement of the tunnelling current in the positive branch, while the neutral ferrocene facilitates the charge transfer in the negative regime.

The exponential shape of the STS curves can be explained by the exponential dependence of the carrier density on surface potential. This slope is called the subthreshold slope in a FET terminology. The inverse of the slope is the FET parameter known as the subthreshold swing.[8] The subthreshold swing is estimated to be 250 mV per decade and 480 mV per decade for the positive and negative regions respectively. In both cases the swings are larger than the optimal theoretical value of 60 mV per decade. Therefore, the electrolyte gate modulates the band energies by 24% and 13%, for the positive and the negative regimes respectively. The control experiments carried out with the **OCT** surface demonstrate very clearly that, the ferrocenes on the **EFc** electrode are

responsible for the FET-like behaviour. The redox-mediated tunnelling response, observed here on the **EFc** silicon surface is noticeably different from that recorded at a metal (gold or platinum) substrate.[4, 5] In conclusion, the in situ STS study demonstrated ambipolar FET behaviour of the **EFc** sample. Control experiments of **OCT** surface show that all enhancement effects observed in the tunnelling current response are directly related to the presence of the redox active ferrocene units.

6.2 Photoelectrochemical transients

The following experiments were performed jointly with Shaun Cook (Chemical Nanoscience Laboratory, Newcastle University) using the surfaces prepared in Chapter 3 and Chapter 4. In this section, a chronoamperometric experiment in which the light intensity is stepped instantaneously from zero to a finite value provides a straightforward means to determine the rate of electron transfer from surface-bound ferrocenes to Si substrates is described.[9, 10] The n-type Si electrode is poised at a fixed potential in the dark and the current transient when the light is switched on is measured. The current transient is modelled by the following equation:

$$i(t) = i_0\left[\beta\exp(-k_1 t) + (1-\beta)\exp(-k_2 t)\right] + i_\infty \qquad (1)$$

where $i(t)$ is the instantaneous photocurrent, i_∞ allows for the possibility of a steady-state photocurrent and β is a parameter which determines the relative amplitude of the two exponential components described by the rate constants k_1, k_2 and the magnitude of i_0 peak current of the transient. Equation (1) was fitted to experimental measurements of $i(t)$ to determine values of parameters k_1, k_2, β, and i_0.

Typical transients and the fits of equation (1) to the data are shown in Figure 6.3. The data for a control surface an undecenyl modified silicon surface, **UND**, is shown in Figure 6.3a. The two decay components, collapse into a single exponential equivalent to the faster non-faradaic process with rate constant k_1 and therefore β approximates to one (Beta is the fraction of the current that occurs due to trapping and recombination of photogenerated carriers)

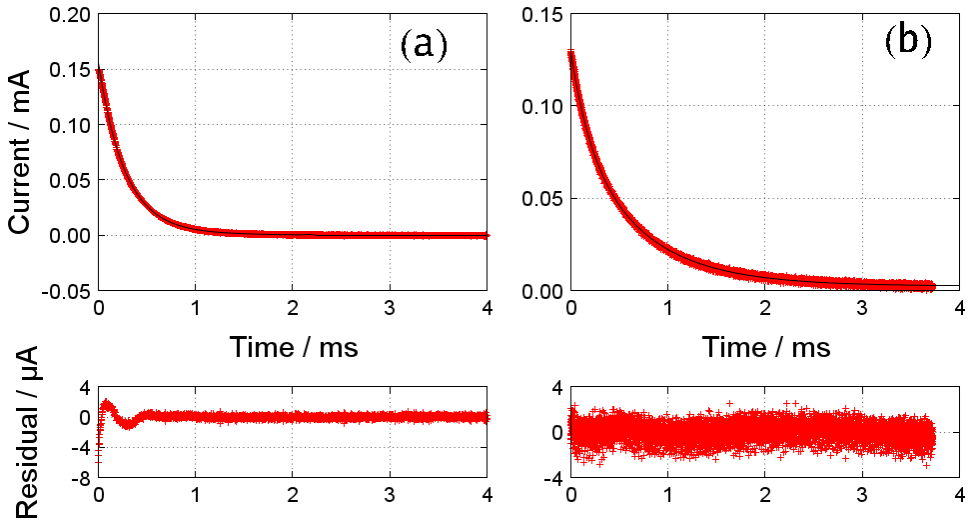

Figure 6.3. Transient data recorded after a light step from no light to full light intensity. (a) an **UND** surface with +50 mV applied potential against Ag/AgCl in 0.1M KCl (aq) and (b) an **EFc** surface with -80 mV applied potential (right). The **UND** data gave a best fit β value of 0.96 corresponding to an almost pure single exponential decay. The best fit value of β was 0.34 for the **EFc** surface indicating two exponential decay components.

This fast process is not typical of a redox reaction but rather a non-faradaic process corresponding to photocapacitance.[9, 10] In contrast, Figure 6.3b shows the photocurrent transient for the **EFc** electrode where $\beta < 1$ and two exponential decay components are required to fit the data. The faster decay is likely to be the non-faradaic process, k_1 discussed above, where the value is similar to that for the **UND** situation. The slower component is assigned to the rate of electron transfer from the ferrocene to the Si surface, k_2.

Having established the presence of two processes during the transient decay, an investigation into the effect of dilution on the redox active ferrocenyl monolayer was performed. A series of measurements was recorded for each of the following electrodes, 100% **EFc**, 50:50 **EFc/C$_8$** and 1:99 **EFc/C$_8$**. The photocurrent transients were recorded in 20 mV steps starting from potentials at the negative side of the voltammetric wave (Figure 6.4). In the case of the pure monolayer, **EFc**, the values of β were about 0.4 indicating that 60% of the photocurrent at $t = 0$ was due to the faradaic process. This proportion increased at more positive potentials as expected on the basis of the voltammograms. However, at about -60 mV there is a sudden decrease in the proportion of faradaic current as indicated by the increase of β to a value close to 1.0; the current at these positive potentials is dominated by the non-faradaic process. The reason for this behaviour is that the experiment requires the faradaic reaction not to happen in the dark when the electrode is poised at the chosen potential. If the faradaic reaction does

proceed in the dark, the ferrocene/ferrocenium ratio will equilibrate prior to the photocurrent transient and a single exponential is observed at very positive potentials because no ferrocene remains that can be photo-oxidised. In fact, this technique proved to be a very sensitive means to detect slow faradaic processes which may correspond to dark currents too small to measure directly. Interestingly, the phenomenon did not occur for the 50:50 diluted **EFc/C$_8$** monolayer (Figure 6.4b) but it was observed at -160 mV for the 1:99 diluted monolayer (Figure 6.4c). As discussed in Chapter 3, some dilution of ferrocenes with inert alkyl groups at Si electrodes produces more stable monolayers and so leads to the observed variations in coverage when aqueous voltammetric experiments are performed.

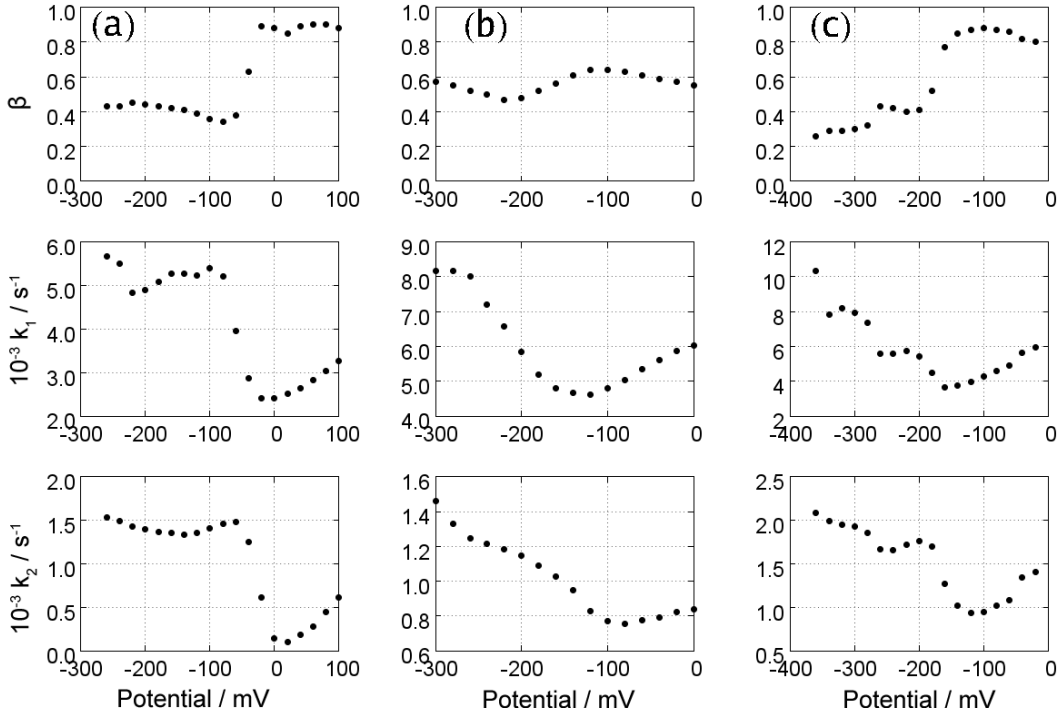

Figure 6.4. Kinetic parameters determined for (a) **EFc**, (b) **EFc/C$_8$** 50:50 and (c) **EFc/C$_8$** 1:99 by fitting equation (3) to photoelectrochemical chronoamperometry data using non-linear least squares regression. Electrode potentials are measured with respect to Ag/AgCl in 0.1 M KCl (aq).

Finally, the surface coverages of the surfaces used here are relatively low compared to those in previous reports. It has been reported that the rates are faster at low coverage and therefore, this study considered the possibility that measured rates are in fact limited by counterion transport.[11] This possibility was tested by preparing mixed monolayers with alk-1-enes of varying chain length, C_6, C_8, C_{10}. Ferrocene groups in mixed monolayers with decene, (1.31 nm), are thought to be 'buried' in the monolayer, but not in the hexene monolayers whose thickness (0.79 nm) is comparable to the ferrocene-Si distance of **EFc** (0.72 nm). The values of k_2 were found to be independent

of the n-alkyl component of the monolayer which suggests that counterion penetration to the ferrocenium is not rate-limiting.

References

1. A. Mishchenko, M. Abdualla, A. Rudnev, Y. Fu, A. R. Pike and T. Wandlowski, *Chem. Commun.*, 2011, **47**, 9807-9809.

2. B. Fabre, *Accounts of Chemical Research*, 2010, **43**, 1509-1518.

3. T. Albrecht, K. Moth-Poulsen, J. B. Christensen, A. Guckian, T. Bjornholm, J. G. Vos and J. Ulstrup, *Faraday Discussions*, 2006, **131**, 265-279.

4. A. V. Rudnev, I. V. Pobelov and T. Wandlowski, *Journal of Electroanalytical Chemistry*, 2011, **660**, 302-308.

5. W. Haiss, T. Albrecht, H. van Zalinge, S. J. Higgins, D. Bethell, H. Hobenreich, D. J. Schiffrin, R. J. Nichols, A. M. Kuznetsov, J. Zhang, Q. Chi and J. Ulstrup, *J. Phys. Chem. B*, 2007, **111**, 6703-6712.

6. W. J. Zhang, J. Y. Zhang, P. J. Li, X. Shen, Q. F. Zhang and J. L. Wu, *Nanotechnology*, 2008, **19**.

7. P. L. Levesque, S. S. Sabri, C. M. Aguirre, J. Guillemette, M. Siaj, P. Desjardins, T. Szkopek and R. Martel, *Nano Lett.*, 2011, **11**, 132-137.

8. S. Rosenblatt, Y. Yaish, J. Park, J. Gore, V. Sazonova and P. L. McEuen, *Nano Lett.*, 2002, **2**, 869-872.

9. L. M. Peter, *Chem. Rev.*, 1990, **90**, 753-769.

10. L. M. Abrantes and L. M. Peter, *Journal of Electroanalytical Chemistry and Interfacial Electrochemistry*, 1983, **150**, 593-601.

11. K. M. Roth, A. A. Yasseri, Z. M. Liu, R. B. Dabke, V. Malinovskii, K. H. Schweikart, L. H. Yu, H. Tiznado, F. Zaera, J. S. Lindsey, W. G. Kuhr and D. F. Bocian, *Journal of the American Chemical Society*, 2003, **125**, 505-517.

Chapter 7

Chapter 7 - Conclusions

7.1 Summary

The modification of both hydrogen-terminated Si(111) single crystal and porous silicon with a range of ferrocene derivatives has been studied.

Hydrosilylation modification of both hydrogen-terminated Si(111) single crystal and porous silicon with vinylferrocene and ethynylferrocene is shown to proceed with the formation of three different Si-C_2-Fc surfaces. The three different linkages, Si-CH_2-CH_2-Fc, Si-CH=CH-Fc, and Si-C≡C-Fc were successfully produced using three different methods. The thermally activated method (at 110 °C in toluene) using vinylferrocene produced the Si-CH_2-CH_2-Fc monolayer, **EFc**. In addition, hydrosilylation at room temperature using ethynylferrocene in the minimum amount of DCM produced the Si-CH=CH-Fc surface, **VFc**. Whereas, the reaction of butyl lithium with ethynylferrocene via a nucleophilic substitution reaction (acetylide anion) at the silicon hydride surface produced the Si-C≡C-Fc surface, **EnFc**. Transmission FTIR analysis on porous silicon of the **EFc** surface showed the disappearance of the C=C stretching mode peak of the vinylferrocene and indicates rehybridisation of the vinyl carbon atoms (sp^2 to sp^3) and confirmed chemisorption of vinylferrocene on the **EFc** surface. FTIR also indicated the rehybridisation of the terminal alkynyl *v* (≡C-H) of ethynylferrocene in the formation of the Si-CH=CH- linkage in the **VFc** surface. Whereas, in **EnFc** FTIR also indicated the disappearance of the terminal alkynyl *v* (≡C-H) and the concurrent appearance of the Si-C≡C- stretching mode. AFM studies on the three ferrocenyl modified surfaces **EFc**, **VFc** and **EnFc** indicate that in all cases the different linkages between the silicon and the ferrocene result in monolayers, which were stable to imaging and retain some of the topography of the underlying silicon substrate. XPS characterisation provided further confirmation of chemisorbed monolayers of ferrocene on each silicon surface. Elemental peaks for Si 2s, Si 2p, C 1s, and Fe 2p core levels were observed in all samples and were characteristic of the three samples. Cyclic voltammograms of the Si(111) wafers modified with ferrocenyl derivatives showed the characteristic single electron redox response of the ferrocene and gave surface coverage (aqueous solvent) 1.8×10^{-12} mol cm^{-2} and 1.9×10^{-12} mol cm^{-2} for **EFc** and **VFc** respectively. CV in acetonitrile gave maximum surface coverage values of 1.3×10^{-10} mol cm^{-2} for **EFc**, 2.7×10^{-11} mol cm^{-2} for **VFc,** and 5.4×10^{-11} mol $cm^{-2}$for

EnFc. The cyclic voltammetry showed that ferrocenyl silicon monolayers in acetonitrile are more stable than in aqueous electrolyte. It could be because some ferrocene is lost from the surface during the CV measurement in aqueous electrolyte. The reproducibility of these monolayers were not easy to control. The highest coverage was reported for the **EFc** surface, which could be due to the method of preparation, where thermal activation was used to produce this surface. It could be that high temperatures help ferrocene to react at more Si-H sites than at room temperature in both of **VFc** and **EnFc**.

Due to the low non-reproducibility of the surfaces prepared in Chapter 4, mixed monolayers were investigated as a way to improve reproducibility using thermal activation. Hydrogen terminated Si(111) single crystal was then modified with a 50:50 mixture of vinylferrocene and a range of simple alkenes, hexene C_6, octene C_8, decene C_{10}, or undecene C_{11}. These mixed allkene reactions resulted in the formation of mixed ferrocenyl/alkyl monolayers; **EFc/C$_6$**, **EFc/C$_8$**, **EFc/C$_{10}$**, and **EFc/C$_{11}$**. AFM studies on these mixed monolayers showed once again that the monolayers were stable during imaging. Moreover, the different mixed ferrocenyl modified silicon surfaces also showed similar topography however, a slight increase in surface roughness was observed for the **EFc/C$_6$** surface compared to the 100% ferrocenyl monolayers. XPS characterisation confirmed the chemical attachment of the vinylferrocene/alkene components through the element peaks from the Si 2s, Si 2p, C 1s, and Fe 2p core levels. Analysis of the cyclic voltammograms of 50:50 **EFc/C$_6$**, **EFc/C$_8$**, **EFc/C$_{10}$**, and **EFc/C$_{11}$** gave different surface coverages in two different electrolytes, aqueous and acetonitrile. The higher coverage was again observed in acetonitrile. The reason for this is likely to be that these surfaces are more stable in acetonitrile, where in aqueous electrolyte some ferrocene may be lost from surface during CV measurement through oxidation. The coverage in aqueous electrolyte is 1.04×10^{-11} mol cm^{-2} for **EFc/C$_6$**, 9.5×10^{-12} mol cm^{-2} for **EFc/C$_8$**, 1.57×10^{-11} mol cm^{-2} for **EFc/C$_{10}$**. Whereas, in acetonitrile electrolyte the coverage were estimated at 3.49×10^{-11} mol cm^{-2} for **EFc/C$_6$**, 4.0×10^{-11} mol cm^{-2} for **EFc/C$_8$**, 4.0×10^{-11} mol cm^{-2} for **EFc/C$_{10}$**, 3.06×10^{-11} mol cm^{-2} for **EFc/C$_{11}$** surface. The CV showed that the **EFc/C$_8$** was the more reproducible surface.

Therefore, the **EFc/C$_8$** surface was chosen to prepare more dilute monolayers. A range of dilute **EFc/C$_8$** surfaces 20:80, 10:90 and 1:99 were fabricated from vinylferrocene:octene mixture in the alkylation solution and were characterised. AFM showed that, these dilute monolayers were stable to prolonged imaging and that roughness decreased with decreasing proportion of the ferrocene units in the monolayer.

XPS characterisation presented ethylferrocenyl/alkyl components by the appearance of peaks due to Si 2s, Si 2p, C 1s, and Fe 2p core levels. The ratio of Fe/Si approximately increased with increasing mole fraction of vinylferrocene in solution. The cyclic voltammograms of the dilute mixed monolayers **EFc/C$_8$** gave different surface coverages in acetonitrile electrolyte. The coverages observed were 3.03×10^{-11} mol cm^{-2}, 1.84×10^{-12} mol cm^{-2} and 7.95×10^{-13} mol cm^{-2} for 20:80, 10:90 and 1:99 **EFc/C$_8$** surfaces respectively. The coverage of mixed **EFc/C$_8$** monolayers estimated form CV found that, coverage is depended on the mole fraction of vinylferrocene in initial alkylation solution, therefore, it is possible to control the separation of ferrocene units on silicon surface.

In a final set of studies, longer alkyl chain linkages between the ferrocene and silicon surface were investigated by two different approaches. In the first approach a ferrocenyl group with an extended tether was first synthesised, 1-(but-1-en-3-yne)ferrocene, which was then attached as a complete unit to the silicon surface using a one-step reaction to give the **BuFc** surface. Whereas, in the second approach the ferrocene monolayer was built up from the silicon surface in a step-wise fashion via a series of surface reactions. The silicon hydride surface was first modified with 5-iodo-3-ethyl-2-ethynylthiophene to give the **Tp** surface. **Tp** was coupled to ethynylferrocene via the Sonogashira reaction to give the **TpFc** surface. The synthesis of compounds 1-(but-1-en-3-yne)ferrocene and 5-iodo-3-ethyl-2-ethynylthiophene were confirmed by ^{1}H-NMR, ^{13}C-NMR spectroscopy and. ESI-MS. The silicon modified surfaces **BuFc**, **Tp** and **TpFc** were characterised by AFM, XPS and for surfaces **BuFc** and **TpFc** electrochemically by CV. AFM studies on the extended ferrocenyl modified surfaces **BuFc**, **TpFc** and **Tp** surfaces indicated stable monolayers during imaging which retained some of the topography of the silicon hydride surface. However, the roughness of surface **BuFc** is twice that of the **TpFc** and **Tp** surfaces, this could be due to polymerisation of the alkene and alkynyl groups during surface modification. On the other hand, after performing the Sonogashira reaction with ethynylferrecene at the **Tp** surface to give the **TpFc** surface, the AFM image shows the expected terrace/step edge structures. The surface was surprisingly clean with a similar roughness value to the original **Tp** surface. This is despite the fact that a Pd catalyst and other ligands were used in the coupling reaction to produce the **TpFc** surface, suggesting the reaction proceeds with little surface contamination or monolayer deterioration. XPS characterisation was used for confirmation of thiophene and ferrocene on the silicon surfaces **Tp, BuFc** and **TpFc.** XPS analysis of the **Tp** surface indicated the presence of

the thiophene derivative by the appearance of S 2s and I 3d signals. In addition, after the Sonogashira coupling of ethynylferrocene with the **Tp** surface, XPS showed a new Fe 2p peak and the concurrent disappearance of the I 3d peak; confirmation of replacement of the iodine by ethynylferrocene. Moreover, for the **BuFc** surface the Fe 2p peak confirmed that ferrocene is present on the surface. Cyclic voltammetry studies of the **BuFc** and **TpFc** surfaces gave different coverage values ranging from 10^{-10} to 10^{-12}. The ferrocenyl coverage of **BuFc** (6.25×10^{-11} mol cm^{-2}) was an order of magnitude higher than the coverage of **TpFc** (7.2×10^{-12} mol cm^{-2}). This could be due to the two step reaction required to produce the **TpFc** surface resulting in a lower overall reaction yield. Not all of the silicon hydrogen sites are alkylated with thiophene in the first step as it is impossible to get 100% coverage for molecules that have a radius larger than 2 Å. The second reaction, Sonogashira coupling with ethynylferrocene, is also unlikely to yield 100% modification and so it is expected that the overall coverage will be significantly reduced, as noted by the electrochemical studies.

7.2 Conclusion and further work

In light of this summary, the modification and characterisation of silicon surfaces modified with ferrocene is difficult to consistently reproduce at high level. Reproducibility of these monolayers was difficult to control especially for pure monolayers **EFc**, **VFc** and **EnFc**. However, reproducibility of diluted monolayers was achieved more regularly.

Due to these interesting results ferrocenyl silicon surfaces, pure and mixed monolayers, were examined by STS and photoelectrochemical transient experiments for possible potential. It is interesting to prepare more ferrocenyl silicon monolayers, and study their possible applications through these studies. Perhaps more control over the surface preparation may lead to the realisation of ferrocenyl monolayers in memory charge storage devices. In addition, further studies of more complex ferrocene silicon surface, is expected.

Appendix

The following calculation was obtained by calculation on pages 68 and 69 for the surface coverage.

The statistic calculation was obtained for the percentage of coverage (%).

Sample	coverage mol cm^{-2}	coverage (%)
EFc surface **Mean 15.8, Median 15.0, Std. deviation 9.9**		
1	7.2×10^{-11}	16
2	4.5×10^{-11}	10
3	1.08×10^{-10}	24
4	4.4×10^{-11}	10
5	1.30×10^{-10}	29
6	1.08×10^{-10}	24
7	1.32×10^{-10}	29
8	1.31×10^{-10}	29
9	1.8×10^{-11}	4
10	1.33×10^{-11}	3
11	3.5×10^{-12}	1
12	9.0×10^{-12}	2
13	1.26×10^{-10}	28
14	5.81×10^{-11}	13

15	1.07×10^{-10}	24
16	7.6×10^{-11}	17
17	9.5×10^{-11}	22
18	1.2×10^{-10}	26
19	1.12×10^{-10}	25
20	1.30×10^{-10}	29
21	1.3×10^{-11}	3
22	1.33×10^{-11}	3
23	5.4×10^{-11}	12
24	3.0×10^{-11}	7
25	6.9×10^{-11}	15
26	6.8×10^{-11}	15
27	3.0×10^{-11}	7
VFc surface **Mean 3.7, Median 4.0, Std. deviation 1.9**		
1	3.8×10^{-12}	1
2	2.7×10^{-11}	6
3	4.2×10^{-12}	1
4	2.50×10^{-11}	5
5	2.60×10^{-11}	6
6	1.33×10^{-11}	3

7	9.0×10^{-12}	2
8	1.80×10^{-11}	4
9	1.3×10^{-11}	3
10	2.65×10^{-11}	6
11	1.9×10^{-11}	4
EnFc surface **Mean 6.8, Median 7.0, Std. deviation 4.0**		
1	4.4×10^{-11}	10
2	5.4×10^{-11}	12
3	1.81×10^{-11}	4
4	2.6×10^{-11}	6
5	3.1×10^{-11}	7
6	1.3×10^{-11}	3
7	9.1×10^{-12}	2
8	4.1×10^{-12}	1
9	4.9×10^{-11}	11
10	5.3×10^{-11}	12
11	3.2×10^{-11}	7
50:50 EFc/C_6 surface **Mean 7.8, Median 7.0, Std. deviation 3.6**		
1	5.3×10^{-11}	12

2	3.6×10^{-11}	8
3	2.6×10^{-11}	6
4	2.25×10^{-11}	5
5	6.3×10^{-11}	14
6	5.85×10^{-11}	13
7	4.4×10^{-11}	10
8	1.23×10^{-11}	3
9	5.3×10^{-11}	12
10	2.3×10^{-11}	5
11	1.26×10^{-11}	3
12	1.6×10^{-11}	4
13	3.0×10^{-11}	7
14	4.2×10^{-11}	9
15	2.7×10^{-11}	6
50:50 EFc/C_8 surface **Mean 7.5, Median 7.0, Std. deviation 2.6**		
1	3.5×10^{-11}	8
2	4.0×10^{-11}	9
3	3.6×10^{-11}	8
4	3.0×10^{-11}	7
5	6.8×10^{-11}	15

6	4.1×10^{-11}	9
7	3.2×10^{-11}	7
8	3.4×10^{-11}	8
9	4.0×10^{-11}	9
10	3.1×10^{-11}	7
11	1.6×10^{-11}	4
12	1.3×10^{-11}	3
13	3.0×10^{-11}	7
14	2.9×10^{-11}	6
15	2.8×10^{-11}	6
50:50 EFc/C_{10} surface **Mean 6.7, Median 7.5, Std. deviation 3.0**		
1	1.2×10^{-11}	3
2	1.5×10^{-11}	3
3	3.0×10^{-11}	7
4	2.8×10^{-11}	6
5	3.4×10^{-11}	8
6	9.2×10^{-12}	2
7	3.9×10^{-11}	9
8	4.5×10^{-11}	10
9	4.1×10^{-11}	9

10	4.6×10^{-11}	10
50:50 EFc/C_{11} surface **Mean 8.2, Median 9.5, Std. deviation 3.4**		
1	5.4×10^{-11}	12
2	4.5×10^{-11}	10
3	1.13×10^{-11}	3
4	1.36×10^{-11}	3
5	4.8×10^{-11}	11
6	2.7×10^{-11}	6
7	5.4×10^{-11}	12
8	4.4×10^{-11}	10
9	4.0×10^{-11}	9
10	2.7×10^{-11}	6
20:80 EFc/C_8 surface **Mean 5.6, Median 6.0, Std. deviation 1.5**		
1	2.9×10^{-11}	6
2	3.03×10^{-11}	7
3	2.6×10^{-11}	6
4	1.3×10^{-11}	3
5	2.7×10^{-11}	6

10:90 EFc/C_8 surface **Mean 0.5, Median 0.4, Std. deviation 0.2**		
1	1.84×10^{-12}	0.4
2	4.5×10^{-12}	1
3	1.9×10^{-12}	0.4
4	1.8×10^{-12}	0.4
1:99 EFc/C_8 surface **Mean 0.1, Median 0.2, Std. deviation 0.5**		
1	7.95×10^{-13}	0.2
2	4.5×10^{-13}	0.1
3	7.8×10^{-13}	0.2
BuFc surface **Mean 8.0, Median 11.0, Std. deviation 6.0**		
1	6.2×10^{-11}	13
2	2.3×10^{-12}	1
3	9.1×10^{-12}	2
4	4.8×10^{-11}	11
5	5.6×10^{-11}	13
TpFc surface		
1	6.2×10^{-12}	1
2	7.2×10^{-12}	2

Publication